Scuola di Dottorato in Ingegneria Civile e Architettura

Dottorato in Ingegneria Strutturale e Geotecnica

MASONRY NONLINEAR RESPONSE: MODELING AND ANALYSIS OF THE EFFECTS OF DAMAGING MECHANISMS

Cristina Gatta

XXXI Ciclo - A.A. 2018/2019

Dipartimento di Ingegneria
Strutturale e Geotecnica

Sapienza
Università di Roma

SAPIENZA
UNIVERSITÀ DI ROMA

Faculty of Civil and Industrial Engineering
Department of Structural and Geotechnical Engineering

PhD Thesis in Structural Engineering

Masonry nonlinear response: modeling and analysis of the effects of damaging mechanisms

PhD Candidate:
Cristina Gatta

Advisor:
Prof. Daniela Addessi

Co-Advisor:
Prof. Fabrizio Vestroni

Rome, February 2019

To my family.

Abstract

Over the last decades, many efforts were devoted to develop efficient and accurate numerical procedures for the assessment of the structural capacity of masonry constructions. The main difficulties in modeling this type of material are due to its heterogeneous nature. Indeed, masonry is composed by blocks, stones or bricks, connected with or without mortar, whose geometry, mechanical properties and arrangement strongly affect the overall response. Among the available modeling strategies, finite element models appear to be suitable tools to describe the evolution of the nonlinear mechanisms developing in the material under typical loading conditions. Within this framework, macromechanical models, which consider masonry as an equivalent homogeneous, isotropic or anisotropic medium, are a fair compromise between accuracy and computational burden.

Stemming on the above considerations, this work focuses on the development of constitutive laws involving damage and plasticity inner variables, tailored to the macromechanical analysis of $2D$ masonry structures. Herein, a new isotropic damage-plastic model, which is an enhanced version of that presented by Addessi et al. (2002), is proposed. This model is able to capture the degrading mechanisms due to propagation of microcracks and accumulation of irreversible strains, as well as the stiffness recovery related to cracks re-closure. Moreover, to account for the variation of the mechanical properties in the different material directions, a novel orthotropic damage model is developed to deal with regular masonry textures.

The proposed models are implemented in finite element procedures, where the mesh-dependency problem is efficiently overcome by adopting nonlocal integral formulations. Numerical applications are performed to assess the models capacity of describing the material inelastic behavior and comparisons of numerically and experimentally evaluated responses are also provided for some masonry panels. Finally, the effects of degrading mechanisms on masonry dynamic behavior are investigated. For this purpose a systematic approach is adopted, based on the evaluation of the frequency response curves of masonry walls. The obtained curves show peculiar characteristics due to the irreversible effect of damage, which leads to degradation of the structural mechanical properties and the related variation of the natural frequencies, which in turn significantly influence the dynamic amplification of the response. The numerical results are also confirmed by shaking table tests performed on tuff masonry walls loaded out-of-plane.

Acknowledgements

Sono molte le persone che mi sono state accanto durante questi anni di studio e a cui voglio dedicare i miei sentiti ringraziamenti.

Per primi, vorrei ringraziare la Professoressa Addessi ed il Professor Vestroni per tutto il tempo e le energie che mi hanno dedicato. Loro mi hanno guidato in questo percorso ed a loro devo tutto ciò che ho imparato. Il supporto professionale ed umano di entrambi mi spinge ogni giorno a fare meglio.

Ringrazio i miei genitori, mia sorella e mia nonna per essersi sempre presi cura di me e per avermi dato la forza di reagire nei momenti di sconforto.

Ringrazio Eleonora, Marilù, Marla, Angelo, Enrico e Paolo. Li ringrazio per la loro sincera amicizia, per aver condiviso con me le loro conoscenze e per aver reso più allegre le nostre giornate di lavoro. Loro sono stati un ulteriore regalo di questo dottorato.

Vorrei anche ringraziare i miei compagni di corso di dottorato, perchè insieme abbiamo raggiunto tanti piccoli traguardi. Vorrei dedicare un pensiero particolare a Giulia, in quanto in lei ho trovato un'amica.

Infine ringrazio Valerio, perchè mi spinge a credere di più in me stessa e perchè lui vive con me le mie ansie e le mie gioie.

There are many people I want to thank because they took care of me during these years of study.

First of all, thanks to Professor Addessi and Professor Vestroni for the time and energy that they dedicated to me. They guided me and I owe them everything I learned. Their professional and human support spurs me every day to do better.

I thank my parents, my sister and my grandmother for always taking care of me and for giving me the strength to react in discouragement times.

I would like to express my gratitude to Eleonora, Marilù, Marla, Angelo, Enrico and Paolo. I thank them for their honest friendship, for sharing their knowledge with me and for making our days of work more cheerful. They were a further gift from this PhD course.

I would also like to thank all PhD students of my doctorate program, as together we achieved several small goals. I dedicate a special thought to Giulia, because she became my friend.

Finally, I thank Valerio. He provokes me to believe more in myself and he lives with me my anxieties and my joys.

Contents

List of Figures

List of Tables

Chapter 1

Introduction

1.1 Motivations and objectives

In many countries, masonry structures are a significant part of historical and architectural heritage. This is to due the several advantages that the material offers, such as economy, high fire resistance and recyclability. However, as known, a complex mechanical response emerges due to the heterogeneous nature of the material, composed of units, stones or bricks, connected with o without mortar, whose geometry, mechanical properties and arrangement strongly affect the overall response. A large variety of textures can be found for both stone and brick masonry walls. Based on the stones arrangement in the construction and degree of refinement in the surface finish, stone masonry can be broadly classified in two categories: Rubble or Ashlar masonry. The former is obtained by adding undressed or roughly dressed stones in the mortar, the last is built from accurately dressed stones with uniform and fine joints, as shown in Figures 1.1(a-c).

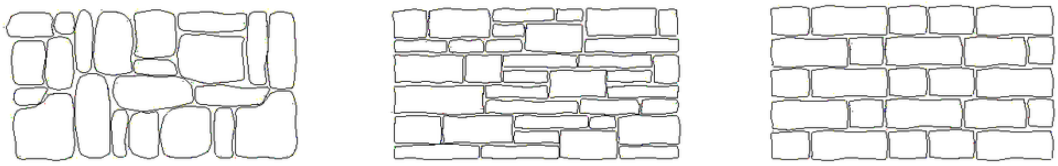

(a) Rubble (b) Ashlar (c) Coursed ashlar

Figure 1.1: Stone masonry textures.

Several types of brick masonry can also be found, depending on the stretchers (bricks laid flat with the long face parallel to the wall) and headers (bricks laid flat with their width at the face of the wall) arrangement. Figures 1.2(a-d) show some examples of the most widespread textures: running, flemish, english and header bond texture, respectively.

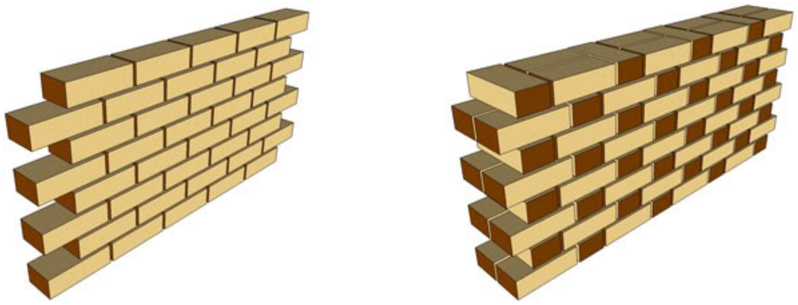

(a) Running bond

(b) Flemish bond

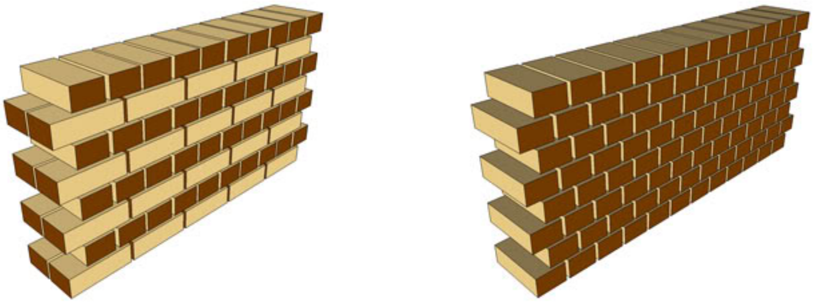

(c) English bond

(d) Header bond

Figure 1.2: Brick masonry textures.

Despite different behavior can occur depending on the adopted masonry typology, some recurrent features can be identified. During the deformation process under typical loading conditions, complex nonlinear mechanisms start and evolve, making masonry global response strongly nonlinear, non-symmetric, with the possible presence of strain-softening branches. Irreversible strains develop mainly due to the activation of friction mechanisms at interface between mortar and units and, due to the components brittle nature, microvoids and microcracks appear and propagate in the mortar joints, in the bricks and at the interfaces, leading to formation of macro-fractures and, eventually, to masonry collapse. Furthermore, in cases of regular texture, as those sketched in Figure 1.2, mortar joints act as plane of weakness and, consequently, directional mechanical properties emerge with strongly anisotropic responses.

At structural level, masonry buildings exhibit good resistance to vertical loads, while they perform badly against horizontal actions. This is testified by their high seismic vulnerability, mainly due to the low material tensile strength and often inadequate structural configurations. Figures 1.3(a-c) show the main collapse mechanisms identified on the basis of earthquake's effects on masonry structures, namely crumbling, out-of-plane and in-plane failures. When proper masonry textures are adopted, thus preventing the crumbling phenomenon, it was widely assessed that out-of-plane collapse mechanisms are the most frequent. The walls loaded normally to their plane undergo flexure and, when internal stresses exceed the material strength, crack patterns develop with directions depending on the edge restraint positions. In fact, boundary conditions are a relevant point, as the response can involve one-way bending or two-way bending, as depicted in Figures 1.4(a-b) and (c), respectively.

(a) Masonry crumbling (b) Out-of-plane failure (c) In-plane failure

Figure 1.3: Failure mechanisms of masonry structures.

Experimental tests on uncracked masonry panels loaded out-of-plane (Griffith et al., 2004, 2007) carried out a typical load-displacement curve. This results characterized by an initially linear elastic branch until tensile strength is reached, followed by a nonlinear phase, where cracks start and evolve. With increasing deformation the wall becomes fully cracked and, under cyclic loadings, behaves as a rocking block. Figures 1.5(a) and (b) compare the load-displacement curves of

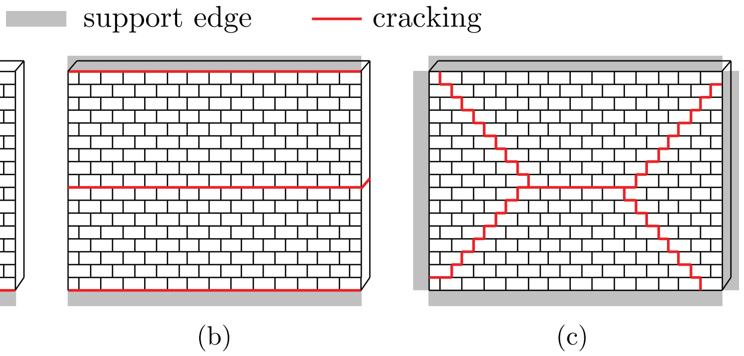

(a) (b) (c)

Figure 1.4: Typical out-of-plane failure cracking: (a) and (b) vertically spanning one-way walls and (c) two-way spanning walls.

simply supported 'uncracked' and 'precracked' one-way vertically spanning walls experimentally obtained by Griffith et al. (2004). Here, the benefit of the material tensile strength can be noted, as the maximum force of the uncracked panel is much higher than that of the corresponding cracked wall. Traditional force-based approach relates the seismic resistance of fully cracked walls to the maximum force at the threshold of overturning, determined from simple equilibrium conditions. In contrast, recent research showed that dynamically loaded walls can sustain accelerations higher of their 'quasi-static' resistance, thus leading to the development of displacement-based methods, which define the seismic resistance of the walls on the basis of the maximum sustainable displacement. However, as underlined by Abrams et al. (2017), response to out-of-plane actions is affected by many factors: the level of the axial forces, size and position of openings, quality of connections between the structural elements and, also, by the in-plane damage of the adjacent walls. In-plane failure can involve sliding of mortar joints, diagonal cracking bands or damaged zones located at the corners of the panels, depending on geometry, loading and boundary conditions (Anthoine et al., 1995; Frumento et al., 2009). Typically, flexural responses (Figure 1.6(a)) lead to cyclic load-displacement curves resulting in 'S-shape' cycles, as the response is controlled by opening and subsequent re-closure, under load reversal, of the tensile crack at the ends of the panels. On the contrary, shear failure (Figure 1.6(b)) is associated with a more brittle behavior usually due to the formation of diagonal damaged zones in the central part of the walls.

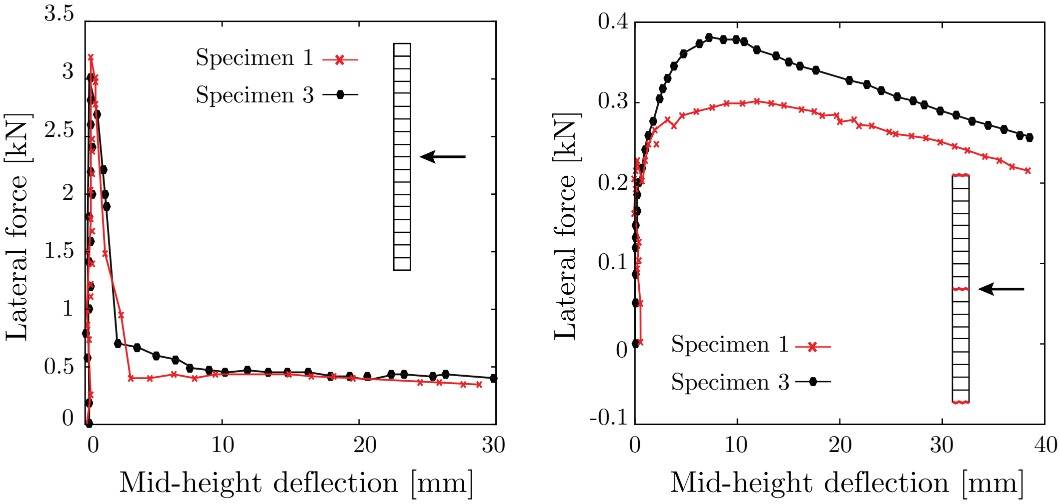

(a)

(b)

Figure 1.5: Griffith et al. (2004): pushover curves of (a) uncracked and (b) pre-cracked walls loaded out-of-plane (adapted by Minga et al., 2018).

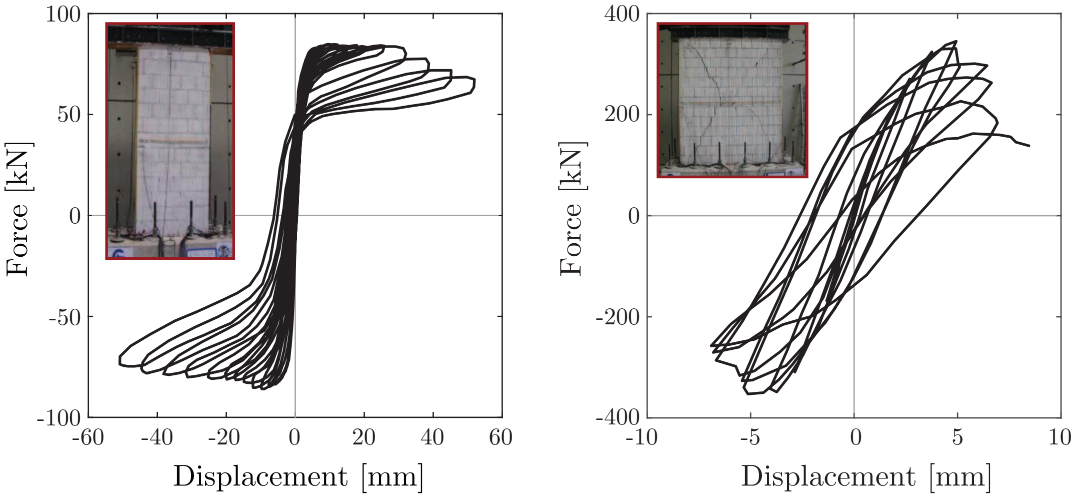

(a)

(b)

Figure 1.6: Frumento et al. (2009): in-plane response of double-fixed masonry walls undergoing (a) flexural and (b) shear failure modes.

On the basis of the activated failure modes, different strength-stiffness decay and hysteretic dissipation characteristics emerge. These translate in very complex dynamic responses, as the evolution of degrading mechanisms modify the dynamic structural properties. In fact, as extensively employed to damage identification and structural health monitoring, onset and propagation of damage leads to degradation of the structural mechanical properties and the related variation of the natural frequencies, which in turn significantly affect the resonant conditions (Toti et al., 2015). Thus, in last decades, many efforts were devoted to understand and predict the complex behavior of masonry in the dynamic field. In particular, shaking table tests (Benedetti et al., 1998; AlShawa et al., 2012; Candeias et al., 2017) on scaled or full-scale prototypes were performed with the aim of assessing structural performances under both seismic actions and harmonic excitations.

To now, many methods and computational tools were proposed to deal with the problem of assessing structural capacity of masonry constructions (see Chapter 3). The choice of the adopted methodology depends on several factors: searched information, computational cost and available input data, just to cite some. Thus, the identification of a unique model with general validity represents a hard, perhaps unrealistic, task. Among the others, finite element approaches appear as attractive tools to describe evolution of nonlinear mechanisms evolving in masonry material. In particular, models based on Damage Mechanics allow to describe the degrading effects by making use of the consolidate principles of Continuum Mechanics. These, differently from models based on Fracture Mechanics Theory, do not represent the cracks as embedded in the material, but take into account the degradation phenomena by means of nonlinear constitutive laws involving damage inner variables. Usually, damage models are combined with plasticity formulations, with the purpose to introduce also the effects of irreversible strains and, thus, provide a more realistic description of the material mechanical response in terms of hysteretic dissipation properties.

The aim of this study relies on the above considerations, as it is focused on the modeling and analysis of the effects of degrading mechanisms on the mechanical response of statically and dynamically loaded masonry walls. The main objectives can be summarized as follows:

- Development of suitable constitutive laws involving damage and plasticity inner variables to account for strength and stiffness degradation and hysteretic dissipation typically characterizing masonry response. Based on a macromechanical description of the material, an isotropic damage-plastic model and an orthotropic damage model are proposed to numerically describe behavior of various masonry typologies;
- Implementation of the proposed models into efficient finite element procedures able to avoid the well-known mesh-dependency drawback emerging in cases of strain-softening behavior;
- Analysis of the effects of nonlinear mechanisms on the static and dynamic response of masonry structural elements. Particular attention is devoted to the dynamic characterization of masonry walls by framing dependency of their response on the main properties of the loading history, such as frequency and amplitude.

1.2 Organization of the thesis

The thesis is organized as follows:

- Chapter 2 offers on overview of experimental tests performed on masonry and its constituent materials with the aim of identifying recurrent features of the mechanical response.
- Chapter 3 describes the available modeling strategies for masonry structures, with particular emphasis to the finite element (FE) approach.
- Chapter 4 presents a new isotropic damage-plastic model for the macromechanical analysis of $2D$ masonry structures. First, the constitutive relationship and the computation aspects related to the finite element implementation are illustrated. Then, comparison between numerical and experimental outcomes are provided for some masonry panels with the aim of validating the proposed model.

- Chapter 5 proposes a modified version of the damage model presented in Chapter 4 with the purpose to account for the anisotropic response of the material. Thus, an orthotropic description of the elastic and inelastic behavior is introduced. Validation examples are presented, which are chosen to evaluate the model capability to describe the substantial discrepancies among phenomenological properties observed in different material directions.

- Chapter 6 moves towards exploration of dynamic response of masonry walls. The effects of nonlinear phenomena, such as damage and plasticity, on the dynamic amplification of the response are analyzed by using a systematic approach based on evaluation of frequency response curves (FRCs). Furthermore, shaking table tests performed on tuff masonry walls are described and the experimental outcomes are compared with the numerical results.

- Chapter 7 summarizes the main contributions and offers overall concluding remarks.

Chapter 2

Masonry mechanical response

This chapter is aimed at characterization of masonry mechanical response through an overview of experimental investigations. Particular attention is devoted to masonry with regular arrangement of constituent materials, i.e. bricks and mortar, where bed joints act as weak planes. The described tests testify that detailed informations about the material properties can be obtained and used to rationally design procedures based on numerical models. First, in section 2.1, the main properties of the constituent materials are discussed. Then, in section 2.2, response of small and large masonry assemblages, as well as of more complex structures, is analyzed with reference to some well-known experimental campaigns.

2.1 Constituent materials mechanical response

Heterogeneous masonry can be decomposed into three components, that is mortar, units and interfaces (representing the interaction behavior between mortar and units). Their main mechanical properties are analyzed in the current section.

2.1.1 Mortar and units

Despite masonry mechanical response can not be simply considered as an average of its constituents, this results strongly affected by strength and deformability characteristics of mortar and units.

Compressive tests on masonry components are the most widespread, because of their more reliability with respect to tensile and shear tests. Compressive strength of masonry units is usually investigated through standard tests with solid platens. The resulting maximum strengths have to be corrected with proper factors to take into account the restraint effect of the platens. Furthermore, it should be remarked that these tests do not provide information on the post-peak behavior. As concern mortar compressive response, this is usually explored by using cylindrical and prismatic specimens with resulting compressive strength dependent on water-binder ratio and cement content. Compressive tests allow also to determine deformability characteristics, in terms of Young's modulus and Poisson ratio, by measuring longitudinal and transversal strains to the load direction. The Young's modulus (E) is obtained as the slope of the linear part of the stress-strain relationship, whereas Poisson ratio (ν) results from the ratio between transversal and longitudinal strains. In general, different characteristics in strength and deformability are found for units and mortar: the former exhibit a brittle response with high resistance, the last shows a more ductile behavior characterized by low strength.

Additionally, indirect tensile and flexural tests are performed to obtain mortar properties in terms of tensile strength. Indirect tensile tests are carried out on cylindrical specimens loaded diametrically across the circular cross section, by causing a tensile deformation perpendicular to loading direction. In flexural test a more localized vertical load is applied at the middle part of the specimen. By registering the ultimate load and by knowing the specimen dimensions, tensile strength of the material can be computed, which is usually characterized by linear correlation with compressive strength (see Figure 2.1).

Some attempts were made to relate tensile strength of masonry unit to its compressive strength, but difficulties arise due to variety of available sizes, shapes and manufacture processes. In general, very low tensile strength is found with respect to the compressive one, with ratio approximatively varying between 0.03 and 0.1.

A significant study concerning mortar and bricks properties can be found in McNary and Abrams (1985). Tri-axial compression tests on four types of mortar, with different cement-to-water ratio (M, S, N, O), were carried out to determine Poisson ratio and Young's modulus, as well as compressive strength for different values of the lateral confining stresses p. As an example, Figure 2.2 shows variation

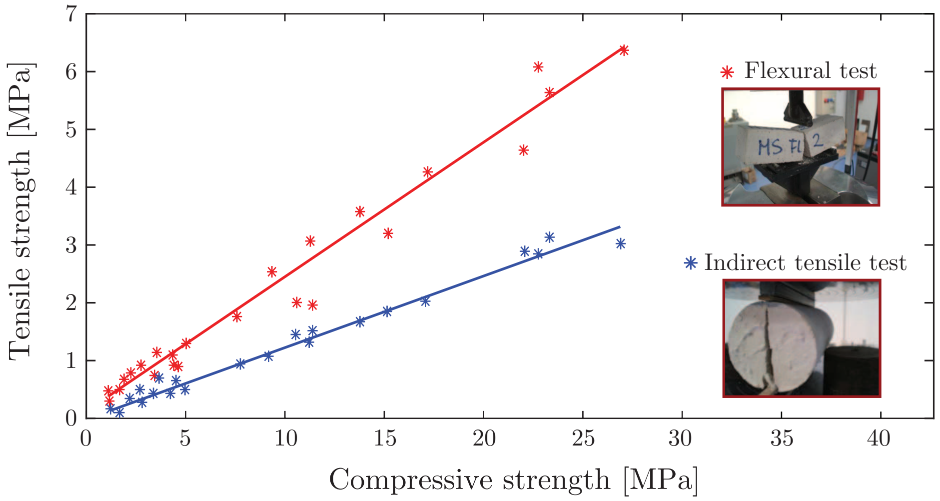

Figure 2.1: Typical correlation between tensile and compressive strength of mortar.

of Young's modulus with normal and confining stresses for the tested type M mortar. Furthermore, it emerged that higher maximum axial stress and strain were associated to larger confining pressure and the nonlinear response occurred already for small strains (see Figure 2.3(a)).

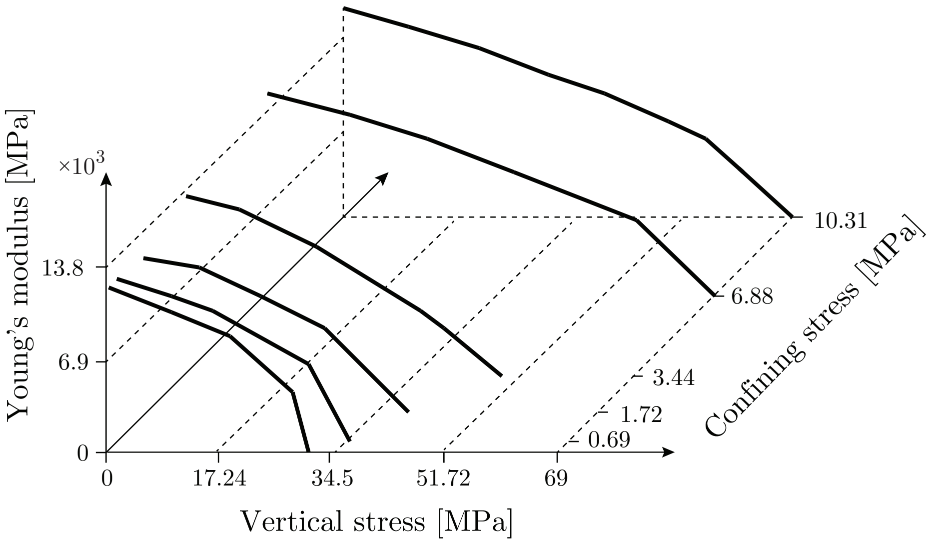

Figure 2.2: McNary and Abrams (1985): variation of Young's modulus with vertical and confining stresses for type M mortar.

Regarding units behavior, bi-axial tests made of axial compressive and bilateral tensile stresses were performed on two types of brick with the purpose to determine the splitting strength. Figure 2.3(b) presents the obtained relationship between compressive C and tensile T stress in bricks, nondimensionalized with respect to uni-axial compressive strength C_0 and direct tensile strength T_0, by showing a concave nonlinear trend of the failure curve obtained as the best fit of experimental data.

Described phenomena testify complexity of the mechanical response of bricks and mortar, whose interaction effects define behavior of masonry composite material.

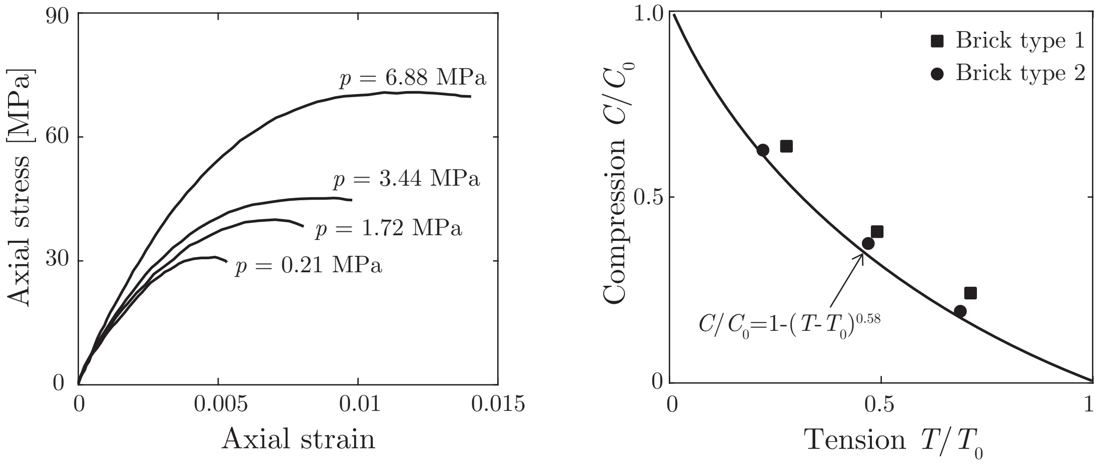

(a) (b)

Figure 2.3: McNary and Abrams (1985): (a) variation of compressive strength with confining pressure p for type M mortar; (b) measured bi-axial interaction diagram for brick specimens.

2.1.2 Unit-mortar interface

Unit-mortar interface is often regarded as the weakest component of masonry composite material. Thus, joints response was largely investigated under both tensile and shear loads by pointing out peculiar characteristics in terms of strength, fracture energy and stress-strain relationship. All these features are discussed in what follows.

2.1.2.1 Tensile response

Experimental tests showed that tensile failure, usually occurring at the unit-mortar interface, is one of the main cause of collapse of masonry assemblages. Different test set-up, including flexural testing, diametral compression (splitting test) and direct tension testing, were used to characterize tensile behavior. For instance, Van der Pluijm (1997) performed tensile and flexural tests on small masonry assemblages of solid clay bricks and calcium-silicate bricks in combination with different mortar types. Tensile tests were conducted on masonry couplets in displacement control, as schematically shown in Figure 2.4(a).

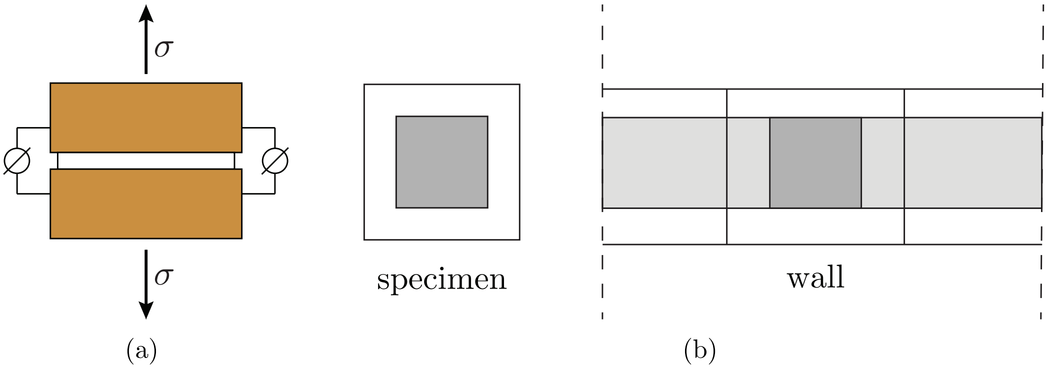

(a) (b)

Figure 2.4: Van der Pluijm (1997): (a) test specimen in direct tension, (b) net bond surface of the wall extrapolated from the specimen.

Experimental outcomes highlighted low tensile bond strength, exponential softening branches in the stress-strain relationship with mode I fracture energy G_f^I ranging from 0.005 to 0.02 Nmm/mm^2, according to the unit-mortar combination. This fracture energy G_f^I was defined as “the amount of energy by unit of area that is needed to create a crack in which no tensile stresses can be transferred". Furthermore, the bond area of the cracked specimens, the so-called net bond surface, was smaller (on average 35%) than the cross sectional area of the specimens and usually located at the samples inner part. This was probably due to the mortar shrinking and the setting of the mortar in its plastic phase. The net bond surface of a common wall was approximately estimated 1.7 times greater than that of the specimen, as two of the four edges are not present, as shown in Figure 2.4(b). Similar considerations were made for the fracture energy and tensile strength of the wall.

The 4-point bending arrangement, sketched in Figure 2.5, was used to perform flexural tests on stack bonded prisms 6 brick high. By measuring specimen deflection, it was possible to push the tests beyond the maximum strength and measure the fracture energy G_f^I.

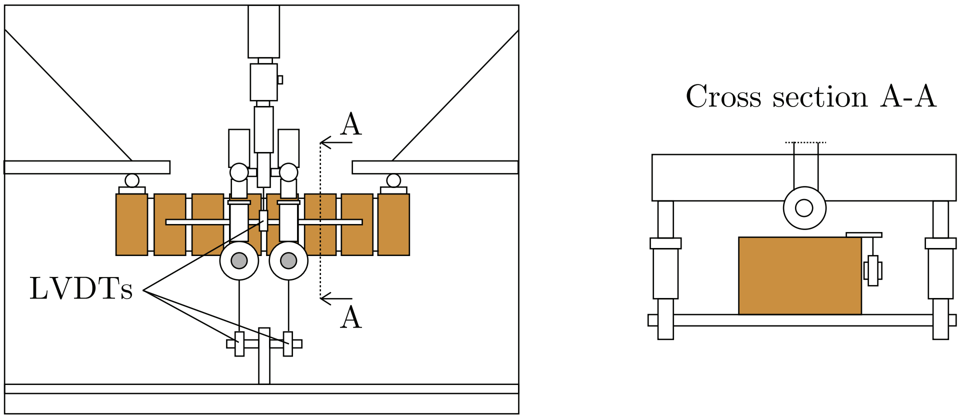

Figure 2.5: Van der Pluijm (1997): detailed view of a specimen in the 4-point bending test arrangement.

Fracture energy values determined by the flexural tests were compared to those obtained by the tensile tests, resulting 2 or 3 times higher. This difference was partially explained with reference to the bonding surface shape. Indeed, as pointed out above, a ratio of 1.7 was estimated between the net bond surface of the wall and the couplets, as concerns the tensile test, while the bonding surface of the flexural specimen was almost the same of the wall, because two slices on the head sides of specimens were cut off.

The characterization of the tensile behavior of unit-mortar interface plays a significant role in the overall response of masonry structures, as in many cases the tensile strength of composite material can be regarded as the tensile bond strength between mortar and units.

2.1.2.2 Shear response

Several studies were focused on the shear behavior of bed joints, as shear failure is a dominant collapse mechanism for masonry structures subjected to horizontal loads. Usually, shear actions are accompanied by compression or tension loads. Thus, pure shear modes are alternated to shear-compression and shear-tension modes in experimental investigations.

The main difficulties in performing shear test are related to ability of the test set-up to induce an uniform stress state in joints. Van der Pluijm (1993) developed the test set-up shown in Figure 2.6(a), able to keep a constant normal confining pressure upon shearing. As the test arrangement could not be used to perform shear-tension tests, it was modified (Figure 2.6(b)) in Van der Pluijm et al. (2000) with the purpose to experience masonry assemblages under programmable combination of tension and compression perpendicular to bed joint and, thus, to establish a complete failure envelope for joints and bond interface loaded in shear.

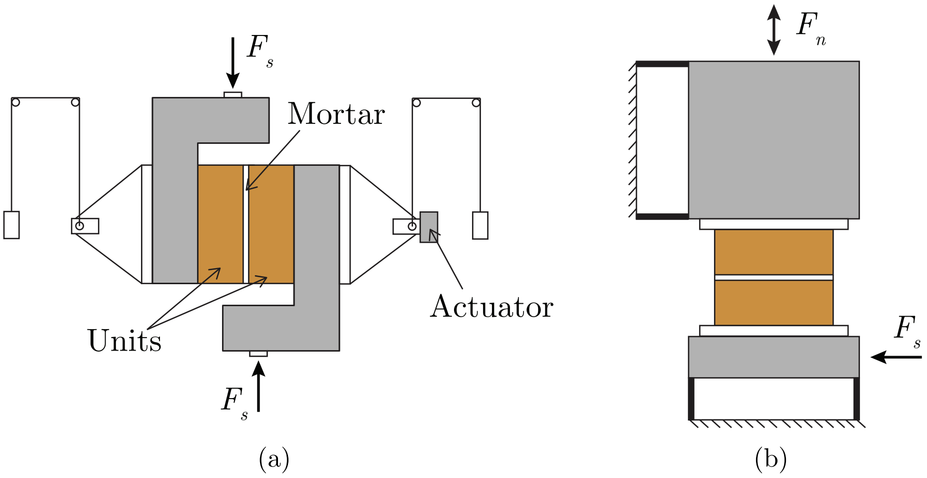

(a) (b)

Figure 2.6: Experimental set-up for shear test from (a) Van der Pluijm (1993) and (b) Van der Pluijm et al. (2000).

In Figure 2.7(a) the experimental outcomes are contained in terms of shear stress τ vs. shear displacement u_s, obtained by Van der Pluijm (1993) by applying three confining (compressive) stress levels p: -0.1, -0.5 and $-1.0\,\text{MPa}$. The overall behavior showed a great similarity with the tensile response, as exponential softening branches appeared. However, the curves did not fall to zero, but became stable at a certain value of the shear stress, namely residual dry friction shear. It can be remarked that, depending on the compression level, different strengths and friction levels were obtained, as well as different slopes of descending branch. Moreover, fracture energy G_f^{II} associated to shear mode (defined as the area under the stress-displacement diagram and the residual dry friction shear level) increased with the compressive stress.

A further significant phenomenon in a shear test is the dilatant behavior, that is the occurrence of a lifting displacement u_n directed perpendicularly to the imposed shear displacement u_s (Figure 2.7(b)). It is usually described in terms of dilatancy angle Ψ, defined as:

$$\Psi = \arctan\frac{u_n}{u_s}\ . \tag{2.1}$$

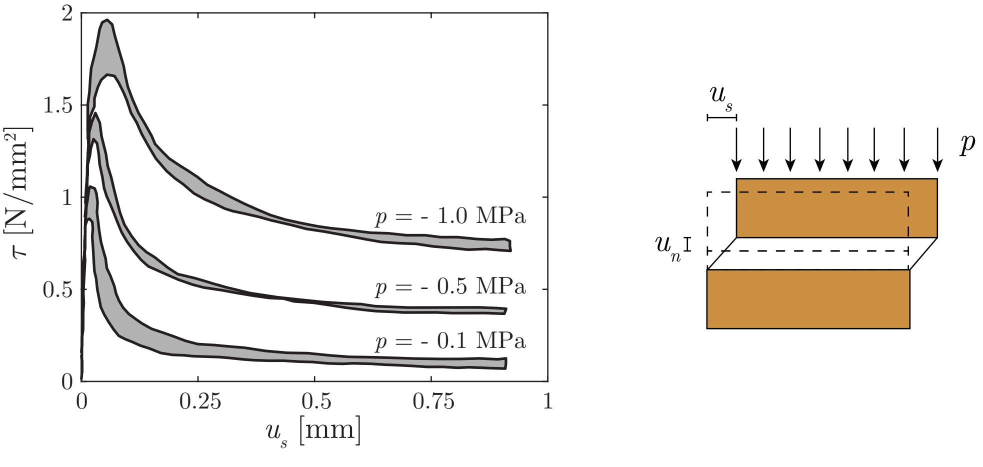

(a) (b)

Figure 2.7: Van der Pluijm (1993): (a) shear stress-shear displacement curves for different values of confining stress p; (b) dilatant behavior.

Physically, this is due to a non-smooth cracked surface, so shearing goes together with an uplift, whose maximum value is related to the roughness of the cracked surface. The experimental evidences showed decreasing dilatancy with increasing shear displacement due to the smoothing of the sheared surfaces, as shown in Figure 2.8(a) by the typical evolution of u_n for increasing values of u_s at constant confining pressure (u_n positive if lifting). Furthermore, sensibility to the confining pressure was found, with tan Ψ tending to zero for increasing compression stresses (Figure 2.8(b)).

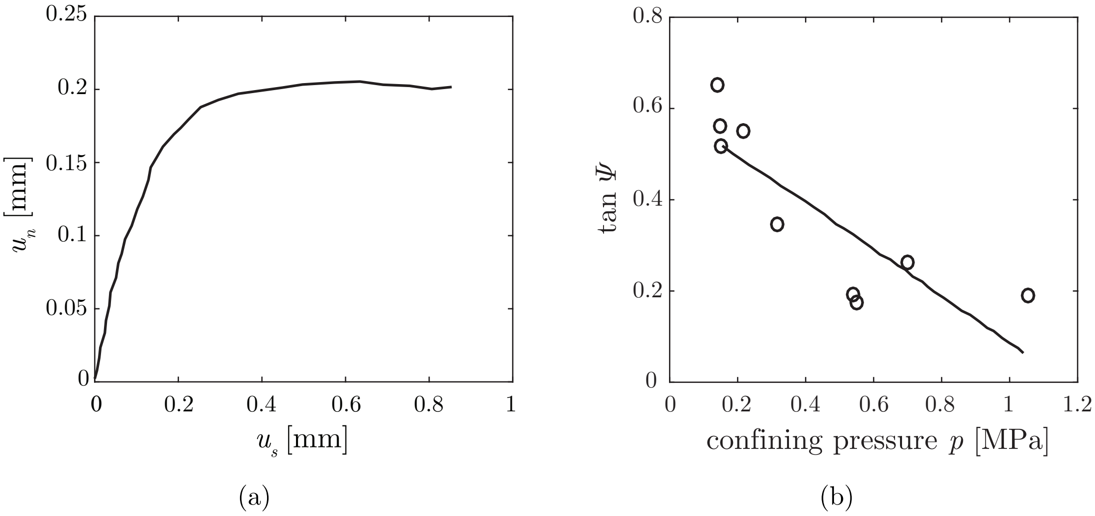

(a) (b)

Figure 2.8: Van der Pluijm (1993): (a) typical variation of normal displacement u_n with increasing shear displacement u_s; (b) evolution of dilatancy tan Ψ with the confining pressure p (adapted by Lourenço, 1996).

Similar trends were observed in Van der Pluijm et al. (2000), where normal stress levels of -0.6, -0.3, 0, 0.05, 0.1, 0.15, 0.2 MPa and increasing shear deformation were applied to masonry consisting of clay bricks (wc-JO96) with general purpose mortar (GPM) and masonry made of calcium silicate blocks (CS-block96) with prefabricated thin layer mortar (TLM). Bond failure at the interface and bond failure combined with tensile failure of bricks were the most frequent mechanisms observed during the tests. However, also other failure modes can take place, as depicted in Figure 2.9(a-d). Referring to the test series where only one failure mode occurred, linear relation between fracture energy, G_f^{II}, and normal stress,

p, was found, as plotted in Figure 2.10(a). Thus, two equations of the regression lines were proposed to identify the lower and upper bound (G_f^{II} in N/mm and p in MPa), respectively:

$$\begin{aligned} G_f^{II} &= -0.02\ p + 0.005\ , \\ G_f^{II} &= -0.14\ p + 0.02\ . \end{aligned} \tag{2.2}$$

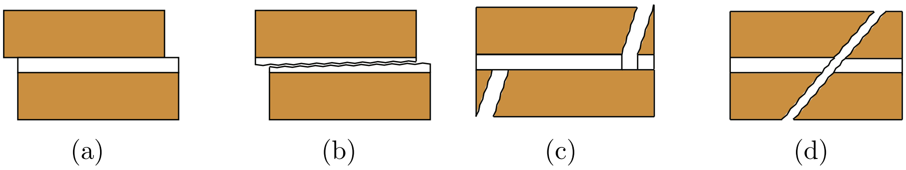

Figure 2.9: Failure mechanisms for combined normal and shear stress: (a) bond failure, (b) failure in mortar and bond failure, (c) bond failure and tensile failure of units and (d) diagonal tensile failure of units.

The bed joint shear failure was investigated also applying cyclic loading. Atkinson et al. (1989) conduced direct shear experiments on three series of masonry specimens consisting of old clay units, modern clay units and specimens collected from brick walls damaged during the 1987 Whittier earthquake. With reference to old brick specimens, Figure 2.10(b) shows a typical load-relative displacement (between the upper and lower side of the samples) curve obtained from four cycles direct shear test at a constant normal compressive load. A steep growth in the shear load, followed by a decreasing shear resistance and residual strength, can be noted, similarly to the experimental outcomes in Figure 2.7(a). After the first cycle, no further peaks were found and the shear resistance settled on a constant value, which was not affected by the number of cycles. The small peak obtained during the reversal shear in the first cycle appeared at low level of normal loads and it vanished to higher stress values. Similar considerations hold for the other series of tested masonry. On the overall, a much higher peak strength is emerged for new brick assemblages with respect to the old ones, while residual strength was essentially the same. In the investigated normal stress range, it was noticed that both peak and residual strengths could be modeled by a Mohr-Coulomb criterion ($\tau = c + \sigma_n \tan\phi$) accounting for cohesive strength c and friction angle ϕ.

However, nonlinear relationship of strength with normal stress can be also found, as obtained by Drysdale et al. (1979) to for high normal stress values.

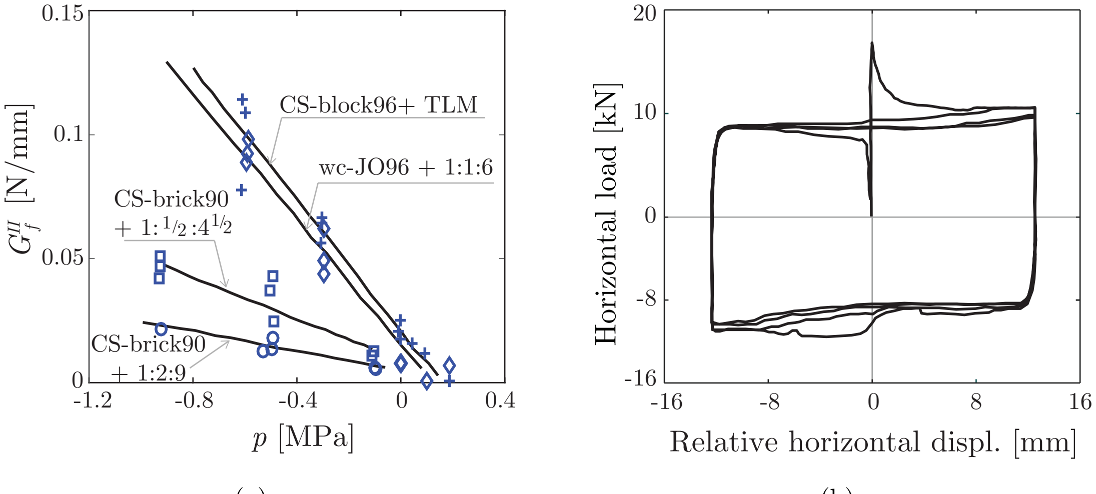

(a)

(b)

Figure 2.10: Shear response of bed joints: (a) correlation between fracture energy G_f^{II} and normal applied stress p (Van der Pluijm et al., 2000); (b) typical response curve for four-cycle shear test (Atkinson et al., 1989).

2.2 Masonry composite material

Behavior of the composite material is described next with reference to small and large masonry assemblages. Strength characteristics are discussed by pointing out influence of orientation of the applied stresses with respect to bed joints direction. Furthermore, attention is devoted to investigate mechanical response of shear walls, as these represent the main reaction systems in masonry building. Monotonic and cyclic loads are considered and effects of geometry, boundary and loading conditions are underlined.

2.2.1 Tests on small assemblages

2.2.1.1 Uni-axial tensile stress

Masonry tensile strength is strongly dependent on both mechanical properties of the constituent materials and orientation of the applied stresses with respect to bed joint direction. Failure in tension is usually associated to a localized fracture process, namely cracking of the material, which is reflected into stress-strain relationships with strength-stiffness decay and marked softening branches, as shown in Figures 2.11(a).

In general, for tensile stress normal to bed joints, tensile strength can be considered equal to tensile bond strength between mortar and units. On the contrary, failure is associated to excessive stresses in the bricks when masonry characterized by low strength units and high tensile bond strength are considered.

To characterize the response under tensile stress parallel to bed joints, Backes (1985) tested masonry wallets in direct tension. The test results showed that the crack paths were strongly affected by quality of components: cracks passed along the head joints and the center of the bricks (Figure 2.11(b)) for masonry composed by strong mortar and weak units, while zigzag paths (Figure 2.11(c)) appeared for weak mortar and strong bricks.

Tensile strength and failure modes were also investigated under tensile loads having different orientation ϑ from the bed joint direction. Drysdale and Hamid (1982) performed axial tension tests on masonry samples made of three different types of mortar (mortar M, S and N characterized by increasing compressive strength). Figures 2.12(a) and (b) provide exemplary failure modes obtained for loads parallel and normal to bed joints, characterized by mortar debonding accompanied by tensile failure of bricks and mortar debonding alone, respectively. For tension oriented between 15° and 75° always debonding along combination of bed and head joints appeared, as shown in Figure 2.12(c) with reference to tensile load rotated of 30° from bed joints. Furthermore, Figure 2.13 summarizes all the available data of tensile strength, by clearly highlighting sensitivity to orientation of the applied stress and by showing that bond characteristics of the mortar are not directly related to its strength properties.

Similar considerations hold for the tensile tests performed by Page (1983) on

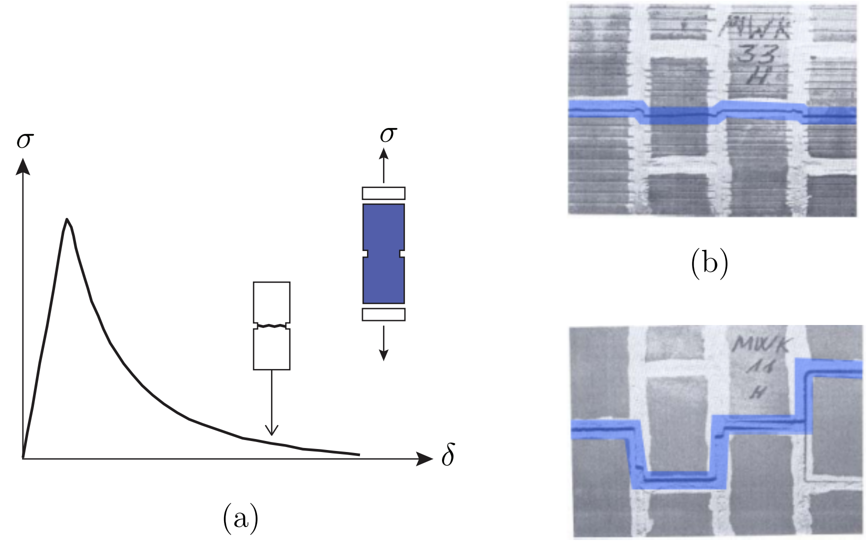

(a)

(b)

(c)

Figure 2.11: Tensile behavior: (a) typical response under uni-axial tension; failure paths (Backes, 1985) with (b) cracks passing along mortar and bricks and (c) zigzag type for load parallel to bed joint orientation.

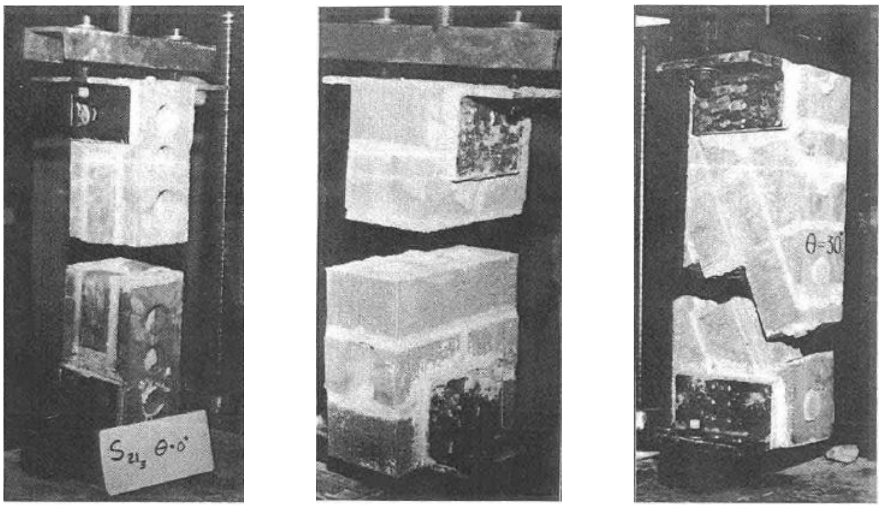

(a) ϑ=0°

(b) ϑ=90°

(c) ϑ=30°

Figure 2.12: Drysdale and Hamid (1982): failure modes obtained for different values of the ϑ angle between applied tensile stress and bed joints orientation.

clay brick masonry (more detailed test description will be provided next), whose results are reported in Figure 2.14 in terms of failure crack paths obtained for different values of the ϑ angle between the applied stress and bed joints direction.

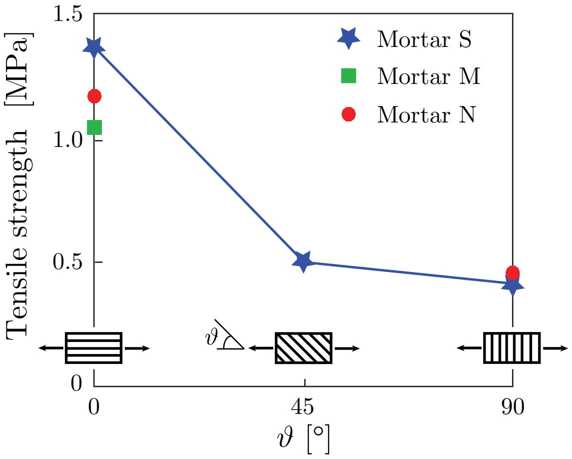

Figure 2.13: Tensile strength obtained by Drysdale and Hamid (1982).

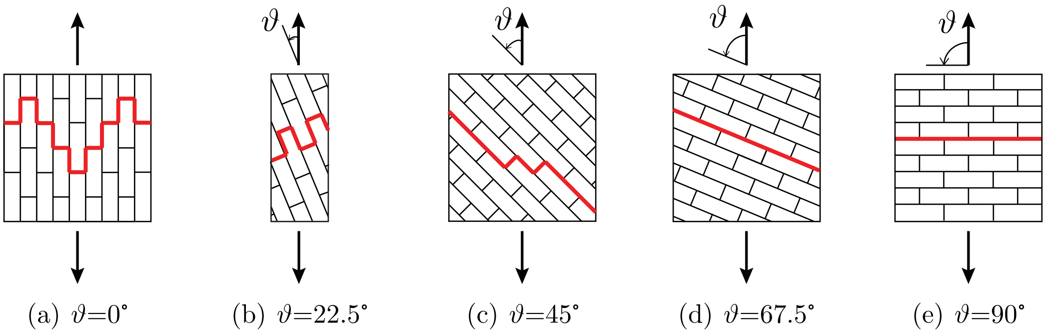

(a) ϑ=0° (b) ϑ=22.5° (c) ϑ=45° (d) ϑ=67.5° (e) ϑ=90°

Figure 2.14: Page (1983): failure modes for uni-axial tensile loads with different orientation ϑ from the bed joint direction.

2.2.1.2 Uni-axial compressive stress

Compressive strength normal to bed joints is regarded as one of the most relevant material property. Experimental studies pointed out its strong dependency on the mechanical properties of the component materials, i.e mortar and units. As remarked in Section 2.1.1, brick response to compressive load usually shows brittle behavior characterized by high strengths, while mortar exhibits a more ductile response with lower resistance. In this case, the response of the composite material is placed between that of its constituents, as Figure 2.15(a) shows with reference to uni-axial compressive tests performed Binda et al. (1996). However, this result can not be considered as general.

Kaushik et al. (2007) experienced masonry prisms made of four brick types and three mortar grades. Experimental outcomes highlighted that the generally believed compressive behavior of masonry placed between that of bricks and mortar, no longer holds when strength and stiffness of bricks and mortar are comparable, as the stress-strain curves of masonry fall on the lower strength of those corresponding constituent materials (Figure 2.15(b)). Anyhow, the different strength and deformable characteristics of units and mortar are precursor of failure, as demonstrated by the pioneer work of Hilsdorf (1969). For instance, considering mortar softer than bricks, as usually happens, a tri-axial compression state in the mortar and a combined compression/bi-axial tension in the brick occur under uni-axial compressive load normal to bed joints (Figure 2.16(a)). Thus, the mortar lateral expansion is confined by the bond and friction between brick and mortar and, as a consequence, vertical cracks appear in the units leading to the specimen collapse (see Figure 2.16(b)).

Less attention was devoted to compressive strength under uni-axial load parallel to bed joints. However, the ratio between parallel and normal compressive strengths usually ranges from 0.2 to 0.8 (Hoffmann and Schubert, 1994). As an example, Page (1981, 1983), within his aforementioned experimental campaign, found a ratio about equal to 0.6.

Further research explored the mechanical response to uni-axial compressive load with different orientations ϑ with respect to bed joints, by obtaining sundry strength values and failure modes (see Figure 2.17).

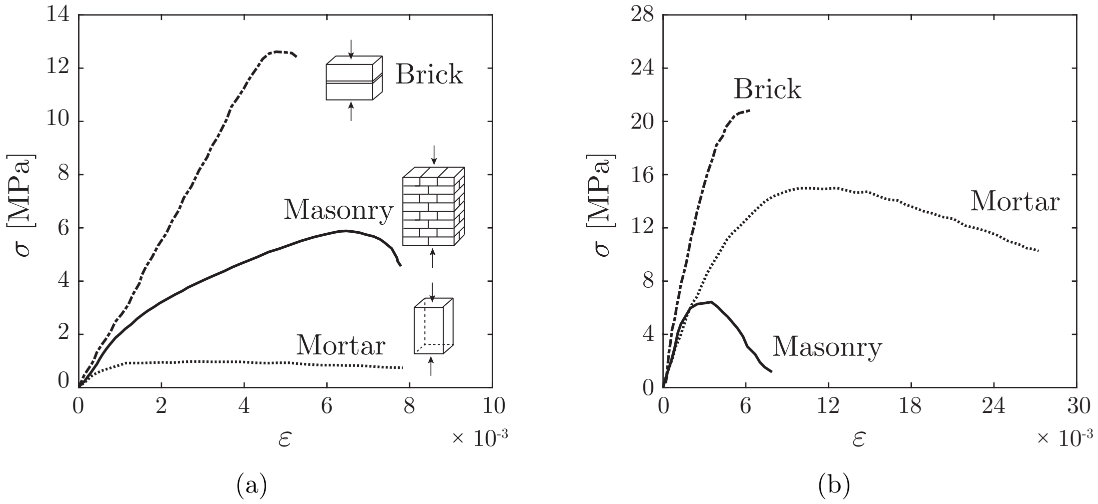

Figure 2.15: Stress-strain curves for bricks, mortar and masonry prisms: (a) weak mortar (Binda et al., 1996) and (b) strong mortar (Kaushik et al., 2007).

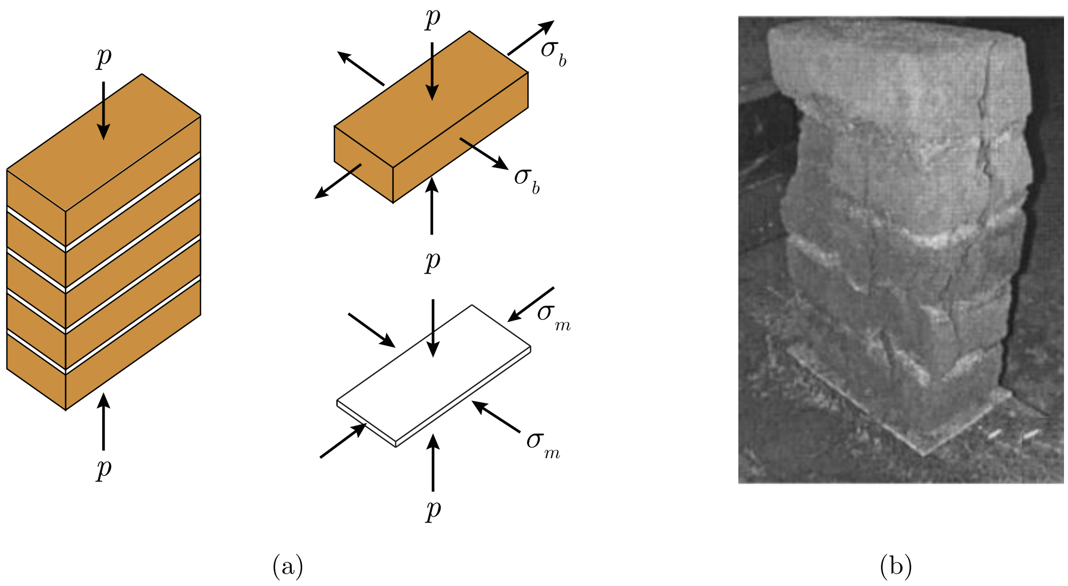

Figure 2.16: Compressive behavior for uni-axial load normal to bed joints: (a) state of stress in masonry prisms and (b) failure mode.

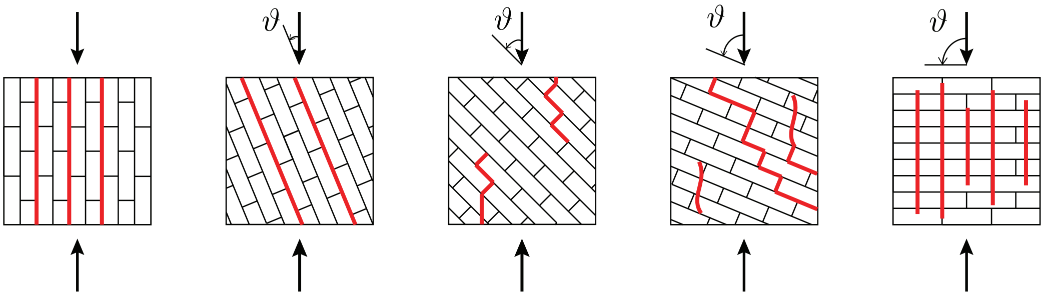

(a) ϑ=0° (b) ϑ=22.5° (c) ϑ=45° (d) ϑ=67.5° (e) ϑ=90°

Figure 2.17: Page (1981, 1983): failure modes for uni-axial compressive loads with different orientation ϑ from the bed joint direction.

2.2.1.3 Bi-axial stress

To fully characterize masonry mechanical behavior, the response under bi-axial stresses was investigated. Page (1981, 1983), as already mentioned, provided a complete set of experimental data by testing 360 mm square panels, made of half-scale solid clay units arranged in running bond texture. These samples were subjected to bi-axial loads, whose orientation with respect to bed joints direction was varied. Indeed, mortar joints act as planes of weakness and their orientation, with respect to applied stresses, strongly affects overall response. Thus, differently from isotropic materials, failure cannot be described in terms of principal stresses only. By defining material axes T and N, as directions parallel and perpendicular to bed joints (Figure 2.18(a)), failure can be defined either in terms of stress state related to the material axes ($\boldsymbol{\sigma}_{TN} = \{\sigma_T, \sigma_N, \tau_{TN}\}^{\mathrm{T}}$), or in terms of principal stresses σ_x and σ_y and orientation ϑ of σ_x with respect to T-axis (Dhanasekar et al., 1985).
The experimental set-up, schematically shown in Figure 2.18(b), was used to test a total of 180 panels with the bed joints orientation and principal stress ratio summarized in Table 2.1.

Basing on the relative proportion of the applied loads, different failure modes occurred: cracking and sliding in bed and/or head joints for uni-axial compression and collapse for cracking in the joints alone or combined failure in bricks and joint for tension-compression loads. In bi-axial compression cases, typical splitting of the specimen at mid-thickness, in a plane parallel to its free surface, was found.

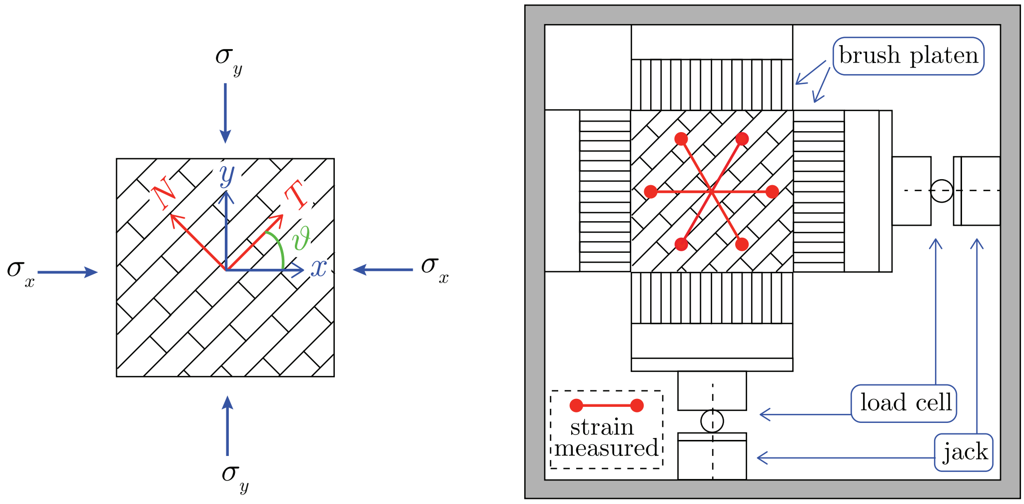

(a) (b)

Figure 2.18: (a) principal stress axes (blue) and material axes (red); (b) arrangement for bi-axial tests performed by Page (1981, 1983).

Stress state	ϑ [°]	σ_y/σ_x ratio	Number of panels
Bi-axial compr.-compr.	0, 22.5, 45, 67.5, 90	1, 2, 4, 10	75
Bi-axial tens.-compr.	0, 22.5, 45, 67.5, 90	-0.5, -0.2, -0.1, -0.03	66
Uni-axial compression	0, 22.5, 45, 67.5, 90	0	21
Uni-axial tension	0, 22.5, 45, 67.5, 90	∞	18

Table 2.1: Summary of bi-axial tests from Dhanasekar et al. (1985).

Figures 2.19 (a-c) show the experimental data in terms of bi-axial strength for different values of ϑ with the aim of studying the influence of the shear stress τ_{TN} in failure surfaces. Anisotropic behavior is markedly shown, as tensile and compressive strengths parallel and normal to bed joints differed. Furthermore, increasing resistance was obtained for bi-axial compressive loads.

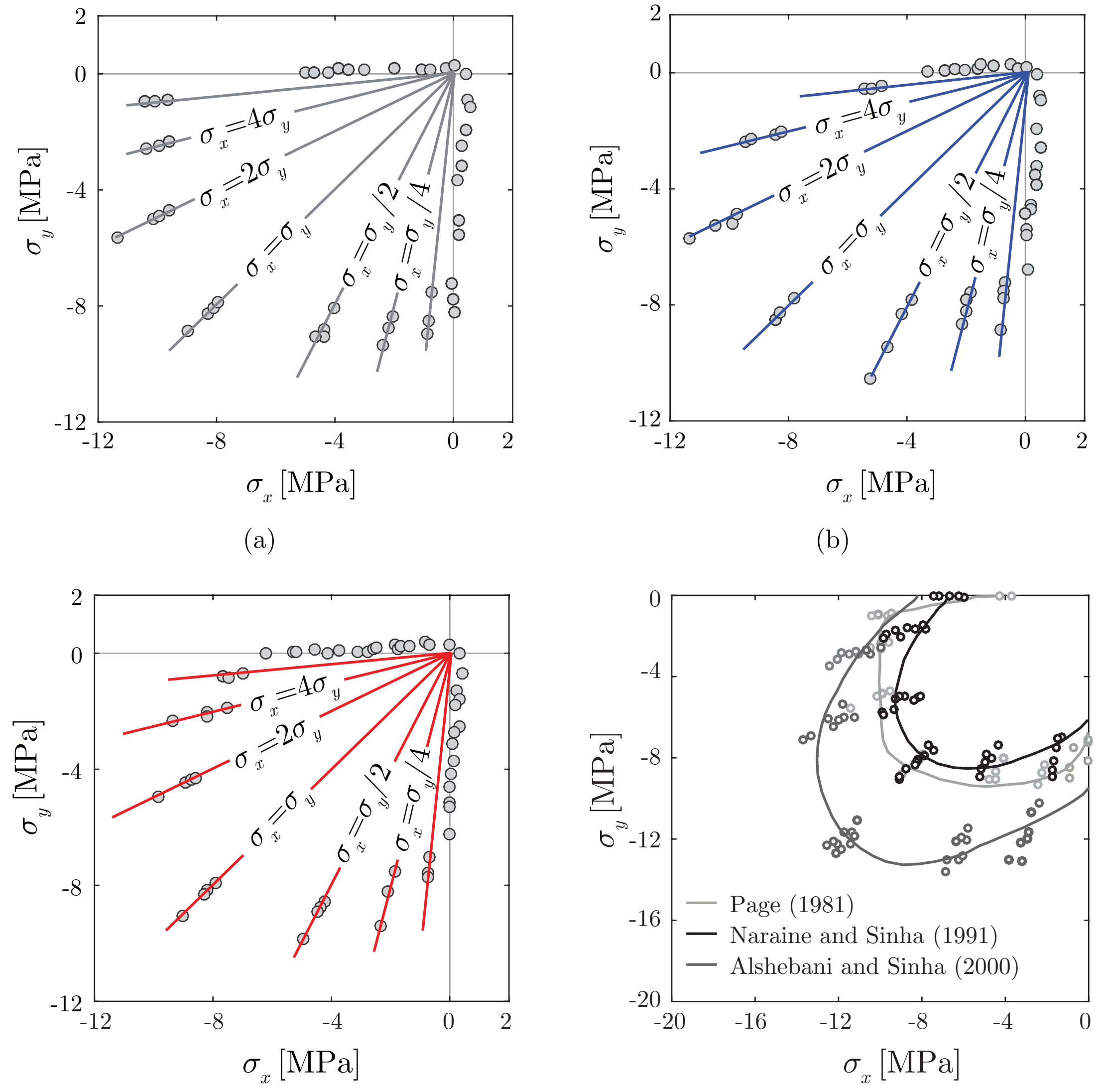

(a)

(b)

(c)

(d)

Figure 2.19: Masonry bi-axial strength: experimental results of Page (1981, 1983) for (a) $\vartheta = 0°$, (b) $\vartheta = 22.5°$and (c) $\vartheta = 45°$; (d) comparison between strength envelopes obtained for clay brick (light and dark gray lines) and sand plast (black line) masonry ($\vartheta = 0°$).

Bi-axial tests were conducted also by other researchers. Among others, Ganz and Thürlimann (1982) experienced hollow clay brick masonry, Naraine and Sinha (1991) tested half-scale clay brick specimens, while Alshebani and Sinha (2000) dealt with sand plast (a form of calcium silicate) brick masonry. A comparison between experimental outcomes obtained for clay brick masonry (Page, 1981 and Naraine and Sinha, 1991) and sand plast masonry (Alshebani and Sinha, 2000) is shown in Figure 2.19(d). Here, a reasonable accordance emerges between the enveloped curves extracted for clay brick masonry, except for the ratio between the parallel and normal compressive strength: it was approximately 0.6 and 1.1 in Page (1981) and Naraine and Sinha (1991), respectively. More relevant discrepancies emerge for the sand plast envelope, due to the differences in strength and behavior of sand plast and clay bricks. However, on the overall, the shape of all curves is similar.

2.2.2 Tests on full-scale masonry elements

2.2.2.1 Influence of vertical compressive load

Raijmakers and Vermeltfoort (1992) performed deformation controlled tests on masonry shear walls by considering different vertical compression loads. Solid clay bricks, arranged in running bond texture, with dimensions 210 × 52 × 100 mm^3 and 10 mm thick mortar were used to built up specimens. Width of 990 mm and height of 1000 mm were obtained by assembling 18 courses, only 16 of which were activated, as the upper and lower courses were clamped in steel beams (see Figure 2.20(a)).

Two-step tests were performed on each wall: first, a vertical uniformly distributed load p was applied and, then, a horizontal monotonically increasing displacement s was imposed through the upper steel beam, keeping bottom and top boundaries horizontal and preventing any vertical movement, as shown in Figures 2.20(a) and (b), respectively.

Four specimens without openings, the so-called JD walls, were tested by imposing three different values of the compression load p, that is 0.3 MPa ($\equiv$ 30 kN) for J4D and J5D, 1.21 MPa ($\equiv$ 120 kN) for J6D and 2.12 MPa ($\equiv$ 210 kN) for J7D. The global response curves (horizontal load vs. horizontal imposed displacement), plotted in Figure 2.21, showed failure loads and brittleness behavior increased with the increasing vertical load. Also vertical reaction was measured during the test, which moved from the middle line of the wall in the direction of the compressed

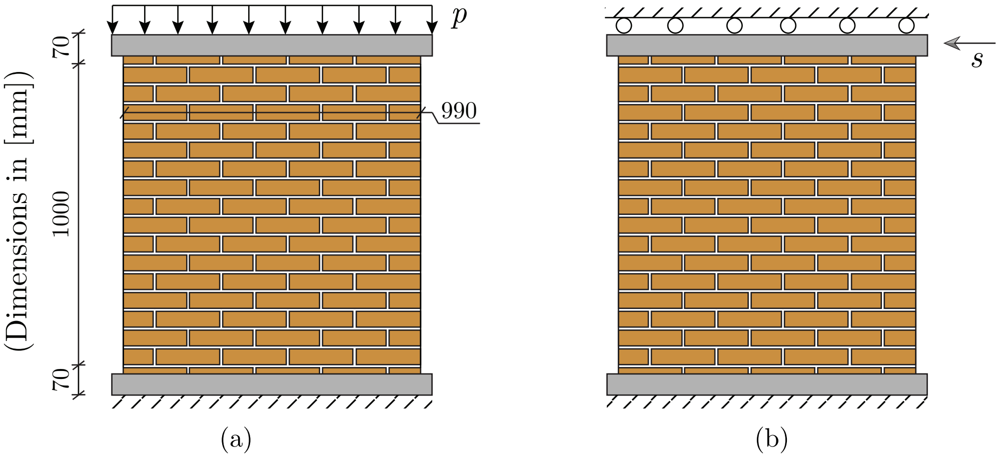

Figure 2.20: Test phases for Raijmakers-Vermeltfoort panels: (a) vertical precompression load and (b) horizontal loading under displacement control.

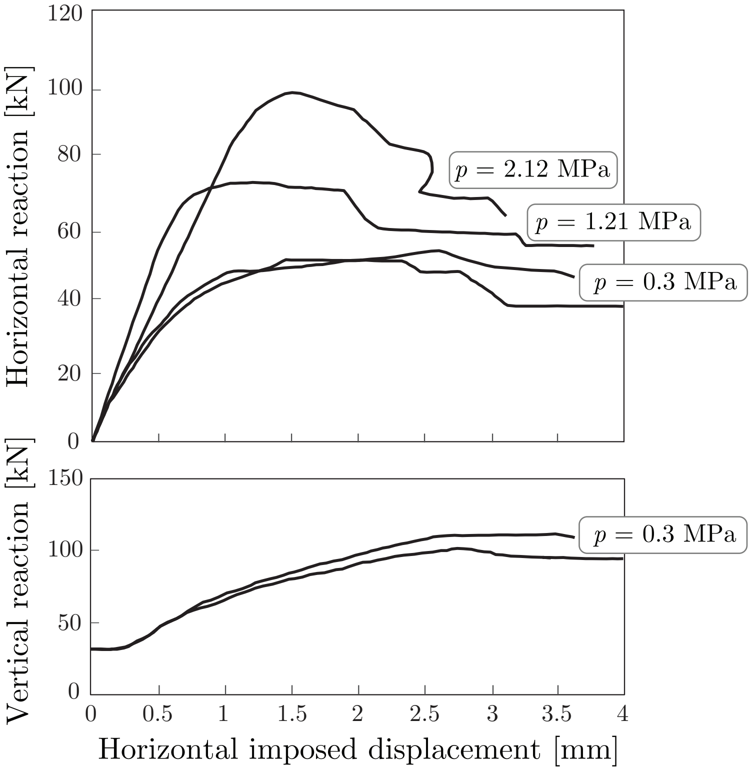

Figure 2.21: Raijmakers-Vermeltfoort panels: global response curves.

zones. In Figure 2.21 the variation of vertical force with the applied horizontal displacement is shown with reference to the lower compression load. It can be noted an increasing trend due to the dilatant phenomenon.

Finally, Figures 2.22 (a-d) show the experimental crack patterns obtained for all tested panels. Similar collapse mechanisms were found with diagonal cracked band in the middle part of the wall and crushing of the compressed toes. However, marked crack also developed at the bottom and top corners undergoing tensile stresses, as concerns the lower initial vertical load, that is walls J4D and J5D.

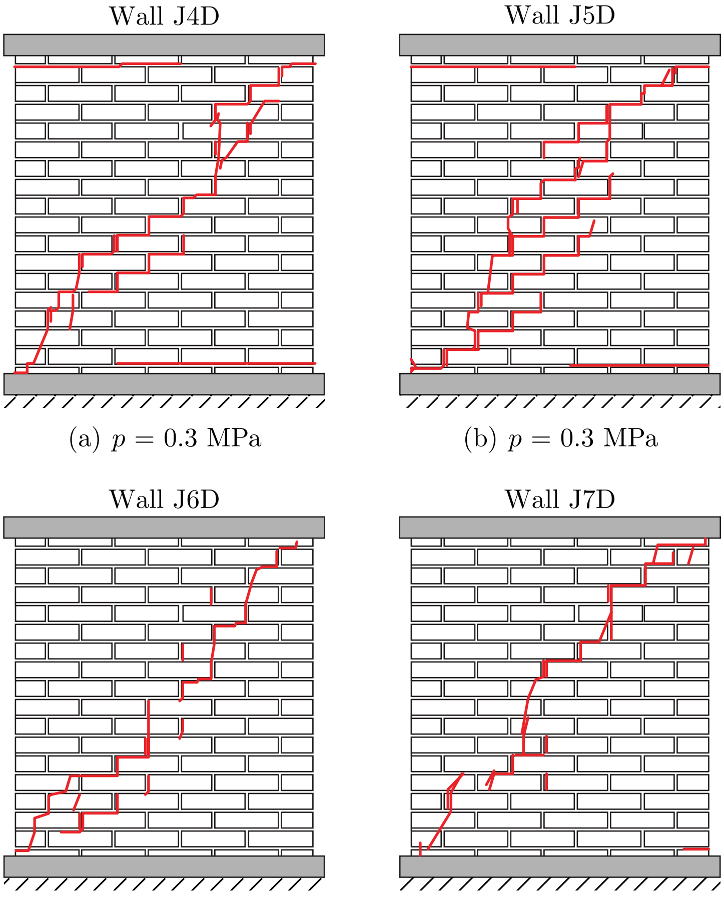

(a) $p = 0.3$ MPa (b) $p = 0.3$ MPa

(c) $p = 1.21$ MPa (d) $p = 2.12$ MPa

Figure 2.22: Raijmakers-Vermeltfoort panels: experimental crack patterns for different levels of vertical compression p.

2.2.2.2 Effect of panel geometry

To highlight the effect of geometry on the degrading and collapse mechanisms of shear walls, reference is made to experimental tests performed at the Joint Research Centre of Ispra (Anthoine et al., 1995). The test conditions were designed so as to reproduce those of masonry piers under seismic actions. Two panels, characterized by different height/width ratio, were analyzed, assuming the same boundary conditions in which the bottom side of the walls was completely restrained while the top side was prevented to rotate. These were firstly subjected to a vertical compressive stress of $p = 0.6\,\mathrm{MPa}$ ($\equiv 150\,\mathrm{kN}$), kept constant during the test and, then, a cyclic horizontal displacement history was applied on a steel beam rigidly connected to the top of the walls. The lateral displacement was imposed quasi-statically and characterized by increasing amplitude. Two or three cycles were performed for each amplitude, depending on the level of strength degradation. With reference to Figure 2.23, loading conditions can be summarized as follows:

$$\begin{cases} F_{v1} + F_{v2} = ptW = F_v \\ s_{v1} = s_{v2} = s_v \\ s_h \text{ imposed, } F_h \text{ measured} \end{cases} \tag{2.3}$$

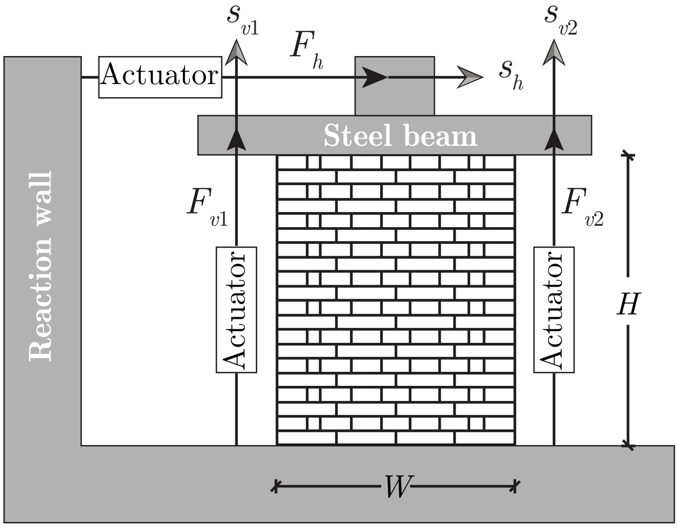

Figure 2.23: Schematic view of the test set-up for Ispra walls.

The specimens were built up with brick units of 250 × 120 × 55 mm^3 and 10 mm thick hydraulic lime mortar, arranged in two-wythes thickness English bond pattern. The panels overall sizes were: $W_1 = W_2 = W = 1000\,\text{mm}$, $H_1 = 2000\,\text{mm}$ (high wall), $H_2 = 1350\,\text{mm}$ (low wall) and thickness $t = 250\,\text{mm}$.

Figures 2.24 and 2.25 show the experimental outcomes for the high and low wall in terms of force-displacement global curve (a) and crack patterns (b). The different trends of the global response curves were a consequence of the different onset and evolution of degrading mechanisms: low wall exhibited a brittle failure with diagonal cracks in the middle of the panel due to the dominant shear mechanism, while flexural response characterized behavior of the high wall with the formation of high damaged zones located at the top and bottom sides starting from the corners. Thus, low wall showed a softening behavior more severe than high wall, as well as larger hysteretic dissipation.

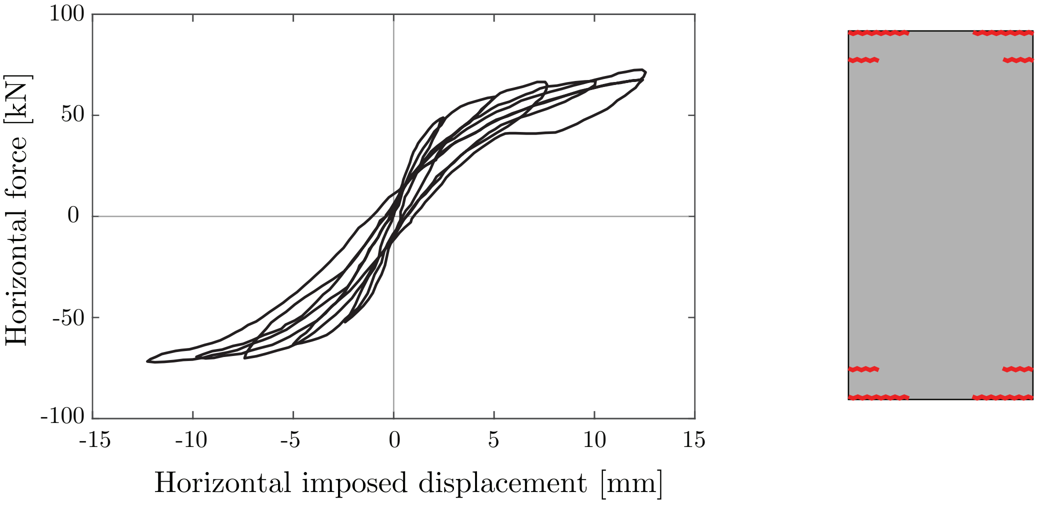

(a) (b)

Figure 2.24: Ispra high wall: (a) experimental cyclic load-displacement global curve and (b) experimental failure path from Anthoine et al. (1995).

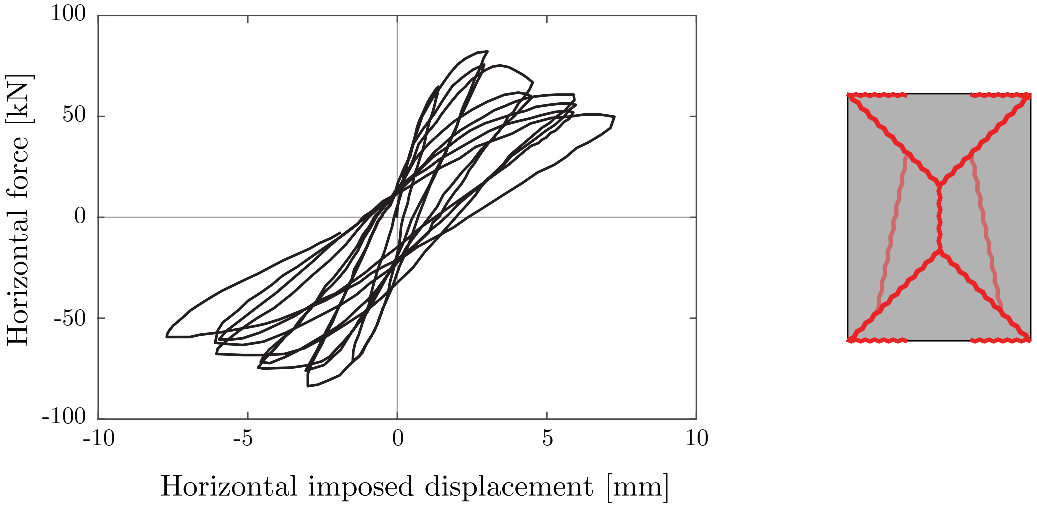

(a) (b)

Figure 2.25: Ispra low wall: (a) experimental cyclic load-displacement global curve and (b) experimental failure path from Anthoine et al. (1995).

2.2.2.3 Two-story masonry building

A full-scale two-story masonry building was tested at University of Pavia (Magenes et al., 1995) under quasi-static loading conditions with the aim of evaluating its seismic capacity. A schematic representation of the prototype geometry is sketched in Figure 2.26. Four two-wythes solid brick walls, 250 mm thick, composed the building, which was characterized by plan dimensions $6 \times 4.4\,\mathrm{m}^2$ and height of 6.4 m. The longitudinal walls were with openings, that is wall D and wall B, also known as 'door' and 'window' wall, respectively. Wall D was disconnected from transverse walls (A and C), as opposed to wall B, which was properly linked with interlocking brick pattern at the adjacent walls. This allowed to consider wall D as plane structure and wall A+B+C as overall independent system. Flexible diaphragms at the floor levels were simulated with a series of steel beams (with I section and 140 mm depth), which were also used to impose, by means of concrete blocks, distributed loads about equal to $10\,\mathrm{kN/m}^2$, resulting in vertical additional loads of 248.4 kN and 236.8 kN at the first and second level, respectively. By using displacement controlled screw jacks, seismic loads were applied as concentrated

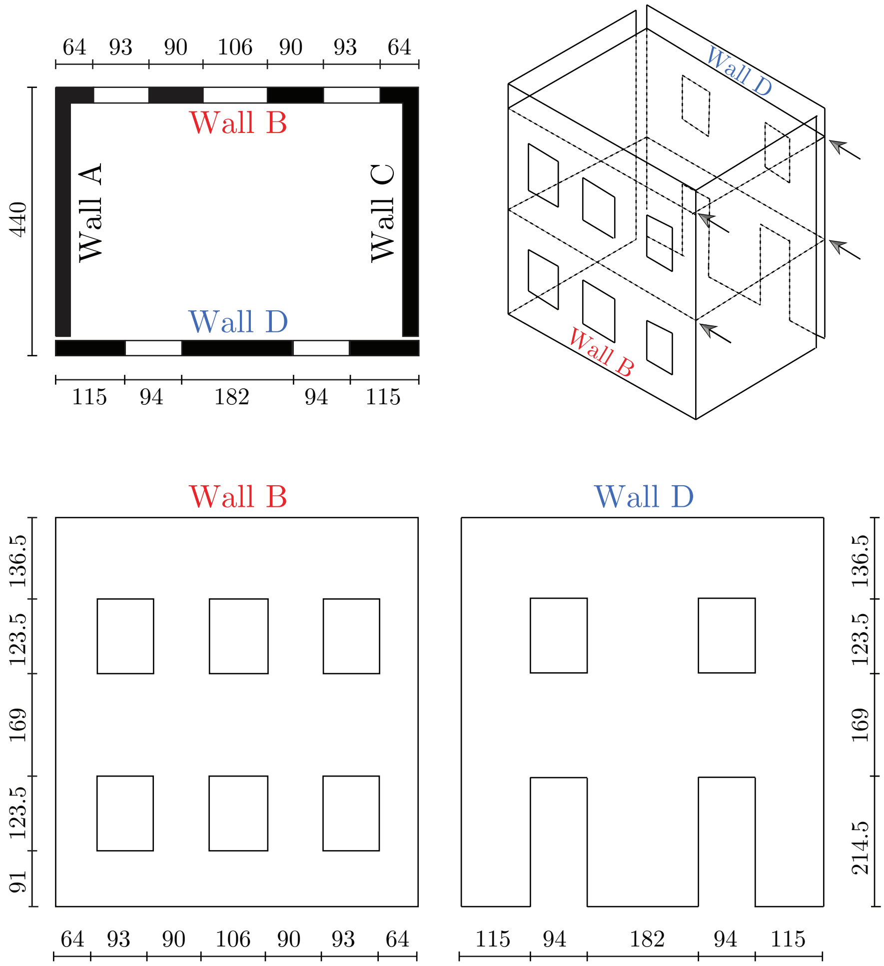

Figure 2.26: Geometry and loading conditions of the two-story masonry building tested by Magenes et al. (1995) (dimensions in [cm]).

horizontal forces at the longitudinal walls. The imposed displacements were controlled so that to obtain equal applied forces at first and top floor levels and were characterized by repeated cyclic with increasing amplitude (see Figure 2.27).

Before starting the test, characterization of the material mechanical properties was performed, resulting in mean compressive strength of 6.2 MPa and joints shear strength written as $\tau = 0.23 + 0.57\sigma$ (evaluated from a linear regression on tested triplets).

Figures 2.28(a-d) show experimental outcomes in terms of global response curves (base shear vs. second floor displacement) and crack patterns for both longi-

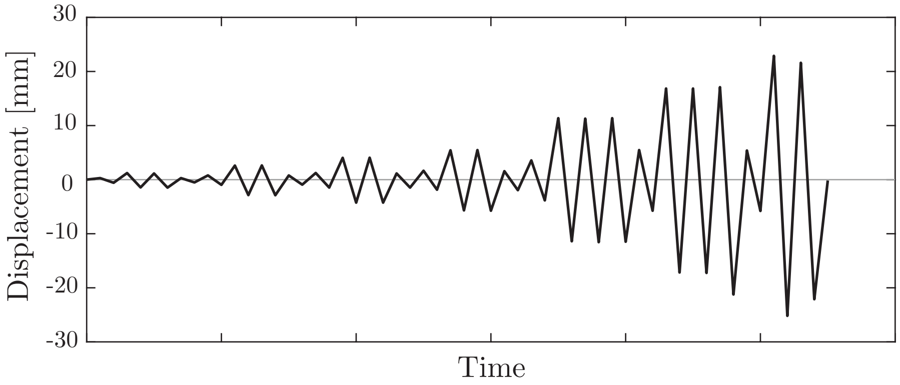

Figure 2.27: Sequence of the displacement applied at the second floor level.

tudinal walls. It can be noted a similar response with strength-stiffness decay and hysteretic dissipation. Maximum base shear was approximately 150 kN and 140 kN for the door and window wall, respectively.

Regarding damage progression, this was quite complex. Initially, cracks developed in the spandrels between the openings by decreasing the coupling between piers, then, with increasing deformation, shear cracking in central piers appeared for both walls. Different behavior was found for the external piers: wall D exhibited diagonal cracks due to shear failure, while wall B behaved in a rocking mode with no diagonal damaged shear bands. This different response was imputed to the aspect ratio of the piers and to the test arrangement, because wall B was connected with the transverse walls, as opposed to wall D.

Finally, differences emerged in the measured vertical displacements. Wall D exhibited significant displacements due to flexure mechanisms, while wall B showed small uplift, as its response resulted characterized by shear mechanisms in the central piers.

The described test points out the complexity of failure mechanisms characterizing unreinforced masonry buildings. Indeed, the global responses result strongly affected by loading conditions and level of anchorage between structural elements.

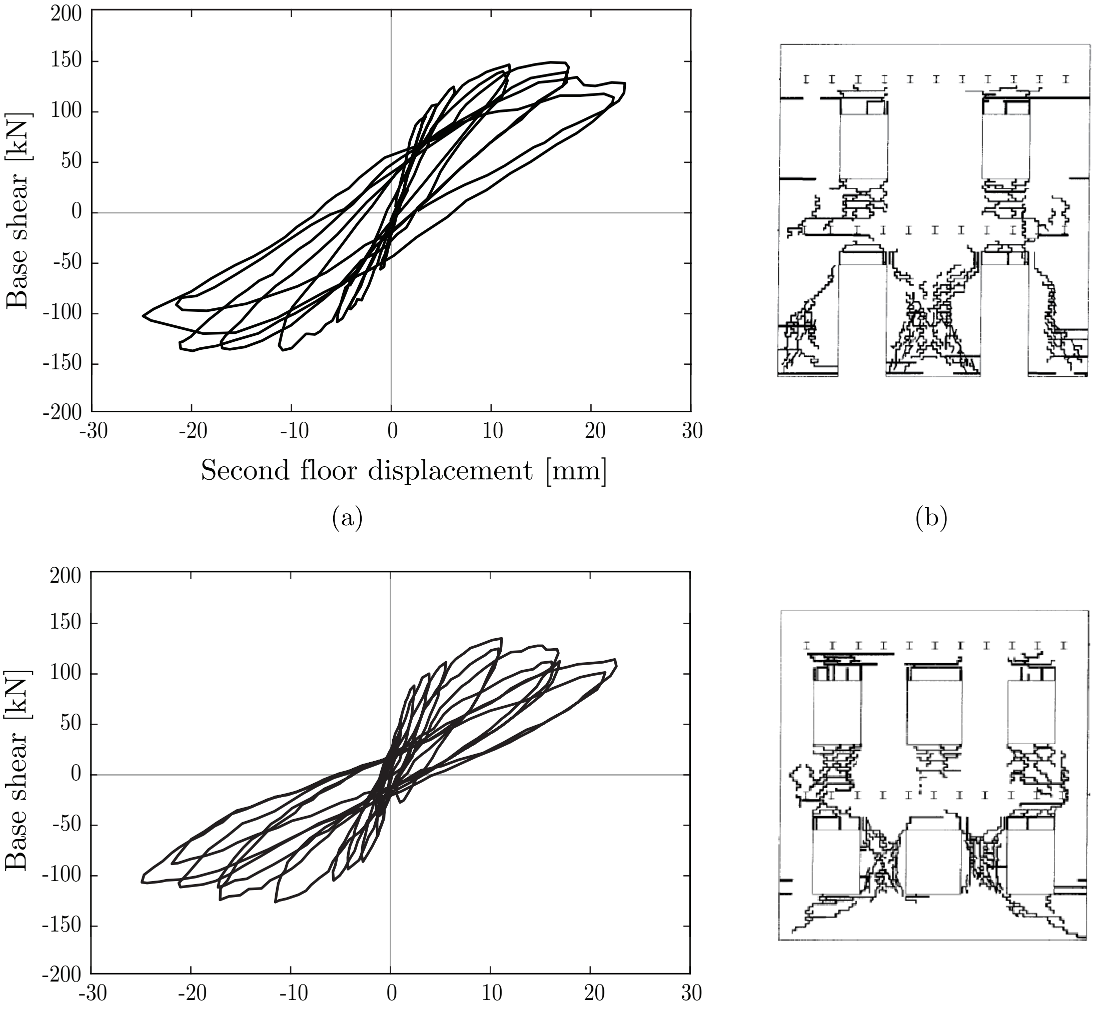

(a)

(b)

(c)

(d)

Figure 2.28: Base shear-second floor displacement curves for (a) wall D and (c) wall B; experimental failure paths for (b) wall D and (d) wall B.

2.3 Summary

This chapter provided an overview of significant experimental tests performed on masonry and its constituent materials. Starting from the main properties of units and mortar, behavior of masonry material was analyzed, by highlighting its nonlinear and non-symmetric mechanical response. Failure in tension is usually associated to a localized fracture process, while failure in compression is due crushing of the material. Furthermore, irreversible strains develop mainly due to friction mechanisms at interface between mortar and units, leading to dissipative process. It was also remarked that, in cases of regular texture, anisotropic response emerges, as the strength characteristics result strongly affected by direction of the applied loads with respect to bed joints orientation.

Finally, tests on large scale masonry assemblages, representing structural elements or more complex systems, highlighted the influence of geometry, loading and boundary conditions on masonry overall response.

Chapter 3

Modeling approaches for masonry structures

The development of efficient numerical procedures to deeply understand and accurately predict masonry mechanical behavior is still a challenging task. The main difficulties in modeling are due to the heterogeneous microstructure of the material which conduces to complex stress distributions among constituents. Several modeling strategies were developed, ranging from simplified to very sophisticated models. This chapter offers a brief review of the available methods, by emphasizing limits and advantages of each of them in terms of computational cost, applicability to large structures and accuracy of results. According to the purpose of this research, particular attention is paid to the finite element models description.

3.1 FEM based approaches

Finite element models, involving nonlinear constitutive laws with damage and plasticity inner variables, appear as promising tools for the assessment of the structural capacity of masonry buildings. Despite several criteria can be adopted, these models are usually classified with regard to the modeling scale used (Lourenço, 1996; Roca et al., 2010; Addessi et al., 2014), thus distinguishing between micromechanical, macromechanical and multiscale models.

3.1.1 Micromechanical models

Micromechanical approaches provide very accurate results, as masonry components (units, mortar and interfaces) are separately modeled and all the information about the microstructure are accounted for (Gambarotta and Lagomarsino, 1997; Lourenço and Rots, 1997; Oliveira and Lourenço, 2004; Sacco and Toti, 2010; Minga et al., 2018). Within this framework, different constitutive laws were proposed for each constituent material, according to the assumptions reported below (Addessi and Sacco, 2012):

- Model for the brick:
  (a) rigid;
  (b) deformable with linear response;
  (c) interface or continuum material with nonlinear response.
- Model for the mortar:
  (a) interface or continuum material characterized by linear response;
  (b) interface or continuum material characterized by nonlinear response.

Figure 3.1 schematically shows the most common micromodels. In the so-called *detailed* micromodeling strategy, blocks and mortar are described through continuum finite elements, whereas the unit-mortar interfaces are modeled by discontinuous elements (Figure 3.1(a)). Alternately, *simplified* micromodels were developed, which consider joints as mechanical units representing both mortar and unit-mortar interface and adopt either expanded units with elastic response and potential crack interfaces or continuum nonlinear model for bricks (Figures 3.1(b) and (c), respectively).

Lourenço and Rots (1997) proposed a largely used interface constitutive model, based on the plasticity theory. The authors suggested a composite yield surface (Figure 3.2(a)) to simulate tensile failure of mortar joints, shear response of joints and crushing of units under monotonic loading. Moreover, similarly to how shown in Figure 3.1(b), cracks in the units were taken into account by placing potential crack interface in the middle part of the each unit. A modified version of

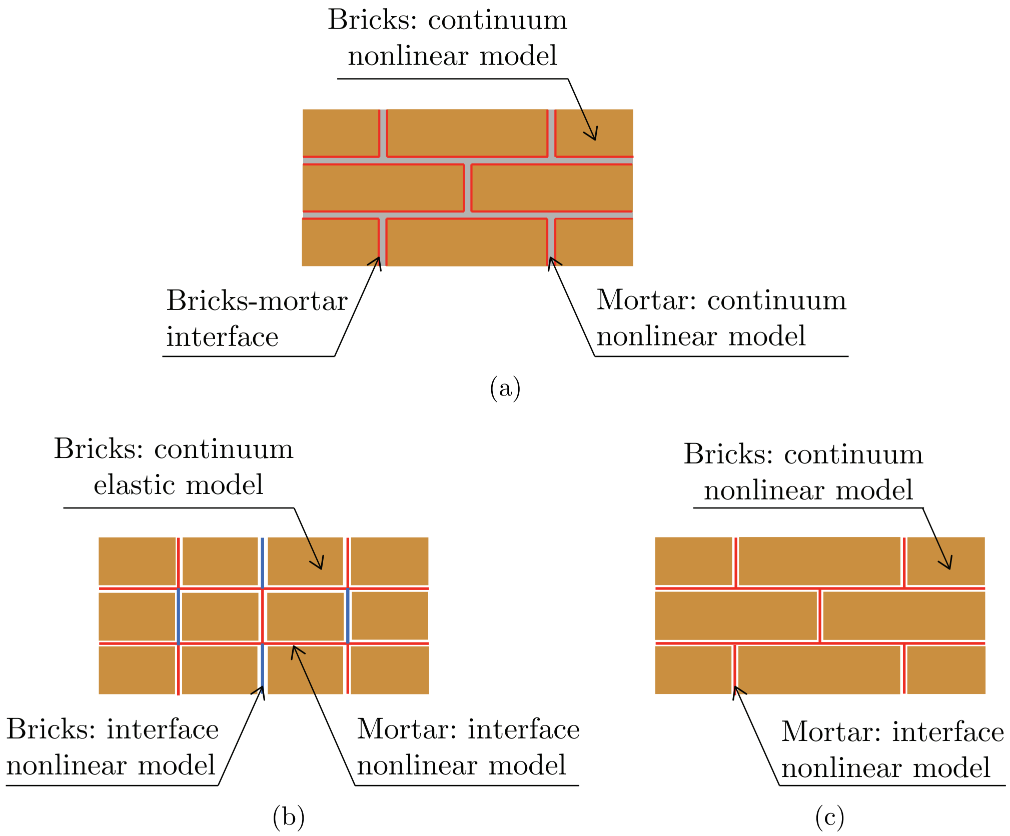

Figure 3.1: Micromodeling technique: (a) detailed micromodel, (b) simplified micromodel with potential crack in the units and (c) simplified micromodel.

the model was later presented by Oliveira and Lourenço (2004) with the aim of accurately reproducing the main characteristics of the interface cyclic behavior. The monotonic model was enriched by introducing two auxiliary yield surfaces with the purpose to simulate the unloading to tension and compression, as Figure 3.2(b) shows with reference to an example case of unloading to tension.

Another interesting interface model, accounting for damage and friction, was presented by Sacco and Toti (2010). With reference to the interface zone depicted in Figure 3.3(a), the authors recognized three states in the damaging process: at point A the connection block-mortar is undamaged, at point B a partial decohesion is occurred and, finally, the decohesion phenomenon is full at point C. A representative elementary volume (REV) was also introduced, being characterized by height h, accounting for mortar and brick thicknesses involved in the degrada-

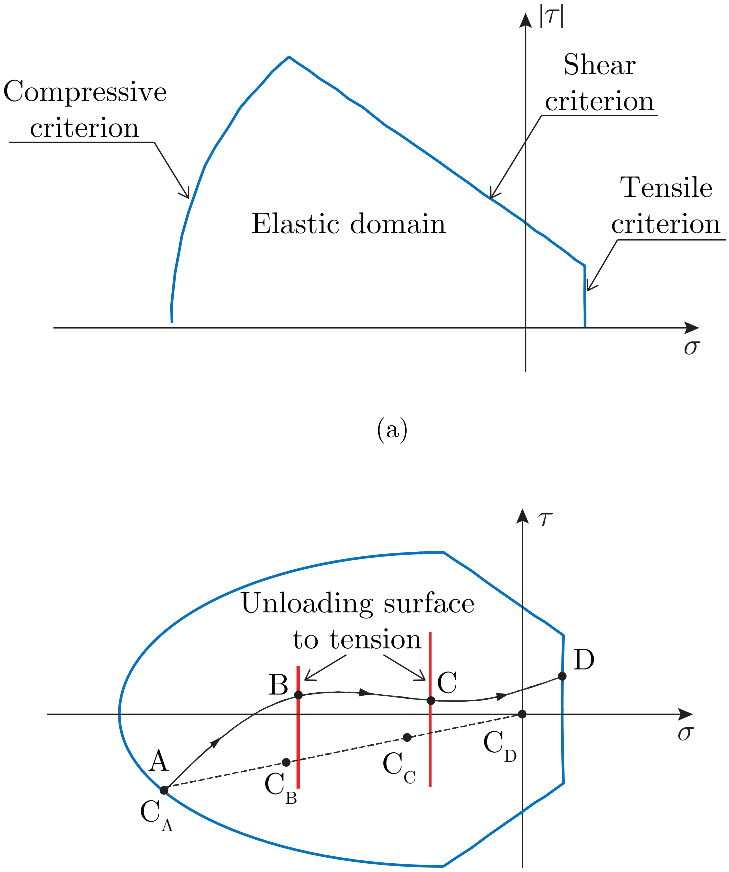

(a)

(b)

Figure 3.2: Multisurface interface model: (a) monotonic model proposed by Lourenço and Rots (1997) and (b) auxiliary yield surfaces for the cyclic model of Oliveira and Lourenço (2004).

tion phenomenon, length b, representative of the distance between microcracks, and width w, depending on the size of the mortar-brick. Thus, the total area $A = b\,w$ at the interface was decomposed into an undamaged part $A_u = (b-a)w$ and a fully damaged portion $A_d = a\,w$. Based on these quantities and the main concepts of the continuous damage mechanics, a scalar damage parameter was defined as:

$$D = \frac{A_d}{A} = \frac{a}{b}\,. \tag{3.1}$$

Furthermore, by denoting with $\mathbf{s} = \{s_T \; s_N\}^T$ the relative displacement vector at the typical point of the mortar-block interface, collecting the displacement components in tangential T and normal N direction to the interface, the constitutive relationship was written as:

$$\boldsymbol{\tau} = (1 - D)\boldsymbol{\tau}^u + D\boldsymbol{\tau}^d = \mathbf{K}[\mathbf{s} - D(\mathbf{c} + \mathbf{p})] \, , \tag{3.2}$$

where $\boldsymbol{\tau}$ is the interface stress vector, $\mathbf{K}$ is the stiffness diagonal matrix and $\mathbf{c} + \mathbf{p}$ is an inelastic displacement vector accounting for friction and unilateral contact.

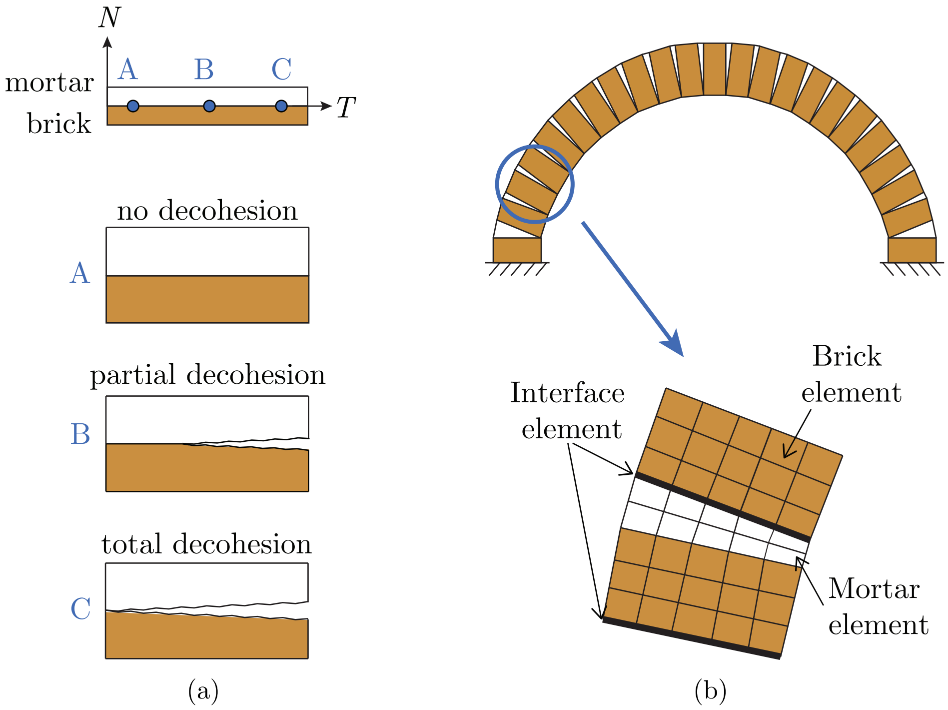

(a) (b)

Figure 3.3: Sacco and Toti (2010): (a) damaging states of brick-mortar interface and (b) detailed micromodeling of a masonry arch.

The model was used for the micromodeling of masonry elements, mainly for unreinforced and reinforced masonry arches, where two different models were adopted for bricks and mortar. Indeed, in case of unreinforced arch a linear elastic model was used, whereas elasto-plastic constitutive law was assumed for the strengthed arch, thus developing a detailed micromodel (Figure 3.3(b)). Satisfactory agree-

ment was found between experimental and numerical results in terms of peak load, collapse mechanisms and nonlinear response.
These are just few examples of micromodels proposed for masonry, which realistically took into account the elastic and inelastic properties of units and mortar. Such high level of refinement translates in high computational cost and several attempts were developed to speed up numerical simulations. For instance, Minga et al. (2018) used the domain decomposition and parallel processing technique to improve the performance of their mesoscale model (Figure 3.4).

To summarize, micromodels are considered as the most accurate available tool to analyze masonry, but their applicability is limited to the analysis of small elements or structural details because of the high computational burden required.

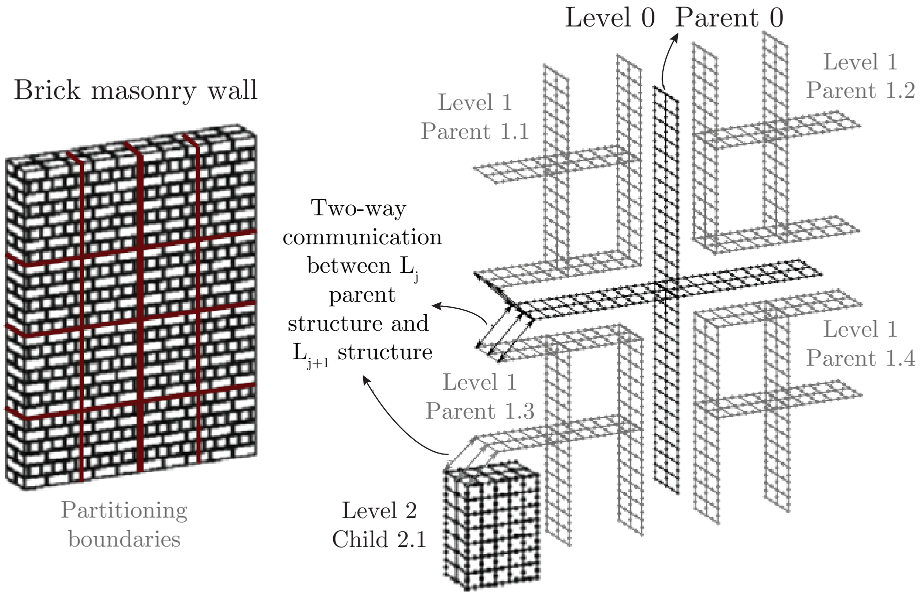

Figure 3.4: Minga et al. (2018): domain decomposition and parallel processor technique.

3.1.2 Macromechanical models

To reduce the computational burden, a large number of macromodels (Lourenço et al., 1997; Addessi et al., 2002; Berto et al., 2002; Karapitta et al., 2011; Pelà et al., 2013; Addessi, 2014; Toti et al., 2015; Tesei and Ventura, 2016) was developed, which consider masonry as an equivalent homogeneous, isotropic or anisotropic medium, where the constituent materials are no longer distinguishable (Figure 3.5) and properly formulated relationships are established between the average masonry strains and stresses.

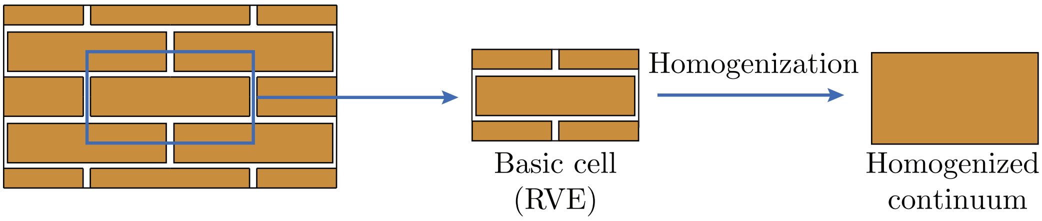

Figure 3.5: Macromodeling technique: masonry as a homogeneous material.

Despite some difficulties arise in identifying the constitutive laws of the equivalent homogenized material, as well as the mechanical parameters (usually determined by means of tests on large sized specimens or through homogenization procedures) and the evolution laws of the inelastic variables, macromechanical models are widely used to analyze complex real structures. Figures 3.6 and 3.7 show some examples of macromodeling of large scale structures.

Valente and Milani (2016) used the Concrete Damage Plasticity model, originally proposed by Lubliner et al. (1989) and later modified by Lee and Fenves (1998), for the seismic safety assessment of historical masonry towers (see Figure 3.6). The mentioned material model was primarily developed to study response of concrete structures, but its applicability is reasonably extensible to masonry. Indeed, the model, based on the assumption of scalar isotropic damage (see Section 4.1), is able to capture the degrading processes developing in masonry material, as well as the stiffness recovery related to the re-closure of the tensile cracks upon transition from tensile to compressive states. Lee and Fenves (1998) introduced in the constitutive law distinct damage parameters in tension, D_t, and compression, D_c, and combined the damaging responses by means of the weighting factor r,


(a) (b)

Figure 3.6: Tower located in Luisa: (a) real structure and (b) FE model used by Valente and Milani (2016).

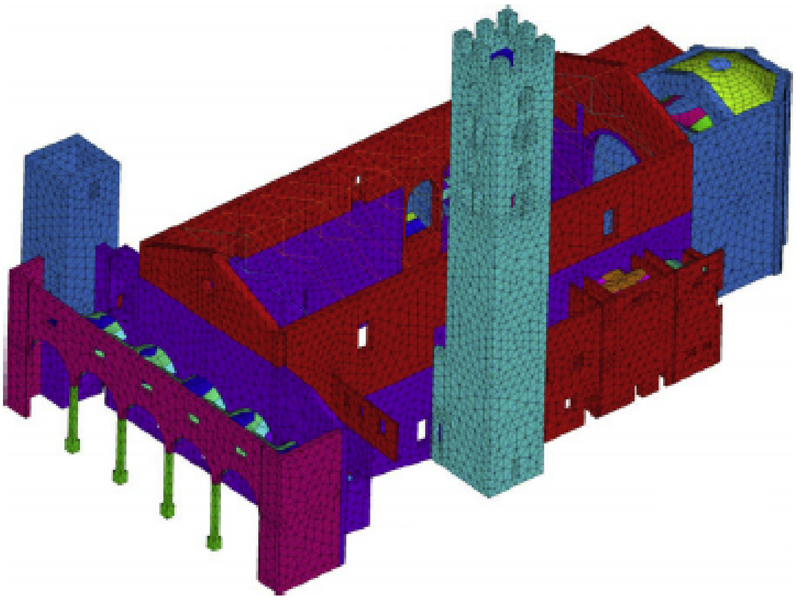

Figure 3.7: Betti and Vignoli (2011): FE model of the Basilica of Santa Maria all'Impruneta.

defined on the basis of the effective principal stresses $\hat{\tilde{\boldsymbol{\sigma}}}$. The total stress results as:

$$\boldsymbol{\sigma} = (1 - D_c)(1 - sD_t)\tilde{\boldsymbol{\sigma}} \ , \tag{3.3}$$

with

$$s = s_0 + (1 - s_0)r(\hat{\tilde{\boldsymbol{\sigma}}}) \ , \tag{3.4}$$

being s_0 a constant used to set the minimum value of s, thus allowing a proper representation of the unilateral damage recovering upon load reversal.

Among macromodels developed for masonry, others proposals exist to model the unilateral phenomenon. Toti et al. (2015) used a regularized form of the Heaviside function H for the elastic strain first invariant J_1^e by introducing the following isotropic damage model:

$$\boldsymbol{\sigma} = \tilde{\boldsymbol{\sigma}} \left[(1 - D_t)H(J_1^e) + (1 - D_c)(1 - H(J_1^e))\right] \ , \tag{3.5}$$

where $\boldsymbol{\sigma}$ and $\tilde{\boldsymbol{\sigma}}$ denote the stress and effective stress tensors, respectively; D_t and D_c are the damage variables which capture the stiffness degradation in tension and compression.

Addessi (2014) presented a $2D$ Cosserat model with damage-plastic isotropic constitutive law, where the volumetric strain energy is split into the positive and negative part, according to the strategy proposed by Comi and Perego (2001) for concrete. The resulting stress-strain law is expressed as:

$$\begin{aligned} \mathbf{T} =& K(1 - D_s)\langle \mathrm{tr}\mathbf{E}_e^{\mathrm{sym}} \rangle_+ \mathbf{I} + K(1 - D_c)\langle \mathrm{tr}\mathbf{E}_e^{\mathrm{sym}} \rangle_- \mathbf{I} \\ &+ 2G(1 - D_s)\mathrm{dev}\mathbf{E}_e^{\mathrm{sym}} + 2G_c(1 - D_s)\mathbf{E}^{\mathrm{skw}} \ , \\ \boldsymbol{\mu} =& 2Gl_c^2 \, (1 - D_s)\boldsymbol{\kappa}_e \ , \end{aligned} \tag{3.6}$$

where K and G are the bulk and shear modulus, respectively, and G_c is the Cosserat shear modulus. In Eq. 3.6 damage variable D_s is defined as a proper combination of damage variables in tension, D_t, and compression, D_c, as:

$$(1 - D_s) = (1 - D_t)\,(1 - D_c) \ . \tag{3.7}$$

In other words, by subdividing the strain tensor **E** into volumetric and deviatoric part, the shear and pure tensile behavior are influenced by both tensile and compressive damages, while the pure compressive response is only affected by the compressive damage, thus representing the unilateral effect.

It should be noted that, despite it is well recognized that regular masonry exhibits anisotropic behavior, constitutive laws involving isotropic damage and plasticity are largely adopted. Consequently, the orthotropic response is completely lost, but the overall behavior can be satisfactorily captured if average strength and stiffness values along the material axes are adopted. However, the most advanced macromodels represent masonry as an orthotropic material exhibiting marked directional properties. The main assumption of these models is the acceptance of material axes, which are parallel and normal to the bed joints orientation. Lourenço et al. (1997) proposed a constitutive law fully based on the plasticity theory, which employs a Rankine-type and a Hill-type criteria to simulate tensile and compressive behavior, respectively. Within the damage approach framework, Berto et al. (2002) interpreted the material axes as principal axes of damage, as microcracks forming the damage are usually parallel and perpendicular to material directions. Four independent internal damage parameters, one in compression and one in tension for each natural axis, were introduced by defining a proper damage matrix. Onset and evolution of the damage parameters was ruled by equivalent stress measures and the resulting damage limit surface was geometrically represented by a double pyramid with rectangular base.
More recently, Pelà et al. (2013) simulated masonry orthotropic response by exploiting the concept of mapped tensors from the anisotropic field to an auxiliary workspace (Figure 3.8). The different behavior along the material axes was simulated by means of linear transformation between the real anisotropic space and the auxiliary one, where simple isotropic damage model and criteria were adopted.

The large number of proposed macromodels confirms the timeless interest towards this modeling technique, which represents, despite its intrinsic limits, a fair compromise between accuracy and computational effort.

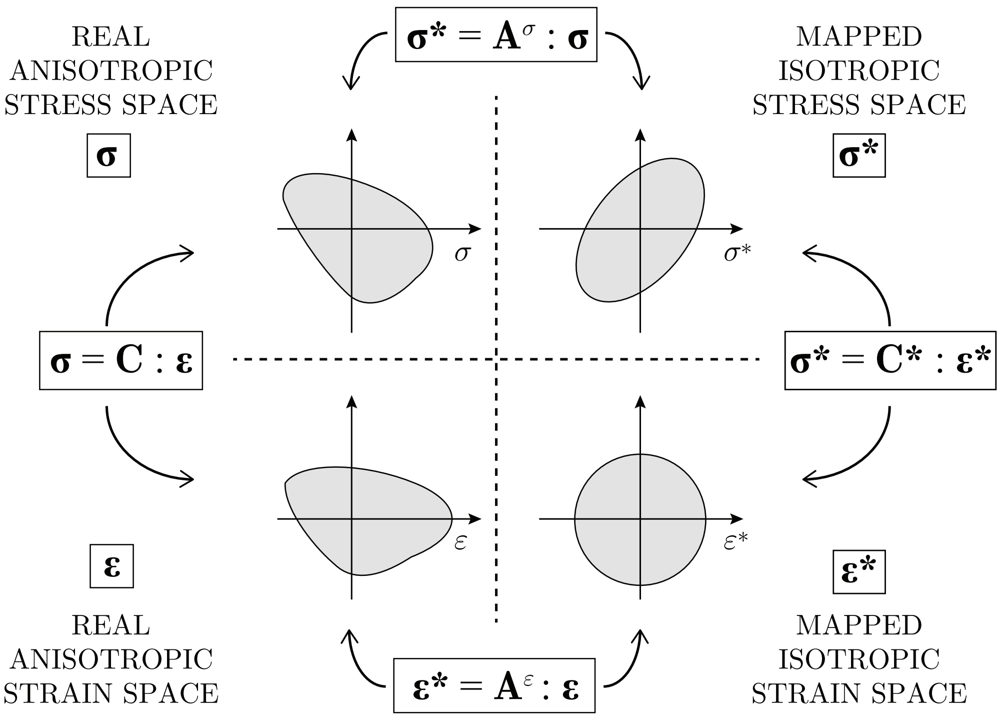

Figure 3.8: Technique of the mapped stress and strain tensors used by Pelà et al. (2013).

3.1.3 Multiscale models

Between the micro and macro approaches, the multiscale modeling has taken hold in last decades to study the mechanical response of heterogeneous microstructured materials and, in particular, of masonry. This approach splits the structural problem into two scales: an equivalent homogenized medium is studied at macrolevel, where the constitutive response at each material point is derived by homogenizing the stress field computed in a properly selected representative volume element (RVE). This contains the detailed description of masonry components, geometry, arrangement and constitutive behavior and is analyzed at microscale. Indeed, the constitutive response at macrolevel, initially unknown, is derived by applying concepts of localization and homogenization within a scale transition procedure (Figure 3.9). A *strain driven formulation* is usually adopted, consisting of the evaluation of the macroscopic strain vector **E** at each material point of the macrolevel model, which is used as input data for the linked sub-domain (the aforementioned RVE). At this stage, a properly defined boundary values problem (BVP) has to be solved to determine the stress field on the RVE and, then, the corresponding macroscopic stress $\mathbf{\Sigma}$ by means of the Hill-Mandel equivalence principle. Different boundary conditions, that is prescribed displacements, prescribed tractions and periodic conditions, were considered for the RVE with the aim of obtaining the best estimation of the homogenized mechanical properties. It has been established, as Figure 3.10 shows, that periodic boundary conditions strike a good balance and provide the best response, as uniform displacements and traction conditions lead to an overestimation and underestimation of the elastic properties of the composite material, respectively.

A significant issue related to multiscale models is the choice of the most suitable continuum to be applied to the macrolevel. The standard first order homogenization schemes are based on the use of the classical Cauchy continuum for both micro and macrolevel, but, as found by Kouznetsova (2002) and remarked by De Bellis and Addessi (2011), these models suffer from some limitations and can be adopted only if the following assumptions hold:

- microstructure very small if compared to the characteristic size of the macroscale;
- mechanical properties of the homogenized medium not affected by the absolute dimension of the constituents material;
- low deformation gradients of stresses and strains.

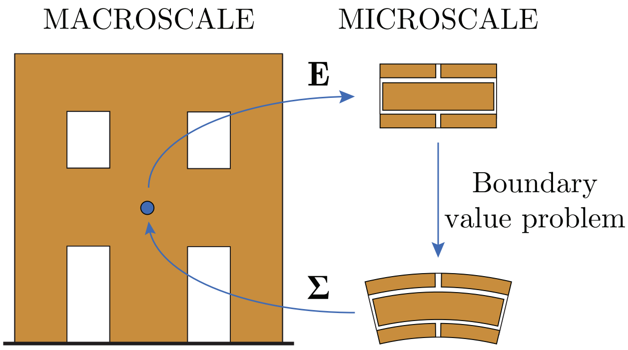

Figure 3.9: Multiscale technique: transition between macro and microscale.

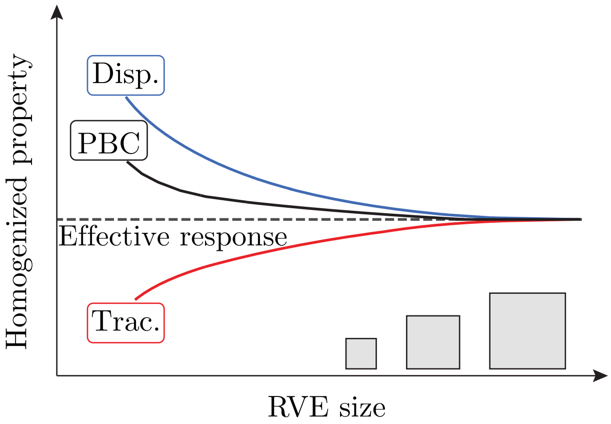

Figure 3.10: Typical convergence of the homogenized properties as function of the RVE size obtained by imposing different boundary conditions.

To overcome such restrictions, an enriched model can be used at macrolevel. A Cosserat continuum was adopted by De Bellis (2009) and De Bellis and Addessi (2011) with the aim of introducing a material length scale which naturally accounts for the absolute size of the constituents and even permits to mitigate the computational problems related to the strain localization. Furthermore, as shown in Figure 3.11 with reference to a two-dimensional case, the adoption of such enriched continuum allows to consider three additional deformation modes, that is two micro-curvatures (K_X, K_Y) and the rotational deformation ($\mathit{\Theta}$), besides the standard Cauchy extensional (E_X, E_Y) and shear symmetric ($\mathit{\Gamma}_{XY}$) strains.

The available literature shows that multiscale models were largely adopted to describe both in-plane and out-of-plane behavior of masonry. Mercatoris and Massart (2011) used a shear-enhanced element with the Reissner-Mindlin description to explore the out-of-plane failure of masonry walls. Petracca (2016) developed a computational multiscale homogenization technique for the quasi-static analysis of in-plane and out-of-plane loaded masonry structures, by focusing attention to the localization problem and, thus, offering an extension of the fracture-energy based regularization. Massart et al. (2007) proposed an enhanced multiscale model based on nonlocal implicit gradient isotropic damage models for both brick and mortar.

The briefly described multiscale technique is usually implemented in finite ele-

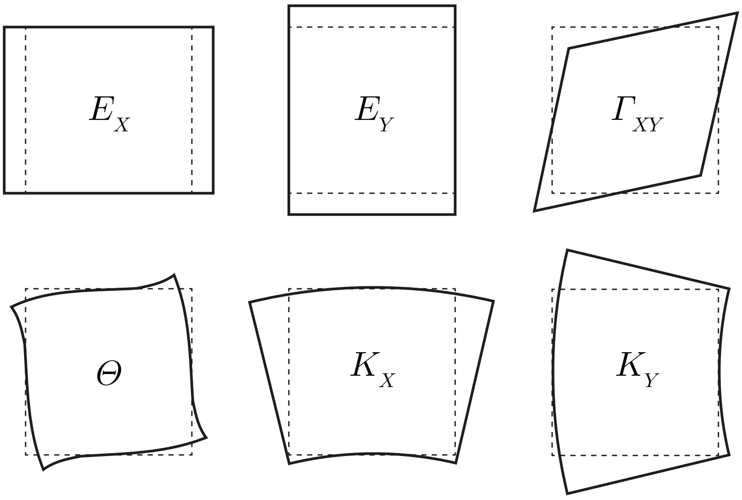

Figure 3.11: Cosserat deformation modes for two-dimensional case.

ment procedures, the so-called FE^2 approach. This consists of scale transitions at each step, iteration and integration point of the analysis. As a consequence of this continuous up-scaling and down-scaling, parallel processors are needed to perform and speed up the numerical simulations. An alternative multiscale approach is the Transformation Field Analysis (TFA), firstly proposed by Dvorak (1992) and then extended to the analysis of periodic masonry panels (Sacco, 2009; Addessi and Sacco, 2012). This deals with a nonlinear homogenization procedure based on the superposition of the effects that requires the computation of localization and transformation tensors. To this purpose, micromechanical analyses are performed on a properly selected masonry unit cell and the obtained information (in terms of localization e transformation tensors) is used to solve the structural problem at macrolevel. To clarify the procedure, the simple example described in Sacco (2009) is here summarized with reference to Figure 3.12. The overall behavior of the two spring system, B and M, characterized by linear and nonlinear behavior is determined by superimposing the responses to an average elastic strain $\bar{e}$ and an inelastic strain π. The extension of such approach to masonry provides for imposition of average elastic strains $\bar{e}$ at whole masonry unit cell and inelastic strains π_i on each mortar joints (in the most simplified analyses bricks are characterized by linear elastic response and, consequently, no inelastic strains are applied). Satisfactory results were obtained in terms of both accuracy and computational cost. Indeed, as opposed to FE^2 model, the TFA technique performs the scale transition only at the first stage of the analysis, thus resulting in a significant computational saving.

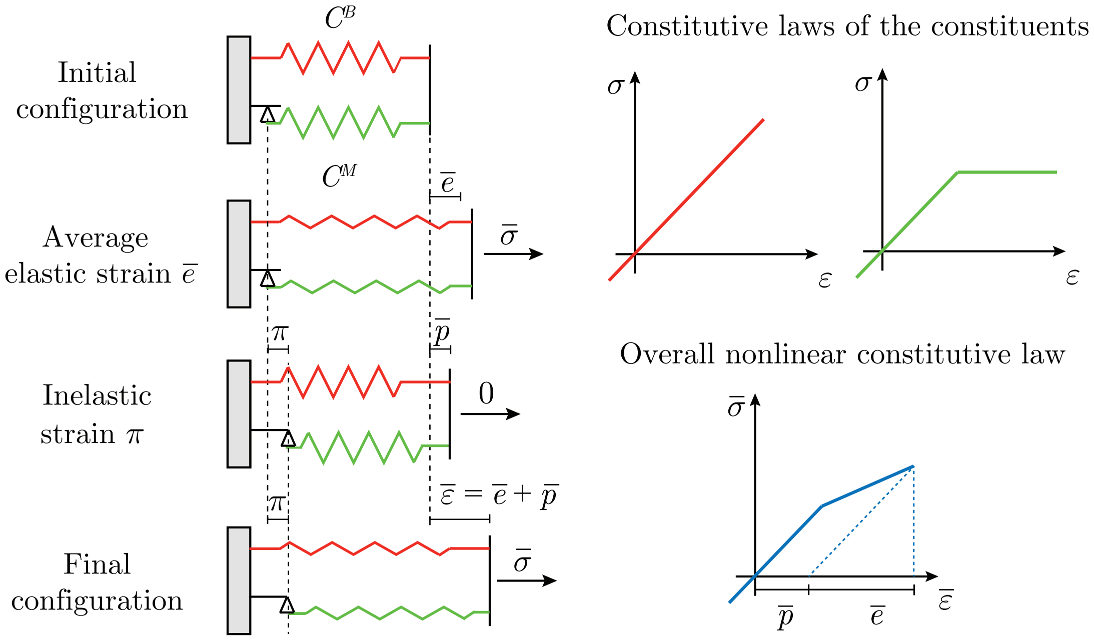

Figure 3.12: Sacco (2009): scheme of the nonlinear homogenization procedure based on the TFA technique.

3.2 Other approaches

3.2.1 Limit analysis

Limit analysis is a consolidate approach largely used to estimate the safety of masonry block structures. By using the limit theorems of plasticity, it is aimed at determining the factor for which the external load has to be increased until structural collapse. Based on the observation of recurrent failure modes of masonry constructions, rigid body systems are identified and the collapse mechanisms are analyzed.

According to the pioneer work of Heyman (1982), the limit theorems of plasticity can be applied to masonry structures by assuming the following properties for the material:

- Zero tensile strength, that is no tensile forces can be transmitted between the masonry blocks. This hypothesis is usually realistic for dry masonry or masonry made with weak mortar, but it can result too safe for spandrel masonry with high interlocks;
- Infinite compressive strength of the material. This assumption, which translates into neglecting the masonry crushing, is obviously unsafe, but the introduced errors can be considered small;
- Sliding can not occur between joints.

These conditions allow for the application of the lower-bound and upper-bound theorems, which lead to the so-called static and kinematic approaches for the analysis of masonry structures, respectively. The former states that if a statically admissible state of equilibrium can be found, the structure will not collapse. The last looks for the limit load by forcing the work of the external forces to zero for a properly selected collapse mechanism. For instance, Giuffrè (1994) and Carocci (2001) applied the kinematic limit analysis to study the vulnerability of masonry structures through their decomposition into rigid blocks (Figure 3.13).
Recently, computer-based limit methods, mainly based on the kinematic approach, were developed by adopting the following hypothesis:

- Material is characterized by zero tensile and infinite compressive strength;
- Shear failure at joints is perfectly plastic;
- Limit load occurs with small displacements.

It should be remarked that the mentioned plastic limit theorems can be applied only if the normality condition stands, that is if a simple frictional Coulomb law with associated flow rule is considered. In this case, the normality condition leads to a fixed dilatancy characterized by an angle Ψ equal to the friction angle φ, as

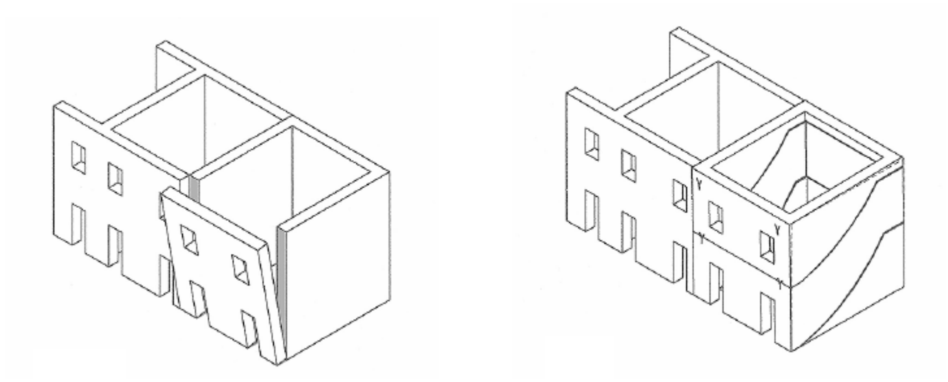

(a) (b)

Figure 3.13: Carocci (2001): failure mechanism of outside walls without (a) cross connections and with (b) cross connections.

shown in Figure 3.14(a). However, no dilatancy occurs in some real cases and, consequently, non-associative rules should to be adopted (Figure 3.14(b)) . The non-compliance with the normality rule means that the fundamental theorems of plasticity will not in general provide a unique solution, as highlighted by Drucker (1954) almost half a century ago.

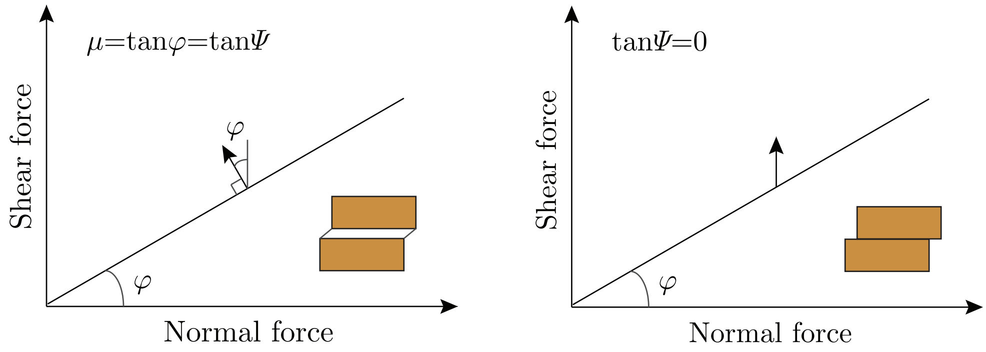

(a) (b)

Figure 3.14: Associative (a) flow rule and non-associative (b) flow rule with null dilatancy.

Several methods were proposed to solve problems involving non-associated flow rule, which are nonlinear and non-convex. For instance, Gilbert et al. (2006)

proposed a simple iterative procedure based on the successive solution of linear programming sub-problems. Baggio and Trovalusci (2000) suggested a two-step procedure: in the first step a linear problem is solved by applying the upper-bound limit theorem and the obtained solution is used to explore the solution of the nonlinear and non-convex problem. As an example, Figure 3.15 shows some of their results with reference to a masonry typology characterized by large vertical stones, called 'opus africanum'. The considered external forces were the self-weight and the horizontal mass actions factorized by the multiplier α_0. The collapse mechanism resulting from a nonlinear limit analysis with casual initial guess is sketched in Figure 3.15(a), by showing an unsatisfactory result, as it provides interpenetration of two stones in the left bottom corner of the wall and a load multiplier ($\alpha_0 = 0.1056$) far from the actual one. Thus, other analyses were performed by solving the linearized problem and by employing its solution to evaluate the initial guess for the nonlinear problem. The obtained results, reported in Figure 3.15(b) and (c), were more accurate, as no interpenetration was found and the load multiplier was similar. However, some differences in the final configurations emerged in these two solutions as the dilatant effects are not negligible in this problem.

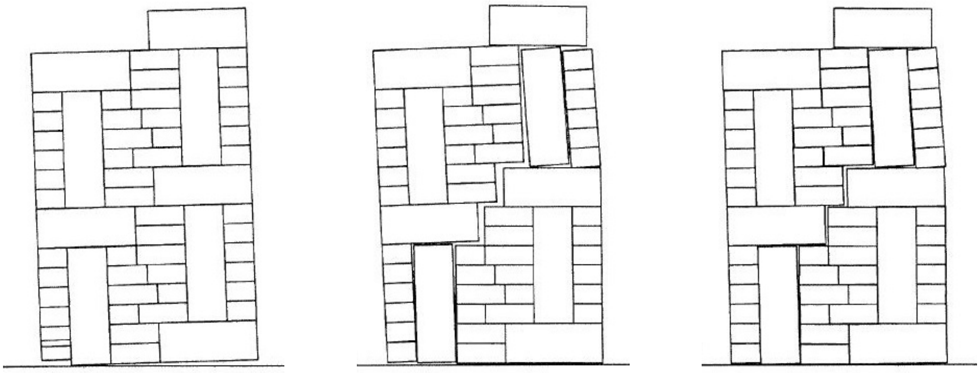

(a) $\alpha_0 = 0.1056$ (b) $\alpha_0 = 0.3766$ (c) $\alpha_0 = 0.3469$

Figure 3.15: Baggio and Trovalusci (2000). Collapse load multipliers and failure mechanisms obtained from: (a) nonlinear limit analysis with arbitrary initial guess, (b) linear limit analysis and (c) nonlinear analysis starting from the solution of (b).

On the overall, the described method is a powerful tool to realistically identify the safety level of the structures, but it can not describe the structural response for loads far from the limit conditions, as well as the damage progression. However, limit analysis should be always used at least like complementary tool, when more sophisticated analyses are performed. For instance, Betti and Vignoli (2011) evaluated the seismic vulnerability of the Basilica of the Santa Maria all'Impruneta by using both a finite element macromodel (Figure 3.7) and the limit analysis (Figure 3.16).

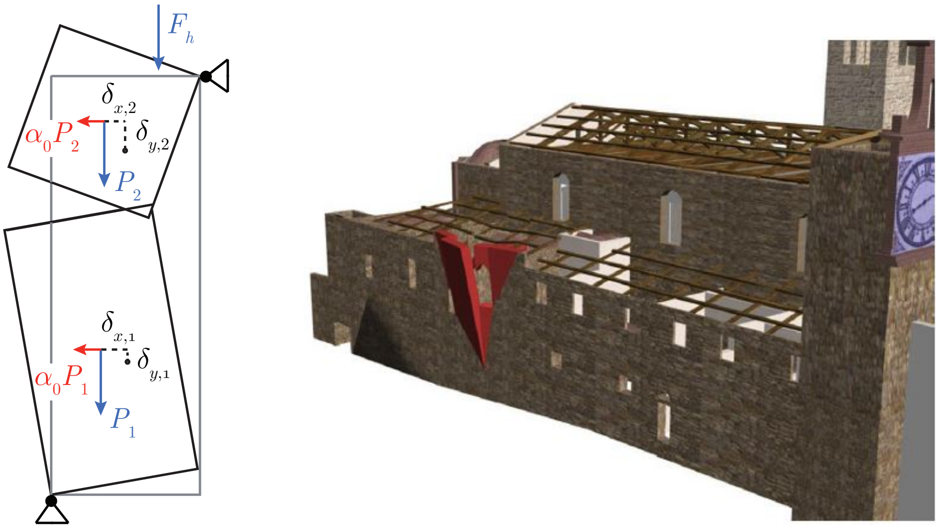

(a) (b)

Figure 3.16: Betti and Vignoli (2011): (a) reference case for the limit analysis and (b) lateral wall overturning of the Basilica of Santa Maria all'Impruneta.

The simple reference scheme shown in Figure 3.16(a) was adopted and the collapse multiplier α_0 was evaluated by applying the Theorem of Virtual Work according to the following equation:

$$\alpha_0 \left(\sum_{i=1}^{n} P_i \delta_{x,i} + \sum_{j=n+1}^{n+m} P_j \delta_{x,j} \right) - \sum_{i=1}^{n} P_i \delta_{y,i} - \sum_{h=1}^{l} F_h \delta_h = W_{fe} \tag{3.8}$$

where $\delta_{x,i}$ and $\delta_{y,i}$ are the virtual displacements of the elementary blocks centroids; P_i is the own weight of each element composing the kinematic chain; P_j and F_h are the weights and loads transmitted by the confining elements with $\delta_{y,j}$, δ_h

indicating the virtual displacements of their application points. Limit analysis and pushover results were in agreement, as these predicted a critical behavior of the structure when the seismic load is acting in the transverse direction of the church (Figure 3.16(b)). Similarly, Sacco and Toti (2010) used the limit analysis result to compare the ultime load of a masonry arch predicted with their micromechanical finite element model.

3.2.2 Macroelement method

The so-called macroelement strategy was developed to combine an accurate description of the nonlinear behavior of masonry elements with the need to perform analyses with reduced computational cost. The method is based on a preliminary discretization of masonry walls or structures, mainly according to empirical criteria inspired by the observation of post-earthquake damage patterns, and the analysis is performed on an assemblage of macroelements. Each of them consists of a single finite element with few degrees of freedom, ensuring a considerable reduction of computational effort.

The 'equivalent frame' method (Chen et al., 2008; Addessi et al., 2015; Liberatore et al., 2017) considers the walls as an assemblage of deformable one-dimensional element connected through rigid nodes, which are indeed undamaged part of the walls. When crumbling and out-of-plane mechanisms are prevented, in-plane behavior of the walls can be studied to assess the global response of the building to horizontal actions. Piers and spandrels can be identified as the two main load-bearing components, being the first able to carry both vertical and horizontal loads. Spandrels, usually regarded as 'secondary', strongly affect piers boundary conditions, thus playing a crucial role. As Figure 3.17(a) shows, walls are discretized through frame elements, representing piers or spandrels, and rigid offsets. The nonlinear behavior of beam elements can be modeled by means of either distributed or lumped inelasticity. Lumped approaches consist in placing flexural and shear hinges at both the ends and mid-span of the elements, respectively. The Italian code (NTC, 2008) establishes a rigid-perfectly plastic response for piers, which can translate in rigid-plastic constitutive laws for the hinges. However, past and recent scientific literature offers even more sophisticated approaches, as that recently presented in Liberatore et al. (2017). The authors introduced the Bouc-Wen and Bouc-Wen-Baber-Noori hysteretic models, accounting for strength and stiffness degradation, in the constitutive laws of flexural and shear hinges (Figure 3.17(b)), with the aim of simulating the complex nonlinear behavior of masonry panels under cyclic loads. Indeed, these hysteresis models are able to reproduce a wide range of different shapes by using a limited set of parameters.

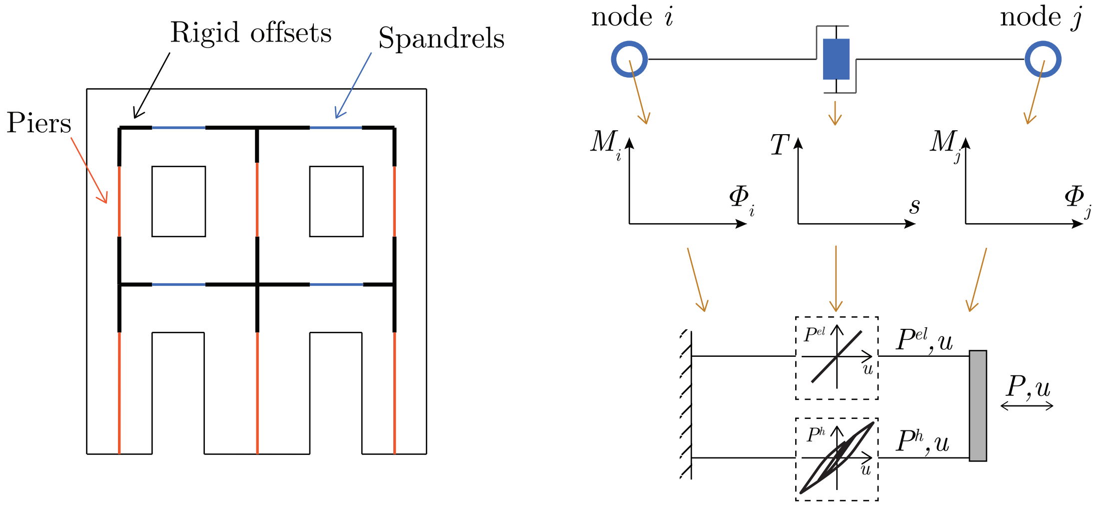

(a) (b)

Figure 3.17: Equivalent frame method: (a) conventional subdivision of masonry walls in deformable frame elements and rigid zones and (b) $2D$ frame element proposed by Liberatore et al. (2017)

Many other macroelement approaches make use of bi-dimensional finite elements (Braga and Liberatore, 1990; Caliò et al., 2012). Among the others, the two-node macroelement proposed by Brencich et al. (1998), whose governing kinematic and static variables are shown in Figures 3.18(a) and (b), should be mentioned. Classification of this element is not straightforward: kinematic and static quantities used to describe its response are in line with a one-dimensional approach, but further degrees of freedom are introduced to take into account rocking and shear-sliding phenomena stand for a more bi-dimensional nature. This element is able to account for damage, overturning and frictional shear mechanisms. It is composed of a top and bottom part (gray zones in Figure 3.18(a) and (b)), where the extensional and bending effects are concentrated and a central part (orange zone in Figure 3.18(a) and (b)) undergoing shear effects. Figure 3.18(c) shows an example of macroelement mesh for a bi-dimensional wall with nodes placed in the center of the rigid elements, so that the flexible extremities of the macroelements are eccentric with respect to the nodes themselves.

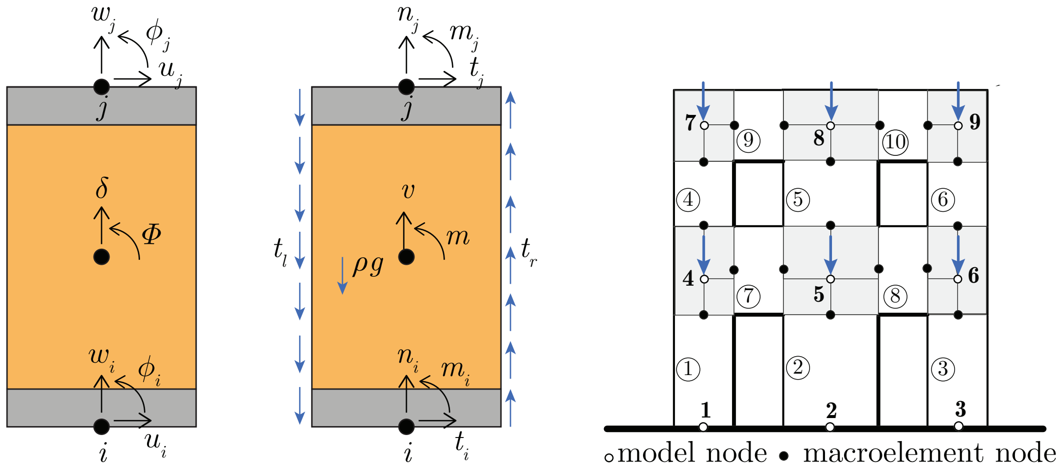

(a) (b) (c)

Figure 3.18: Brencich et al. (1998): (a) kinematic and (b) static variables of the proposed macroelement, (c) example of macroelement mesh with piers, spandrels and rigid zones (gray areas).

Recent developments of computer codes based on macroelement methods, as that proposed by Lagomarsino et al. (2013), testify a lively interest towards this modeling technique, which represents also an efficient tool for practice oriented applications.

3.2.3 Discrete element method

It should be also mentioned the discrete element (DE) approach, as it was largely employed for seismic assessment of masonry buildings. According to the pioneer proposal of Cundall (1971), this method enables finite displacements and rotations of discrete bodies including their complete separation and new contacts among bodies as the analysis goes on. Within the framework of masonry structures, the heterogeneous material is idealized as an assembly of bodies, the masonry units, interacting at the boundaries through mortar joints regarded as contact surfaces between bodies. By an overview of the proposed DE methods (Lemos, 2007), a variety of formulations emerges, whose main differences can be found in the contact assumptions, block representation and solution methods.

The contact representation can involve the point contact hypothesis with the resulting contact forces expressed as function of the relative block displacement at that point. Alternatively, interacting line segments are assumed by allowing a linear variation of stresses on the contact surface. Two main classes of contact can be recognized, that are based on the *soft* and *hard* contact assumptions, also known as deformable and rigid contact approaches. The former enforces the no overlap condition between blocks, the latter involves small overlap for contact in compression. For instance, Acary and Jean (1998) apply the Contact Dynamic Method, accounting for Coulomb friction law and unilateral contact conditions with no block overlap (i.e rigid contact approach), for the numerical simulation of monuments.

Regarding the mechanical behavior of blocks, most of the DE models take on the rigid block assumption, as this hypothesis is acceptable in many practical problems involving the evaluation of collapse loads of stone masonry structures. In $2D$ problems, three degrees of freedom (two translations and one rotation) characterize the motion of each block and explicit time-stepping algorithms are used as solution method for both static and dynamic problems. However, the block deformability is sometimes taken into account, especially in cases of structure made of weak material.

Several examples of DE method application to masonry structures can be found. These concern, just to cite some, the rocking motion of block, analyses of basilicas, stone bridges and arches. As an example, Figures 3.19(a) and (b) show the cracking pattern and collapse mechanism obtained for a stone house by Alexandris et al. (2004), with reference to Kalamata earthquake (1986, Greece) scaled to peak ground acceleration (PGA) equal to $0.54g$ and $0.8g$ (with g gravity acceleration), respectively. However, the interested reader can refer to large number of references reported in Lemos (2007), Roca et al. (2010) and Smoljanović et al. (2013).

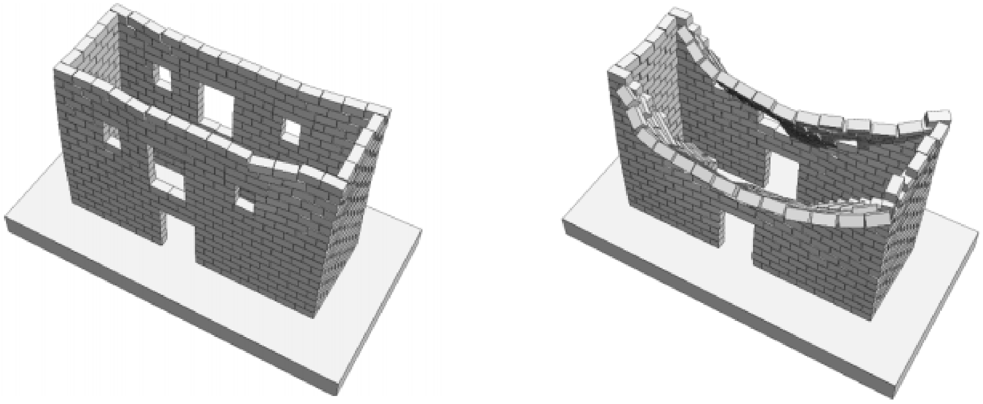
(a) (b)

Figure 3.19: Alexandris et al. (2004): cracking pattern and collapse mechanism of the model house under the Kalamarata earthquake with (a) PGA=0.54g and (b) PGA=0.8g.

3.3 Summary

Traditional and modern methods for modeling of historic masonry structures were briefly described. These largely differ in accuracy, required input data and computational cost. Consequently, structural capacity predictions can depend on the assumed modeling technique and personal intuitions should be used to critically analyze the results. It emerged that FE models, involving properly formulated nonlinear constitutive laws, are a powerful tool to describe evolution of degrading mechanisms over time. Sophisticated micro and multiscale models, accounting for the material microstructure, provide very accurate results but require high computational effort. To overcome this drawback, the macromodeling technique is nowadays largely used, mainly to analyze large scale structures. However, the development of accurate phenomenological models represents still a challenging task, because of difficulties in identifying proper constitutive laws of the equivalent homogenized masonry material.

Chapter 4

Isotropic damage-plastic model

Within the FE modeling approaches, macromechanical models appear as a fair compromise between accuracy and computational cost. In this chapter, a novel isotropic damage-plastic model is proposed for the macromechanical analysis of masonry structures. The adopted constitutive relationship is able to capture the main degrading mechanisms due to propagation of microcracks and accumulation of irreversible strains. Moreover, the stiffness recovery, due to re-closure of tensile cracks when the material undergoes compression states, is taken into account to properly simulate masonry cyclic response.

The assumption of isotropic damage formulation is usually suitable for ancient constructions characterized by strong uncertainty in textures and mechanical properties, but it can result inaccurate for regular arrangements where anisotropic constitutive laws are required (Lourenço et al., 1997; Berto et al., 2002; Karapitta et al., 2011; Pelà et al., 2013). However, isotropic damage models were efficiently adopted (Addessi et al., 2002; Addessi, 2014; Toti et al., 2015; Valente and Milani, 2016), as these allow to capture the main effects of microcracks propagation on the masonry overall response by using few material parameters. For a more detailed discussion concerning the adoption of isotropic and anisotropic damage models, reader can refer to Fichant et al. (1999).

As the proposed model is implemented into a finite element procedure, details about the computational aspects are also provided together with information on the solution algorithm used to solve the nonlinear evolution problem of damage

and plastic variables. Furthermore, to avoid the well-known numerical problems typical of finite element models, due to strain localization and subsequent spurious mesh sensitivity, a regularized formulation is adopted basing on a nonlocal continuum approach.
Finally, numerical applications are performed to explore the model capability of describing masonry inelastic behavior and comparisons between numerical and experimental outcomes are also provided for some masonry panels.

4.1 Isotropic damage models: the basis

Main purpose of Continuum Damage Mechanics is to represent and model, within the continuum-mechanics framework, the onset and propagation of distributed defects in material. Kachanov (1958) proposed the first continuum damage model by introducing a scalar internal variable to model the creep failure of metals. This variable did not have a clear physical meaning, but it was intended to provide a suitable measure of the state of internal degradation. Further developments have clearly defined the damage variable as the reduction of the cross-sectional area due to microcracking.

With reference to Figure 4.1(a), where a representative volume element (RVE) in the neighborhood of point M of a damaged medium and a plane passing through M with normal $\mathbf{n}$ are shown, the damage variable is expressed as follows:

$$D(M,\mathbf{n}) = \frac{A_d}{A} \,, \tag{4.1}$$

where A is the sectional area and A_d represents area of defects. On the basis of its definition, damage variable can varies between 0 and 1, corresponding to the virgin material and completely damaged material, respectively. If isotropic damage is considered, dependency from the normal $\mathbf{n}$ is neglected and Eq. 4.1 is further simplified:

$$D(M) = \frac{A_d}{A} \,. \tag{4.2}$$

Formulation of continuum damage models requires definition of equivalent criterion between the damaged material configuration and a fictitious undamaged one, so that to use classic laws of continuous mechanics. To this purpose the net stress concept has to be introduced. This is usually done by considering a simple uni-axial tensile test, sketched in Figure 4.1(b). As the applied force F is increased, the transversal section A_0 decreases due to both Poisson's effect and onset of microcracks. Thus, by denoting with A the reduced cross-sectional area caused by the transverse strains, the nominal, σ_0, and 'true', σ, tension, are expressed as:

$$\sigma_0 = \frac{F}{A_0}\,, \quad \sigma = \frac{F}{A}\,. \tag{4.3}$$

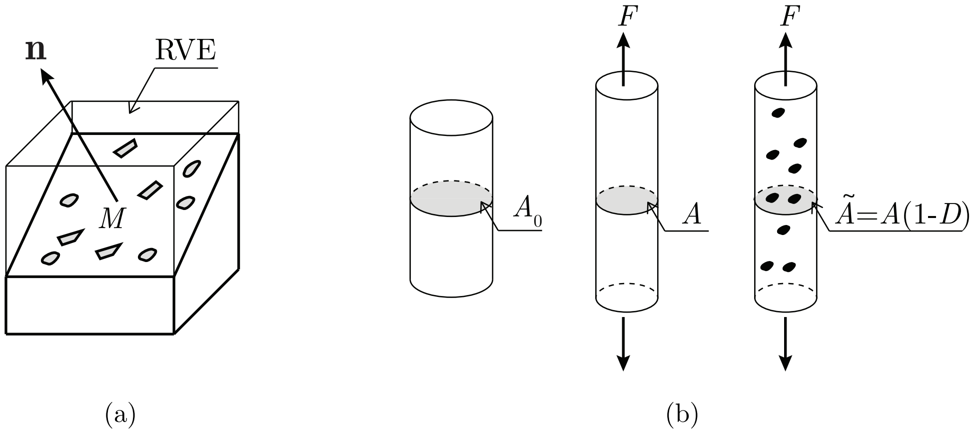

Figure 4.1: Damage Mechanics concepts: (a) RVE, (b) effective area $\tilde{A}$.

If small strains hypothesis holds $A_0 = A$ and, consequently, $\sigma_0 = \sigma$. Thus, by accounting for the microvoids area, the net stress $\bar{\sigma}$ results as:

$$\bar{\sigma} = \frac{F}{\tilde{A}} = \frac{F}{A(1-D)} = \frac{\sigma}{1-D}\,. \tag{4.4}$$

Extension of previous concepts to the pluri-axial case is trivial when isotropic damage is considered, with net stress $\bar{\boldsymbol{\sigma}}$ defined as:

$$\bar{\boldsymbol{\sigma}} = \frac{\boldsymbol{\sigma}}{1-D}\,. \tag{4.5}$$

With the introduced quantities at hand, strain and energy equivalence principles are described below, as suggested by Marfia (2000).

4.1.1 Strain equivalence principle

Hypothesis of equivalent strain, based on empirical nature, establishes that “the strain behavior of a damaged material is represented by constitutive equations of the virgin material (without any damage) in the potential of which the stress is simply replaced by the effective stress”(Lemaitre, 1985).

The constitutive laws for a virgin and damaged material result, by neglecting effect of plastic strain, respectively:

$$\boldsymbol{\sigma} = \mathbf{C}\boldsymbol{\varepsilon} \ , \quad \bar{\boldsymbol{\sigma}} = \mathbf{C}\boldsymbol{\varepsilon} \ , \tag{4.6}$$

where $\mathbf{C}$ is the stiffness matrix of the undamaged material. It is useful to introduce the $\tilde{\mathbf{C}}$ matrix, which takes into account the mechanical properties degradation. Thus, the stress-strain relationship of the damaged material can be rewritten as a function of $\boldsymbol{\sigma}$ and $\tilde{\mathbf{C}}$:

$$\boldsymbol{\sigma} = \tilde{\mathbf{C}}\boldsymbol{\varepsilon} \ , \tag{4.7}$$

By deducing $\boldsymbol{\varepsilon}$ from the previous equation and replacing it in Eq. 4.6_2, the following condition is obtained:

$$\bar{\boldsymbol{\sigma}} = (\mathbf{C}\tilde{\mathbf{C}}^{-1})\boldsymbol{\sigma} \ , \tag{4.8}$$

where $\mathbf{C}\tilde{\mathbf{C}}^{-1}$ represents the damage operator, which can be expressed, by assuming isotropic damage, as follows:

$$\mathbf{C}\tilde{\mathbf{C}}^{-1} = (1 - D)^{-1}\mathbf{I} \ , \tag{4.9}$$

with $\mathbf{I}$ identity matrix. Consequently, the effective damage matrix $\tilde{\mathbf{C}}$ and the net stress $\bar{\boldsymbol{\sigma}}$ are expressed as:

$$\tilde{\mathbf{C}} = (1 - D)\mathbf{C} \ , \tag{4.10}$$

and

$$\bar{\boldsymbol{\sigma}} = \frac{\boldsymbol{\sigma}}{1 - D} \ . \tag{4.11}$$

Finally, it should be remarked that, by defining the effective stress $\tilde{\boldsymbol{\sigma}}$ as the stress acting on the undamaged material, the described principle establishes equivalence between effective and net stress:

$$\bar{\boldsymbol{\sigma}} = \tilde{\boldsymbol{\sigma}} = \frac{\boldsymbol{\sigma}}{1-D} \; . \tag{4.12}$$

4.1.2 Energy equivalence principle

Energy equivalence principle postulates that “the elastic energy stored in a damaged material Λ_d is equal to the elastic energy of an undamaged equivalent material Λ_0 except that the stresses are replaced by the net stresses”(Cordebois and Sidoroff, 1982).
The energy stored in the material Λ_d is:

$$\Lambda_d = \frac{1}{2}\boldsymbol{\sigma}^T \tilde{\mathbf{C}}^{-1} \boldsymbol{\sigma} \; , \tag{4.13}$$

while the elastic strain energy of the equivalent undamaged material Λ_0 is defined as:

$$\Lambda_0 = \frac{1}{2}\bar{\boldsymbol{\sigma}}^T \mathbf{C}^{-1} \bar{\boldsymbol{\sigma}} \; . \tag{4.14}$$

Thus, by using energy equivalence and net stress definition (Eq.4.5), the material damaged stiffness matrix $\tilde{\mathbf{C}}$ results:

$$\tilde{\mathbf{C}} = (1-D)^2 \mathbf{C} \; , \tag{4.15}$$

and, consequently, the effective stress is:

$$\tilde{\boldsymbol{\sigma}} = \mathbf{C}\boldsymbol{\varepsilon} = \frac{1}{(1-D)^2}\tilde{\mathbf{C}}\boldsymbol{\varepsilon} \; . \tag{4.16}$$

4.2 Damage-plastic model

The heterogeneous masonry wall, schematically depicted in Figure 4.2(a), is modeled as an equivalent homogenized medium (Figure 4.2(b)), adopting a $2D$ plane stress formulation under the hypothesis of small displacements and strains. At each material point M located at $\mathbf{x} = (x_1,\, x_2)$ on the wall surface A, the displacement vector $\mathbf{u} = \{u_1\, u_2\}^T$ is defined. By applying the compatibility operator $\mathbf{B}$, the total strain vector is deduced as:

$$\boldsymbol{\varepsilon} = \mathbf{B}\,\mathbf{u}\,, \tag{4.17}$$

where $\boldsymbol{\varepsilon} = \{\varepsilon_1\, \varepsilon_2\, \gamma_{12}\}^T$ and:

$$\mathbf{B} = \begin{bmatrix} \partial/\partial x_1 & 0 \\ 0 & \partial/\partial x_2 \\ \partial/\partial x_2 & \partial/\partial x_1 \end{bmatrix}. \tag{4.18}$$

The stress vector is accordingly introduced as $\boldsymbol{\sigma} = \{\sigma_1\, \sigma_2\, \tau_{12}\}^T$. The stress-strain constitutive relationship is based on a damage-plastic model, coupling an isotropic two-variable damage model and a Drucker Prager plasticity formulation with isotropic and kinematic hardening. The following stress-strain law, derived on the basis of the equivalence energy principle (see Section 4.1.2), is adopted:

$$\boldsymbol{\sigma} = (1 - D)^2\, \mathbf{C}\, (\boldsymbol{\varepsilon} - \boldsymbol{\varepsilon}^p)\ , \tag{4.19}$$

where

$$D = \alpha_t D_t + \alpha_c D_c\ . \tag{4.20}$$

D_t and D_c are the damage variables in tension and compression, respectively, $\boldsymbol{\varepsilon}^p$ is the plastic strain vector, and $\mathbf{C}$ the elastic constitutive matrix of the undamaged material, resulting as:

$$\mathbf{C} = \frac{E}{1 - \nu^2} \begin{bmatrix} 1 & \nu & 0 \\ \nu & 1 & 0 \\ 0 & 0 & (1-\nu)/2 \end{bmatrix}\ , \tag{4.21}$$

being E and ν Young's modulus and Poisson ratio, respectively. The two quantities α_t and α_c in Eq. 4.20 are weighting coefficients, defined in the following on the basis of the strain state at point M, and rule the combined effect of the two damage variables.

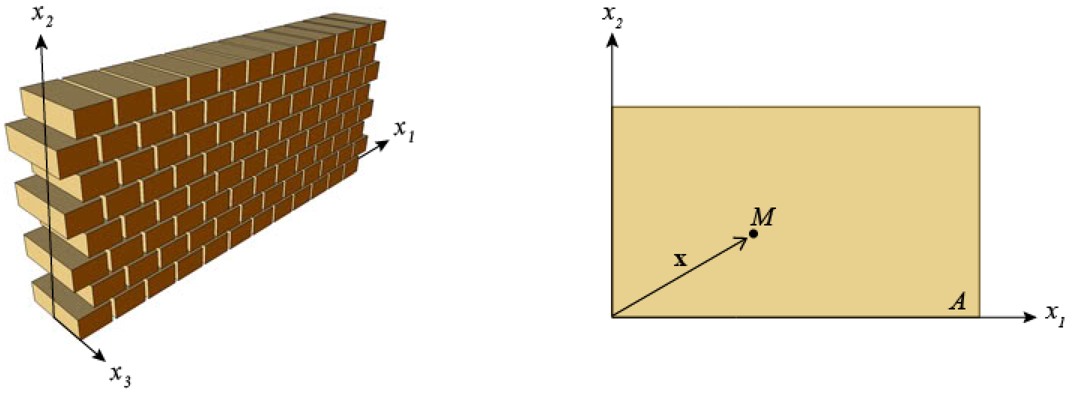

(a) (b)

Figure 4.2: (a) Heterogeneous masonry wall; (b) equivalent homogenized medium.

4.2.1 Damage model

The model here proposed is an enhancement of that presented in Addessi et al. (2002), where a single scalar damage variable was introduced and the non-symmetric behavior in tension and compression typical of brittle-like materials was described by properly defining the damage associated variable. To account for the unilateral effect related to re-closure in compression of the tensile cracks, a modified version is here developed, where two different damage variables are introduced, D_t and D_c, measuring the damage for prevailing tensile and compressive states, respectively, and evolving independently, but satisfying the constraint $D_t \geq D_c$. Both range between 0, corresponding to undamaged state of the material, and 1, attained when the material is completely degraded. Furthermore, the thermodynamic irreversibility condition is enforced, such that $\dot{D}_t \geq 0$ and $\dot{D}_c \geq 0$. Accordingly, to drive the evolution of D_t and D_c two damage associated variables are defined as:

$$Y_t = \sqrt{\sum_{i=1}^{3} \langle e_i \rangle_+^2} \,, \quad Y_c = \sqrt{\sum_{i=1}^{3} \langle e_i \rangle_-^2 + \frac{\kappa}{2} \sum_{i=1}^{3} \sum_{j \neq i=1}^{3} \langle e_i \rangle_- \langle e_j \rangle_-} \,, \tag{4.22}$$

where the brackets $\langle \bullet \rangle_{+/-}$ compute the positive/negative part of a quantity, κ is a material parameter influencing the shape of the damage limit function in compression, and:

$$e_i = (1-2\nu)\,\hat{\varepsilon}_i + \nu \sum_{j=1}^{3} \hat{\varepsilon}_j \ , \tag{4.23}$$

denoting with $\hat{\varepsilon}_i$ the principal total strains. The principal strain component $\hat{\varepsilon}_3$ is computed by adding to the corresponding principal elastic strain $\hat{\varepsilon}_3^e = -\nu/(1-\nu)(\hat{\varepsilon}_1^e + \hat{\varepsilon}_2^e)$ the plastic strain $\hat{\varepsilon}_3^p$. The evolution processes of the two damage variables are governed by the tensile and compressive damage limit functions, defined as:

$$\begin{aligned} F_t &= (Y_t - Y_{t0}) - D_t\,(a_t Y_t + b_t) \ , \\ F_c &= (Y_c - Y_{c0}) - D_c\,(a_c Y_c + b_c) \ , \end{aligned} \tag{4.24}$$

and ruled by the classical Kuhn-Tucker and consistency conditions:

$$\begin{array}{llll} F_t \le 0\,, & \dot{D}_t \ge 0\,, & F_t\dot{D}_t = 0, & \dot{F}_t\dot{D}_t = 0 \\ F_c \le 0\,, & \dot{D}_c \ge 0\,, & F_c\dot{D}_c = 0, & \dot{F}_c\dot{D}_c = 0 \end{array} \ . \tag{4.25}$$

The material parameters Y_{t0} and Y_{c0} are the damage initial thresholds in tension and compression, b_t and b_c regulate mainly the uni-axial tension and compression peak strengths, whereas a_t and a_c affect the slope of the softening branches. The weighting coefficients combining the two damage variables in Eq. 4.20 are defined as:

$$\alpha_t = \frac{Y_t^e/Y_{t0}}{Y_t^e/Y_{t0} + Y_c^e/Y_{c0}} \ , \quad \alpha_c = 1 - \alpha_t \ , \tag{4.26}$$

where:

$$Y_t^e = \sqrt{\sum_{i=1}^{3} \langle e_i^e \rangle_+^2} \ , \quad Y_c^e = \sqrt{\sum_{i=1}^{3} \langle e_i^e \rangle_-^2 + \frac{\kappa}{2} \sum_{i=1}^{3} \sum_{j \ne i=1}^{3} \langle e_i^e \rangle_- \left\langle e_j^e \right\rangle_-} \ , \tag{4.27}$$

and

$$e_i^e = (1 - 2\nu)\, \hat{\varepsilon}_i^e + \nu \sum_{j=1}^{3} \hat{\varepsilon}_j^e \,, \tag{4.28}$$

being $\hat{\varepsilon}_i^e$ the principal elastic strains.

In Figure 4.3 the damage limit domains are shown in the principal (a) strain and (b) stress space, adopting the material parameters contained in Table 4.1 and for different values of the damage variables D_t and D_c and the parameter κ (if not specified κ is assumed equal to 0). In the stress space, the hardening phase, where the limit domain enlarges, and the softening phase, during which the domain shrinks, can be noted. On the contrary, in the strain space, domains are always widening, as expected. Finally, it should be remarked that, for $\kappa = 0$, circular shape for compressive strain states is found, while negative values of κ (positive values are unacceptable) lead to limit domains characterized by elliptical shape in order to capture the increasing strength typical of the pluri-axial compressive states.

Elastic parameters		Damage parameters					
E [MPa]	ν	Y_{t0}	b_t	a_t	Y_{c0}	b_c	a_c
1800	0.1	1×10^{-4}	1.5×10^{-4}	0.9	5×10^{-4}	7×10^{-3}	0.8

Table 4.1: Material parameters adopted in Figures 4.3, 4.4, 4.5 and 4.9;.

In Figure 4.4 influence of the parameters (a) b_t and (b) a_t on the uni-axial tensile constitutive law is shown, considering for the other parameters values contained in Table 4.1. As b_t increases (Figure 4.4(a)), higher values of the tensile strength are obtained moved up rightward. Differently, the parameter a_t (Figure 4.4(b)) affects the slope of the descending post-peak branch, i.e. the severity of the strain-softening behavior. Therefore, b_t and a_t parameters can be identified on the basis of the material fracture energy G_f and the assigned material tensile strength. Same observations hold in the case of the uni-axial compressive response.

Finally, a cyclic uni-axial stress-strain law is depicted in Figure 4.5(a) with reference to the applied strain history of Figure 4.5(b). Model capability to account for the unilateral effect is highlighted by the variation of the damage variables D,

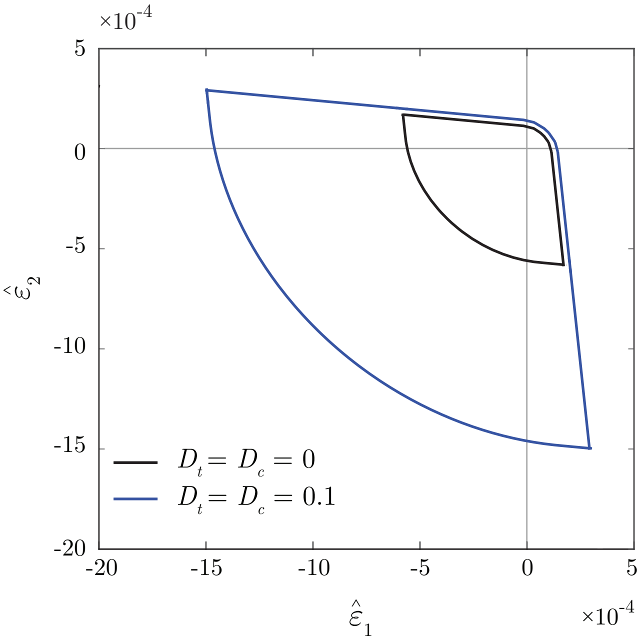

(a)

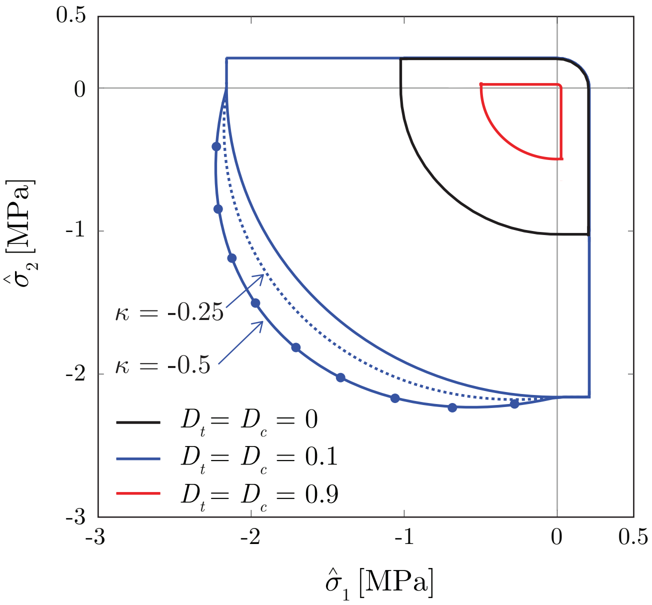

(b)

Figure 4.3: Damage domains for different values of the damage variables in the principal (a) strain and (b) stress space.

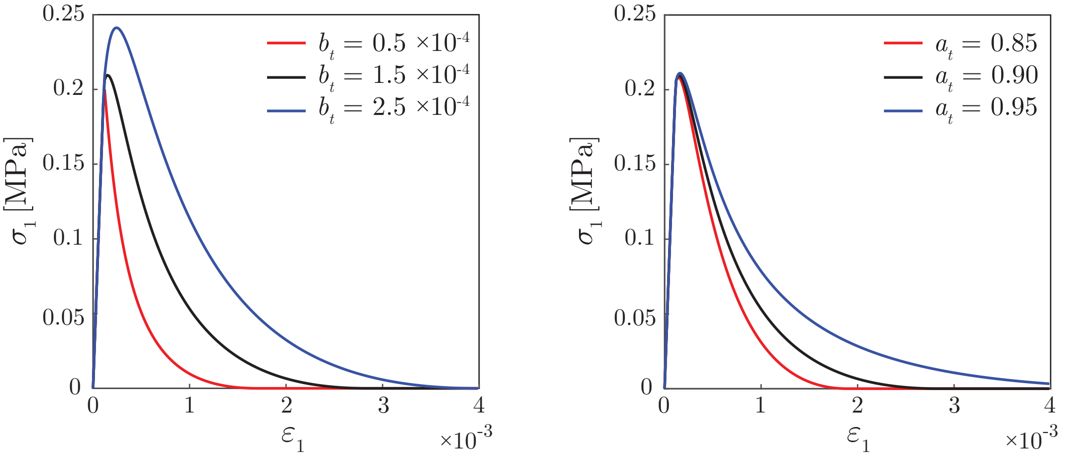

(a) (b)

Figure 4.4: Uni-axial tensile stress-strain law: effect of the parameters (a) b_t and (b) a_t.

D_t and D_c with respect to the fictitious time variable, as shown in Figure 4.5(b). It can be noted that D assumes the same value of D_t for tensile states and, then, when a reversal strain occurs, returns equal to D_c.

4.2.2 Plasticity model

A classic Drucker-Prager plasticity model is adopted to phenomenologically describe frictional mechanisms evolving in masonry material, as this is capable to capture the non-symmetric behavior under tensile and compressive states, as well as introduce pressure-sensitivity. A plane stress formulation with linear isotropic and kinematic hardening is considered. First, the formulation is presented with reference to the general three-dimensional states of stress and strain and, then, the original three-dimensional constitutive equations are constrained so that the plane stress counterpart is obtained. Indeed, when a plane stress problem is considered (Figure 4.6), the out-of-plane stress components, that is σ_3, τ_{13} and τ_{23}, are constrained to be zero and some modifications of the numerical algorithm are needed.

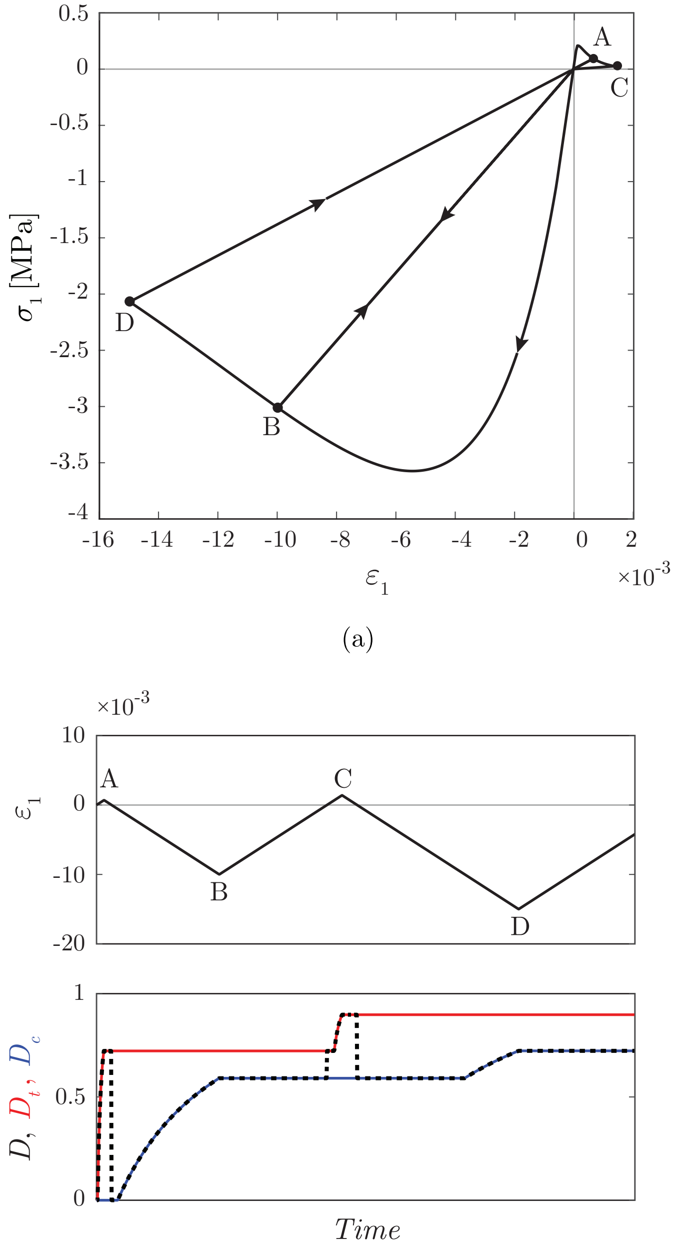

(a)

(b)

Figure 4.5: Damage model: (a) uni-axial cyclic stress-strain law, (b) applied strain history and variation of damage variables.

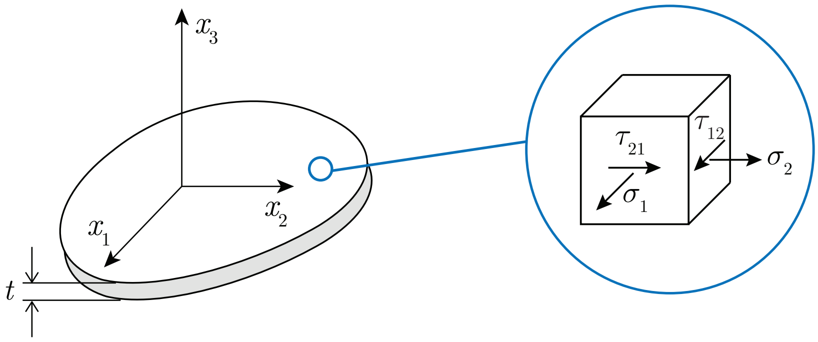

Figure 4.6: Plane stress state.

4.2.2.1 Three-dimensional Drucker Prager model

The Drucker-Prager yield function for the $3D$ case is expressed as follows:

$$F^p = |\mathbf{P}\widetilde{\boldsymbol{\sigma}}^{3D} - \boldsymbol{\zeta}| - \sqrt{\frac{2}{3}}\,(\sigma_y + H_i\alpha) + \mu\mathbf{1}^T\widetilde{\boldsymbol{\sigma}}^{3D}\ , \tag{4.29}$$

where vector $\mathbf{1} = \{1\,1\,1\,0\,0\,0\}^T$ and operator $\mathbf{P}$ are introduced to evaluate the first invariant and the deviatoric part of the six-component effective stress vector $\widetilde{\boldsymbol{\sigma}}^{3D} = \{\widetilde{\sigma}_1\,\widetilde{\sigma}_2\,\widetilde{\sigma}_3\,\widetilde{\tau}_{12}\,\widetilde{\tau}_{23}\,\widetilde{\tau}_{13}\}^T$, respectively. $3D$ and $2D$ representations of the yield function are given in Figures 4.7(a) and (b) in the principal effective stress space, adopting the material parameters contained in Table 4.2.
$\widetilde{\boldsymbol{\sigma}}^{3D}$ is computed on the basis of the $3D$ elastic constitutive matrix $\mathbf{C}^{3D}$ as below:

$$\widetilde{\boldsymbol{\sigma}}^{3D} = \mathbf{C}^{3D}(\boldsymbol{\varepsilon}^{3D} - \boldsymbol{\varepsilon}^{3Dp}) \tag{4.30}$$

The effective stress vector $\widetilde{\boldsymbol{\sigma}}^{3D}$ is introduced to govern the evolution of the plastic strains, thus resulting that the plastic mechanism is not influenced by the damage progression and evolves independently. In Eq. 4.29, $\boldsymbol{\zeta}$ is the back stress vector describing the kinematic hardening, σ_y is the yield stress, μ is the frictional coefficient, while α is the isotropic hardening variable and H_i the isotropic hardening modulus. Material parameters σ_y and μ are defined as function of uni-axial tension and compression strengths, σ_t and σ_c, as follows:

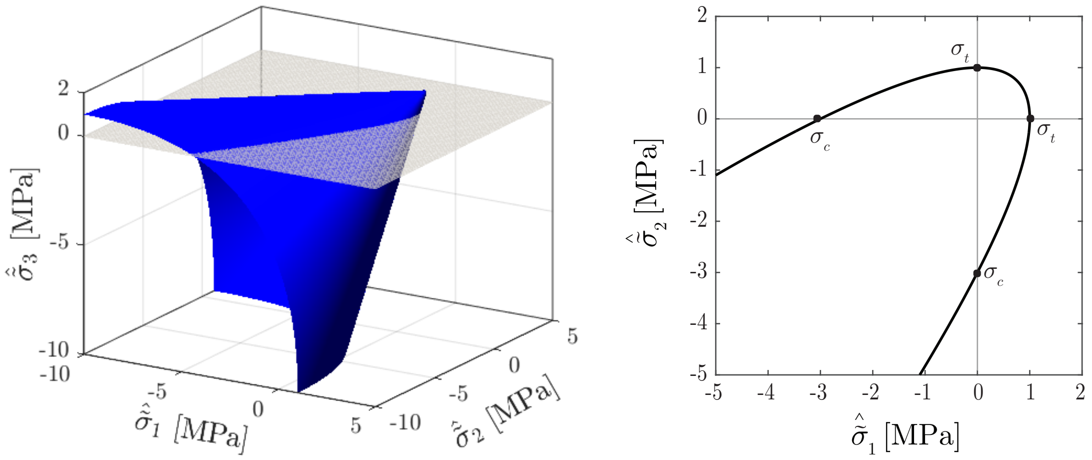

(a) (b)

Figure 4.7: Drucker-Prager yield function at the first onset of the plastic process ($\alpha = 0$, $\boldsymbol{\zeta} = \mathbf{0}$, $\dot{\boldsymbol{\varepsilon}}^{3Dp} = \mathbf{0}$): (a) $3D$ and (b) $2D$ representation.

$$\sigma_y = \frac{2\sigma_c\sigma_t}{\sigma_c + \sigma_t} \tag{4.31}$$

$$\mu = \sqrt{\frac{2}{3}}\left(\frac{\sigma_c - \sigma_t}{\sigma_c + \sigma_t}\right) \tag{4.32}$$

The evolution laws of the plastic variables are introduced as:

$$\dot{\boldsymbol{\varepsilon}}^{3Dp} = \dot{\lambda}^p \frac{\partial F^p}{\partial \widetilde{\boldsymbol{\sigma}}^{3D}} \,, \tag{4.33}$$

$$\dot{\boldsymbol{\zeta}} = \frac{2}{3} H_k \dot{\boldsymbol{\varepsilon}}^{3Dp} \,, \tag{4.34}$$

$$\dot{\alpha} = \dot{\lambda}^p \sqrt{\frac{2}{3}} \,, \tag{4.35}$$

the parameter H_k being the kinematic hardening coefficient and λ^p the plastic multiplier. The plasticity evolution is also governed by the Kuhn-Tucker and consistency conditions:

$$F^p \leq 0\,, \quad \dot{\lambda}^p \geq 0, \quad F^p\dot{\lambda}^p = 0\,, \quad \dot{F}^p\dot{\lambda}^p = 0 \ . \tag{4.36}$$

In Eqs. 4.33-4.36 the dot symbol denotes increment of the quantity with respect to the pseudo-time variable.
Finally, the incremental form of Eq. 4.30 is expressed as:

$$\dot{\boldsymbol{\sigma}}^{3D} = \mathbf{C}^{3Dt}\dot{\boldsymbol{\varepsilon}}^{3D} \,, \tag{4.37}$$

where $\mathbf{C}^{3Dt}$ is the elasto-plastic tangent stiffness matrix evaluated as:

$$\mathbf{C}^{3Dt} = \mathbf{C}^{3D} - \frac{4G^2\dot{\lambda}^p}{|\boldsymbol{\eta}|}\left(\mathbf{I} - \frac{\mathbf{1}\mathbf{1}^T}{3} - \mathbf{n}\mathbf{n}^T\right) - \frac{4G^2\mathbf{n}\mathbf{n}^T + 6GK\mu\mathbf{n}\mathbf{1}^T}{2G + 2/3\,(H_i + H_k)} \,, \tag{4.38}$$

being K and G the bulk and shear moduli, respectively; $\mathbf{I}$ the 6×6 identity matrix and $\mathbf{n} = \boldsymbol{\eta}/|\boldsymbol{\eta}|$ the normal to yield surface, with $\boldsymbol{\eta} = \mathbf{P}\widetilde{\boldsymbol{\sigma}}^{3D} - \boldsymbol{\zeta}$.

As an example, Figures 4.8(a) and (b) show plastic uni-axial stress-strain laws, setting $H_i = 0$ and for two values of H_k, i.e. $H_k = 0.3E$ and $H_k = 0.1E$ (for the other material parameters reference is made to Table 4.2).

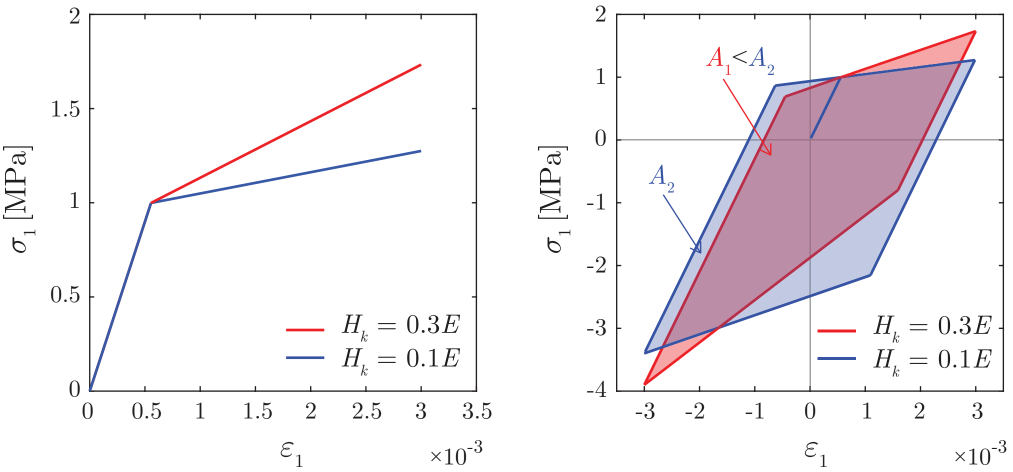

(a) (b)

Figure 4.8: Plastic uni-axial stress-strain law: (a) monotonic tensile response and (b) cyclic response.

Note that H_k value effects the slope of the post-yield stress-strain relationship and that non-symmetric response in tension and compression emerges. Furthermore, the higher value of H_k, that is $H_k = 0.3E$, leads to less energy dissipation, as shown by areas contained in the stress-strain graphs in Figure 4.8(b).

4.2.2.2 Procedure for plane stress plasticity

It is possible to deal with a plane stress problem by using the original three-dimensional formulation of the Drucker-Prager plasticity model and by enforcing the plane stress constraints at the material point level, as already done by others (Saritas and Filippou, 2009).

In what follows, a suitable matrix notation is introduced to distinguish between the retained stress components (σ_1, σ_2, τ_{12}) and those that are constrained to be zero (σ_3, τ_{23}, τ_{13}). Furthermore, the symbol '$\tilde{\ }$', denoting the effective stresses, is neglected for sake of simplicity.

The six-component stress and strain vectors, $\boldsymbol{\sigma}^{3D}$ and $\boldsymbol{\varepsilon}^{3D}$, are obtained by a proper arrangement of vectors collecting in-plane and out-of-plane components, which are:

$$\boldsymbol{\varepsilon}^c = \{\varepsilon_3\, \gamma_{23}\, \gamma_{13}\}^T \ , \quad \boldsymbol{\sigma}^c = \{\sigma_3\, \tau_{23}\, \tau_{13}\}^T \ , \tag{4.39}$$

$$\boldsymbol{\varepsilon} = \{\varepsilon_1\, \varepsilon_2\, \gamma_{12}\}^T \ , \quad \boldsymbol{\sigma} = \{\sigma_1\, \sigma_2\, \tau_{12}\}^T \ . \tag{4.40}$$

The out-of-plane strain vector $\boldsymbol{\varepsilon}^c$ contains unknown components and is determined so that to obtained zero corresponding stress vector $\boldsymbol{\sigma}^c$. It should be remarked that, in the isotropic case, stress and strain transverse shear components vanish (de Souza Neto et al., 2011). However, the procedure is here illustrated for the more general case, where all the out-of-plane components are considered.

The fully $3D$ plasticity problem is solved by setting initial guesses for the strains $\boldsymbol{\varepsilon}^c$ and, then, an iterative procedure is developed including a corrector phase of the strains $\boldsymbol{\varepsilon}^c$. At each iteration, the updated value of $\boldsymbol{\varepsilon}^c$ is computed as:

$$\boldsymbol{\varepsilon}^c = \boldsymbol{\varepsilon}^c + \mathrm{d}\boldsymbol{\varepsilon}^c = \boldsymbol{\varepsilon}^c - (\mathbf{C}_{22}^{3Dt})^{-1}\boldsymbol{\sigma}^c \ , \tag{4.41}$$

where $\mathbf{C}_{22}^{3Dt}$ denotes the sub-matrix, referred to the out-of-plane components, of the elasto-plastic tangent stiffness matrix $\mathbf{C}^{3Dt}$. This is obtained by reorganizing the incremental stress-strains law in Eq. 4.37 as follows:

$$\left[\begin{array}{c} \dot{\sigma}_1 \\ \dot{\sigma}_2 \\ \dot{\tau}_{12} \\ \hline \dot{\sigma}_3 \\ \dot{\tau}_{23} \\ \dot{\tau}_{13} \end{array}\right] = \left[\begin{array}{c|c} \mathbf{C}_{11}^{3Dt} & \mathbf{C}_{12}^{3Dt} \\ \hline \mathbf{C}_{21}^{3Dt} & \mathbf{C}_{22}^{3Dt} \end{array}\right] \left[\begin{array}{c} \dot{\varepsilon}_1 \\ \dot{\varepsilon}_3 \\ \dot{\gamma}_{12} \\ \hline \dot{\varepsilon}_3 \\ \dot{\gamma}_{23} \\ \dot{\gamma}_{13} \end{array}\right] . \tag{4.42}$$

Once updated strains $\boldsymbol{\varepsilon}^c$, the plasticity problem is solved again until $\boldsymbol{\sigma}^c$ vanishes. The briefly described procedure, developed within the solution algorithm presented in the Section 4.3.2, is explained in details in Box 4.1. Here, reference is made to an incremental plastic process, where the known solution at the previous step is denoted with the subscript ‘n’.

Once qualified all aspects related to damage and plasticity, the model results completely defined. As an example, Figure 4.9 shows the uni-axial stress-strain law, under the cyclic deformation history detailed in figure, with reference to the material parameters in Table 4.1 and Table 4.2. The constitutive law correctly reproduces the unilateral effect, thanks to the introduction of the two distinct damage variables D_t and D_c, as well as the growth of the plastic strains, thus accounting for the activation of the friction mechanisms in masonry material.

Plastic parameters

σ_t [MPa]	σ_c [MPa]	H_i [MPa]	H_k [MPa]
1.0	3.0	0.001 E	0.8 E

Table 4.2: Material parameters adopted in Figures 4.7 and 4.9.

```
1. Set initial guess for strains:
   $\boldsymbol{\varepsilon} = \{\varepsilon_1 \, \varepsilon_2 \, \gamma_{12}\}^T$ prescribed
   $\boldsymbol{\varepsilon}^c = \boldsymbol{\varepsilon}^c_n = \{\varepsilon_3 \, \gamma_{23} \, \gamma_{13}\}^T_n$

2. Call variables from last convergence step:
   $\boldsymbol{\varepsilon}^{pc} = \boldsymbol{\varepsilon}^{pc}_n = \{\varepsilon^p_3 \, \gamma^p_{23} \, \gamma^p_{13}\}^T_n$
   $\boldsymbol{\varepsilon}^p = \boldsymbol{\varepsilon}^p_n = \{\varepsilon^p_1 \, \varepsilon^p_2 \, \gamma^p_{12}\}^T_n$
   $\alpha = \alpha_n$
   $\boldsymbol{\zeta} = \boldsymbol{\zeta}_n$

3. Organize the six-component strain vectors $\boldsymbol{\varepsilon}^{3D}$ and $\boldsymbol{\varepsilon}^{3Dp}$:
   $\boldsymbol{\varepsilon}^{3D} = \{\varepsilon_1 \, \varepsilon_2 \, \varepsilon_3 \, \gamma_{12} \, \gamma_{23} \, \gamma_{13}\}^T$
   $\boldsymbol{\varepsilon}^{3Dp} = \{\varepsilon^p_1 \, \varepsilon^p_2 \, \varepsilon^p_3 \, \gamma^p_{12} \, \gamma^p_{23} \, \gamma^p_{13}\}^T$

4. Compute the six-component effective stress vector $\boldsymbol{\sigma}^{3D}$:
   $\boldsymbol{\sigma}^{3D} = \mathbf{C}^{3D}(\boldsymbol{\varepsilon}^{3D} - \boldsymbol{\varepsilon}^{3Dp})$

5. Evaluate yield function $F^p$:
   $F^p = |\mathbf{P}\boldsymbol{\sigma}^{3D} - \boldsymbol{\zeta}| - \sqrt{\frac{2}{3}}\,(\sigma_y + H_i\alpha) + \mu\mathbf{1}^T\boldsymbol{\sigma}^{3D}$

6. Check consistency:
   if $F^p < 0$
       i. $\mathbf{C}^{3Dt} = \mathbf{C}^{3D}$
       ii. no variables update
   else
```

```
        i. solve plasticity and update isotropic hardening variable $\alpha$, back
           stress vector $\boldsymbol{\zeta}$, plastic strains vector $\boldsymbol{\varepsilon}^{3Dp}$ and stress vector $\boldsymbol{\sigma}^{3D}$
        ii. compute the elasto-plastic tangent matrix $\mathbf{C}^{3Dt}$
    end if
7. Check plane stress convergence:
    if $|\boldsymbol{\sigma}^c| \geq tol$
        i. $\mathrm{d}\boldsymbol{\varepsilon}^c = -(\mathbf{C}_{22}^{3Dt})^{-1}\boldsymbol{\sigma}^c$
        ii. $\boldsymbol{\varepsilon}^c = \boldsymbol{\varepsilon}^c + \mathrm{d}\boldsymbol{\varepsilon}^c$
        iii. return to 2.
    else
        go to 8.
    end if
8. Evaluate the plane stress elasto-plastic tangent matrix $\mathbf{C}^t$:
    $\mathbf{C}^t = \mathbf{C}_{11}^{3Dt} - \mathbf{C}_{12}^{3Dt}(\mathbf{C}_{22}^{3Dt})^{-1}\mathbf{C}_{21}^{3Dt}$
```

Box 4.1: Procedure for plane stress plasticity.

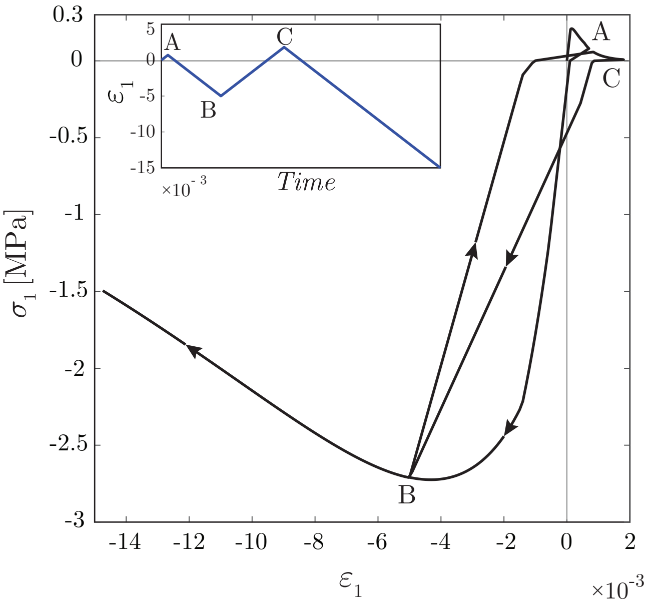

Figure 4.9: Damage-plastic model: uni-axial cyclic stress-strain law.

4.2.3 Nonlocal regularization

When materials exhibit strain-softening behavior, the principle of local action does not hold anymore. Indeed, the onset and evolution of the degrading process at a material point is influenced by the mechanical state of the points lying in a properly defined neighborhood. This can be accounted for by adopting nonlocal constitutive formulations to overcome the analytical problems related to the loss of ellipticity of the governing equations and the related numerical mesh-dependency drawbacks. Here, the nonlocal integral definition (Pijaudier-Cabot and Bažant, 1987) of the damage associated variables is introduced as:

$$\begin{aligned} \bar{Y}_{t/c}\left(\mathbf{x}\right) &= \frac{1}{\int_A \psi\left(\mathbf{x},\mathbf{s}\right)\, dA\left(\mathbf{s}\right)} \int_A Y_{t/c}\left(\mathbf{s}\right) \psi\left(\mathbf{x},\mathbf{s}\right)\, dA\left(\mathbf{s}\right) \ , \\ \bar{Y}^e_{t/c}\left(\mathbf{x}\right) &= \frac{1}{\int_A \psi\left(\mathbf{x},\mathbf{s}\right)\, dA\left(\mathbf{s}\right)} \int_A Y^e_{t/c}\left(\mathbf{s}\right) \psi\left(\mathbf{x},\mathbf{s}\right)\, dA\left(\mathbf{s}\right) \ , \end{aligned} \tag{4.43}$$

where $\bar{Y}_{t/c}(\mathbf{x})$ and $\bar{Y}^{e}_{t/c}(\mathbf{x})$ are the nonlocal quantities at point $\mathbf{x}$, while $Y_{t/c}(\mathbf{s})$ and $Y^{e}_{t/c}(\mathbf{s})$ are the corresponding local variables at the generic point located at $\mathbf{s}$ lying in the neighborhood of $\mathbf{x}$. The classical Gaussian is assumed as weighting function:

$$\psi(\mathbf{x},\mathbf{s}) = e^{-\left(\frac{\|\mathbf{x}-\mathbf{s}\|}{l_c}\right)^2} , \tag{4.44}$$

with l_c denoting the nonlocal radius related to the material internal characteristic length. Once the nonlocal damage associated variables have been computed, these are introduced in Eqs. 4.24, 4.25 and 4.26 to solve the evolution problem of the damage variables D_t and D_c and determine the weighting coefficients α_t and α_c.

4.3 Computational aspects

4.3.1 Finite element formulation

The model presented was implemented in 4-node and 9-node isoparametric quadrilateral FEs, based on a classical displacement formulation. Each node is provided with two displacement degrees of freedom and bi-linear (4-node FE) and bi-quadratic (9-node FE) interpolation functions are used for the two displacement fields u_1 and u_2. The discretized equations of motion governing the FE nonlinear problem are written as:

$$\mathbf{M}\ddot{\mathbf{u}} + \mathbf{R}\dot{\mathbf{u}} + \mathbf{P}^{int}(\mathbf{u}) = \mathbf{P}^{ext} , \tag{4.45}$$

where $\mathbf{u}$, $\dot{\mathbf{u}}$ and $\ddot{\mathbf{u}}$ are the nodal displacement, velocity and acceleration vectors, respectively. $\mathbf{M}$ is the global mass matrix, evaluated by using a lumped approach, while the global damping matrix $\mathbf{R}$ is calculated as a linear combination of mass and stiffness proportional terms. These matrices are obtained by assembling the corresponding element submatrices, given by:

$$\mathbf{M}^e = t^e \int_{A^e} \rho\, \mathbf{S}^e \, dA^e , \tag{4.46}$$

$$\mathbf{R}^e = a_0 \mathbf{M}^e + a_1 \mathbf{K}^e , \tag{4.47}$$

where ρ denotes masonry mass density, t^e the element thickness, A^e the element area and $\mathbf{S}^e$ is a diagonal matrix, whose diagonal terms are the two displacement shape functions associated to the degrees of freedom of each node. In case of 4-node FE, $\mathbf{S}^e$ is defined as:

$$\mathbf{S}^e = \begin{bmatrix} N_1^1 & 0 & 0 & 0 & 0 & 0 & 0 & 0 \\ 0 & N_2^1 & 0 & 0 & 0 & 0 & 0 & 0 \\ 0 & 0 & N_1^2 & 0 & 0 & 0 & 0 & 0 \\ 0 & 0 & 0 & N_2^2 & 0 & 0 & 0 & 0 \\ 0 & 0 & 0 & 0 & N_1^3 & 0 & 0 & 0 \\ 0 & 0 & 0 & 0 & 0 & N_2^3 & 0 & 0 \\ 0 & 0 & 0 & 0 & 0 & 0 & N_1^4 & 0 \\ 0 & 0 & 0 & 0 & 0 & 0 & 0 & N_2^4 \end{bmatrix} , \tag{4.48}$$

with N_i^j ($i = 1, 2$ and $j = 1, 2, 3, 4$) representing the shape function associated to the $i-$ degree of freedom of the $j-$node. Extension to 9-node FE is trivial.

The definition of the element damping matrix $\mathbf{R}^e$ in Eq. 4.47 follows the classical Rayleigh approach, with the coefficients a_0 and a_1 multiplying the element mass and initial undamaged stiffness matrix, $\mathbf{M}^e$ and $\mathbf{K}^e$, respectively, computed as function of the structural natural frequencies. The element stiffness matrix is defined as:

$$\widetilde{\mathbf{K}}^e = t^e \int_{A^e} \mathbf{L}^{eT} \, (1 - D)^2 \mathbf{C}^t \, \mathbf{L}^e \, dA^e \; , \tag{4.49}$$

where $\mathbf{L}^e = \mathbf{B}\mathbf{N}^e$ is obtained by applying the compatibility operator $\mathbf{B}$ introduced in Eq. 4.18 to the shape function matrix $\mathbf{N}^e$, and $\mathbf{C}^t$ is the elasto-plastic tangent constitutive operator. $\mathbf{P}^{int}(\mathbf{u})$ is the internal force vector, accounting for the nonlinear structural response, obtained by assembling the element contributions, defined as:

$$\mathbf{P}^{int,e} = t^e \int_{A^e} \mathbf{L}^{eT} \boldsymbol{\sigma} \, dA^e \; . \tag{4.50}$$

Finally, vector $\mathbf{P}^{ext}$ collects all the external loads applied to the structure, both distributed and concentrated to the nodes.

4.3.2 Solution algorithm

The implicit Newmark-β scheme is used to perform the time integration of the FE differential equations (Eq. 4.45) with values of the coefficients γ and β, which define the variation of acceleration over a time step and accuracy of the method, equal to 0.5 and 0.25, respectively. The nonlinear solution within each time step Δt is determined adopting the Newton-Raphson procedure.

To solve the nonlinear evolution problem of damage and plastic variables at each Gauss point of the FE discretization within the global Newton-Raphson iterative scheme, a predictor-corrector procedure based on the splitting method is developed. This is based on an elastic-plastic predictor phase, followed by a damage correction. During the first stage, the damage evolution is blocked and the plasticity problem governed by Eqs. 4.33 - 4.36 with 4.29 is solved, by further subdividing this phase into an elastic predictor and a plastic corrector step. The damage corrector stage is then performed, by considering the plastic variables evolution as blocked.

The adopted solution strategy is schematically illustrated in Table 4.3, where the symbol Δ denotes the increment of the variable in the time step Δt. A detailed description of the procedure is also provided in Box 4.2, in which the superscript 'i' denotes the Newton-Raphson iteration within the current time step 'n+1'.
The developed finite element and solution algorithm have been implemented in the FE code FEAP (Taylor, 2017) used to perform the numerical analyses. 2×2 and 3×3 Gauss integration rules are adopted in each 4-node and 9-node FE, respectively.

Elastic-plastic predictor		Damage corrector
Elastic predictor	Plastic corrector	
$\Delta\boldsymbol{\varepsilon} = \mathbf{L}^e \Delta\mathbf{u}^e$	$\Delta\boldsymbol{\varepsilon} = \mathbf{0}$	$\Delta\boldsymbol{\varepsilon} = \mathbf{0}$
$\Delta\boldsymbol{\varepsilon}^p = \mathbf{0}$	$\Delta\boldsymbol{\varepsilon}^p = \begin{cases} \textit{updated} & \text{if } F^p \geq 0 \\ \mathbf{0} & \text{if } F^p < 0 \end{cases}$	$\Delta\boldsymbol{\varepsilon}^p = \mathbf{0}$
$\Delta\boldsymbol{\zeta} = \mathbf{0}$	$\Delta\boldsymbol{\zeta} = \begin{cases} \textit{updated} & \text{if } F^p \geq 0 \\ \mathbf{0} & \text{if } F^p < 0 \end{cases}$	$\Delta\boldsymbol{\zeta} = \mathbf{0}$
$\Delta\alpha = 0$	$\Delta\alpha = \begin{cases} \textit{updated} & \text{if } F^p \geq 0 \\ 0 & \text{if } F^p < 0 \end{cases}$	$\Delta\alpha = 0$
$\Delta D_t = 0$	$\Delta D_t = 0$	$D_t = \dfrac{\bar{Y}_t - Y_{t0}}{a_t \bar{Y}_t + b_t}$
$\Delta D_c = 0$	$\Delta D_c = 0$	$D_c = \dfrac{\bar{Y}_c - Y_{c0}}{a_c \bar{Y}_c + b_c}$

Table 4.3: Predictor-corrector solution algorithm.

1. Displacements from the global Newton-Raphson procedure:

   $\mathbf{u}^e$ known

2. Compute strains and call variables from last iteration:

   $\boldsymbol{\varepsilon}^{(i+1)} = \mathbf{L}\mathbf{u}^{(i+1)}$

   $\boldsymbol{\varepsilon}^{p^{(i+1)}} = \boldsymbol{\varepsilon}^{p^{(i)}}$

   $\boldsymbol{\varepsilon}^{e^{(i+1)}} = \boldsymbol{\varepsilon}^{(i+1)} - \boldsymbol{\varepsilon}^{p^{(i+1)}}$

   $\varepsilon_3^{p^{(i+1)}} = \varepsilon_3^{p^{(i)}}$

   $\varepsilon_3^{e^{(i+1)}} = f(\varepsilon_1^{e^{(i+1)}}, \varepsilon_2^{e^{(i+1)}}, \nu)$

   $\varepsilon_3^{(i+1)} = \varepsilon_3^{e^{(i+1)}} + \varepsilon_3^{p^{(i+1)}}$

3. Compute variables for damage evolution:
    - 3.1. Principal total $\hat{\boldsymbol{\varepsilon}}$ and elastic $\hat{\boldsymbol{\varepsilon}}^e$ strains

      $\hat{\boldsymbol{\varepsilon}}^{(i+1)} = prin(\boldsymbol{\varepsilon}^{(i+1)})$

      $\hat{\boldsymbol{\varepsilon}}^{e^{(i+1)}} = prin(\boldsymbol{\varepsilon}^{e^{(i+1)}})$
    - 3.2. Damage associated variable Y_t and Y_c

      $Y_{t/c} = f(\hat{\boldsymbol{\varepsilon}}^{(i+1)}, \hat{\varepsilon}_3^{(i+1)}, \nu)$
    - 3.3. Variables to evaluate weighting coefficients α_t and α_c

      $Y^e_{t/c} = f(\hat{\boldsymbol{\varepsilon}}^{e^{(i+1)}}, \hat{\varepsilon}_3^{e^{(i+1)}}, \nu)$
    - 3.4. Compute the nonlocal quantities
        - i. Nonlocal damage associate variables $\bar{Y}_t$ and $\bar{Y}_c$
        - ii. Weighting coefficients α_t and α_c:

          $\alpha_t = f(\bar{Y}^e_t, \bar{Y}^e_c, Y_{t0}, Y_{c0}), \quad \alpha_c = 1 - \alpha_t$

4. Call history variables to build strain vector $\boldsymbol{\varepsilon}^c$:

   $\boldsymbol{\varepsilon}^{c^{(i+1)}} = \boldsymbol{\varepsilon}^c_n = \{\varepsilon_3 \, \gamma_{23} \, \gamma_{13}\}^T_n$

5. Predictor-corrector algorithm
    - 5.1. Elastic-plastic predictor
        - i. Elastic predictor
            - i.i Call history variables from last convergence:

              $\alpha^{(i+1)} = \alpha_n, \qquad \boldsymbol{\zeta}^{(i+1)} = \boldsymbol{\zeta}_n,$

              $\boldsymbol{\varepsilon}^{p^{(i+1)}} = \{\varepsilon^p_1 \, \varepsilon^p_2 \, \gamma^p_{12}\}^T_n, \quad \boldsymbol{\varepsilon}^{cp^{(i+1)}} = \{\varepsilon^p_3 \, \gamma^p_{23} \, \gamma^p_{13}\}^T_n$
            - i.ii Build strain vectors $\boldsymbol{\varepsilon}^{3Dp}$ and $\boldsymbol{\varepsilon}^{3D}$:

```
            $\boldsymbol{\varepsilon}^{3Dp^{(i+1)}} = \{\varepsilon_1^p\,\varepsilon_2^p\,\varepsilon_3^p\,\gamma_{12}^p\,\gamma_{23}^p\,\gamma_{13}^p\}^T$
            $\boldsymbol{\varepsilon}^{3D^{(i+1)}} = \{\varepsilon_1\,\varepsilon_2\,\varepsilon_3\,\gamma_{12}\,\gamma_{23}\,\gamma_{13}\}^T$
        i.iii Compute trial stress $\widetilde{\boldsymbol{\sigma}}^{3Dtrial}$
            $\widetilde{\boldsymbol{\sigma}}^{3Dtrial^{(i+1)}} = \mathbf{C}^{3D}(\boldsymbol{\varepsilon}^{3D^{(i+1)}} - \boldsymbol{\varepsilon}^{3Dp^{(i+1)}})$
        i.iiii Compute yield function $F^p$ according to Eq. 4.29
    ii. Plastic corrector
        if $F^p < 0$
            ii.i $\mathbf{C}^{3Dt} = \mathbf{C}^{3D}$
            ii.ii no variables update
        else
            ii.i update $\boldsymbol{\varepsilon}^{3Dp}$, $\boldsymbol{\zeta}$, $\alpha$ according to Eqs. 4.33, 4.34, 4.35
            ii.ii compute the elasto-plastic tangent stiffness $\mathbf{C}^{3Dt}$
        end if
    iii. Check plane stress convergence
        if $|\widetilde{\boldsymbol{\sigma}}^c| \geq tol$
            iii.i $\mathrm{d}\boldsymbol{\varepsilon}^c = -(\mathbf{C}_{22}^{3Dt})^{-1}\widetilde{\boldsymbol{\sigma}}^c$
            iii.ii $\boldsymbol{\varepsilon}^{c^{(i+1)}} = \boldsymbol{\varepsilon}^c + \mathrm{d}\boldsymbol{\varepsilon}^c$
            iii.iii return to 5.1
        else
            iii.i go to 5.2
        end if
5.2 Damage corrector
    i. $D_t = \dfrac{\bar{Y}_t - Y_{t0}}{a_t\bar{Y}_t + b_t}, \quad D_c = \dfrac{\bar{Y}_c - Y_{c0}}{a_c\bar{Y}_c + b_c}$
```

i.ii $D = \alpha_t D_t + \alpha_c D_c$

i.iii $\boldsymbol{\sigma}^{(i+1)} = (1 - D)^2 \tilde{\boldsymbol{\sigma}}^{(i+1)}$

Box 4.2: Predictor-corrector algorithm.

4.4 Model validation

The model presented in previous sections is used to perform nonlinear static and dynamic analyses on $2D$ masonry structural elements. Here, to validate the proposed damage-plastic model and the developed FE procedure, the nonlinear static response of experimental walls loaded in-plane is investigated, analyzing both their global load-displacement response and the damage distribution. Reference is made to experimental campaigns performed at Joint Research Centre of Ispra (Anthoine et al., 1995) and at University of Pavia (Magenes et al., 1995).

4.4.1 Ispra walls simulation

To show the effectiveness of the proposed model in describing nonlinear behavior of masonry structures, response of the panels experimentally tested at the Joint Research Centre of Ispra (Anthoine et al., 1995) is numerically investigated. Test conditions, in detail described in Section 2.2.2.2, were designed so as to reproduce those of masonry piers under seismic actions. Two walls (see Figure 2.23), characterized by different height/width ratio (equal to 2 and 1.35 for the high and low wall, respectively), are analyzed with the aim of highlighting effect of the geometry on the degrading and collapse mechanisms. Both panels are 1000 mm wide and 250 mm thick. The mechanical parameters, deduced from literature, are contained in Table 4.4, setting $\kappa = 0$ and $H_i = 0$. The selected damage and plastic parameters lead to tensile and compressive strengths equal to 0.25 MPa and 5.8 MPa, respectively. These values are close to joint cohesion and masonry compressive strength experimentally measured by Magenes and Calvi, 1997. Furthermore, the same value of the adopted Young's modulus can be found in Karapitta et al., 2011 and Liberatore et al., 2017, where a macromechanical and a macroelement approach were respectively adopted to numerically describe the Ispra panels response. The nonlocal radius l_c is assumed equal to 200 mm, setting this on the basis of the brick and mesh size. A mesh made of (8×16) 9-node FEs is adopted for high wall, while (8×10) 9-node FEs are used for low wall.

Elastic parameters	
E [MPa]	ν
1700	0.15

Plastic parameters		
σ_t [MPa]	σ_c [MPa]	H_k [MPa]
1.0	1.8	$0.95E$

Damage parameters					
Y_{t0}	b_t	a_t	Y_{c0}	b_c	a_c
6×10^{-5}	3.5×10^{-4}	0.97	6×10^{-4}	1.6×10^{-2}	0.99

Table 4.4: Ispra panels: material parameters.

Figure 4.10 shows the global response curves of the two panels in terms of total base reaction versus applied horizontal displacement, for the high (a) and (b) low wall. As shown, the developed numerical model is capable to satisfactorily reproduce the experimental cyclic response of the two walls.

Looking at the nonlinear behavior of the two walls, the different trends of the global response curves are a consequence of different onset and evolution of damage and plasticity mechanisms. The strongly nonlinear load-displacement curve of the high panel is due to the opening and re-closing, under reversal loads, of tensile cracks located at the top and bottom corners, while damage localizes in the middle of the panel for the low wall. Thus, the latter shows a softening behavior more severe than the high wall, as well as larger cycles. Figures 4.11 and 4.12 contain the distribution of the tensile damage D_t for the high and low wall, respectively, at points A and B of the load-displacement curves in Figures 4.10(a) and (b), together with experimental damage patterns for comparison. As known, tensile damage D_t is the most relevant for the onset and evolution of microcracking processes in brittle-like materials, like masonry. In accordance with the experimental outcomes, it emerges that flexural degrading mechanisms definitely characterize the response of the high wall, which shows formation of high damaged zones located at the top and bottom sides starting from the corners, as evidenced in Figure 4.11(c) by the crack lines in the experimentally tested panel.

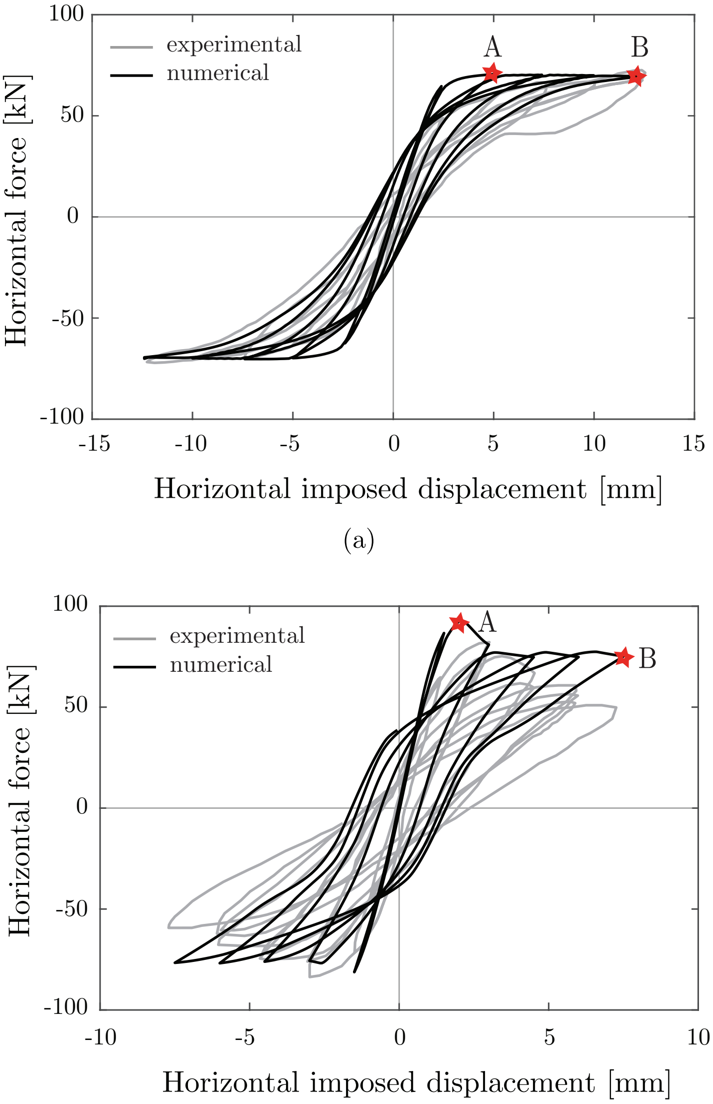

(a)

(b)

Figure 4.10: Ispra walls: comparison between numerical (black lines) and experimental (gray lines) load-displacement global curves for (a) high and (b) low wall.

Regarding the low wall, the shear mechanism is predominant with respect to the flexural ones and diagonal damage bands appear, spread and rotate similar to the experimental evidences (Figure 4.12(c)). This causes a steeper post-peak response, together with a more evident hysteretic behavior due to growth of plastic irreversible strains.

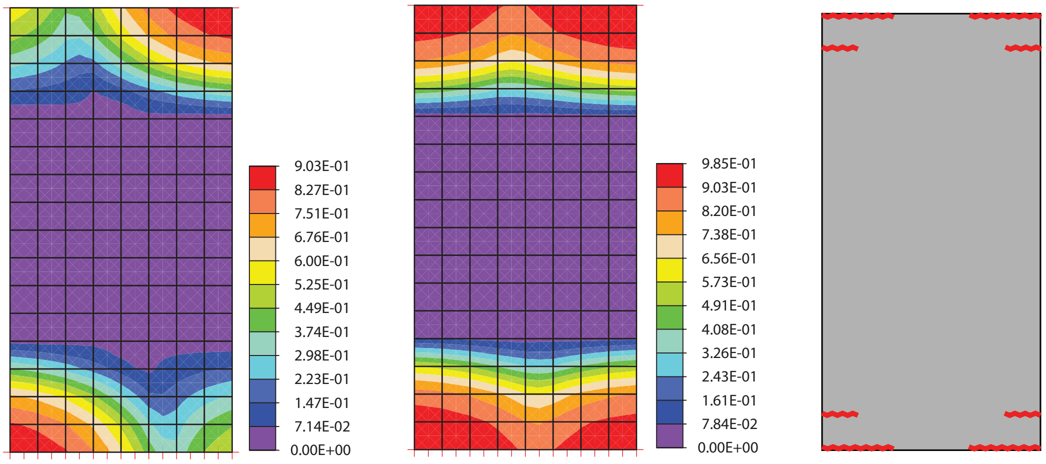

(a) (b) (c)

Figure 4.11: Ispra high wall: distribution of the tensile damage D_t for the top displacement value equal to (a) 5 mm and (b) 12.5 mm and (c) experimental failure paths from Anthoine et al. (1995).

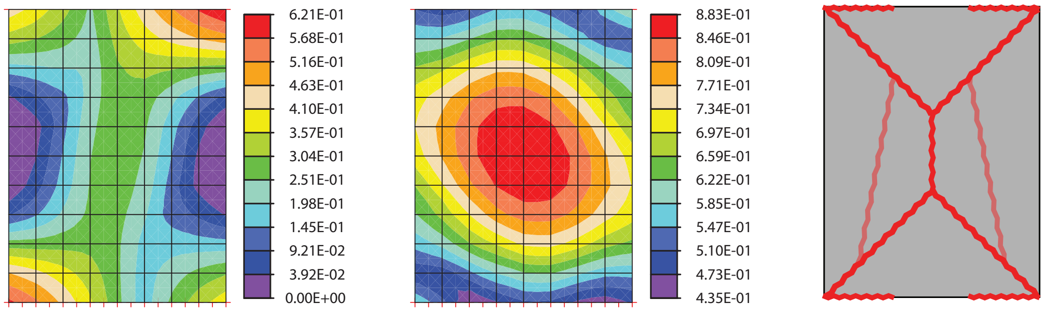

(a) (b) (c)

Figure 4.12: Ispra low wall: distribution of the tensile damage D_t for the top displacement value equal to (a) 2 mm and (b) 7.5 mm and (c) experimental failure paths from Anthoine et al. (1995).

4.4.2 Pavia wall D simulation

A full-scale masonry wall, part of the two-story building experimentally tested at University of Pavia (Magenes et al., 1995), is also selected from the literature to evaluate efficiency of the proposed constitutive model. This is the longitudinal wall D, also referred to as 'door wall', which was disconnected from the adjacent transverse walls and, then, can be analyzed independently. The wall geometry is shown in Figure 4.13 together with the applied vertical loads p_1 and p_2 (equivalent to a uniformly distributed load of 10 kN/m^2 on the slabs of the building) at the first and second floor, respectively. Seismic forces were simulated by imposing cyclic displacement histories at the two floors so that the applied forces were equal.

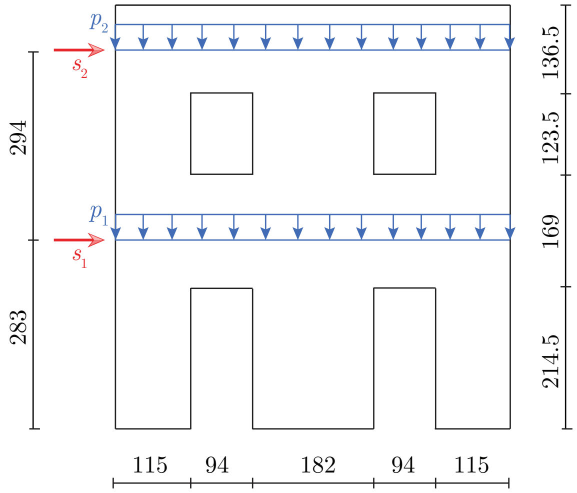

Figure 4.13: Pavia wall D: geometry and loading conditions (dimension in [cm]).

A mesh made of 590 FEs (9-node) is used to perform the numerical analysis, considering a nonlocal radius $l_c = 300$ mm. The material parameters, reported in Table 4.5, are selected in accordance with those deduced by Magenes and Calvi, 1997, so that to obtain tensile and compressive strength equal to 0.2 MPa and 8 MPa, respectively. According to the experimental test, a two-step displacement-controlled analysis is performed: first, self-weight (for which $\gamma = 18$ kN/m^3 is assumed) and additional vertical loads p_1 and p_2 are applied, then horizontal displacements are imposed at each floor level. The displacement histories are calibrated to maintain a constant ratio of 0.65 between first, s_1, and second, s_2, floor displacement (the applied displacement history at the top floor is sketched in Figure 2.27).

Elastic parameters

E [MPa]	ν
1800	0.25

Plastic parameters

σ_t [MPa]	σ_c [MPa]	H_k [MPa]
0.5	1.0	0.9 E

Damage parameters

Y_{t0}	b_t	a_t	Y_{c0}	b_c	a_c
1×10^{-5}	3×10^{-4}	0.99	9×10^{-4}	1.6×10^{-2}	0.99

Table 4.5: Pavia wall D: material parameters.

Figure 4.14 shows the comparison between numerical (black line) and experimental (gray line) base shear-second floor displacement curves. Despite some differences arise during the first cycles of response, where overestimated strength emerges in numerical curve with respect to the experimental one, the proposed model correctly describes both the hysteretic and degradation mechanisms evolving in the structural elements. Indeed, satisfactory agreement is found also in terms of crack pattern (Figure 4.15) with damaged zone located in the spandrels between openings and shear bands in the central pier.

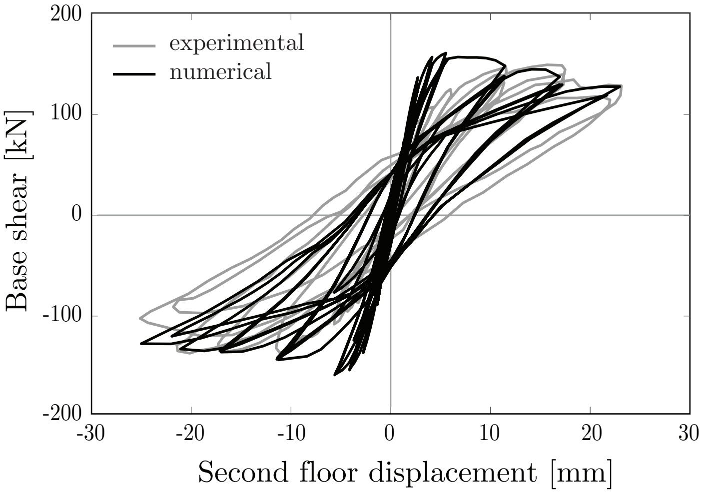

Figure 4.14: Pavia wall D: comparison between numerical (black line) and experimental (gray line) base shear-second floor displacement curves.

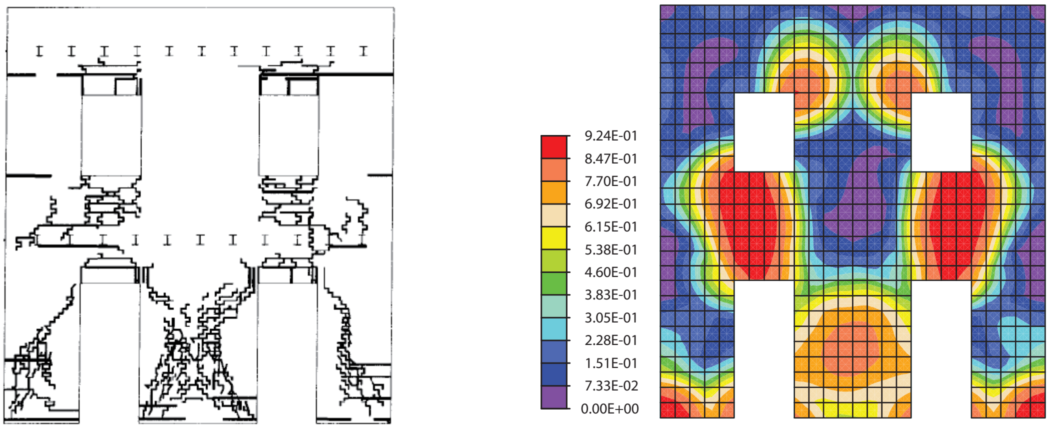

(a) (b)

Figure 4.15: Pavia wall D: (a) experimental crack pattern and (b) distribution of the tensile damage D_t at the end of the analysis.

4.5 Summary

In this chapter a phenomenological model for the $2D$ analysis of masonry structures was presented. The model, accounting for strength-stiffness decay, unilateral effect and hysteretic mechanisms, was introduced in a finite element procedure implemented in the FEAP code. Comparison between numerical and experimental results were provided to prove effectiveness of the proposed constitutive law. A full-scale masonry wall and two panels with different geometry, were analyzed. Numerical outcomes highlighted that the main features of the cyclic experimental load-displacement curves are successfully reproduced. Indeed, peak loads, energy dissipation, damage distribution, as well as collapse mechanisms, are satisfactorily matched.

In conclusion, the performed analyses showed that the proposed model is a suitable and reliable tool to reproduce experimental results, as well as to predict response of masonry walls.

Chapter 5

Orthotropic damage model

Regular masonry textures exhibit anisotropic macroscopic response with substantial discrepancy among properties observed in different material directions. This is due to the spatial organization of bricks and mortar which causes microcraks located at brick-mortar interface. Usually the anisotropic behavior reduces to an orthotropic one. This also emerges in elastic range, as Figure 5.1 shows with reference to the experimentally obtained correlation between the ratios Young's modulus-to-Poisson's coefficient defined along the normal N and parallel T direction to bed joints orientation (Cavaleri et al., 2014). In general, in heterogeneous materials, damage development can alter the initial orthotropic characteristic leading to a more general anisotropic response. However, when dealing with masonry, it is reasonable to assume that damage propagation can result in change of orthotropy intensity without altering the symmetry of the material (Berto et al., 2002).

As few macromechanical models were proposed to describe masonry anisotropic response in the elastic and inelastic range (see Section 3.1.2), this chapter proposes a new orthotropic damage model, tailored to the $2D$ analysis of masonry structures. First, main concepts of anisotropic damage are recalled, then, the adopted constitutive law, the introduced damage limit surface and damage evolution laws are presented. Moreover, model performance is evaluated through numerical and experimental comparisons.

Finally, with the aim of evaluating effect of bricks and mortar relative arrangement on the level of orthotropy of masonry elastic response, a study is presented with reference to different masonry textures and blocks sizes.

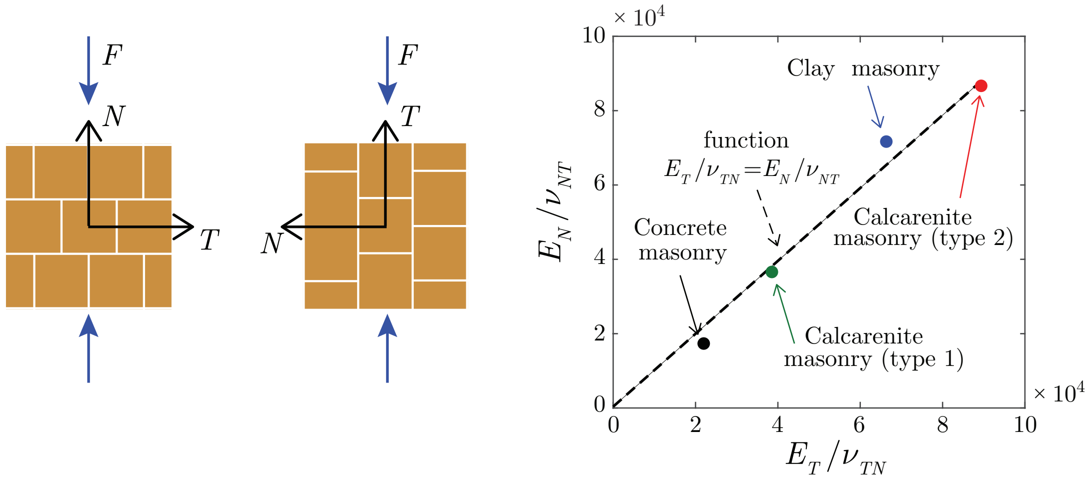

Figure 5.1: Cavaleri et al. (2014): experimental (dots) and theoretical (dashed line) correlation between the ratios Young's modulus-to-Poisson's coefficient obtained from uni-axial compressive tests normal and parallel to bed joints.

5.1 Anisotropic damage models: main concepts

Anisotropic damage models were developed to account for the directional strength properties of materials. These replace the scalar representation of the damage with a tensorial one by introducing vector variables, fourth order or, more frequently, second order damage tensors. In such a case, the effective stress in Eq. 4.12, evaluated on the basis of the strain equivalence hypothesis, is rewritten as:

$$[\tilde{\boldsymbol{\sigma}}] = [\mathbf{M}(\mathbf{D})] : [\boldsymbol{\sigma}] \; , \tag{5.1}$$

where symbol (:) denotes tensorial product, $[\tilde{\boldsymbol{\sigma}}]$ and $[\boldsymbol{\sigma}]$ indicate the effective and actual stress tensor, respectively, and $[\mathbf{M}(\mathbf{D})]$ is the so-called damage-effect tensor, being a transformation tensor which is function of the damage state.
For sake of simplicity, in what follows attention is focused on plane stress conditions. However, analogous considerations hold for three-dimensional constitutive

laws. By adopting matrix notation, Eq. 5.1 becomes:

$$\begin{bmatrix}\sigma_1\\ \sigma_2\\ \tau_{12}\end{bmatrix} = [\mathbf{M}(\mathbf{D})]^{-1}\begin{bmatrix}\tilde{\sigma}_1\\ \tilde{\sigma}_2\\ \tilde{\tau}_{12}\end{bmatrix} = (\mathbf{I}-\mathbf{D})\begin{bmatrix}\tilde{\sigma}_1\\ \tilde{\sigma}_2\\ \tilde{\tau}_{12}\end{bmatrix}\ , \tag{5.2}$$

where $\mathbf{I}$ is the third-order identity matrix and $\mathbf{D}$ is a 3×3 damage matrix.
If the effective area concept is recalled and the area of defects associated to the i-direction is denoted by A_d^i, the corresponding damage D_i results as:

$$D_i = \frac{A_d^i}{A^i}\,. \tag{5.3}$$

Thus, the following relationship holds between the effective, $\tilde{\boldsymbol{\sigma}}'$, and real, $\boldsymbol{\sigma}$, stresses:

$$\begin{bmatrix}\tilde{\sigma}'_1\\ \tilde{\sigma}'_2\\ \tilde{\tau}'_{12}\\ \tilde{\tau}'_{21}\end{bmatrix} = \begin{bmatrix}1/(1-D_1) & 0 & 0\\ 0 & 1/(1-D_2) & 0\\ 0 & 0 & 1/(1-D_2)\\ 0 & 0 & 1/(1-D_1)\end{bmatrix}\begin{bmatrix}\sigma_1\\ \sigma_2\\ \tau_{12}\end{bmatrix}\ . \tag{5.4}$$

It is evident that hypothesis of strain equivalence leads to asymmetric effective stresses and, consequently, to asymmetry of the stiffness matrix when anisotropic damage is considered (Chow and Wang, 1987; Ghrib and Tinawi, 1995). To avoid this drawback, different approaches were proposed. For instance, a symmetrized form of the effective stress can be adopted:

$$\tilde{\boldsymbol{\sigma}} = \begin{bmatrix}\tilde{\sigma}_1\\ \tilde{\sigma}_2\\ \tilde{\tau}_{12}\end{bmatrix} = \begin{bmatrix}\tilde{\sigma}'_1\\ \tilde{\sigma}'_2\\ \sqrt{\dfrac{\tilde{\tau}'^2_{12}+\tilde{\tau}'^2_{21}}{2}}\end{bmatrix}\ , \tag{5.5}$$

thus obtaining the following relationship between the symmetrized effective, $\tilde{\boldsymbol{\sigma}}$, and real, $\boldsymbol{\sigma}$, stresses:

$$\begin{bmatrix}\tilde{\sigma}_1\\ \tilde{\sigma}_2\\ \tilde{\tau}_{12}\end{bmatrix} = \begin{bmatrix}\dfrac{1}{1-D_1} & 0 & 0\\ 0 & \dfrac{1}{1-D_2} & 0\\ 0 & 0 & \sqrt{\dfrac{1}{2}\left(\dfrac{1}{(1-D_1)^2}+\dfrac{1}{(1-D_2)^2}\right)}\end{bmatrix}\begin{bmatrix}\sigma_1\\ \sigma_2\\ \tau_{12}\end{bmatrix} . \tag{5.6}$$

Alternatively, the complementary energy principle can be invoked (see Section 4.1.2). By equating the complementary energy of the damaged material Λ_d:

$$\Lambda_d = \frac{1}{2}\boldsymbol{\sigma}^T\tilde{\mathbf{C}}^{-1}\boldsymbol{\sigma} , \tag{5.7}$$

and the complementary energy of the equivalent undamaged material Λ_0:

$$\Lambda_0 = \frac{1}{2}\bar{\boldsymbol{\sigma}}^T\mathbf{C}^{-1}\bar{\boldsymbol{\sigma}} , \tag{5.8}$$

the damaged stiffness matrix $\tilde{\mathbf{C}}$ results as:

$$\tilde{\mathbf{C}} = (\mathbf{I}-\mathbf{D})^T\mathbf{C}(\mathbf{I}-\mathbf{D}) = \begin{bmatrix}C_{11}d_1^2 & C_{12}d_1d_2 & 0\\ C_{21}d_1d_2 & C_{22}d_2^2 & 0\\ 0 & 0 & C_{33}\dfrac{2d_1^2d_2^2}{d_1^2+d_2^2}\end{bmatrix} , \tag{5.9}$$

where C_{ij} ($i = 1,2,3$ and $j = 1,2,3$) are the components of the undamaged material stiffness matrix $\mathbf{C}$ and $d_i = (1 - D_i)$, with $i = 1,2$. Eq. 5.9 shows that the symmetric form of the constitutive operator $\tilde{\mathbf{C}}$ is restored. Furthermore, as usually proposed (Williams et al., 2003; Lapczyk and Hurtado, 2007), damage affecting shear components is defined as a function of D_1 and D_2. However, several orthotropic damage models (Matzenmiller et al., 1995; Maimí et al., 2007; Simon et al., 2017) take use of independent damage variables for shear. This hypothesis is justified by the different damaged areas for normal and shear stresses. Thus, it could be reasonable dealt with damage parameters in shear as independent unknowns.

5.2 Damage model

Within the macromechanical approach framework, heterogeneous masonry walls are modeled as equivalent homogenized orthotropic media, with the material/ natural axes (T,N) as axes of orthotropy. First, the stress-strain relationship is defined in the material axes system, then, this is expressed in the global x, y-coordinate system (see Figure 5.2) by using standard transformation rules.

The following constitutive law is proposed:

$$\boldsymbol{\sigma}_{TN} = (\mathbf{I} - \mathbf{D})^T \mathbf{C}_{TN} (\mathbf{I} - \mathbf{D}) \boldsymbol{\varepsilon}_{TN} \ , \tag{5.10}$$

with $\boldsymbol{\sigma}_{TN} = \{\sigma_T \, \sigma_N \, \tau_{TN}\}^T$ and $\boldsymbol{\varepsilon}_{TN} = \{\varepsilon_T \, \varepsilon_N \, \gamma_{TN}\}^T$ denoting stress and strain vectors, respectively. $\mathbf{C}_{TN}$ is the elastic constitutive matrix of the undamaged material for plane stress condition:

$$\mathbf{C}_{TN} = \frac{1}{S} \begin{bmatrix} E_T & \nu_{TN} E_N & 0 \\ \nu_{NT} E_T & E_N & 0 \\ 0 & 0 & G_{TN} S \end{bmatrix} \ , \tag{5.11}$$

where $S = (1 - \nu_{TN} \nu_{NT})$ is function of Poisson's coefficients ν_{TN} and ν_{NT}. E_T, E_N and G_{TN} are elastic moduli along the orthotropy directions. In Eq. 5.10, $\mathbf{I}$ is the 3×3 identity matrix, while $\mathbf{D}$ represents a 3×3 damage matrix defined on

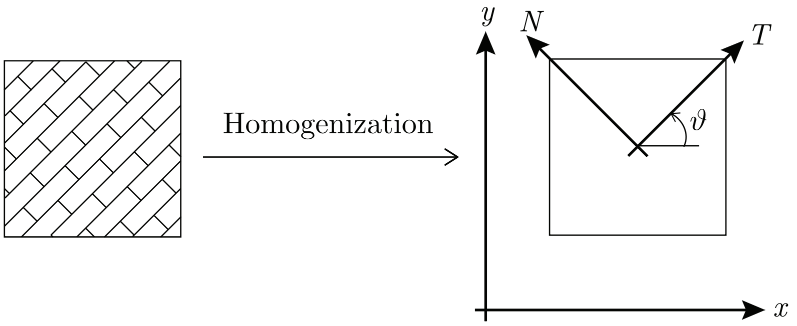

Figure 5.2: Global (x, y) and material (T, N) axes of the homogenized masonry material.

the basis of scalar variables D_1, D_2 and D_3, as:

$$\mathbf{D} = \begin{bmatrix} D_1 & 0 & 0 \\ 0 & D_2 & 0 \\ 0 & 0 & D_3 \end{bmatrix} . \tag{5.12}$$

The resulting damaged constitutive matrix $\tilde{\mathbf{C}}_{TN} = (\mathbf{I} - \mathbf{D})^T \mathbf{C}_{TN} (\mathbf{I} - \mathbf{D})$, derived from the equivalence energy principle, is:

$$\tilde{\mathbf{C}}_{TN} = \frac{1}{S} \begin{bmatrix} (1 - D_1)^2 E_T & \nu_{TN}(1 - D_1)(1 - D_2) E_N & 0 \\ \nu_{NT}(1 - D_1)(1 - D_2) E_T & (1 - D_2)^2 E_N & 0 \\ 0 & 0 & S(1 - D_3)^2 G_{TN} \end{bmatrix} . \tag{5.13}$$

The introduced damage variables, D_1, D_2 and D_3 permit to describe the main failure mechanisms due to shear and both compressive and tensile states, normal and parallel to bed joints, as sketched in Figure 5.3. D_1 and D_2 result as a proper combination of damage parameters in tension D_{it} and compression D_{ic} $(i = 1, 2)$, as follows:

$$\begin{aligned} D_1 &= \alpha_1 D_{1t} + (1 - \alpha_1) D_{1c} , \\ D_2 &= \alpha_2 D_{2t} + (1 - \alpha_2) D_{2c} , \end{aligned} \tag{5.14}$$

where weighting coefficients, α_1 and α_2, are introduced to rule the stiffness recovery at the crack re-closure. These are defined in the following on the basis of strain state at the material point M.

All damage variables, D_{it}, D_{ic} $(i = 1, 2)$ and D_3, can range between 0 and 1, according to their physical meaning and these have to satisfy the irreversible thermodynamic condition, such that $\dot{D}_{it} \geq 0$, $\dot{D}_{ic} \geq 0$ and $\dot{D}_3 \geq 0$. Furthermore, constraints $D_{1t} \geq D_{1c}$ and $D_{2t} \geq D_{2c}$ are enforced.

To rule onset and evolution of damage parameters, associated variables are

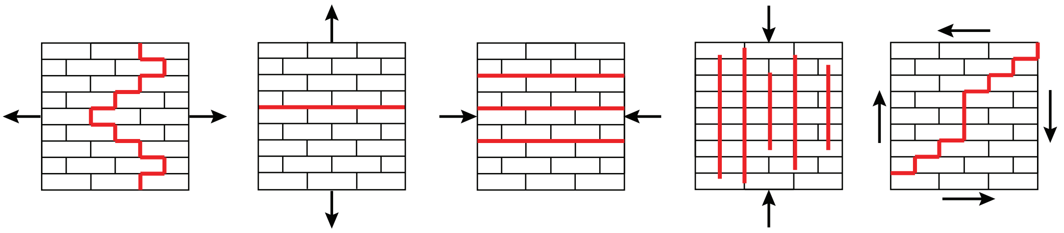

(a) (b) (c) (d) (e)

Figure 5.3: Failure modes associated to (a) D_{1t}, (b) D_{2t}, (c) D_{1c}, (d) D_{2c} and (e) D_3 .

defined on the basis of equivalent strain concept, as follows:

$$\begin{aligned} Y_1 &= \varepsilon_T + \tilde{\nu}_{NT}\,\varepsilon_N \ , \\ Y_2 &= \varepsilon_N + \tilde{\nu}_{TN}\,\varepsilon_T \ , \\ Y_3 &= \gamma_{TN} \ , \end{aligned} \tag{5.15}$$

where $\tilde{\nu}_{NT} = [(1-D_2)/(1-D_1)]\,\nu_{NT}$ and $\tilde{\nu}_{TN} = [(1-D_1)/(1-D_2)]\,\nu_{TN}$ have the physical meaning of degraded Poisson's ratios under uni-axial stress states. Once computed quantities in Eqs. 5.15, the weighting coefficients α_1 and α_2 in Eq 5.10 can be defined:

$$\alpha_1 = H(Y_1) \ , \quad \alpha_2 = H(Y_2) \ , \tag{5.16}$$

with $H(\bullet)$ denoting the Heaviside function (i.e. $H(\bullet) = 1$ if $(\bullet) \geq 0$, otherwise $H(\bullet) = 0$). It can be noted that the proposed model assumes no re-closure effect related D_3, as shear damage is caused mainly by transverse cracks which do not close under reversal shear stresses.

To finalize the model description, the adopted damage criterion and evolution law of the damage variables are defined below.

5.2.1 Damage limit surface

Definition of a proper damage limit surface represents an arduous task, because of various failure modes that may occur depending on the stress state. For regular masonry, the directional properties of the material imply that failure criteria have to take into account the orientation of principal stresses with respect to the material axes. Available experimental results allowed the development of several failure criteria. Most of them refer to the failure surface idealized by Dhanasekar et al. (1985), which consists of the intersection of three elliptic cones in the space of stresses expressed in the natural axes (Figure 5.4). Stemming from this proposal, Berto et al. (2002) interpreted the material damage field as a double pyramid with rectangular base, defined in terms of equivalent effective stresses, as Figure 5.5 shows. Further developments conducted to more complex failure criteria. Figure 5.6 shows the failure surface proposed by Lishak et al. (2012), which results into a very intricate shape composed of five parts corresponding to different failure modes.

On the basis of the aforementioned studies and those of Lourenço et al. (1997) and Pelà et al. (2013), here the damage limit surface F^D is geometrically defined as the intersection of an ellipsoid and elliptic cone in the space of damage associated variables (see Figure 5.7). Only masonry strength properties and some additional properties are required to build it (Appendix A is reference to detailed description of the surface construction). In particular, the uni-axial damage thresholds in the parallel, Y_{1t0} and Y_{1c0}, and normal, Y_{2t0} and Y_{2c0}, direction to the bed joints orientation are needed, by distinguishing them to account for the non-symmetric behavior in tension and compression (as the subscripts 't' and 'c' indicate). Furthermore, the pure shear Y_{s0} threshold and bi-axial compressive Y_{cc0} threshold are required (see Figure 5.8).

The damage criterion imposes that points inside the surface represent material elastic states, otherwise damage evolution occurs and the damage thresholds Y_{10}, Y_{20}, Y_{30} have to be identified. The determination of the damage thresholds allows to define the evolution laws of the damage parameters, as carefully described in next section.

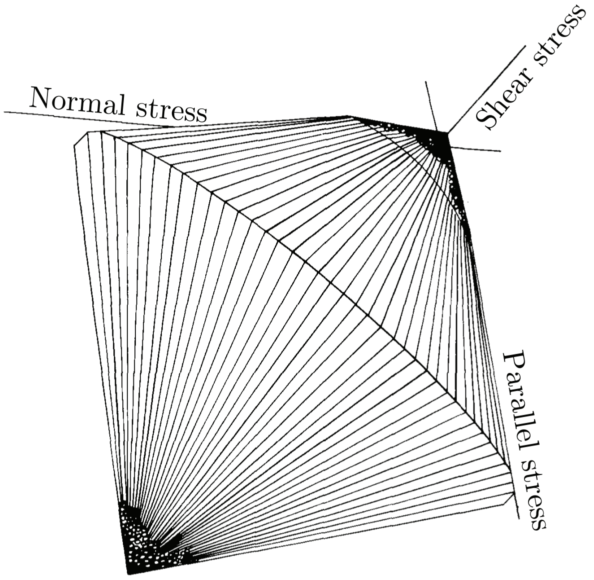

Figure 5.4: Failure surface proposed by Dhanasekar et al. (1985).

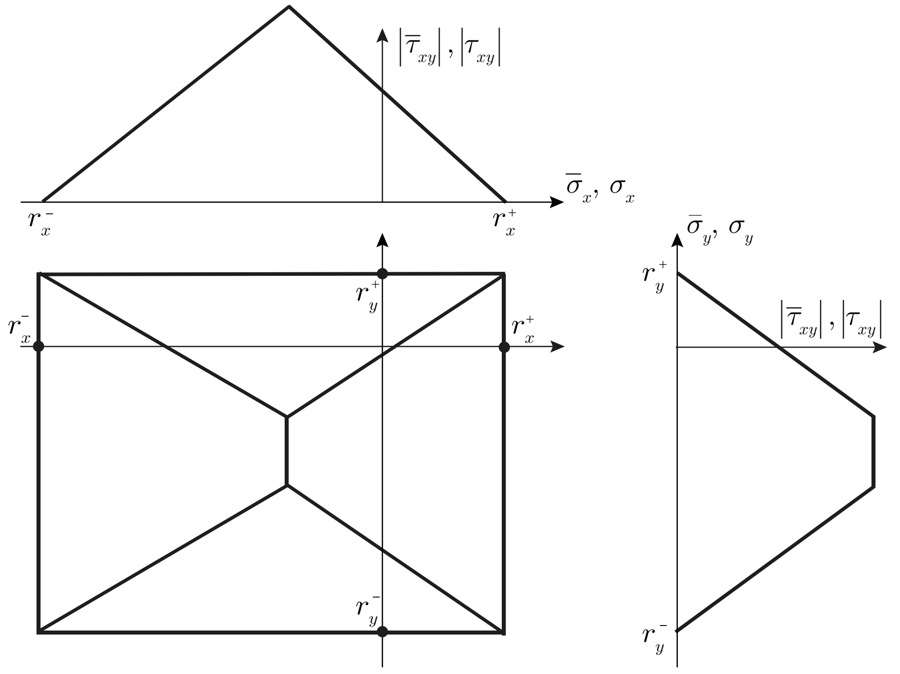

Figure 5.5: Limit surface adopted by Berto et al. (2002).

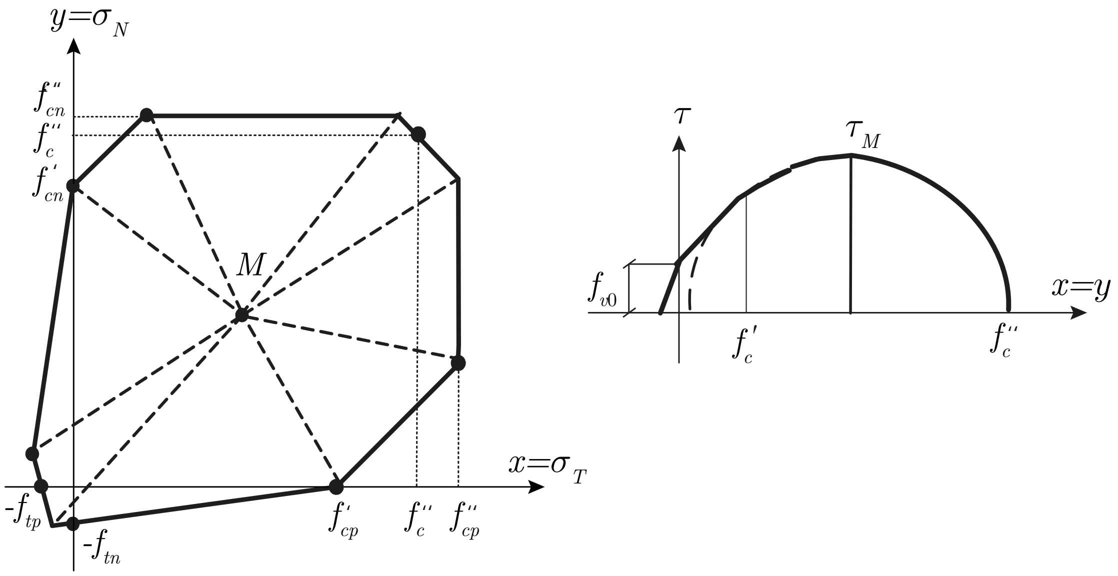

Figure 5.6: Masonry failure surface idealized by Lishak et al. (2012).

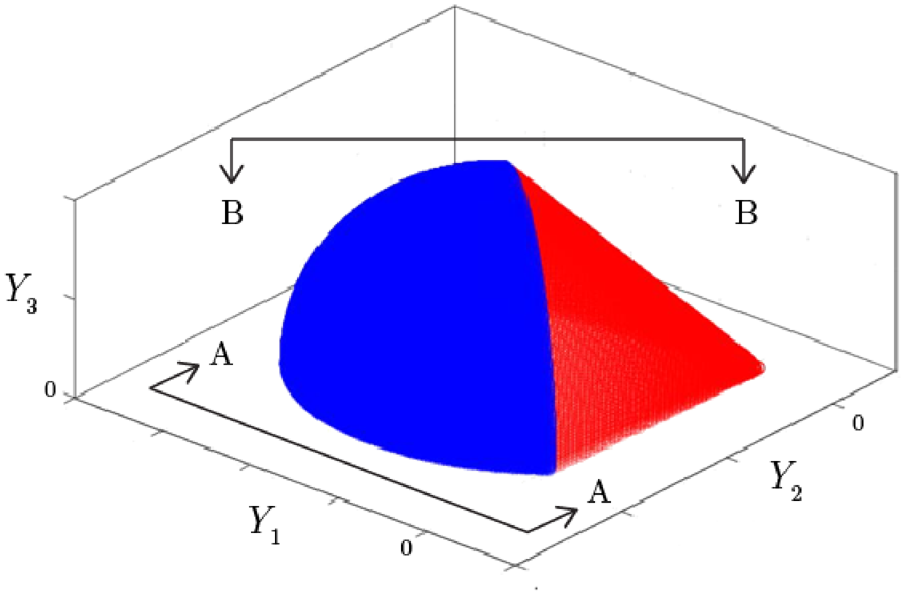

Figure 5.7: Proposed damage limit surface in the Y_3 positive semi-space.

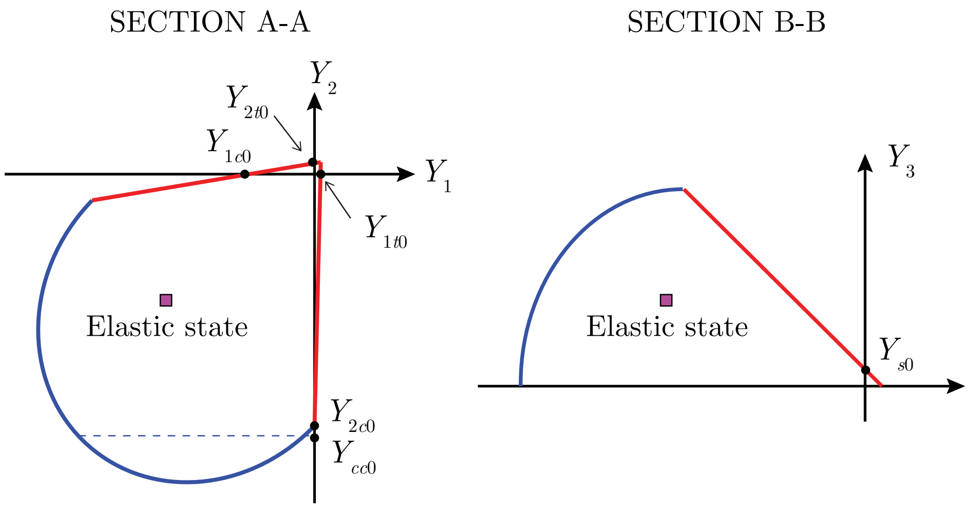

Figure 5.8: Meaningful sections (A-A and B-B in Figure 5.7) of the limit surface.

5.2.2 Evolution laws for damage variables

As far as damage variables evolution is concerned, rational evolution rules are assumed, which require to distinguish between damage in tension and compression along each material axis. Thus, attention should be paid to the sign of Y_i variables, as in detail described in Box 5.1, where reference is made to a step-by-step procedure and the apex 'n + 1', denoting the current time, is omitted for sake of simplicity.

The evolution laws in Box 5.1 result function of material parameters $(a_t, a_c, a_s, b_t,$ $b_c, b_s)$, which are selected on the basis of uni-axial tension and compression and pure shear tests. Peak strengths of stress-strain relationships are mainly govern by b_t, b_c and b_s parameters, while a_t, a_c and a_s influence the slope of softening branches. Graphical representation of material parameters effect can be found in Figure 4.4, as similar evolution laws are used for the isotropic damage model presented in Chapter 4. It should be noticed that a linear variation of the b_s parameter with the compressive stress σ_N is introduced, with the aim of phenomenologically capturing the increment of the fracture energy G_f^{II} with the normal compressive stress (see Eq. 2.2 and Figure 2.10(a)).

```
if $F^D \geq 0$ then
    1. if $Y_1 \geq 0$ then        (tensile state)
        $D_{1c} = D_{1c}^n$
        $D_{1t} = \max\left(\frac{Y_1 - Y_{10}}{a_t Y_1 + b_t}, D_{1t}^n, D_{1c}\right)$
    else
        $D_{1c} = \max\left(\frac{|Y_1| - |Y_{10}|}{a_c |Y_1| + b_c}, D_{1c}^n\right)$
        $D_{1t} = \max(D_{1t}^n, D_{1c})$
    end if
    2. if $Y_2 \geq 0$ then        (tensile state)
        $D_{2c} = D_{2c}^n$
        $D_{2t} = \max\left(\frac{Y_2 - Y_{20}}{a_t Y_2 + b_t}, D_{2t}^n, D_{2c}\right)$
    else
        $D_{2c} = \max\left(\frac{|Y_2| - |Y_{20}|}{a_c |Y_2| + b_c}, D_{2c}^n\right)$
        $D_{2t} = \max(D_{2t}^n, D_{2c})$
    end if
    3. $D_3 = \max\left(\frac{|Y_3| - |Y_{30}|}{a_s |Y_3| + \bar{b}_s}, D_3^n\right)$ , with    $\bar{b}_s = b_s - \langle \sigma_N \rangle_- \, b_s$
else
    $D_{it} = D_{it}^n$ ,   $D_{ic} = D_{ic}^n$ ,   $D_3 = D_3^n$     ($i$=1,2)
end if
```

Box 5.1: Evolution laws of damage variables.

5.2.3 Transformation rules

Stress $\boldsymbol{\sigma}_{TN} = \{\sigma_T \, \sigma_N \, \tau_{TN}\}^T$ and strain $\boldsymbol{\varepsilon}_{TN} = \{\varepsilon_T \, \varepsilon_N \, \gamma_{TN}\}^T$ vectors, defined in the material axes system, are related to those in the global x, y-coordinate system $\boldsymbol{\sigma}_{xy} = \{\sigma_x \, \sigma_y \, \tau_{xy}\}^T$ and $\boldsymbol{\varepsilon}_{xy} = \{\varepsilon_x \, \varepsilon_y \, \gamma_{xy}\}^T$ (see Figure 5.2), by using standard transformation rules:

$$\boldsymbol{\sigma}_{xy} = \mathbf{P} \boldsymbol{\sigma}_{TN} \ , \quad \boldsymbol{\varepsilon}_{xy} = \boldsymbol{\Psi} \boldsymbol{\varepsilon}_{TN} \ , \tag{5.17}$$

where $\mathbf{P}$ and $\boldsymbol{\Psi}$ are rotation matrices expressed as:

$$\mathbf{P} = \begin{bmatrix} m^2 & n^2 & -2mn \\ n^2 & m^2 & 2mn \\ mn & -mn & m^2 - n^2 \end{bmatrix} \ , \quad \boldsymbol{\Psi} = \begin{bmatrix} m^2 & n^2 & -mn \\ n^2 & m^2 & mn \\ 2mn & -2mn & m^2 - n^2 \end{bmatrix} \ , \tag{5.18}$$

being $m = \cos\vartheta$ and $n = \sin\vartheta$, with ϑ rotation angle between T, N-axes and x, y-axes.

5.3 FE formulation and nonlocal regularization

The presented model is introduced in a displacement-based FE formulation, involving 4-node quadrilateral finite elements with two displacement degrees of freedom at each node, based on bi-linear interpolation functions for the two displacement fields u_x and u_y.

As a consequence of the softening branch in the stress-strain relationship, localization problems can arise, inducing the already mentioned mesh dependency of the numerical results evaluated by means of the FE solution procedure. To overcome these numerical drawbacks, the same strategy adopted in Section 4.2.3 is applied. In fact, it is assumed that the damage parameters evolution is governed by the nonlocal damage associated variables, defined as:

$$\bar{Y}_i(\mathbf{x}) = \frac{1}{\int_A \psi(\mathbf{x}, \mathbf{s}) \, dA(\mathbf{s})} \int_A Y_i(\mathbf{s}) \, \psi(\mathbf{x}, \mathbf{s}) \, dA(\mathbf{s}) \qquad i = 1, 2, 3 \ , \tag{5.19}$$

being $\bar{Y}_i$ the nonlocal quantities at $\mathbf{x}$, evaluated by means of the corresponding local variables Y_i at points placed in its neighborhood. ψ is the weighting Gaussian function, which determines the influence on $\mathbf{x}$ of the point $\mathbf{s}$, and depends on the nonlocal radius l_c, as:

$$\psi\left(\mathbf{x},\mathbf{s}\right) = e^{-\left(\frac{\|\mathbf{x}-\mathbf{s}\|}{l_c}\right)^2} \; . \tag{5.20}$$

Once determined the nonlocal quantities in Eq. 5.19, these are introduced in Eq. 5.16 and in the damage evolution laws (Box 5.1), thus allowing to solve the nonlinear evolution problem of the damage variables in each Gauss point. A simplified version of the predictor-corrector procedure adopted in Section 4.3.2 is here developed to determine the updated values of the damage parameters. This simply consists of an elastic predictor phase, followed by a damage corrector step.

5.4 Validation examples

Model validation is carried out by evaluating its ability in reproducing the different strength and stiffness characteristics observed along masonry material axes. First, the uni-axial stress-strain responses are analyzed, then, the exploration is moved towards more complex loading conditions. Experimental failure domains obtained under bi-axial stress states are numerically reproduced and, then, structural applications on shear walls are presented.

5.4.1 Uni-axial stress-strain response

A unit masonry element properly constrained is subjected to a monotonically increasing strain ε_x. With reference to the material parameters listed in Table 5.1, Figure 5.9 shows the uni-axial stress-strain response obtained for three example values of the ϑ angle. The numerical results highlight the model ability to take into account the influence of the applied stresses with respect to the bed joints orientation. In fact, distinct initial elastic stiffnesses, as well as different maximum strengths, are obtained for $\vartheta = 0°$ (blue line), $\vartheta = 45°$ (black line) and $\vartheta = 90°$ (red line). This is a consequence of the stress and strain states acting along the material axes and the adopted definition of the damage associated variables Y_1, Y_2 and Y_3. It can be noted that damage variable D_3 is activated only for $\vartheta = 45°$ (see

Figure 5.10(b)), as this is related to the shear deformation γ_{TN}. On the contrary, when ϑ is equal to 0° or 90° (Figures 5.10(a) and (c), respectively), no shear strain γ_{TN} occurs and, consequently, only D_1 and D_2 arise. In particular, D_1 starts and evolves when $\vartheta = 0°$ because of the T-axis coincides with the x-axis, whereas D_2 appears in case of $\vartheta = 90°$ as a result of the overlap of x and N axes.

Elastic parameters

E_T [MPa]	E_N [MPa]	ν_{TN}	G_{TN} [MPa]
4000	2000	0.1	1500

Damage parameters

$a_t = a_c = a_s$	b_t=b_s	b_c
0.99	1×10^{-5}	5×10^{-3}

Damage thresholds

Y_{1t0}	Y_{1c0}	Y_{2t0}	Y_{2c0}	Y_{s0}	Y_{cc0}
9.95×10^{-5}	9.95×10^{-4}	9.95×10^{-5}	9.95×10^{-4}	2×10^{-4}	$1.1\,Y_{2c0}$

Table 5.1: Material parameters adopted in Figures 5.9, 5.10 and 5.11.

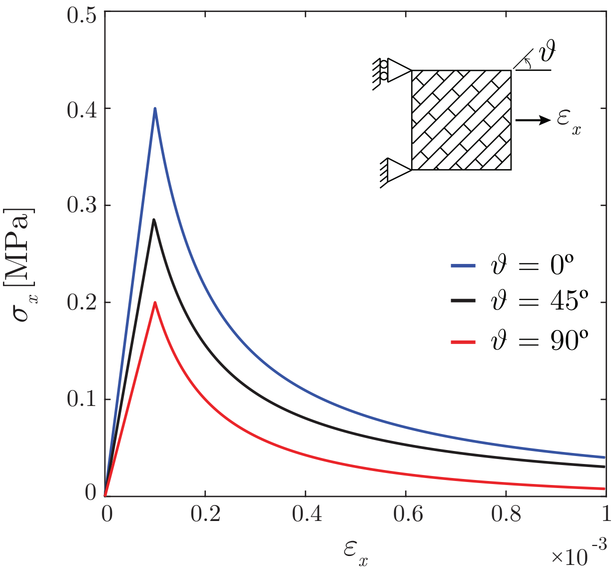

Figure 5.9: Uni-axial tensile stress-strain laws for different values of ϑ.

Furthermore, to prove the effectiveness of proposed model in capturing the unilateral behavior due to the re-closure of tensile cracks under reversal loading, the cyclic deformation history detailed in Figure 5.11(a) is applied to the masonry element with horizontal bed joints ($\vartheta = 0°$). The resulting cyclic stress-strain law,

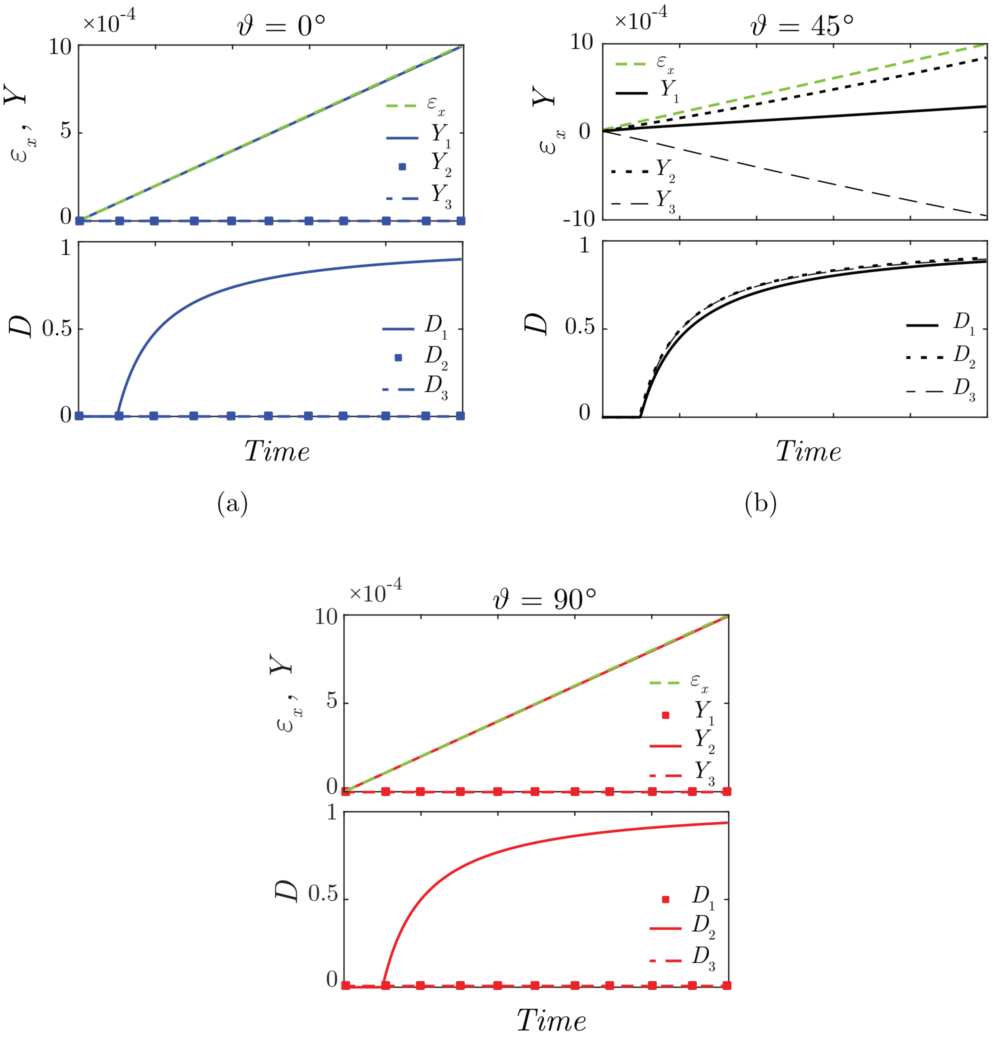

(a)

(b)

(c)

Figure 5.10: Uni-axial tensile test: variation of damage associated variables Y_1, Y_2, Y_3 and damage variables D_1, D_2, D_3 for (a) $\vartheta = 0°$, (b) $\vartheta = 45°$, (c) $\vartheta = 90°$.

depicted in Figure 5.11(b), points out that the stiffness recovery occurs when passing from tension to compression (A-B phase). The subsequent reloading in tension, which leads to point C, is affected by the accumulated compressive damage, because of the constraint $D_{1t} \geq D_{1c}$. The phenomenon is clearly illustrated in Figure 5.11(a), where the variation of the damage variables D_{1t}, D_{1c} and D_1 is plotted with respect to the fictitious time variable. Here, it can be noted that D_1

assumes the same value of D_{1t} for tensile states and, then, when a reversal strain occurs, returns equal to D_{1c}, allowing a proper representation of the unilateral damage recovering upon load reversal.

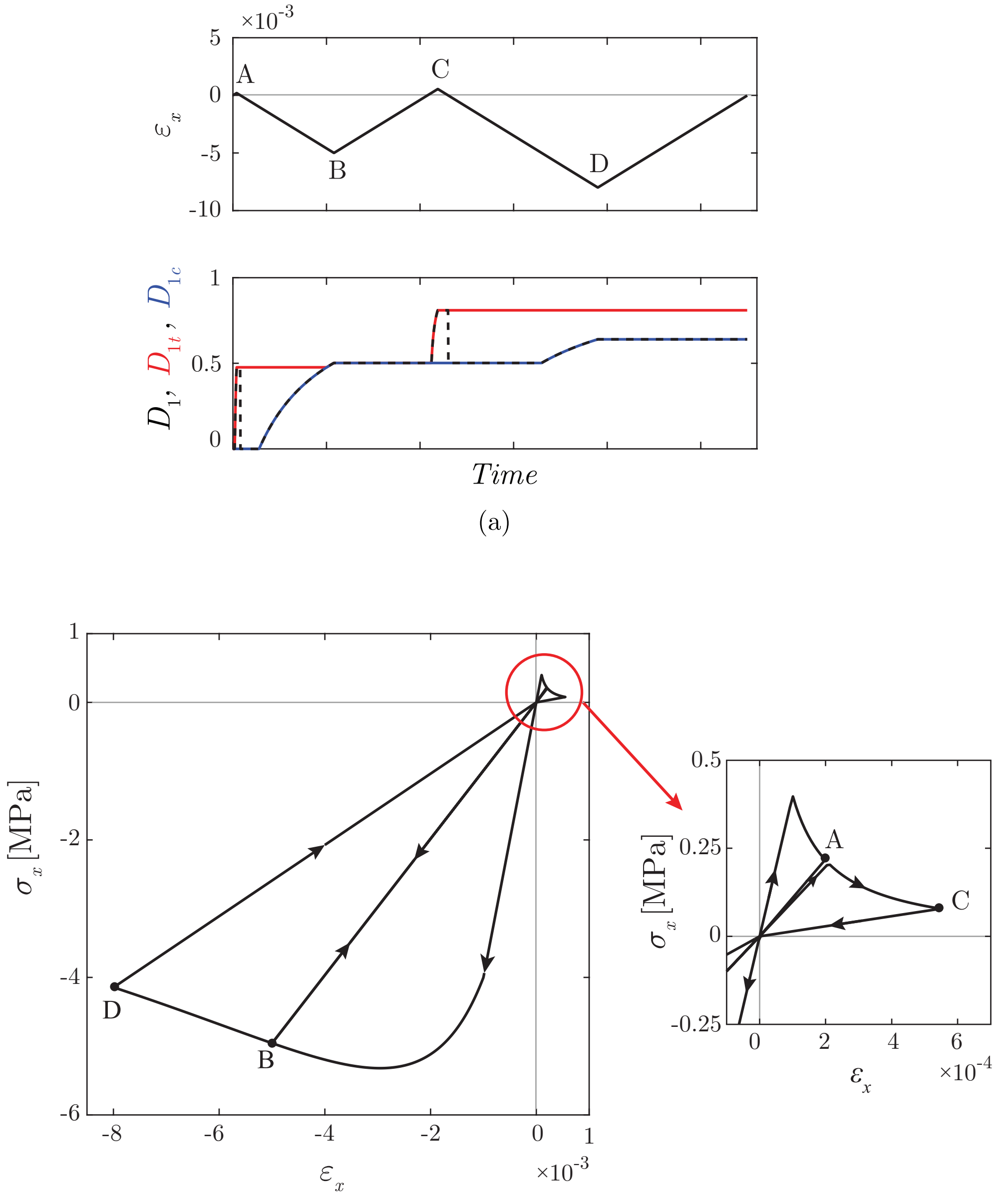

(a)

(b)

Figure 5.11: Cyclic test for $\vartheta = 0°$: (a) applied strain history and variation of the damage variables, (b) uni-axial cyclic stress-strain law.

5.4.2 Bi-axial test on masonry brickwork

The experimental bi-axial tests performed by Page (1981, 1983) on half-scale clay masonry panels are chosen to test the model ability in describing the directional strength characteristics of masonry subjected to in-plane loading conditions. As described in detail in Chapter 2 (Section 2.2.1.3), bi-axial stresses oriented at various angles ϑ to the bed joints were applied and the resulting failure surfaces were obtained in terms of principal stresses and their orientation to the bed joints. Table 5.2 contains the material parameters used to perform the numerical analysis (for which an Arc-length procedure is employed), which are selected according to data provided by Page (1981, 1983); Page et al. (1985).

On the overall, a good agreement is found between numerical and experimental results, as Figures 5.12, 5.13 and 5.14 show by comparing the numerical failure surfaces and experimental data for values of angle ϑ equal to 0°, 22.5° and 45°. Results of 67.5° and 90° are implicitly contained those of 22.5° and 0°, respectively.

In case of $\vartheta = 0°$, non-symmetric shape of the failure surface, with respect to the bisecting axis, emerges with noticeable differences in the compressive strength normal and parallel to bed joints. This testifies that, notwithstanding the quasi-isotropic elastic response (see the elastic mechanical parameters in Table 5.2), the model is able to phenomenologically describe the preferential direction of micro-cracks evolution due to the spatial arrangement of mortar and bricks.

By varying ϑ, the asymmetric characteristic of the failure surface is gradually lost until the symmetric shape is fully restored at $\vartheta = 45°$(see Figure 5.14).

Elastic parameters				Damage parameters			
E_T [MPa]	E_N [MPa]	ν_{TN}	G_{TN} [MPa]	$a_{t/c/s}$	b_t	b_c	b_s
5700	5600	0.19	2350	0.99	4×10^{-5}	2×10^{-3}	1×10^{-4}

Damage thresholds

Y_{1t0}	Y_{1c0}	Y_{2t0}	Y_{2c0}	Y_{s0}	Y_{cc0}
6.8×10^{-5}	6.8×10^{-4}	4.2×10^{-5}	1.2×10^{-3}	1.3×10^{-4}	$1.1\ Y_{2c0}$

Table 5.2: Material parameters for Page panels.

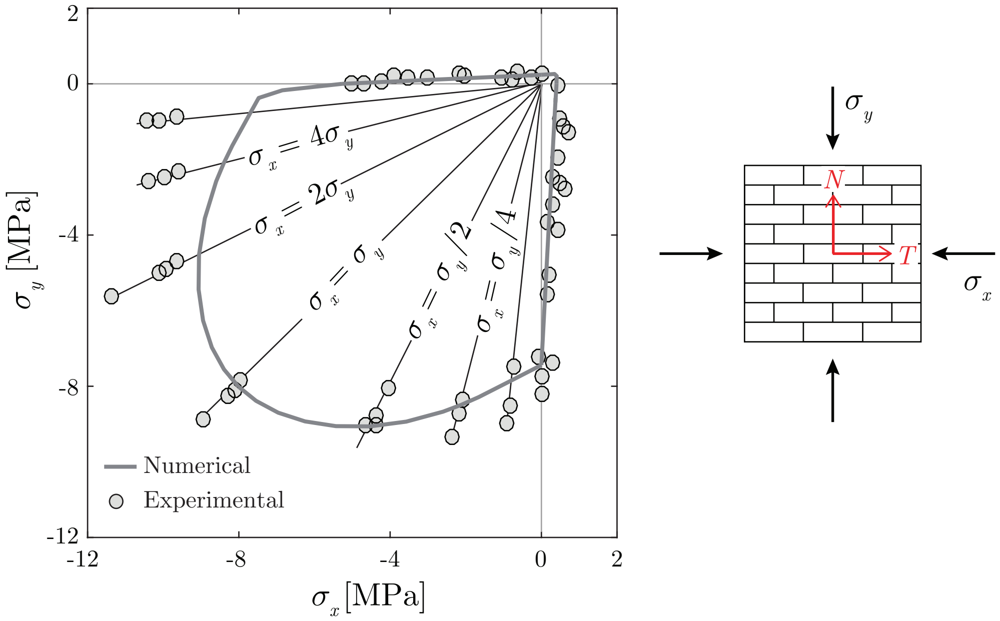

Figure 5.12: Failure surface for $\vartheta = 0°$: comparison between numerical (solid line) and experimental (dots) results from Page (1981, 1983).

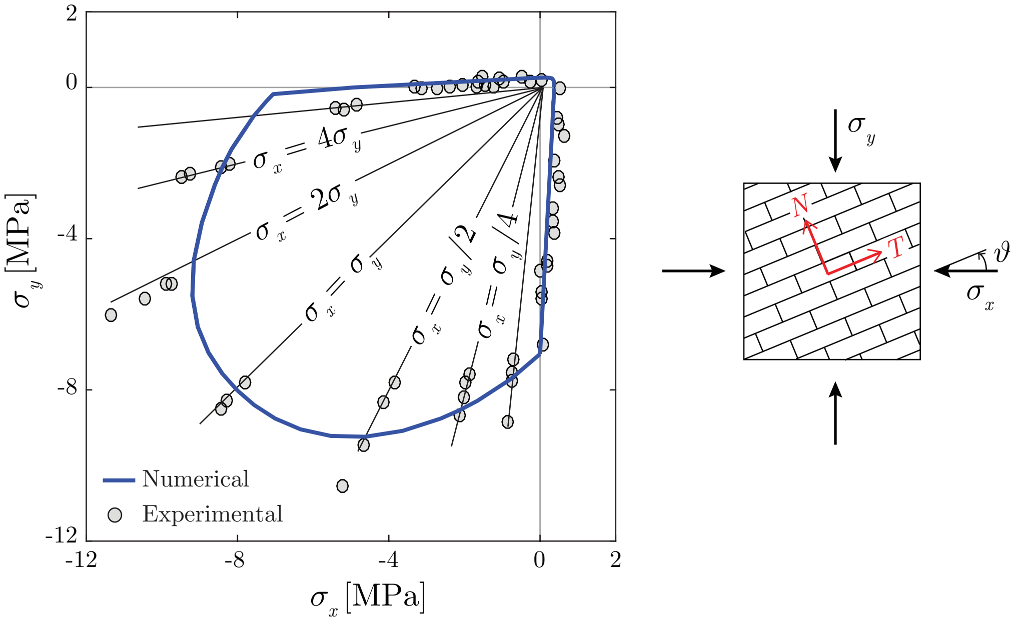

Figure 5.13: Failure surface for $\vartheta = 22.5°$: comparison between numerical (solid line) and experimental (dots) results from Page (1981, 1983).

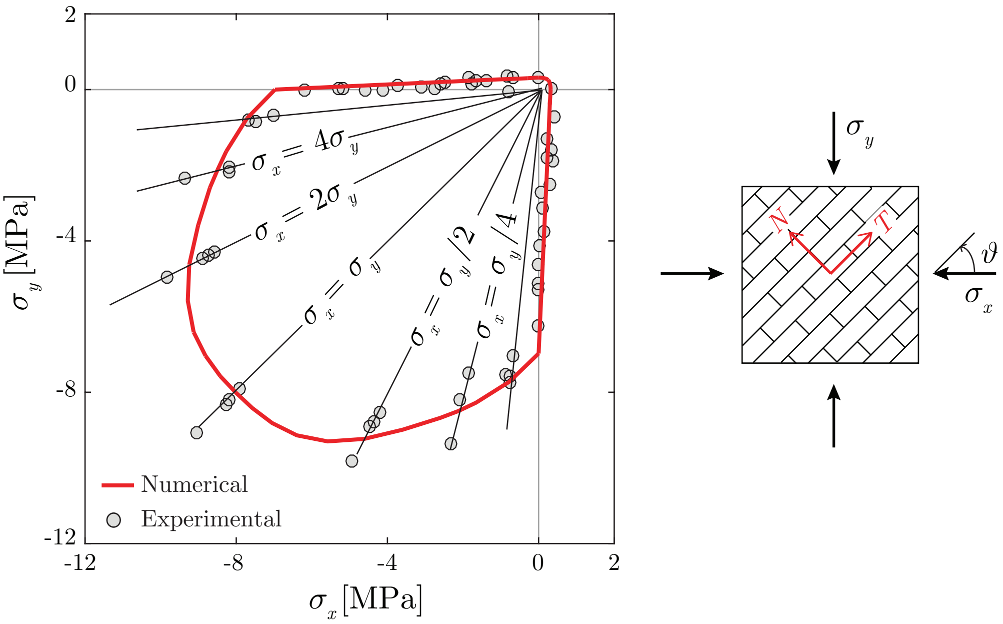

Figure 5.14: Failure surface for $\vartheta = 45°$: comparison between numerical (solid line) and experimental (dots) results from Page (1981, 1983).

5.4.3 Shear walls

To further validate the presented model, the response of the shear walls experimentally tested by Raijmakers and Vermeltfoort (1992) is here numerically analyzed. The panels, whose scheme is shown in Figure 5.15, are composed of 18 courses of clay bricks arranged in running bond texture with 10 mm thick mortar, resulting in overall high $H = 1000\,\text{mm}$, width $W = 990\,\text{mm}$ and thickness $t = 100\,\text{mm}$. According to the experimental investigation, for whose detailed description the reader can refer to Chapter 2 (Section 2.2.2.1), two-step analyses are performed: first, a vertical compressive pressure p is applied and, then, a horizontal monotonically increasing displacement s is imposed at the walls top side, keeping the bottom and top sides horizontal and preventing any vertical movement. Three different values of the vertical load p are considered, i.e. $p = 0.3\,\text{MPa}$, $p = 1.21\,\text{MPa}$ and $p = 2.12\,\text{MPa}$, to assess the model ability in describing effect of increasing vertical pressure on the global force-displacement response curves and activated failure mechanisms.

Before showing the comparison between numerical and experimental outcomes, the performed homogenization procedure, aimed at determining the elastic properties of the homogenized masonry material, is described next.

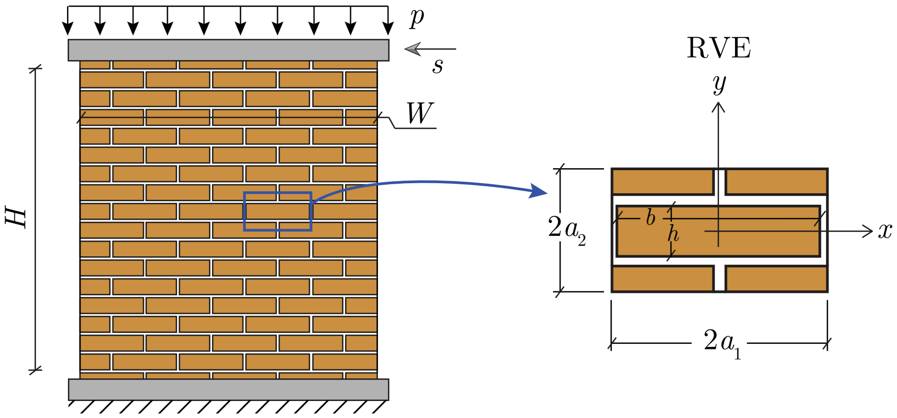

Figure 5.15: Schematic of the analyzed shear walls and selected RVE.

5.4.3.1 Elastic properties of homogenized material

To rationally identify elastic properties of the homogenized orthotropic medium, a classic homogenization procedure is adopted (Sacco, 2009; De Bellis, 2009; Addessi and Sacco, 2014). The unit cell (RVE) shown in Figure 5.15 (where $a_1 = 110\,\mathrm{mm}$ and $a_2 = 62\,\mathrm{mm}$) is considered as representative of the periodic masonry, as this generates the regular arrangement by repeating itself in the continuum domain. The selected RVE is analyzed at micro level by using 4-node quadrilateral finite elements and assuming linear elastic constitutive laws for bricks and mortar. Table 5.3 contains mechanical parameters and sizes of each constituent, selected according to Lourenço (1996) and Addessi and Sacco (2012).

Brick				Mortar		
E_b [MPa]	ν_b	b [mm]	h [mm]	E_m [MPa]	ν_m	t_m [mm]
16000	0.15	210	52	800	0.11	10

Table 5.3: Elastic mechanical parameters and sizes of the constituent materials.

In what follows, $\boldsymbol{\sigma} = \{\sigma_x\, \sigma_y\, \tau_{xy}\}^T$ and $\boldsymbol{\varepsilon} = \{\varepsilon_x\, \varepsilon_y\, \gamma_{xy}\}^T$ refer to the stress and strain vectors at the micro level, while $\boldsymbol{\Sigma} = \{\Sigma_x\, \Sigma_y\, \Sigma_{xy}\}^T$ and $\mathbf{E} = \{\mathrm{E}_x\, \mathrm{E}_y\, \Gamma_{xy}\}^T$

denote the corresponding average homogenized quantities.
Response of the RVE is evaluated by applying macroscopic strain vectors $\mathbf{E} = \{1\,0\,0\}^T$, $\mathbf{E} = \{0\,1\,0\}^T$, $\mathbf{E} = \{0\,0\,1\}^T$ and by considering periodic boundary conditions. Thus, the displacement field, solution of the RVE, results as the superposition of two different fields, as follows:

$$\mathbf{u}(\mathbf{x}) = \mathbf{A}(\mathbf{x})\mathbf{E} + \tilde{\mathbf{u}}(\mathbf{x}) \ , \tag{5.21}$$

where $\mathbf{x} = \{x\,y\}^T$ is the position vector on the RVE, $\mathbf{A}(\mathbf{x})$ is a matrix accounting for the kinematic map linking the macro and micro level, and $\tilde{\mathbf{u}}(\mathbf{x})$ is the periodic micro level fluctuation field respecting the following periodicity conditions:

$$\begin{aligned} \tilde{\mathbf{u}}(a_1, y) &= \tilde{\mathbf{u}}(-a_1, y) \quad \forall y \in [-a_2, a_2] \ , \\ \tilde{\mathbf{u}}(x, a_2) &= \tilde{\mathbf{u}}(x \ , -a_2) \quad \forall x \in [-a_1, a_1] \ . \end{aligned} \tag{5.22}$$

In expanded form Eq. 5.21 becomes:

$$\begin{aligned} u_x(x, y) &= \mathrm{E}_x x + \frac{1}{2}\Gamma_{xy} y + \tilde{u}_x(x, y) \ , \\ u_y(x, y) &= \frac{1}{2}\Gamma_{xy} x + \mathrm{E}_y y + \tilde{u}_y(x, y) \ . \end{aligned} \tag{5.23}$$

The microscopic strain vector $\boldsymbol{\varepsilon}(\mathbf{x})$ is determined as:

$$\boldsymbol{\varepsilon}(\mathbf{x}) = \mathbf{L}(\mathbf{x})\mathbf{E} \ , \tag{5.24}$$

where $\mathbf{E}$ is the prescribed average strain and $\mathbf{L}(\mathbf{x})$ is an localization matrix.
The microscopic stress is evaluated by using the following elastic constitutive laws:

$$\boldsymbol{\sigma} = \mathbf{c}_k \boldsymbol{\varepsilon} \ , \tag{5.25}$$

with $\mathbf{c}_k$ denoting the plane stress elastic constitutive matrix for brick ($k = b$) and mortar ($k = m$). Figures 5.16(a-c) show the distributions of the microscopic stresses σ_x, σ_y and τ_{xy} obtained by imposing the unit macroscopic strain vectors $\mathbf{E} = \{1\,0\,0\}^T$, $\mathbf{E} = \{0\,1\,0\}^T$ and $\mathbf{E} = \{0\,0\,1\}^T$.

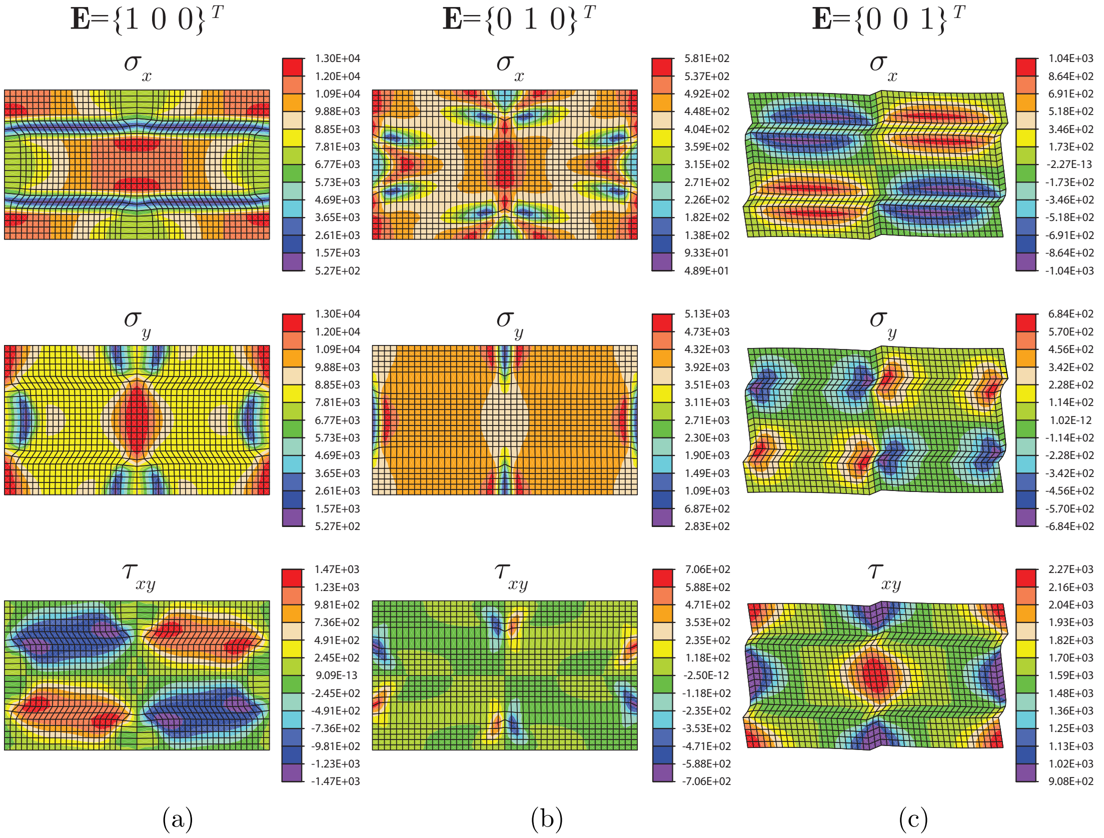

Figure 5.16: Distributions of stresses on the RVE deformed configurations (scaled 0.2).

Finally, by using the Hill-Mandel equivalence principle, the macroscopic stress is determined as:

$$\mathbf{E}^T\mathbf{\Sigma} = \frac{1}{V}\int_V \boldsymbol{\varepsilon}^T\boldsymbol{\sigma}\mathrm{d}V = \frac{1}{V}\int_V (\mathbf{LE})^T\,\mathbf{c}_k\,(\mathbf{LE})\,\mathrm{d}V = \mathbf{E}^T\mathbf{CE}\,, \tag{5.26}$$

where $\mathbf{C}$ is the wanted 3×3 homogenized elastic constitutive matrix, which results as:

$$\mathbf{C} = \begin{bmatrix} 8.6853 & 0.4291 & 0 \\ 0.4291 & 3.9315 & 0 \\ 0 & 0 & 1.6070 \end{bmatrix} \times 10^3\,. \tag{5.27}$$

On the basis of the macroscopic elastic coefficients C_{ij} $(i = 1,2,3,\ j = 1,2,3)$

of **C** matrix, the homogenized Young's moduli and Poisson ratios are determined (see Table 5.4).

Homogenized elastic properties			
$E_x = E_T$ [MPa]	$E_y = E_N$ [MPa]	$\nu_{xy} = \nu_{TN}$	$G_{xy} = G_{TN}$ [MPa]
8638.5	3910.3	0.11	1670

Table 5.4: Elastic mechanical parameters of the homogenized masonry material.

5.4.3.2 Global response curves and damage distributions

A mesh made of (15 × 15) 4-node quadrilateral finite elements is used to perform the numerical analyses, setting the nonlocal radius $l_c = 200\,\mathrm{mm}$ in accordance to mesh and brick sizes. The mechanical parameters deduced by the experimental data and also reported in Zucchini and Lourenço (2009) are contained in Table 5.5. These lead to average tensile and compressive strengths along the material axes equal to 0.18 MPa and 10 MPa, respectively.
In Figure 5.17 experimental (gray lines) and numerical (black lines) global response curves, in term of horizontal base reaction versus applied horizontal displacement, are depicted for all the considered values of the precompression load.

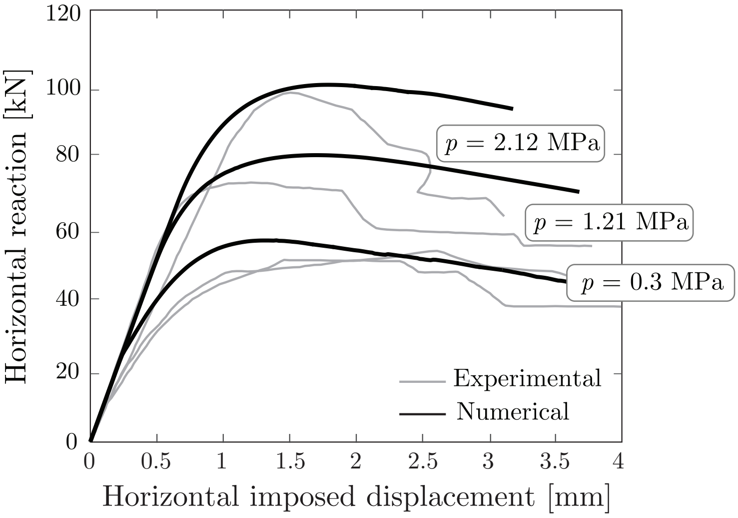

Figure 5.17: Raijmakers-Vermeltfoort panels: comparison between numerical (black lines) and experimental (gray lines) force-displacement response curves.

On the overall, good agreement is found, as the model reproduces the increase of maximum strength with increasing vertical load p. However, differently from the experimental outcomes, the numerical curves do not capture the increasing brittle behavior, as these show softening branches with similar slope.

As concerns the activated failure modes, Figure 5.18 shows comparison between the experimental crack patterns and the damage maps of D_2 and D_3 at the end of the analyses. In accordance with the experimental outcomes, significant damaged zones located at the bottom and top corners of the wall appears in the case of lower compression load, i.e $p = 0.3\,\mathrm{MPa}$. These are a consequence of high tensile stresses normal to bed joints and, consequently, are associated to D_2 damage. For the higher values of p, that is 1.21MPa and 2.12 MPa, damaged zones also appear due to the crushing of the material. Finally, similarly to the experimental crack paths, diagonal bands, associated to D_3 damage, emerge in the middle of the panels due to the dominant shear mechanism.

Damage parameters

$a_t = a_c = a_s$	b_t	b_c	b_s
0.99	4.2×10^{-5}	2.5×10^{-3}	8.5×10^{-4}

Damage thresholds

Y_{1t0}	Y_{1c0}	Y_{2t0}	Y_{2c0}=Y_{cc0}	Y_{s0}
2.3×10^{-5}	9.2×10^{-4}	3.8×10^{-5}	2.5×10^{-3}	1.4×10^{-4}

Table 5.5: Raijmakers-Vermeltfoort panels: material parameters.

5.5 Effect of texture on the level of orthotropy

A brief study is here performed to evaluate the effects of bricks and mortar relative arrangement on the definition of homogenized elastic properties.

The level of orthotropy of the elastic response depends on the geometry, size, mechanical properties and arrangement of the constituent materials. Figures 5.19(a-e) show examples of masonry-like composite textures with rectangular (a-c) and square (d,e) blocks, whose dimensions are selected according to Casolo (2006). Sizes of rectangular blocks are 250 × 55 × 120 mm^3, whereas side of

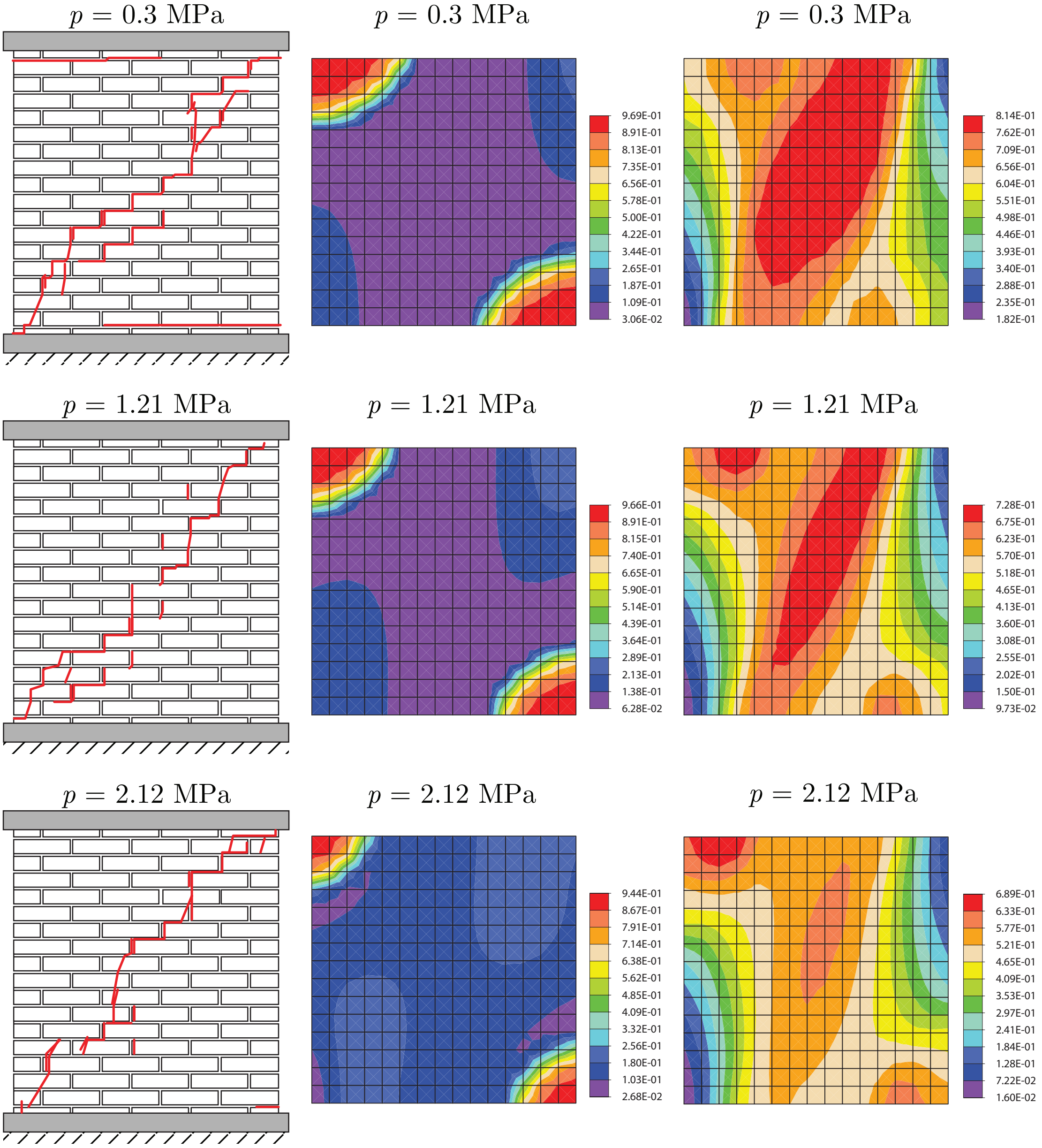

Figure 5.18: Raijmakers-Vermeltfoort panels: comparison between experimental crack paths (first column) and distributions of damage D_2 (second column) and D_3 (third column).

square blocks is 120 mm. Mortar joints thickness is assumed equal to 10 mm. To evaluate the homogenized constitutive matrices, the representative cells depicted in Figures 5.20-5.24 are selected and the homogenization procedure described in

Section 5.4.3.1 is applied by considering isotropic behavior for all components ($E_b = 10000\,\text{MPa}$, $E_m = 1000\,\text{MPa}$, $\nu_b = \nu_m = 0.1$, according to Casolo (2006)). The resulting homogenized stiffness matrices are reported in Eqs. 5.28-5.32 by highlighting the effect of blocks size and arrangement. Focusing the attention on the same typology of texture but different blocks size (for instance running and stack bond arrangements in Figure 5.19), it emerges that rectangular blocks lead to higher level of orthotropy with respect to square ones. This feature can be better valued by the homogenized moduli E_x, E_y and G_{xy} summarized in Table 5.6 for all RVEs. It should be noted that, despite the stack bond texture with square blocks leads to the same value of E_x and E_y, the shear modulus $G_{xy} = 1972.7\,\text{MPa}$ does not match to that determined with the isotropic relationship $G = E/(2(1+\nu)) = 2632.3\,\text{MPa}$, as usual for masonry material.

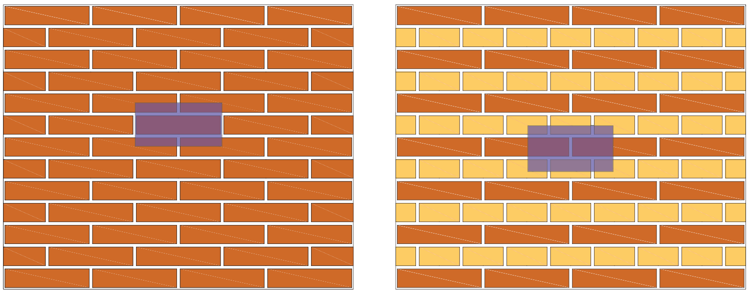

(a) Running bond (b) English bond

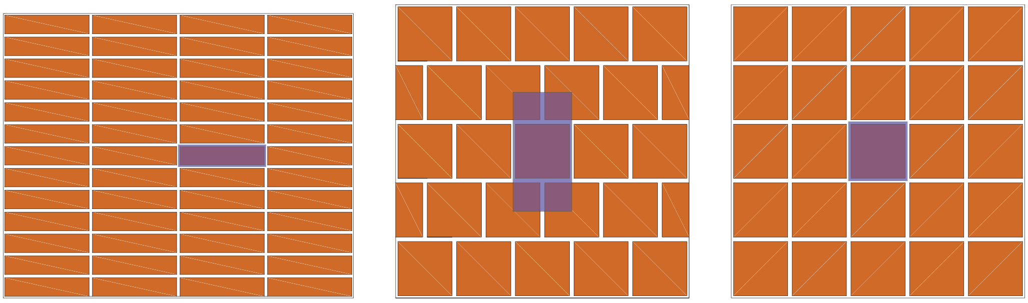

(c) Stack bond (d) Running bond (e) Stack bond

Figure 5.19: Masonry textures: (a-c) rectangular blocks and (d,e) square blocks.

To summarize the performed analyses confirmed that different level of orthotropy of the elastic response can occur depending on geometry and arrangement of the constituent materials. Notwithstanding the initial elastic orthotropic

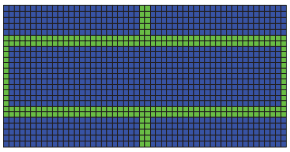

Figure 5.20: RVE running bond (rectangular blocks).

$$\mathbf{C} = \begin{bmatrix} 6893.3 & 381.3 & 0 \\ 381.3 & 4138.7 & 0 \\ 0 & 0 & 1755.5 \end{bmatrix} \quad (5.28)$$

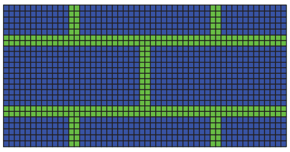

Figure 5.21: RVE english bond (rectangular blocks).

$$\mathbf{C} = \begin{bmatrix} 6177.9 & 365.8 & 0 \\ 365.8 & 4090.3 & 0 \\ 0 & 0 & 1695.3 \end{bmatrix} \quad (5.29)$$

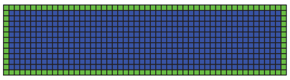

Figure 5.22: RVE stack bond (rectangular blocks).

$$\mathbf{C} = \begin{bmatrix} 6621.4 & 354.6 & 0 \\ 354.6 & 4146.3 & 0 \\ 0 & 0 & 1713.8 \end{bmatrix} \quad (5.30)$$

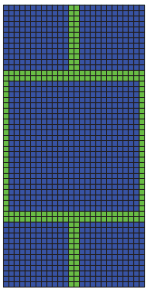

Figure 5.23: RVE running bond (square blocks).

$$\mathbf{C} = \begin{bmatrix} 5738.5 & 437.2 & 0 \\ 437.2 & 5643.6 & 0 \\ 0 & 0 & 2080.4 \end{bmatrix} \quad (5.31)$$

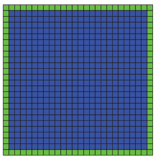

Figure 5.24: RVE stack bond (square blocks).

$$\mathbf{C} = \begin{bmatrix} 5661.3 & 399.2 & 0 \\ 399.2 & 5661.3 & 0 \\ 0 & 0 & 1972.7 \end{bmatrix} \tag{5.32}$$

	Rectangular blocks			Square blocks	
	Running	English	Stack	Running	Stack
E_x [MPa]	6858.2	6145.2	6591.0	5704.7	5633.2
E_y [MPa]	4117.6	4068.6	4127.3	5610.3	5633.2
ν_{xy}	0.092	0.09	0.086	0.077	0.07
G_{xy} [MPa]	1755.5	1695.3	1713.8	2080.4	1972.7
E_x/E_y	1.66	1.51	1.6	1.02	1

Table 5.6: Elastic parameters of the homogenized masonry material for RVE in Figures 5.20-5.24.

characteristics can be significantly modified by the onset and evolution of nonlinear mechanisms (such as damage), these results can provide useful informations to identify cases in which is needed to use a material orthotropic description. However, when the anisotropy level is not significant the simplified hypothesis of isotropic behavior could be satisfactory adopted.

5.6 Summary

This chapter presented a novel orthotropic damage model for the analysis of the in-plane response of masonry structures. The proposed constitutive law and damage criterion appear to be suitable tools to phenomenologically describe mechanical behavior of masonry walls with regular arrangement of bricks and mortar, where bed joints act as plane of weakness. Indeed, the performed analyses showed the model ability in capturing different mechanical properties along material directions. Furthermore, comparison of numerical and experimental responses of some masonry panels showed a good agreement, both in terms of global force-displacement response curves and damage distributions. Obviously, further investigation is needed to test the model performance under different loading and boundary conditions.

Finally, a study was performed to investigate effects of geometry and arrangement of bricks and mortar on the overall elastic properties of masonry. Thus, in cases where the level of anisotropy is significant, it is advisable to use a material orthotropic description instead of an isotropic one.

Chapter 6

Characterization of masonry walls dynamic behavior

The effects of damage and plasticity phenomena on the nonlinear cyclic static response of masonry walls were largely explored. But the presence of damage and irreversible strains substantially modifies the dynamic structural response, too. Indeed, onset and propagation of damage leads to degradation of the structural mechanical properties and related variation of the natural frequencies, which in turn significantly influence the dynamic response.

On the basis of the above considerations, this chapter is aimed at providing a complete characterization of the masonry dynamic behavior. The attention is focused on the effects of nonlinear mechanisms on the frequency response curves (FRCs) of masonry walls, as these represent a relevant tool for the dynamic characterization of systems.

Section 6.1 briefly reports an overview of FRCs by relating their main features to those of the restoring force shape. Then, in Section 6.2 response of a slender wall is investigated: the peculiar characteristics of the cyclic global force-displacement response curve are evaluated and their influence on the FRCs is highlighted. Moreover, the structural response to example natural earthquakes is computed. Finally, Section 6.3 describes experimental and numerical studies performed on the out-of-plane response of tuff masonry walls.

6.1 Main features of frequency response curves

Frequency response curves are relevant tools to dynamic characterization of systems and permit to highlight and distinguish effects of different nonlinear mechanisms. In linear elastic vibration, these curves can be evaluated as frequency response function plot. In nonlinear vibration, the scalability and additivity between input (i.e excitation) and output (i.e response) is no longer valid and, therefore, FRCs represent the response amplitude as a function of the forcing frequency and depend on the excitation amplitude. Several studies on nonlinear oscillators, characterized by geometrical and/or material nonlinearities, clarified that the FRCs features are referable to restoring force shape (that is the force-displacement relationship): hardening or softening behavior, multi-valued curves with jump phenomenon or single-valued curves can occur. The loci of the response peaks give the nonlinear frequency-amplitude relationship, that is the so-called *backbone* curve. Linear systems have straight backbone, while softening and hardening systems are characterized by backbone curves bent on the left and right, as shown in Figures 6.1(a) and (b) respectively.

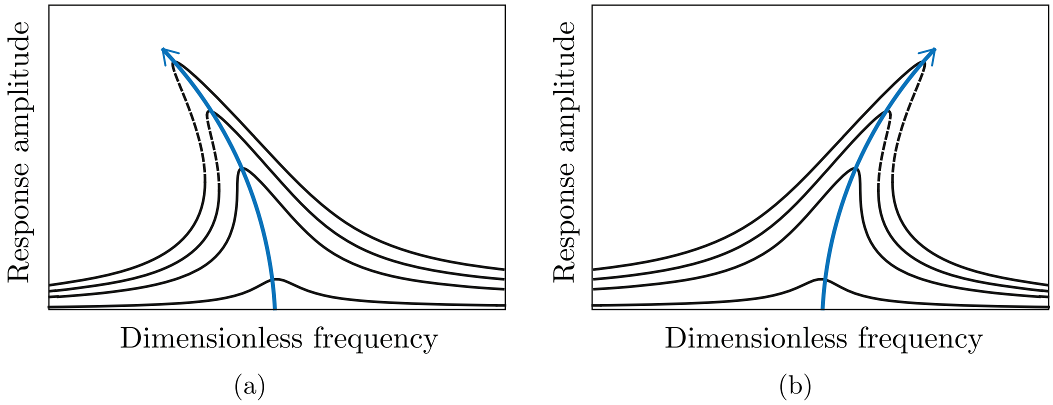

(a) (b)

Figure 6.1: FRCs with (a) softening and (b) hardening behavior.

Multi-valued curves with jump phenomenon introduce a frequency band where two stable and one unstable solution exist. Figure 6.2 shows an example case for a nonlinear viscoelastic single degree of freedom (SDOF) studied by Lacarbonara (2013), whose restoring force is provided by a linear dashpot and a nonlinear elastic spring in parallel. Here, for a given excitation frequency Ω^*, belonging to the range $[\Omega_1 \div \Omega_2]$, three oscillations with different amplitude X_1, X_2 and X_3 can occur: X_1 and X_3 are stable, while X_2 is unstable, that is any small disturbance causes the system to leave this equilibrium state and move towards the stable solution. Indeed, only the stable solutions are possible depending on how the state is approached.

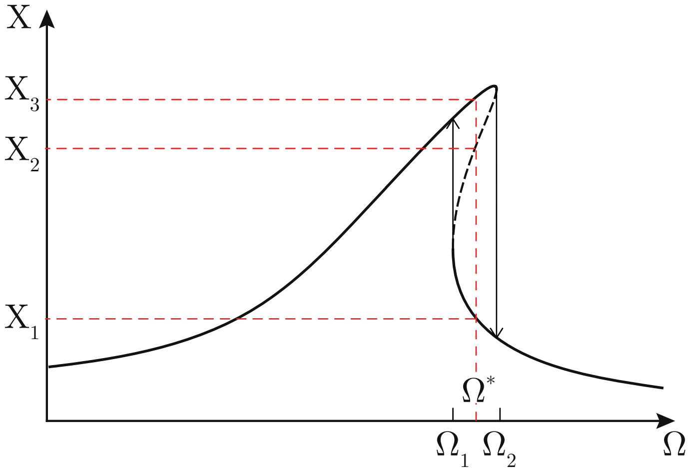

Figure 6.2: Multi-valued FRC with jump phenomenon obtained by Lacarbonara (2013) for a nonlinear viscoelastic SDOF (solid and dashed lines denote stable and unstable solutions, respectively).

The described multi-valued characteristic is typical of system with nonlinear invariant restoring force and this can occur also for hysteretic systems. In fact, studies devoted to nonlinear oscillation of hysteretic models highlighted that hysteresis itself does not guarantee stable single-valued response curves. Already many years ago, Iwan (1965) found multi-valued curves for one degree of freedom double bilinear hysteretic oscillator. Similary, Capecchi and Vestroni (1985, 1990) showed that single-valued curves can be obtained only in the cases of fully hysteretic restoring force. Further developments confirmed these results: Figure 6.3 reports the FRCs and the related restoring force shapes, obtained by Lacarbonara and Vestroni (2003) for a Masing oscillator for different degrees of hysteresis, identified through the α parameter. Here, it can be noted that increasing α from 0.25 to 0.75 a reduction of both response amplitude and multi-valued range occurs. The coexisting solutions disappear and single-valued curve is recovered for $\alpha = 1$, which corresponds to a fully hysteretic restoring force.

Studies performed on the Bouc-Wen model (Wong et al., 1994b,a; Casini and Vestroni, 2018) conducted to a large variety of FRCs. In fact, as known, this model is able to reproduce a significant range of hysteretic shapes, depending on the material parameters chosen. Consequently, single-valued curves are obtained for fully hysteretic restoring forces, while the multi-valued characteristic emerges when the reduced hysteresis occurs.

Analytical techniques, such as the method of harmonic balance and the multiple time scale method (Nayfeh and Mook, 2008), are usually employed to study the FRCs of simple systems characterized by one or few degrees of freedom. However, when dealing with more complex structure, recourse to full numerical techniques becomes unavoidable.

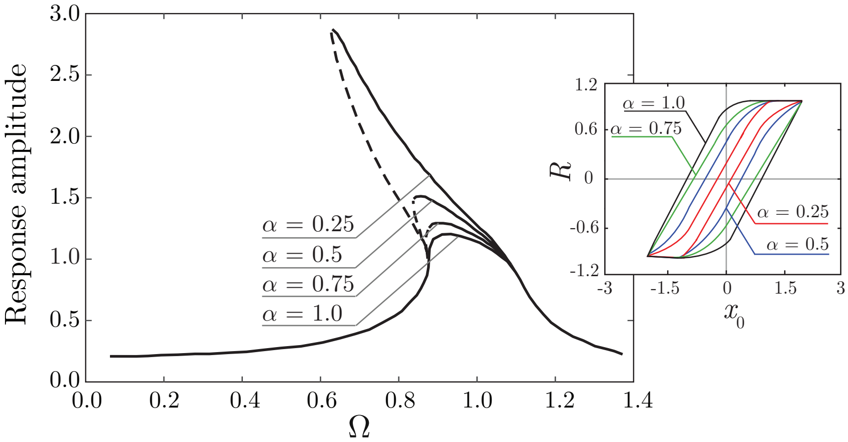

Figure 6.3: Lacarbonara and Vestroni (2003): FRCs and restoring force shapes of the modified Masing oscillator for various values of α parameter.

6.2 Response of a slender wall

6.2.1 Restoring force shape

The static behavior of the slender wall schematically shown in Figure 6.4(a) is here numerically explored by using the damage-plastic model presented in Chapter 4. This is conceived to model the central strip of a wall very long in one direction with respect to the other two, loaded out-of-plane. In fact, wall sizes, that is height $H = 6000\,\mathrm{mm}$, width $W = 1000\,\mathrm{mm}$ and thickness $t = 1000\,\mathrm{mm}$, are selected to reproduce typical geometries of walls of historical buildings and churches, as for example the external walls of the Basilica S. Maria di Collemaggio. The mechanical parameters used to perform the numerical analyses are shown in Table 6.1, setting $\kappa = 0$ and $H_i = 0$. Value of Young's modulus, E, is introduced according to those estimated for the Basilica S. Maria di Collemaggio (Gattulli et al., 2013). Tensile and compressive strengths are set equal to 0.29 MPa and 4.2 MPa, respectively, in accordance with experimental outcomes on masonry material and the Italian guidelines (NTC, 2008). The wall overall response is investigated under monotonic and cyclic loading histories, considering a simple scheme, where the wall is restrained only at the base. Figure 6.5(a) contains the load-displacement global curve obtained by applying the same monotonic horizontal displacement at all the nodes on the top free side. Furthermore, to show the effectiveness of the adopted nonlocal integral regularization technique, the results obtained for two different meshes are compared, considering a nonlocal radius l_c equal to 500 mm: solid line refers to a mesh made of (3×19) 9-node FEs (mesh 1 in Figure 6.4(b)), while dashed line corresponds to (6×38) 9-node FEs (mesh 2 in Figure 6.4(c)). As the two meshes give results in perfect agreement, the coarser discretization is adopted later.

Elastic parameters

E [MPa]	ν
4000	0.2

Plastic parameters

$\sigma_t = \sigma_c$ [MPa]	H_k [MPa]
1.5	0.7 E

Damage parameters

Y_{t0}	b_t	$a_t = a_c$	Y_{c0}	b_c
5.2×10^{-5}	3.6×10^{-5}	0.99	1.3×10^{-4}	6×10^{-3}

Table 6.1: Slender panel: material parameters.

The pushover response curve highlights the presence of strength and stiffness degradation, due to the onset and growth of damaged zone at the bottom left corner of the wall, as the structure is pushed towards right. After the initial linear elastic branch, damage arises in the zone where the highest tensile stresses

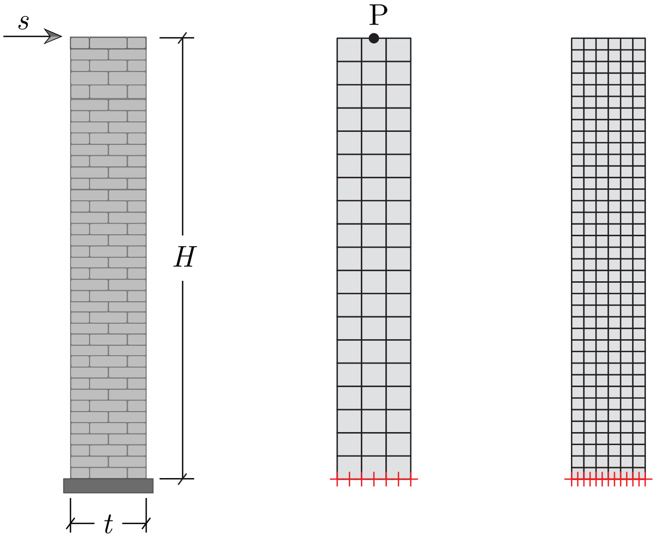

(a) (b) (c)

Figure 6.4: (a) schematic view of the analyzed wall and adopted FE meshes: (b) mesh 1 and (c) mesh 2.

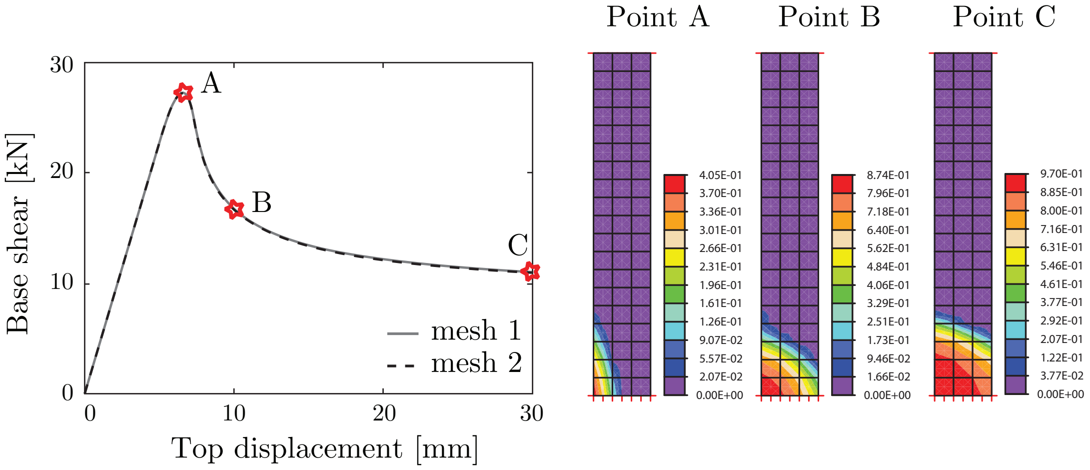

(a) (b)

Figure 6.5: (a) pushover response curve and (b) tensile damage distributions for the applied displacement $s = 6.6\,\mathrm{mm}$ (point A), $s = 10\,\mathrm{mm}$ (point B) and $s = 30\,\mathrm{mm}$ (point C).

occur and, then, spreads around (Figure 6.5(b)), leading to severe damage of the bottom side region. This causes a very steep softening branch in the global response curve. Moreover, in Figure 6.6, the load-displacement global curves are depicted with reference to a cyclic horizontal displacement applied at the top side and for two values of the kinematic hardening parameter, that is $H_k = 0.3\,E$, $0.7\,E$. Steep reduction of strength, which occurred after the maximum force value has been reached, is clearly shown also in the cyclic curve, where a significant drop is observed in the second cycle. Plastic irreversible mechanisms and the related hysteresis loops are presented, these being larger for the lower value of H_k. Furthermore, due to the cyclic nature of the loading, damaged zones appear both at the left and right corner (see the damage maps in Figure 6.6(a) and (b)) together with the partial stiffness recovery linked to the opening and subsequent re-closing of the tensile cracks.

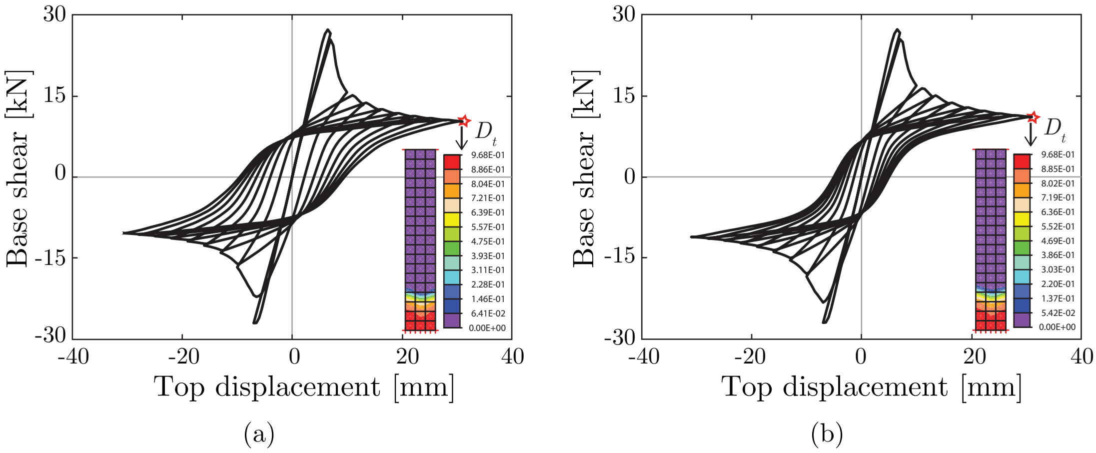

(a)

(b)

Figure 6.6: Cyclic load-displacement curves and tensile damage distributions for two different values of the kinematic hardening parameter (a) $H_k = 0.3\,E$ and (b) $H_k = 0.7\,E$.

A further analysis is performed to deepen the main features of the wall cyclic response and highlight the history-dependent characteristic of the masonry restoring force. To this purpose, the structure is subjected to the cyclic horizontal displacement history applied at the top side shown in Figure 6.7(a). This is characterized by an initially increasing, then kept constant and finally decreasing, amplitude. Figure 6.7(b) focuses on the response cycles obtained in correspondence of the same input amplitudes at the initial and final stage of the analysis. These definitely point out that the structural response is strongly path dependent. For instance, although the structure experiences the same maximum displacement amplitude during the 'd-e-f-g' and 'n-o-p-q' cycles, the obtained force-displacement curves fully differ. In fact, the wall attains a higher displacement (with consequent increased damage) before the 'n-o-p-q' cycle, as opposed to the 'd-e-f-g' cycle and this notably modifies the restoring force loop, mainly due to the variation of the elastic properties of the re-loading branch.

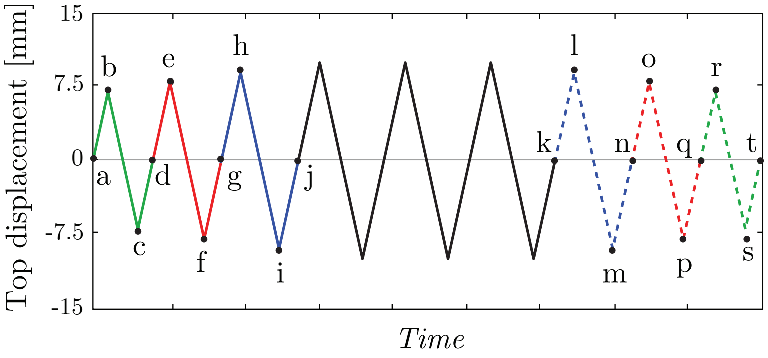

(a)

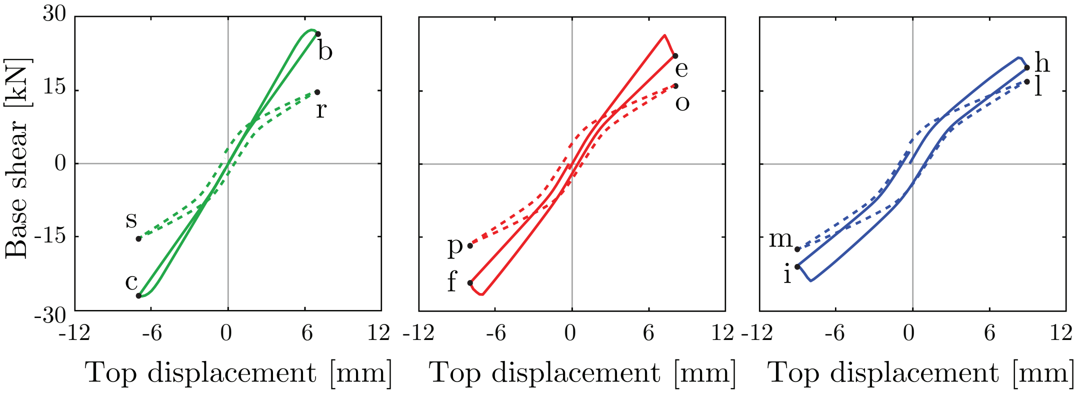

(b)

Figure 6.7: (a) cyclic imposed displacement and (b) response cycles obtained in correspondence of the same imposed displacement amplitudes.

To summarize, the structural response of the wall under static loading conditions appears definitely affected by the evolution of damage and plasticity mechanisms, putting in evidence the structural modifications which substantially change the subsequent response. Investigation on the cyclic nonlinear static response is a useful starting point to move towards exploration of the more complex dynamic behavior.

6.2.2 Frequency response curves

To characterize the main aspects of the dynamic response of masonry walls, harmonic excitations are considered. Assuming a density mass value $\rho = 2000\,\mathrm{kg/m^3}$, the first three natural frequencies of the small amplitude flexural vibrations result $f_1 = 6.23\,\mathrm{Hz}$, $f_2 = 35.16\,\mathrm{Hz}$ and $f_3 = 86.98\,\mathrm{Hz}$. The frequency response curves of the wall are evaluated in terms of relative displacement of the point P in Figure 6.4(b) with respect to the base. These are compared with the corresponding curves obtained by considering a linear elastic behavior. For this purpose, horizontal acceleration histories $\ddot{u}_g = U \sin[\Omega(t)t]$, characterized by a slowly variable excitation frequency over time, are applied at the wall base. The forcing frequency $\Omega(t)$ changes according to linear increasing and decreasing sweep laws, with the ratio $\Omega(t)/\omega_1$ in the range $[0.2 \div 1.5]$, being ω_1 the first initial frequency of the wall. In what follows, these excitation histories will be called sweep 1, increasing frequency, and 2, decreasing frequency, respectively.

Figure 6.8 shows the obtained frequency response curves for three different amplitudes of the applied acceleration $U/g = 0.04$, 0.05, 0.06 (green, red and blue line, respectively), along with the elastic responses (black lines) for comparison, with g gravity acceleration. The curves are derived by associating the maximum displacement amplitude of each response cycle to the corresponding excitation frequency and assuming a damping factor equal to 3% (the same of the elastic case). It can be observed that, for increasing excitation frequency, that is when sweep 1 acceleration history is applied, the onset of damage causes decay of the wall structural stiffness, leading to decrease of natural frequency ω_1, while the forcing frequency $\Omega(t)$ increases. Thus, the wall suddenly comes out from resonance conditions, with a peak response attained at a frequency which decreases with the increasing acceleration intensity and differs from that of the corresponding elastic case (Figure 6.8(a)). Conversely, in the case of sweep 2 history, the wall natural frequency variation follows same trend of $\Omega(t)$: due to damage progression, a

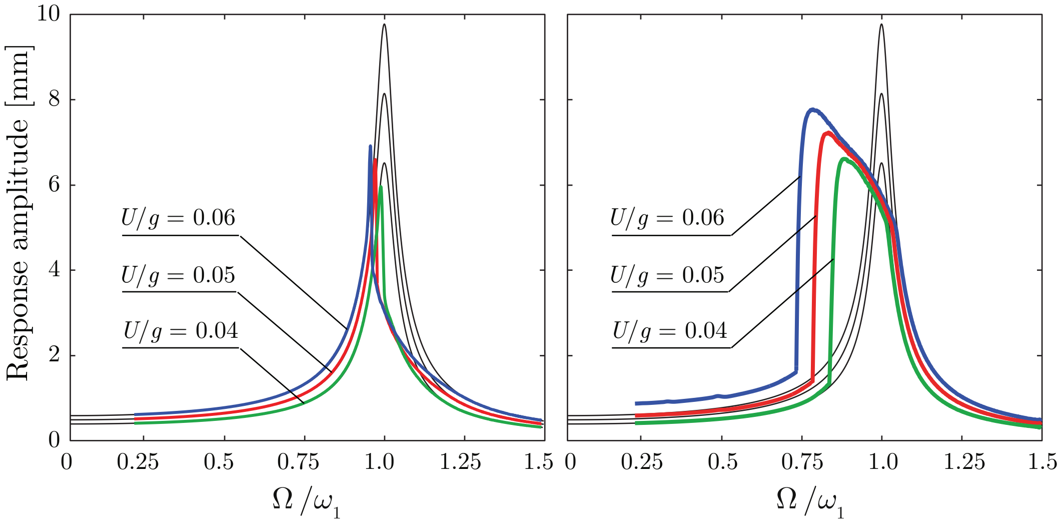

(a) (b)

Figure 6.8: Wall frequency response curves for (a) sweep 1 and (b) sweep 2: elastic response (black lines) and damage-plastic response (green, red and blue lines corresponding to $U/g = 0.04, 0.05, 0.06$, respectively).

modification of the frequency curve slope with respect to the elastic curve arises and the resonance frequency is moved down (Figure 6.8(b)). The curve obtained for decreasing driving frequency furnishes the resonant branch of the frequency response curve: the attained maximum value gives the resonant frequency, which practically coincides with the natural frequency of the system, that clearly depends on the oscillation amplitude, as expected. The loci of the response peaks gives the nonlinear frequency-amplitude relationship. This curve is bent on the left, showing a softening behavior. Moreover, the wall response is markedly affected by the structural decay state, and consequently, by combining the results of sweep 1 and 2, the frequency response curves are multi-valued, as expected. Finally, the accumulation of irreversible strains is higher for higher values of the applied force amplitude.

It is worth noting that, in the case of plastic constitutive response in absence of damage, frequency response curves are single-valued, as in the case of fully hysteretic restoring force (Iwan, 1965; Capecchi and Vestroni, 1985, 1990), regardless of the applied sweep history. This means that, neglecting damage effects, a unique frequency response curve would be computed with both sweep 1 and 2. Instead, due to the kind of nonlinearity, multi-valued and not unique curves are here obtained. In fact, different from the invariant restoring forces, the FRC for increasing frequency cannot run on the resonant branch obtained for decreasing frequency, as a consequence of the structural damage progression.

Figures 6.9(a), (b) and 6.10(a), (b) contain the displacement time histories of the selected point P, for the input amplitude ratio $U/g = 0.04$ and for both sweep histories. Green lines refer to the damage-plastic response, black lines to the elastic case, shown for comparison. Here to be noted is that the elastic responses to the two sweeps show same shape and maximum amplitudes, while the displacement histories for the damage-plastic cases are very different due to the degrading mechanisms evolving in the structure. Furthermore, to better clarify the phenomenon, Figure 6.9(d) and Figure 6.10(d) show the time evolution of the phase angle $\varPhi$ between the input sinusoidal forcing and the structural response. Phase difference is measured by finding the time delay t_r between the two waveforms. With reference to the example case reported in Figure 6.11, where two sinusoidal waves with same frequency f are shown, the phase angle in degree is derived as:

$$\varPhi = \frac{360\, t_r}{T} \tag{6.1}$$

where $T = 1/f$ is the period waves.

As expected, in the elastic cases (black lines in Figures 6.9(d) and 6.10(d)), the phase angle $\varPhi$ results equal to 90°, when the ratio Ω/ω_1 is about 1 (see Figures 6.9(c) and 6.10(c)). Furthermore, a quite regular trend for $\varPhi$ is found, as typical of the considered Rayleigh damping value. Conversely, time variation of $\varPhi$ exhibits very different patterns in cases of damage-plastic response. A sharp growth in a narrow time interval is noted for sweep 1 (green line in Figure 6.9(d)), when the wall experiences resonance conditions, after that this approaches to the constant value of 180°, by testing that the passage through the resonance is occurred. On the contrary, in case of sweep 2, the initial value of $\varPhi$ is 180° and, then, this walks up to 0° by passing for a longer interval of inversion phase (green line in Figure 6.10(d)), as the driving frequency is approaching to the frequency of the damaged structure and, then, the resonance condition is gradually shifted. Time evolution

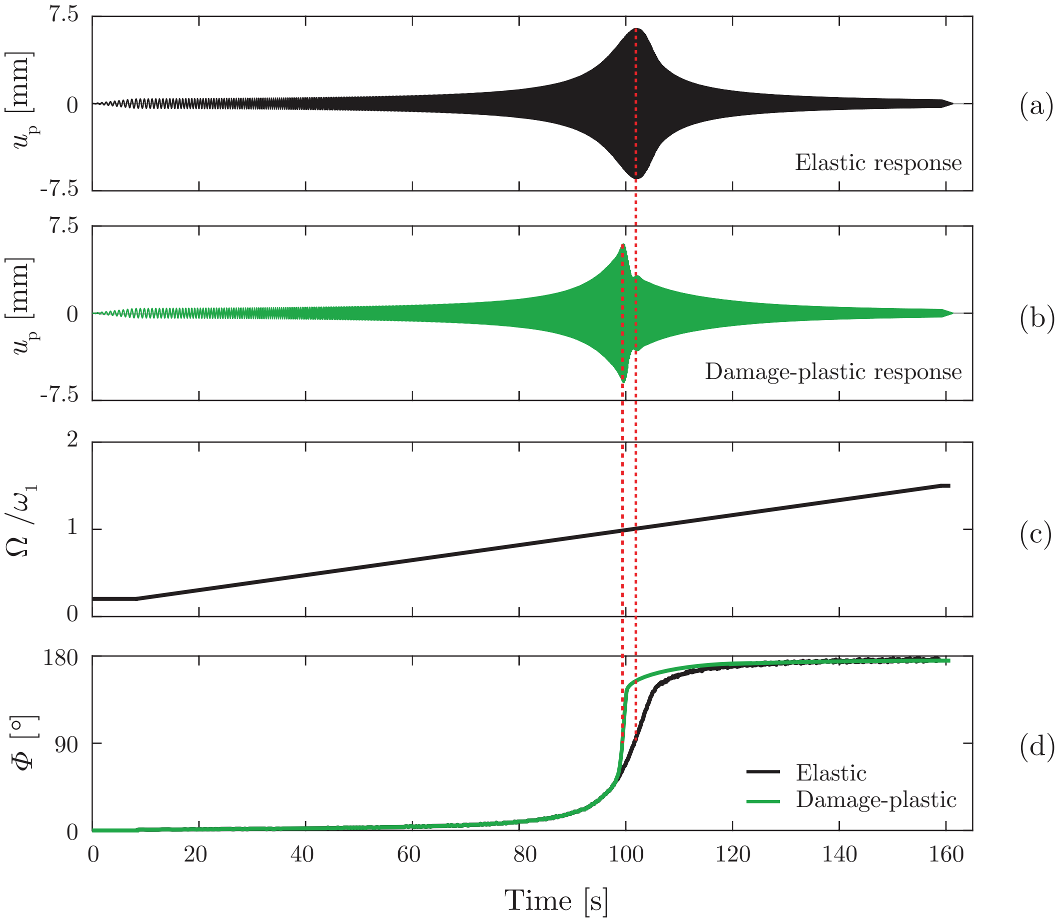

Figure 6.9: Response to sweep 1 setting $U/g = 0.04$: time histories of the top relative displacement in (a) linear elastic case and (b) damage-plastic case, (c) time variation of the ratio Ω/ω_1, (d) time histories of phase angle Φ.

of Φ angle gives indication about the variation of the wall natural frequency ω_1 and, therefore, it is a powerful tool to interpret and understand the phenomenon.

The influence of the adopted constitutive relationship on the wall dynamic response is also explored. To this end, three cases are considered: a damage model (D), a damage-plastic model (DP) with $H_k = 0.3\,E$ and a damage-plastic model with $H_k = 0.7\,E$ (this last value is the one already adopted in the previous analyses). The corresponding cyclic responses are shown in Figure 6.6. Only the more significant sweep 2 is illustrated. Figure 6.12 contains the frequency response curves for two excitation amplitudes (a) $U/g = 0.04$ (green lines) and (b)

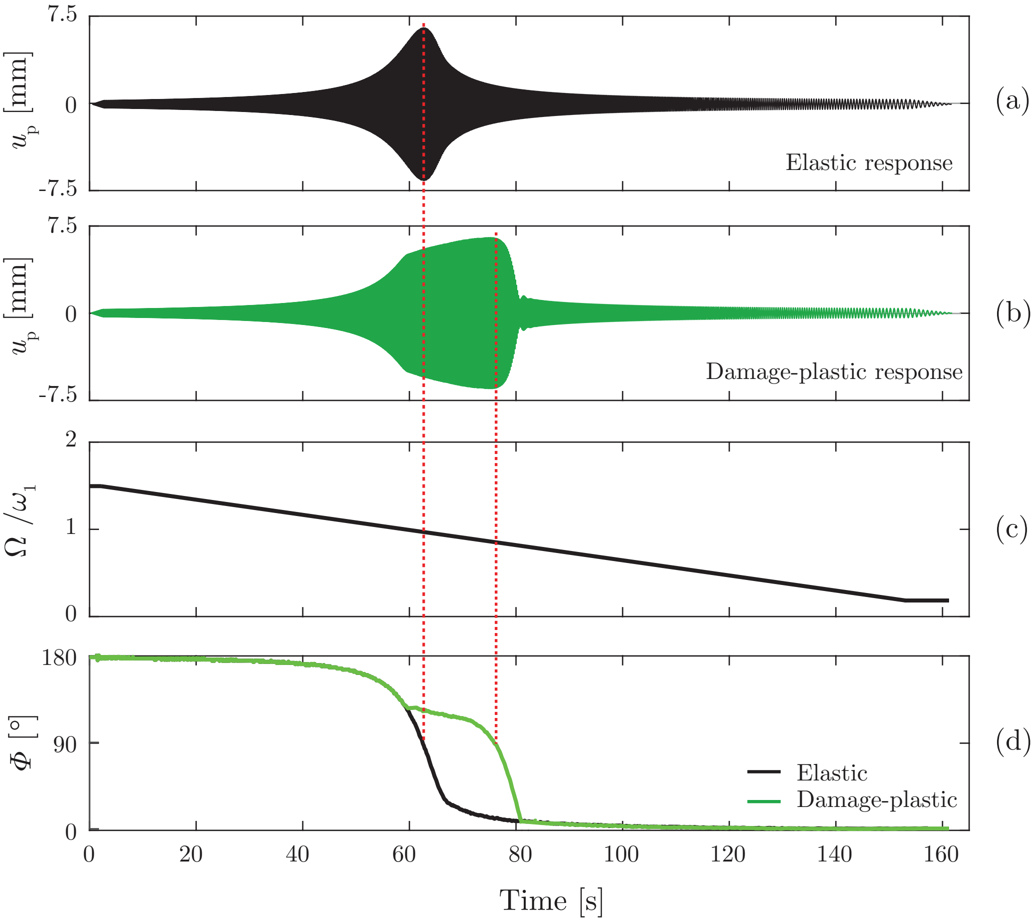

Figure 6.10: Response to sweep 2 setting $U/g = 0.04$: time histories of the top relative displacement in (a) linear elastic case and (b) damage-plastic case, (c) time variation of the ratio Ω/ω_1, (d) time histories of phase angle Φ.

$U/g = 0.06$ (blue lines). The black lines indicate the elastic responses reported for comparison. The damage-plastic curves show a lower peak and a resonant condition attained at higher frequencies with respect to the damage curve, becoming this difference greater for the higher excitation intensity. This latter behavior can be explained also through energy considerations. For the damage and damage-plastic models, Figure 6.13 reports the top displacement responses for (a) $U/g = 0.04$ and (b) $U/g = 0.06$, where it emerges that plasticity reduces the displacement dynamic amplification. In the bottom of Figure 6.13 the evolution of the dissipated energy E_d, measured in each cycle, is shown. When plastic mecha-

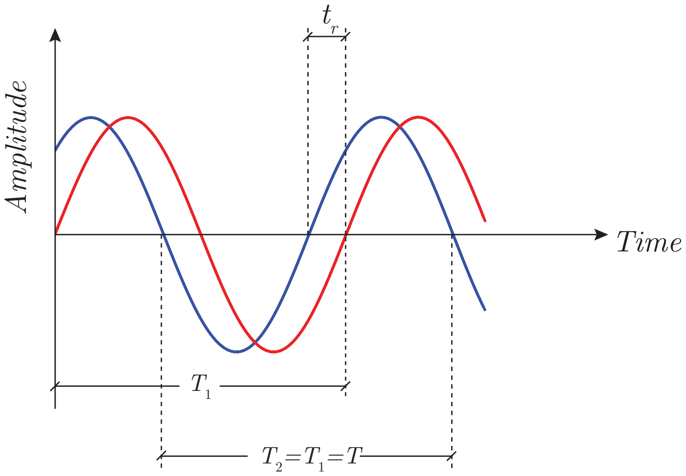

(a)

Figure 6.11: Calculation of the phase angle Φ.

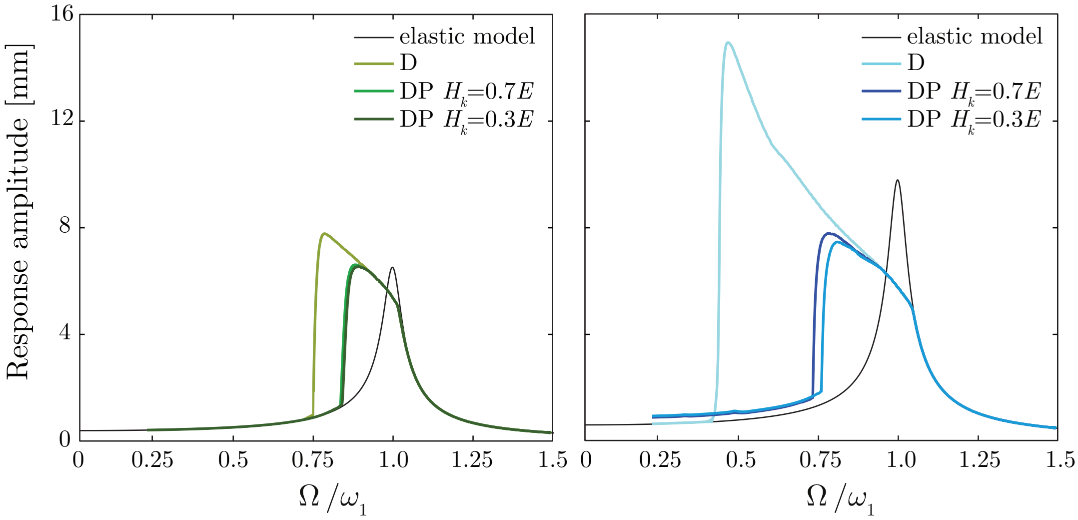

(a) (b)

Figure 6.12: FRCs for sweep 2 and for (a) $U/g = 0.04$ and (b) $U/g = 0.06$, considering elastic, damage and damage-plastic models.

nisms occur and irreversible strains are accumulated, an increase of the dissipated energy appears, which subsequently modifies the resonance condition and the related amplitude. No significant differences arise, in terms of E_d, for the two values set for the hardening parameter H_k in the case of the lower input acceleration amplitude, characterized by a deformation level where plasticity is weakly activated. More evident differences emerge for the higher acceleration input, according to the cyclic load-displacement global curves in Figures 6.6(a) and (b) where an increase of the dissipated energy emerges for the lower hardening value (see effect of H_k also in Figure 4.8).

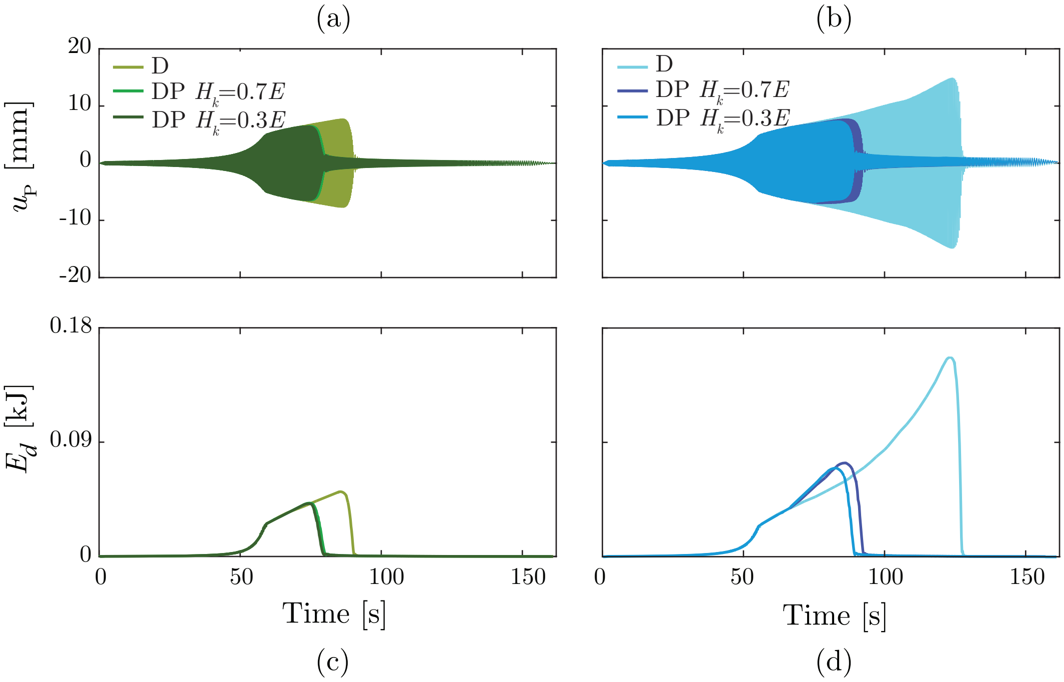

Figure 6.13: Top displacement time histories for sweep 2 and (a) $U/g = 0.04$, (b) $U/g = 0.06$; dissipated energy in each cycle for (c) $U/g = 0.04$ and (d) $U/g = 0.06$.

Finally, effect of the applied acceleration history is explored. To this purpose, wall response is investigated by imposing sine sweep acceleration histories where the forcing frequency Ω is kept constant for 40 cycles and increments $\mathrm{d}\Omega = \pm 0.2\,\mathrm{rad/s}$ are considered for increasing (sweep 1) and decreasing (sweep 2) driving frequency, respectively. Here, only the more significant range $[0.5 \div 1.25]$ is considered for the variation of Ω/ω_1. Figure 6.14 shows the time histories of the selected point P for (a) sweep 1 and (b) sweep 2 with reference to the amplitude excitation $U/g = 0.04$ and damage-plastic model with $H_k = 0.7\,E$. On the overall, similar trends to those in Figures 6.9(b) and 6.10(b) occur, but dis-

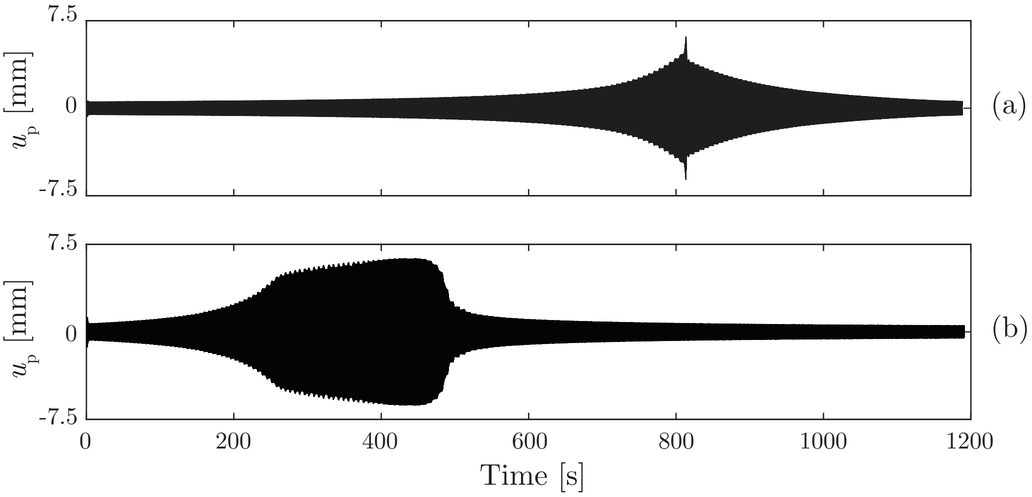

Figure 6.14: Response to sweep histories with excitation frequency 40 cycles constant: time histories of the top relative displacement for (a) sweep 1 and (b) sweep 2, setting $U/g = 0.04$.

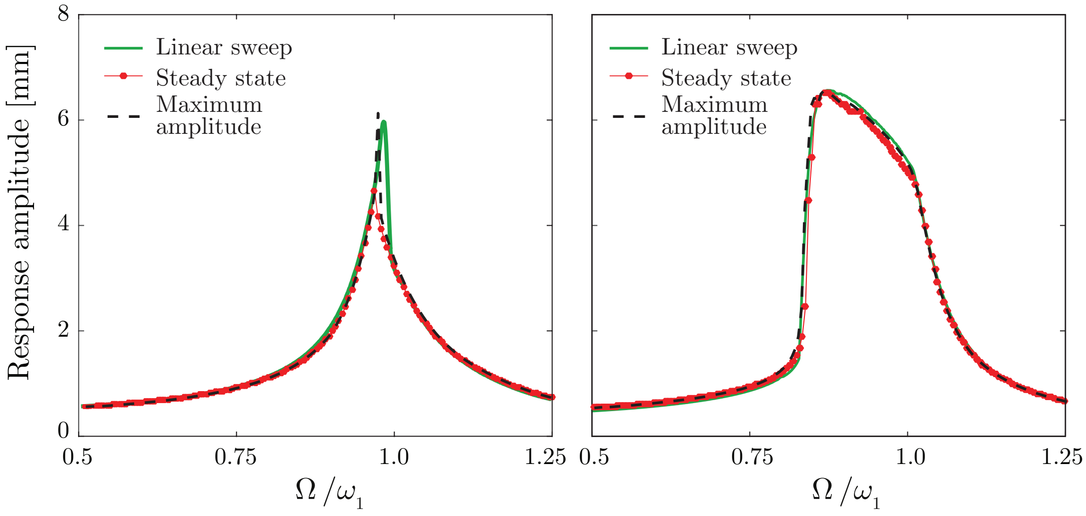

(a)

(b)

Figure 6.15: Comparison between FRCs obtained with different types of sweep histories and for (a) sweep 1 and (b) sweep 2, setting $U/g = 0.04$.

tinction between the maximum response amplitude and the steady state response can be now made. The obtained FRCs are plotted in Figures 6.15(a) and (b): red dot lines refer to steady state response, while black dashed lines correspond to the maximum amplitude response. Furthermore, FRCs above obtained with linear sweep are reported with green solid lines to comparison. In case of sweep 2 (Figure 6.15(b)), no significant differences emerge between the curves. On the contrary, discrepancies are found for sweep 1 (Figure 6.15(a)): the curve derived by the maximum amplitude is close to that obtained by linear sweep and shows a higher peak with respect to that derived by monitoring the steady state response. However, the same overall phenomenon emerges, that is the strong path-dependency characteristic of the response. In fact, in all cases, the FRC for increasing frequency cannot run on the resonant branch obtained for decreasing frequency, as a consequence of the structural damage progression.

6.2.3 Response to earthquake excitations

The effects of nonlinear mechanisms evolution on the wall seismic response are here investigated. Two natural earthquakes are selected: the W-E acceleration component of the 2009 L'Aquila ground motion (Italy) and the N-S component of the ground acceleration recorded at El Centro (California) during the 1940 Imperial Valley earthquake. These signals, whose acceleration time histories are plotted in Figures 6.16(a) and 6.17(a), are characterized by similar peak ground acceleration (PGA) values, that is $0.33\,g$ for L'Aquila and $0.32\,g$ for El Centro, but different frequency content. In fact, as Figures 6.16(b) and 6.17(b) show, the elastic acceleration spectrum of L'Aquila earthquake exhibits a clear maximum value in correspondence of the first elastic period of the panel T_1 (indicated through the dashed red line), whereas widespread peaks appear in the El Centro spectrum, leading to a sort of plateau around T_1.

In what follows, the damage-plastic response of the wall, in terms of top relative displacement of point P (see Figure 6.4(b)) with respect to the base, is evaluated and compared with the corresponding elastic one. Moreover, with the purpose to analyze the influence of the PGA, the natural input signals are scaled to 75%, 100% and 125%.

To monitor the evolution of the damage in the structure, a global damage

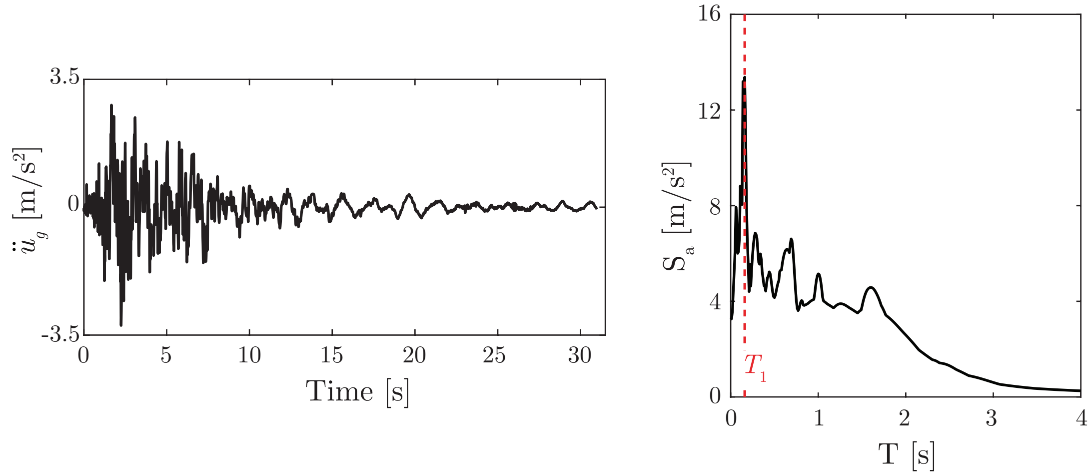

(a) (b)

Figure 6.16: L'Aquila earthquake: (a) acceleration history and (b) elastic response spectrum (damping value 3%).

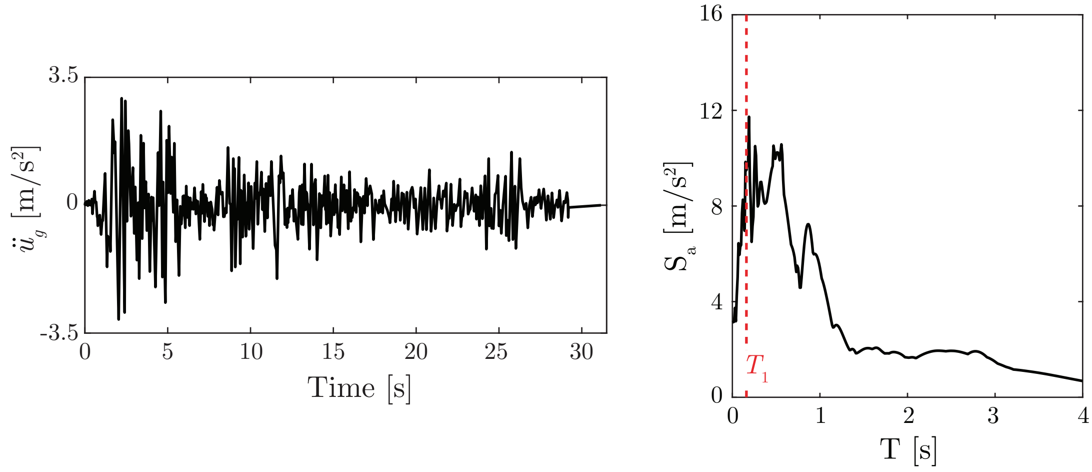

(a) (b)

Figure 6.17: El Centro earthquake: (a) acceleration history and (b) elastic response spectrum (damping value 3%).

variable is also introduced according to Toti et al., 2015, as:

$$D_t^g = \frac{1}{A^d} \int_A D_t \, dA \tag{6.2}$$

where A^d is the damaged area of the structure at the end of the analysis. It should be remarked the difficulty in defining a standard damage index able to give information on the safety level in all possible geometries and boundary conditions. However, despite the introduced measure does not consider the spatial distribution of the damage, it describes the degrading process evolution during loading histories and the damage severity. Ranging from 0 to 1, high values of D_t^g indicate severe tensile damage states. From a computational point of view, the evaluation of D_t^g is fast and simple: it is a weighted average on the damaged area A^d of the local tensile damage D_t defined at each Gauss point.

In Figures 6.18(a), (c) and (e) the wall top displacement time histories are plotted for the adopted values of the scaled L'Aquila earthquake in the significant time interval of the response. On the overall, the displacement amplitudes are reduced with respect to the elastic cases (black lines in Figures 6.18(a), (c) and (e)), as the first frequency of the damaged structure moves away from the range of frequency where the earthquake is more intense. In fact, due to damage progression (see Figure 6.18(g)), a decrease of the first natural frequency occurs, as testified by the Fourier spectra of the elastic and damage-plastic responses shown in Figures 6.18(b), (d) and (f). These point out a dominant peak in correspondence of wall first elastic frequency, that is $f_1 = 6.23\,\mathrm{Hz}$, in case of elastic response, while more spread peaks arise when degrading mechanisms are taken into account, which testify the dependency of the response frequency on the oscillation amplitude.

A different global behavior emerges when the panel is subjected to El Centro ground motion. In this case, the wall experiences a degrading process such that an increase of the amplitude displacement with respect to the elastic response occurs, as Figures 6.19(a), (c) and (e) show. This is due to the coupling of two different phenomena: damage in the structure noticeably reduces the structural stiffness making the panel weaker and, simultaneously, modifies the natural frequencies moving the structure towards a frequency range where the earthquake is still intense. Moreover, as stiffness decay goes together with strength reduction (see the pushover curve in Figure 6.5(a)), the increase of response amplitude is not strictly related to the increase of the PGA, as Figure 6.19(h) emphasizes.

In all the analyzed cases, the panel response is characterized by flexural mechanisms with the formation of damaged zones at the bottom corners of the structure, thus highlighting the dominance of the first vibration mode on the response. The evolution of the global damage index D_t^g in Figures 6.18(g) and 6.19(g) shows that the wall base section becomes strongly damaged, mostly for the higher PGA values. Notwithstanding this severe damage, the panel is able to attain again the initial configuration with some residual displacements due to activation of plastic mechanisms. These latter are clearly visible when the loading history causes non-symmetric response with prevailing positive or negative values of displacement, as in the case of the response depicted in Figure 6.18(c) with blue line.

It can be also noted that, in spite of the steep softening branch of the wall pushover curve (see Figure 6.5(a)), the panel is able to sustain quite high acceleration, as the 125% scaled El Centro and L'Aquila earthquakes correspond to a PGA values of about $0.4\,g$. It emerges that the seismic resistance is not a direct consequence of the maximum static force, but it can be better defined in terms of attained displacements. However, the performed analyses are finalized at evaluating the effect of the degrading mechanisms on the dynamic amplification of the response and are not intended to identify the PGA collapse value. In fact, as experimental tests showed, in such simple structural scheme where the panel is restrained only at the base, once the wall base section becomes fully cracked, the rocking motion occurs, which is not taken into account by the proposed model.

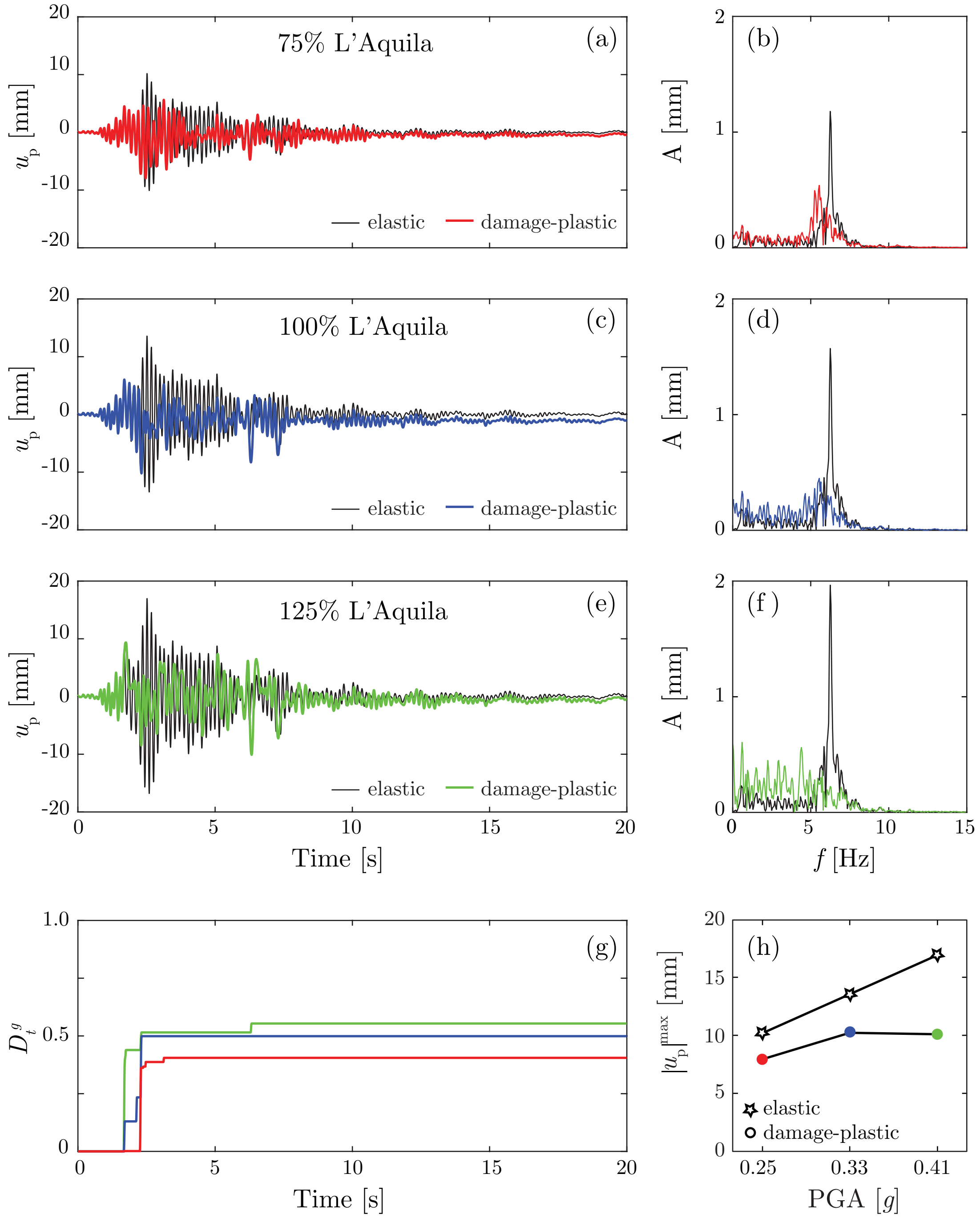

Figure 6.18: L'Aquila earthquake: (a, c, e) response displacement time histories and (b, d, f) their Fourier spectra, (g) evolution of the global damage index, (h) variation of maximum response amplitude versus PGA.

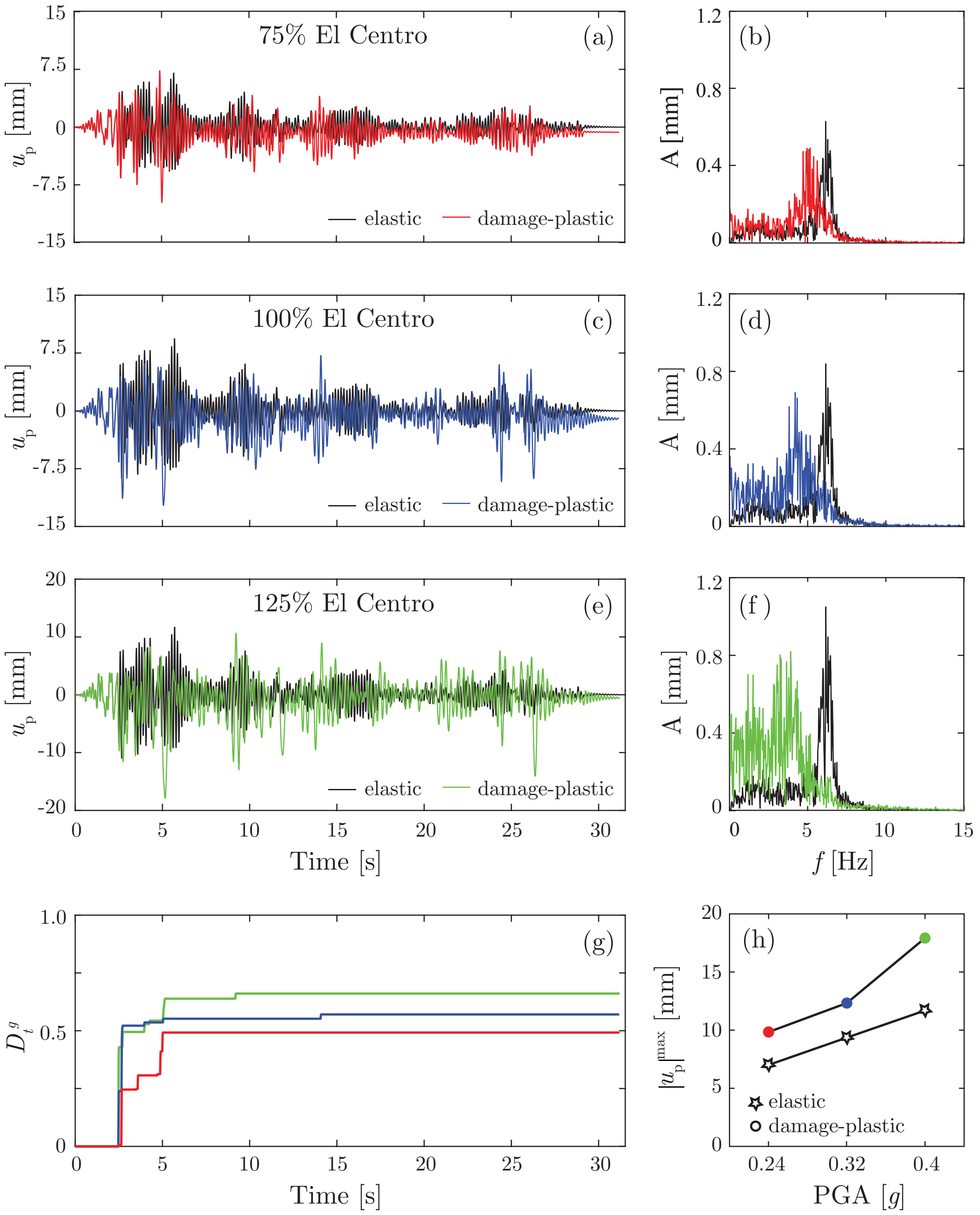

Figure 6.19: El Centro earthquake: (a, c, e) response displacement time histories and (b, d, f) their Fourier spectra, (g) evolution of the global damage index, (h) variation of maximum response amplitude versus PGA.

6.3 Response of tuff masonry walls: experimental test and numerical simulation

Experimental and numerical studies on the out-of-plane dynamic response of tuff masonry walls were performed with the aim of investigating the effects of nonlinear phenomena, such as onset and propagation of microcracks, on walls dynamic response. The experimental test was conducted by using an unidirectional shaking table and considering a simple scheme for walls, rigidly connected to the table at the base and free at the top. Sinusoidal acceleration motions with increasing amplitudes were assigned. Such simple inputs were selected, instead of natural earthquake histories, to better characterize dependency of walls response on the main features of the loading history, such as frequency and amplitude.

In what follows, detailed test description is provided and, then, comparison between numerical and experimental results is presented.

6.3.1 Experimental test

Three specimens, consisting in single leaf walls shown in Figure 6.20, were tested in laboratory of the Department of Structural and Geotechnical Engineering of Sapienza (Italy). These were made of 19 courses of $370 \times 260 \times 110\,\mathrm{mm}^3$ tuff bricks arranged in running bond texture with 10 mm thick natural hydraulic lime mortar joints. With reference to schematic of the specimens in Figure 6.21(a), the overall sizes were $H = 2280\,\mathrm{mm}$, $W = 570\,\mathrm{mm}$ and $t = 260\,\mathrm{mm}$. The brick first row of each panel was clamped in a steel beam C300 (see Figure 6.21(b)) with the interposition of a mortar bed joint and, then, the beam was fixed to the shaking table. Thus, boundary conditions corresponding to fully constrained base were experimentally reproduced.

Firstly, the natural frequencies of the flexural small amplitude vibrations were experimentally determined through the well-known modal analysis technique based on instrumented hammer impact excitation. The hammer impact on the structure represents an impulsive action characterized by a theoretically infinite frequency content, while the structural response provides information about the natural frequencies. Thus, once placed and fixed each wall on the shaking table, accelerometers were set (see Figure 6.21(c)), with the aim of monitoring structural response in terms of accelerations. Figures 6.22(a-c) show Fourier spectra of each impact with black lines and the average curves with blue, red and green lines for the three samples, respectively called M1, M2 and M3 wall. It should be noticed that two resonance peaks occur in the range $[0 \div 80]$ Hz, which represent the first, f_1, and second, f_2, natural frequencies of the out-of-plane flexural modes. Furthermore, the ratio f_2/f_1 confirms that the fully restrained base condition was correctly reproduced, as this approaches to the analytical value of 5.9, evaluated by means of the Timoshenko beam theory (Chui and Smith, 1990). However, small discrepancy emerges between the analytical and experimental ratio f_2/f_1 for M2 wall.

Figure 6.20: Picture of the tested specimens.

Concerning the input motions, sinusoidal accelerations with different amplitudes and frequencies were considered. Hereafter, the most relevant results are presented, corresponding to excitation frequency Ω lower than the wall first natural frequency ω_1, as the resonance frequency decreases, when the degrading processes occur. Table 6.2 contains details about the applied accelerations, all characterized by a ratio $\Omega/\omega_1 = 0.65$. Most of them were characterized by incoming fading cycles to avoid amplified transient responses, while no outgoing fading cycles were considered with the purpose to monitor free vibration characteristics. It is worth underlining that discrepancies between the target inputs and those actually imposed through shaking table were detected, leading to little larger excitation amplitudes. These discrepancies are related to friction force acting in the actuator, asymmetry of the hydraulic cylinder, and so on. Consequently, identification processes, consisting in iterative procedures where the input action is whenever modified on the basis of actually imposed signal, could be needed. This was not possible, as it could have caused undesirable damage in samples due to masonry quasi-brittle behavior. However, the emerged differences were characterized by very high frequencies that did not significantly affect the structural response, making the monitored results suitable at the research aim. As an example, Figure 6.23 shows comparison between the recorded and target input signals for M3 wall.

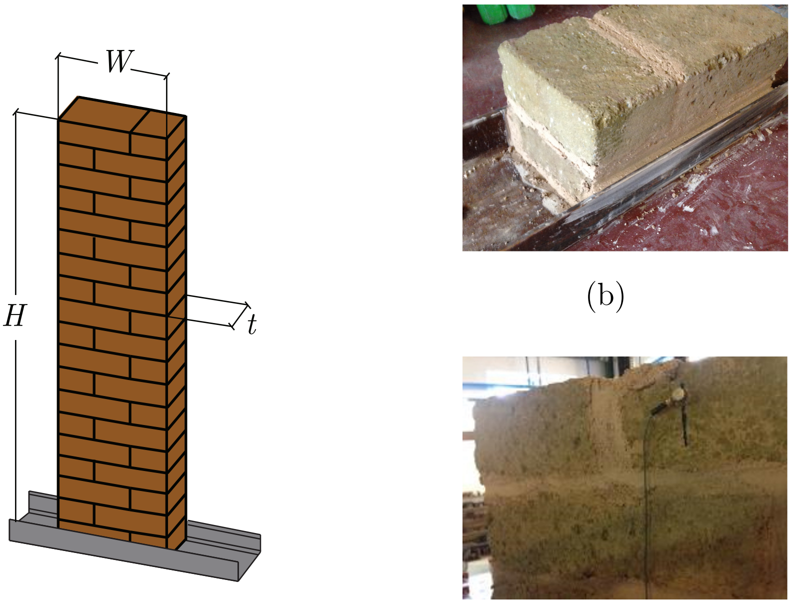

(a)

(b)

(c)

Figure 6.21: Experimental test: (a) schematic of the specimens; (b) base steel beam; (c) accelerometers for the dynamic identification tests.

The out-of-plane dynamic response of walls to the base accelerations listed in Table 6.2, was investigated by measuring acceleration and displacement in the direction of motion. More in details, linear variable displacement transducers

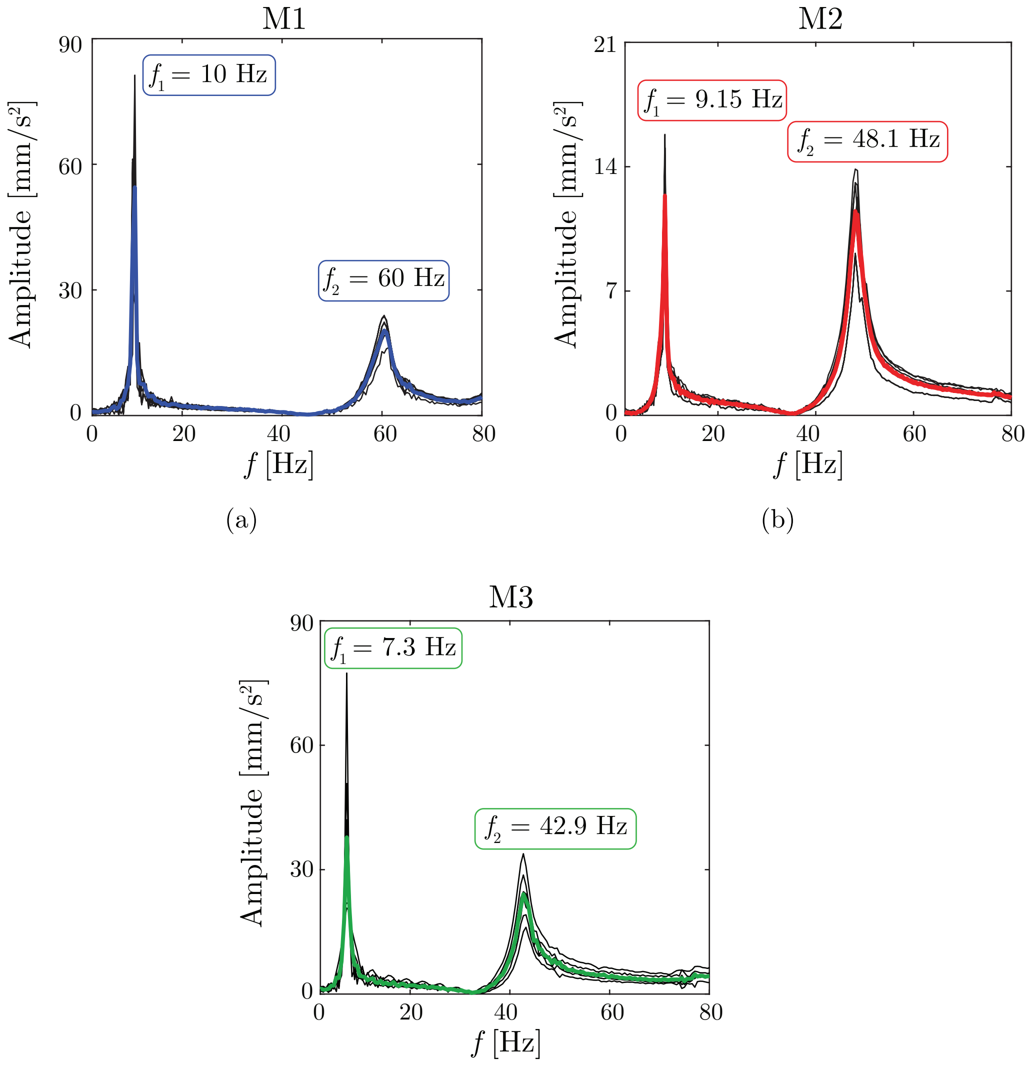

(a)

(b)

(c)

Figure 6.22: Fourier spectra of the acceleration responses to the hammer impacts: (a) M1, (b) M2 and (c) M3 wall.

(LVDTs) were placed: four at the top of both vertical sides of the walls, so as to observe any torsional motions, and one at the shaking table base. Moreover, several accelerometers were set, located as shown in the schematic of experimental set-up in Figure 6.24.

M1 and M2

Run	1	2	3	4	5
Amplitude [mm/s^2]	200	300	500	700	900
Incoming fade in cycle	✓	✓	✓	✓	✓
Outgoing fade in cycle					

M3

Run	1	2a	2b	3	4	5
Amplitude [mm/s^2]	200	300	300	500	700	900
Incoming fade in cycle			✓	✓	✓	✓
Outgoing fade in cycle			✓	✓	✓	✓

Table 6.2: List of the input sinusoidal waves.

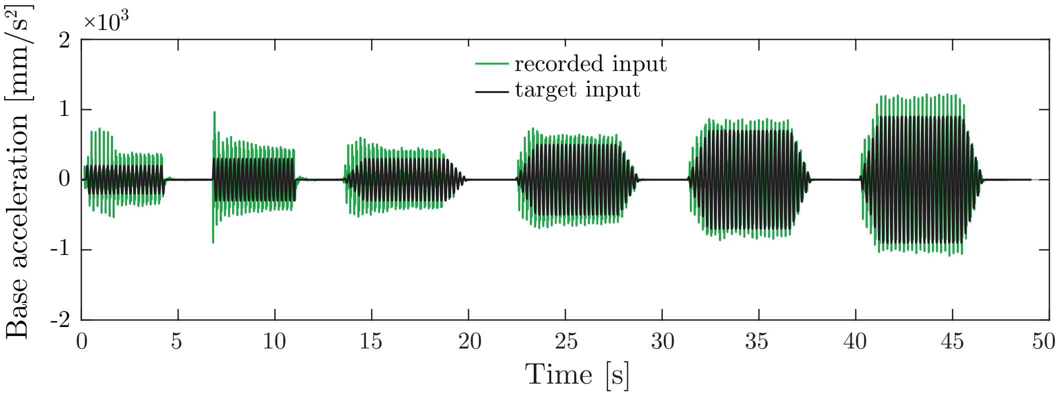

Figure 6.23: Comparison between the recorded and target input signals.

For data acquisition a National Instruments control unit was used, while the elaboration was carried out through the Labview® and Matlab software.

The experimental results, in terms of time histories of wall top relative displacement, are shown in Figure 6.25(a) and Figures 6.26(a) and (b), with reference to M3, M2 and M1 panel, respectively. These highlight that walls structural responses, arranged in sequence according to the imposed input motions in Table 6.2, were strongly affected by nonlinear degrading mechanisms in masonry. Indeed, specimens exhibited degradation of the mechanical properties during the test, causing a relevant modification of their structural response.
As similar behavior was detected for all walls, M3 wall is chosen as representative

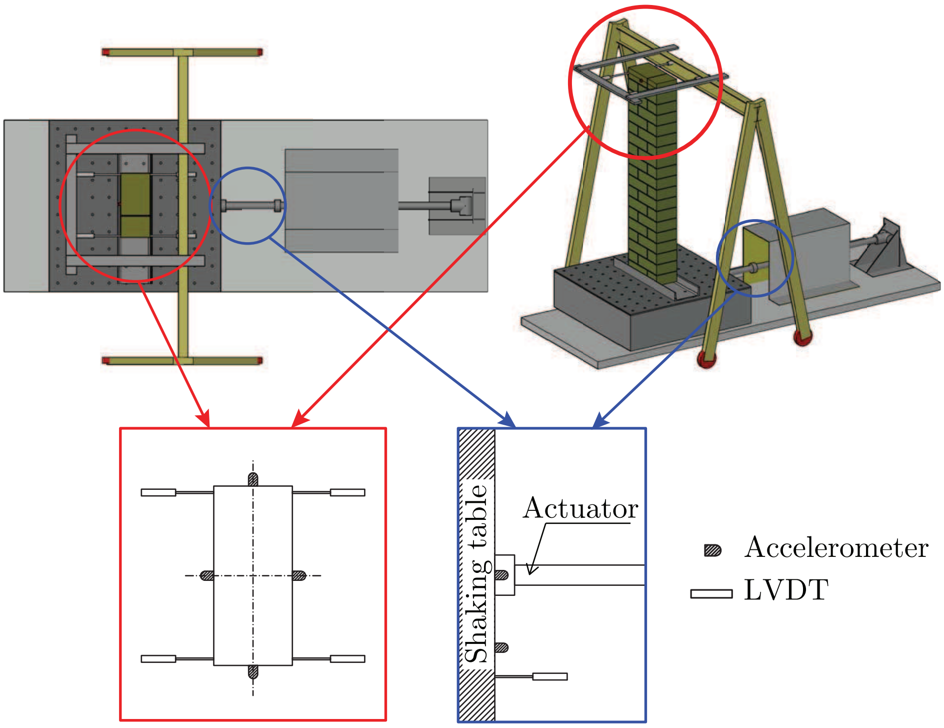

Figure 6.24: Schematic of experimental set-up.

to describe occurred phenomenon and, then, Figure 6.25(a) is reference for what follows. Here, it can be noticed that, as amplitude of applied acceleration was increased, the degrading process evolved and the first natural frequency of the damaged structure approached to the input frequency, moving towards the resonance condition. During Run 3, the wall top displacement showed a progressive slight amplification, while during Run 4 a steep growth, typical of the resonant conditions, occurred. After this, a fairly stable response can be noted, showing that the further variation of the natural frequency during Run 4 distanced the structure from resonance conditions. This is also confirmed in Figure 6.25(b) by the Fourier spectra of the responses, where two main peaks emerge. For all runs, a dominant peak is obtained at the driving frequency along with other peaks representative of the variation of the wall first natural frequency. It is interesting to note how these latter peaks moved from right to left side of the input frequency, by testifying how the structure approached and, then, moved away from the resonant condition. Indeed, the response displacement was in-phase with the applied

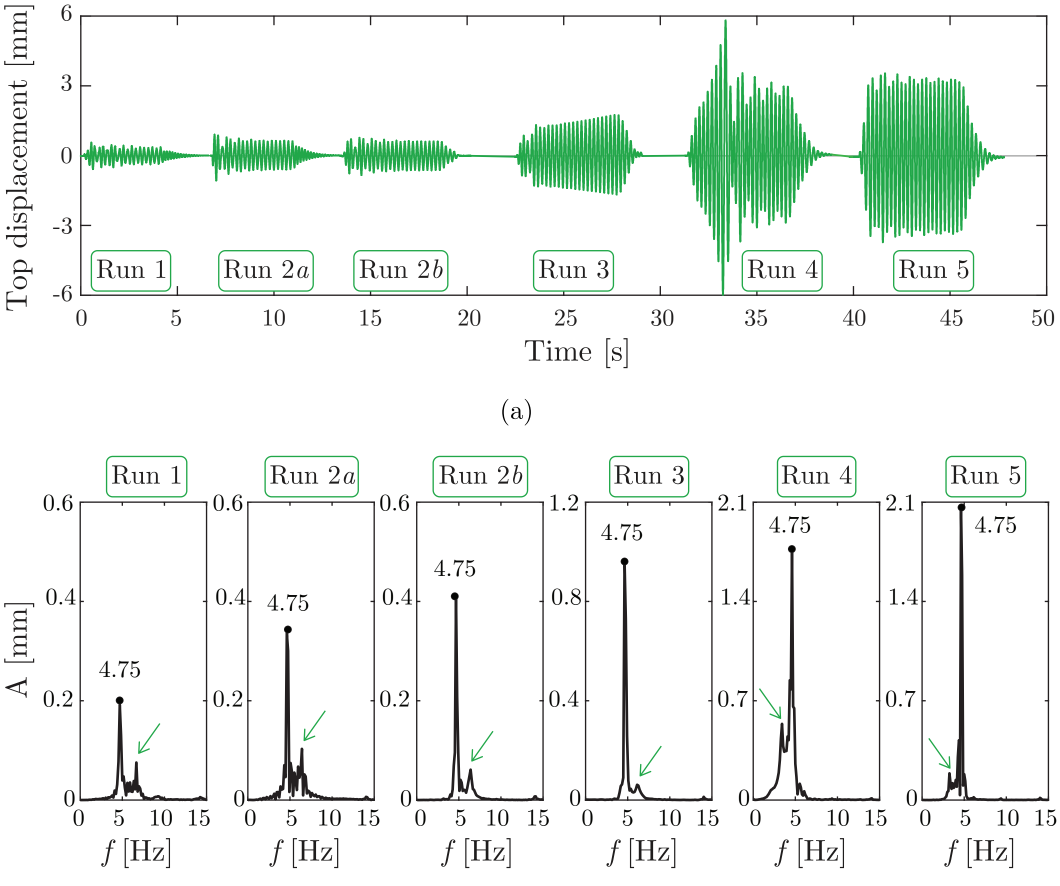

(a)

(b)

Figure 6.25: M3 wall: (a) experimental top displacement response and (b) Fourier spectra of the responses at each run.

sinusoidal force until Run 4, where a phase inversion occurred after the passage through resonance.

Finally, it should be underlined that, as expected, damaging flexural mechanisms located at the wall base were predominant with all damage concentrated in a mortar bed joint near the base, which caused MODE I collapse of masonry.

Similar considerations hold for M2 and M1 walls, for which the passage through resonance seems located in Run 3 and 4, as evident in Figures 6.26(a) and (b), respectively.

For input acceleration amplitudes higher than those analyzed here, large oscillation responses occurred with significant rocking motions of walls. These results are collected and analyzed in Cappelli et al. (2018).

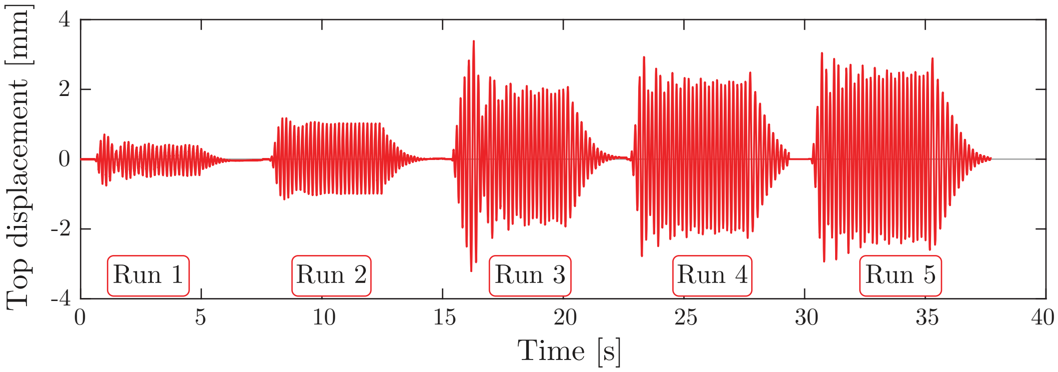

(a)

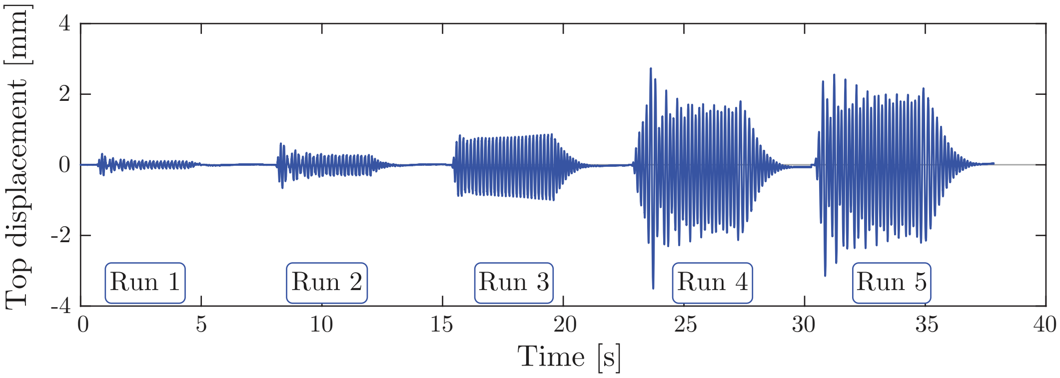

(b)

Figure 6.26: Experimental response of (a) M2 wall and (b) M1 wall.

6.3.2 Experimental-numerical comparison

The experimental outcomes described in previous section are here numerically reproduced by using the damage-plastic model presented in Chapter 4. M3 wall is chosen for numerical and experimental comparison. First, mechanical properties of the homogenized masonry material are computed. Young's modulus is determined through an inverse process on the basis of wall natural frequencies and material mass density. This latter was measured through a load cell, resulting equal to $\rho = 1577\,\mathrm{kg/m^3}$. Some other relevant material properties, such as masonry compressive strength, are derived from previous experimental tests performed on the same masonry material (Marcari et al., 2017). Table 6.3 contains material parameters used for the numerical simulation.

A mesh made of (3 × 26) 9-node quadrilateral FEs is used, setting the nonlocal radius $l_c = 130\,\text{mm}$. A damping ratio of 3% is introduced. The recorded input motions, arranged according to the sequence shown in Figure 6.23 and Table 6.2, are used for the numerical analysis, with the purpose to reproduce the actual pattern of the degrading process.

In Figure 6.27(a) the numerically obtained results are depicted with black line. On the overall, the model is able to describe the main aspects of the wall dynamic response. Indeed, the actual resonance condition and the maximum displacement experienced by the wall are satisfactorily matched. However, the main discrepancy between the experimental and numerical response emerges in Run 3, where the degrading process in the numerical simulation evolves much more slowly than in the experimental response. Indeed, the resonant response starts during Run 3 and ends in Run 4 in the experimental outcomes, whereas this is concentrated in Run 4 as concerns the numerical results.

Elastic parameters

E [MPa]	ν
1300	0.18

Plastic parameters

σ_t [MPa]	σ_c [MPa]	H_k [MPa]
1.5	3.5	0.7 E

Damage parameters

Y_{t0}	b_t	a_t	Y_{c0}	b_c	a_c
1×10^{-5}	3.7×10^{-5}	0.99	1×10^{-3}	4×10^{-3}	0.99

Table 6.3: M3 wall: material parameters.

Furthermore, both numerical and experimental curves show slight differences in the response amplitude between Run 4 and 5, although amplitude of the input signal is increased of 30%. This testifies, once again, that the wall departed from the resonance conditions.

Finally, Figure 6.27(b) shows the tensile damage maps at the end of each run. These are in agreement with the degrading processes observed during the experimental test. During Run 1, no damage occurs in the numerical simulation, despite a slight decay of first natural frequency was experimentally estimated through

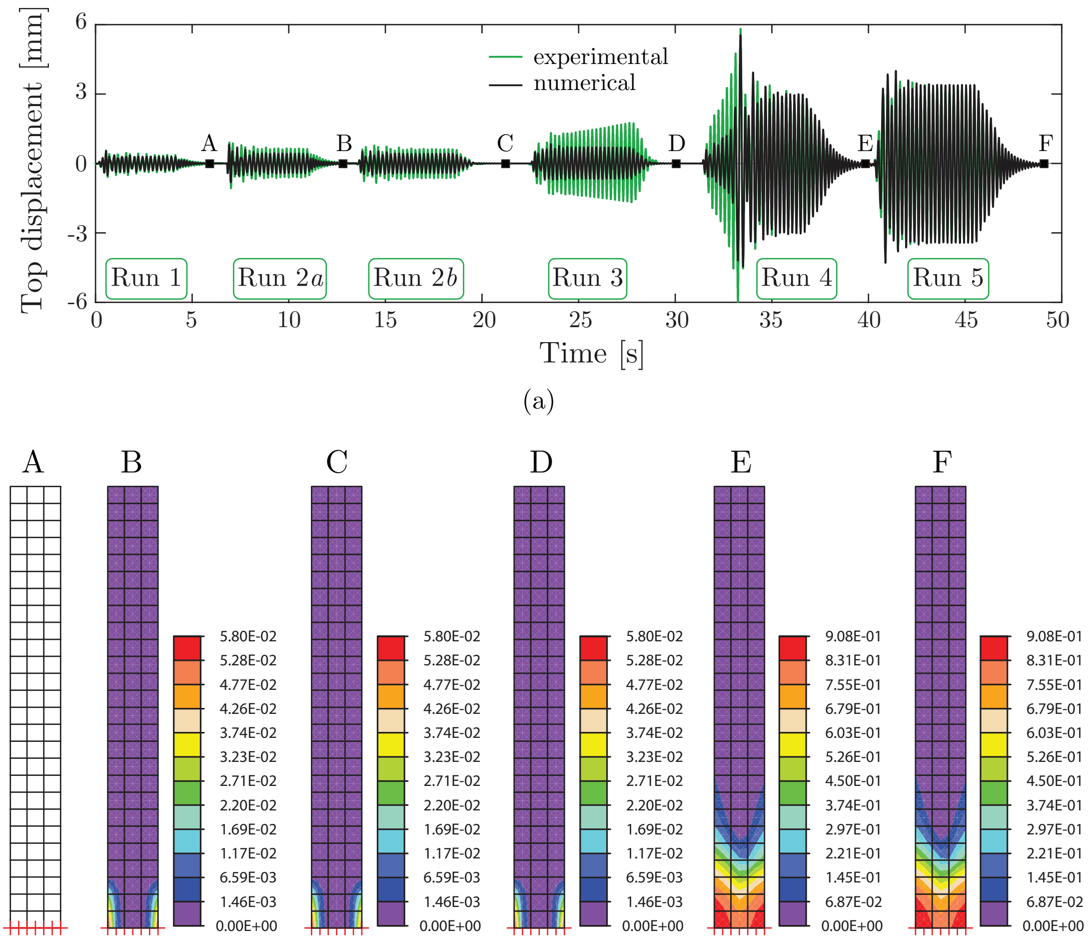

(a)

(b)

Figure 6.27: M3 wall: (a) experimental and numerical top displacement response and (b) tensile damage distribution at the end of each run.

the Fourier spectrum in Figure 6.25(b). However, the displacement responses are overlapped, which means that damaging process has not substantially affected the structural behavior. No increase of damage appears between Run $2a$, $2b$ and 3, as the maximum displacements exhibited by the wall are the same in the numerical simulation. During Run 4, where the wall experiences resonance conditions, the formation of severe damaged zones located at bottom corners of the wall appears, in accordance to the collapse mechanism experimentally occurred.

6.4 Summary

This chapter was devoted to the characterization of dynamic behavior of masonry structural elements. The response of a slender panel, representative of walls of historical buildings and churches loaded out-of-plane, was numerically analyzed. Harmonic base accelerations, with different amplitudes and frequencies, were imposed. It emerged that onset and evolution of the damage substantially change the wall mechanical properties and, then, its natural frequencies decrease. The obtained frequency response curves, exhibiting softening resonance and a peculiar multi-valuedness characteristic, showed the influence of the proposed masonry constitutive relationship with respect to other widely studied models characterized by nonlinear invariant restoring forces. When the structure was subjected to sweep-type horizontal acceleration histories, a different response emerged, depending on the frequency varies from high to low values or vice-versa. In the first case, the evolution of degrading process caused a variation of the wall natural frequency in the same direction of the excitation frequency and, then, the response amplitude increased up to the resonance condition. Conversely, if the excitation frequency ranged from low to high values, the wall suddenly came out from the resonance, as soon as the damage occurred.

The response to earthquake records was also investigated, by showing that the displacement amplitude can be reduced or increased with respect to the elastic case, depending on the evolution of the natural frequencies of the damaged structure, which can approach or move away from the significant earthquake frequencies.

Finally, numerical and experimental studies were performed to analyze dynamic behavior of tuff masonry walls and characterize dependency of their responses on the main properties of the loading history (frequency and amplitude). Both numerical and experimental evidences confirmed that degradation of the mechanical properties strongly modifies the dynamic response, as the variation of walls natural frequencies changes the resonance condition. Indeed, the panels, under sinusoidal acceleration inputs with fixed frequency (lower than the first natural frequency of the specimens) and increasing amplitudes, initially approached to resonance conditions, then, came out when further degradation occurred.

It should be noticed that, once main features of the dynamic response of these structural elements is deeply understood, it could be possible to pursue the goal of a reduced order model to handle complex non-stationary excitations. This can be certainly reached for typologically simple structures, such as the cantilever scheme here considered, but can result harder for less simple boundary conditions and geometries. In these cases it should resort to detailed modeling approaches by accounting for the local nonlinear behavior.

Chapter 7

Conclusive remarks

7.1 Summary and main contributions

The principal goal of this research was the development of macromechanical models to accurately describe the masonry nonlinear behavior. The main difficulties in the formulation of closed-form phenomenological constitutive laws are due to the heterogeneous microstructure of the material, which makes masonry global response strongly affected by shape, sizes and arrangement of blocks and mortar, cohesion and friction between them and their mechanical properties. However, as emphasized in Chapter 2, some recurrent features can be identified, such as non-symmetric response under tensile and compressive loads, strongly nonlinear stress-strain relationship and, in cases of regular texture, the markedly anisotropic behavior. To numerically capture such nonlinear phenomena, the scientific literature proposes several modeling strategies, most of them described in Chapter 3. The choice to adopt phenomenological finite element models is related to their applicability to large scale structures, giving a fair compromise between accuracy and computational cost. Herein, an enriched version of the macromechanical model proposed by Addessi et al. (2002) was presented in Chapter 4. The adopted constitutive relationship involves a new two-parameters isotropic damage model and a Drucker-Prager plasticity formulation, thus accounting for strength-stiffness decay, unilateral effect and hysteretic mechanisms. The model is implemented in a finite element procedure, which adopts a nonlocal integral formulation of the

damage associated variables, being able to provide objective numerical results also in cases of strain-softening response. Moreover, a predictor-corrector procedure, based on the splitting method, is adopted to solve the nonlinear evolution problem of damage and plasticity variables.
Validation examples pointed out the model ability in reproducing the cyclic quasi-static response of experimentally tested masonry panels. Influence of geometry and loading conditions are properly taken into account, as peak loads, energy dissipation, damage distribution, as well as collapse mechanisms satisfactorily matched the experimental outcomes.

Although the simple hypothesis of isotropic behavior is largely accepted for masonry, Chapter 5 moved towards the development of a constitutive model accounting for the variation of the mechanical properties observed for different material directions. The main assumption of the model is the introduction of masonry natural axes, which are parallel and normal to the bed joints direction. An orthotropic description of the elastic and inelastic behavior is considered. Indeed, the scalar representation of damage is replaced by a tensorial description, by defining a proper damage matrix accounting for failure mechanisms due to shear and both compressive and tensile states, normal and parallel to bed joints. A suitable damage criterion is also introduced, which results into a limit surface geometrically defined as the intersection of an ellipsoid and elliptic cone in the space of the damage associated variables. Mesh-dependency drawback is again efficiently overcome by adopting the regularization technique based on the nonlocal formulation. The performed analyses highlighted the model ability in capturing the different strength and stiffness characteristics along the material axes, as well as the influence of the applied stresses with respect to the bed joints orientation.

The proper representation of the nonlinear static response was an essential starting point to move the investigation towards the dynamic field. Thus, Chapter 6 dealt with the characterization of the dynamic behavior of masonry walls, for which a simple structural scheme of constrained base was selected. The choice is due to the weak level of anchorage commonly characterizing the top side of masonry walls in historical buildings. The main aim was to investigate the effects of degrading mechanisms on the dynamic amplification of the response, by adopting a systematic approach based on the evaluation of the frequency response curves. For this purpose sweep-type acceleration histories were selected instead of more complex dynamic excitations (earthquake records), to better identify dependency of wall response on the main properties of the loading history, such as frequency and amplitude. The isotropic damage-plastic model presented in Chapter 4 was chosen to model the wall constitutive behavior, as this accounts for damaging mechanisms and hysteretic dissipation due to the accumulation of irreversible plastic strains. As expected, the studies led to multi-valued frequency response curves characterized by softening behavior, with the backbone curve bent to the left with respect to the corresponding elastic curve. However, a peculiar phenomenon emerged due to the type of nonlinearity. Instead, differently from the invariant restoring force systems, the FRC for increasing driving frequency cannot run on the resonant branch obtained for decreasing frequency, as a consequence of the structural damage progression. Furthermore, the results showed that the coupled effect of damage and plasticity leads to less amplified displacement with respect to the only damage case. Indeed, onset of hysteretic mechanisms and growth of irreversible strains lead to larger hysteretic cycles and, then, to an increased dissipated energy, resulting in a further dissipation effect.

Numerical results were also confirmed by experimental outcomes of shaking table tests performed on tuff masonry walls. The panels, under base sinusoidal acceleration inputs with fixed frequency and increasing amplitudes, exhibited a degradation of mechanical properties, which changed the dynamic structural characteristics. Indeed, when the panels were subjected to an excitation frequency lower than the first natural frequency corresponding to the undamaged state, they approached to the resonance conditions, then, came out when further degradation occurred.

All these nonlinear phenomena led to more complex seismic responses. The performed analyses highlighted that the structural maximum displacement can increase with respect to the elastic case, when the natural frequencies of the damaged structures approach to significant earthquake frequencies. Conversely, a beneficial damage effect can occur with reduced maximum responses.

7.2 Suggests for future work

On the overall, the proposed constitutive models showed to be rather accurate in predicting masonry nonlinear behavior, both in terms of failure mechanisms and force-displacement response curves. Obviously, there is still room for improvements. Most of them deal with the proposed orthotropic damage model because of its higher accuracy paid in terms of formulation complexity. Present and future developments are listed here:

1. Extension of the presented constitutive models and the related FE formulations to the three-dimensional case. This could allow to extend the studies to complex masonry buildings, by properly describing the interaction of in-plane and out-of-plane response of each structural element. This objective can be easily reachable for the proposed isotropic damage-plastic model, as it accounts for the effect of the out-of-plane strain components on the evolution of damaging mechanisms and the adopted plasticity model is already available in its original three-dimensional version. Conversely, it is a challenging task for the orthotropic model, for which further developments would be needed because of its specific in-plane formulation.

2. Research of a simpler analytical formulation of the limit surface for orthotropic damage model, with the aim to make easier the evaluation of the damage variables evolution.

3. Phenomenological introduction of the effects of frictional mechanisms at the interface between bricks and mortar in the orthotropic damage model. To this purpose the Hoffman yield criterion (Hoffman, 1967) could be a suitable option, as it was specifically proposed to model anisotropic behavior as well as the non-symmetric responses under tensile and compressive stress states.

Appendix A

On the construction of the damage limit surface

In Chapter 5 a new orthotropic damage model for the macromechanical analysis of masonry structures was presented. The model requires the introduction of a damage limit surface to rule onset and evolution of damage variables. This surface is geometrically defined, in the damage associated variables space, as the intersection of an ellipsoid with an elliptic cone (see Figure A.1) and only few material properties are required to construct it. In detail, the input parameters represent mechanical properties defined along the material axes, T and N, parallel and normal to the bed joints orientation. These parameters are parallel, Y_{1t0}, and normal, Y_{2t0}, uni-axial tensile thresholds, parallel, Y_{1c0}, and normal, Y_{2c0}, uni-axial compressive thresholds, pure shear, Y_{s0}, threshold and bi-axial compressive, Y_{cc0}, threshold. Some of them can be derived by experimental correlations, if no detailed experimental data are available, as shown in Table A.1. For instance, the compressive strength at load acting parallel to bed joints is, on average, equal to half of the corresponding normal strength (Hoffmann and Schubert, 1994). Similarly, the bi-axial compressive strength results about 1.1-1.2 times the normal uni-axial compressive strength.

Input parameters	
Tensile normal threshold	Y_{2t0}
Compressive normal threshold	Y_{2c0}
Shear threshold	Y_{s0}

Derived input parameters	
Tensile parallel threshold	Y_{1t0}
Compressive parallel threshold	Y_{1c0}
Bi-axial compressive threshold	Y_{cc0}

Table A.1: Material parameters for damage limit surface construction.

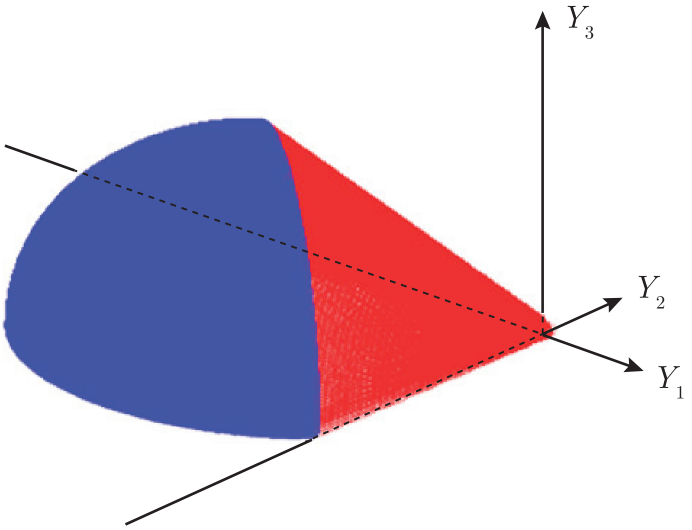

Figure A.1: Damage limit surface in the damage associated variables space.

It should be remarked that some simple manipulations are needed to define the damage thresholds, Y_{1t0}, Y_{2t0}, Y_{1c0}, Y_{2c0}, starting from the stresses, σ_{1t0}, σ_{2t0}, σ_{1c0}, σ_{2c0}, at the onset of damaging process. In case of elastic orthotropic response, uni-axial load parallel to T-axis involves transversal strain ε_N equal to:

$$\varepsilon_N = -\nu_{TN}\varepsilon_T \; , \tag{A.1}$$

while the strain ε_T, caused by uni-axial load parallel to N-axis, is expressed as:

$$\varepsilon_T = -\nu_{NT}\varepsilon_N \; . \tag{A.2}$$

Basing on the above relationships (Eqs. A.1 and A.2), the strains ε_{1c0} and ε_{2c0}, corresponding to σ_{1c0} and σ_{2c0}, under uni-axial compressive stress state, are:

$$\varepsilon_{1c0} = \frac{\sigma_{1c0}}{C_{11} - \nu_{TN} C_{12}} \ , \tag{A.3}$$

$$\varepsilon_{2c0} = \frac{\sigma_{2c0}}{C_{22} - \nu_{NT} C_{21}} \ , \tag{A.4}$$

where C_{ij} (with i=1,2 and j=1,2) are components of the orthotropic elastic constitutive matrix in Eq 5.11. Finally, recalling the definition of the damage associated variables of Eqs. 5.15, the damage thresholds Y_{1c0} and Y_{2c0} are derived as:

$$Y_{1c0} = \varepsilon_{1c0} - \nu_{TN} \nu_{NT} \varepsilon_{1c0} \ , \tag{A.5}$$

$$Y_{2c0} = \varepsilon_{2c0} - \nu_{TN} \nu_{NT} \varepsilon_{2c0} \ . \tag{A.6}$$

It can be noted that Y_{1c0} and Y_{2c0} correspond exactly to ε_{1c0} and ε_{2c0} when $\nu_{TN} = \nu_{NT} = 0$. Similar considerations hold for the damage thresholds in tension, i.e. Y_{1t0} and Y_{2t0}.

In what follows, a detailed description of the damage limit surface construction is provided, based on the input parameters in Table A.1. First, the geometrical parameters of the surface are derived, then, the equations of the elliptic cone and ellipsoid are determined.

A.1 Geometry of the damage surface

To uniquely define the damage surface, the following quantities have to be determined (reference is made to Figures A.2(a) and (b)):

- spatial coordinates of the cone vertex V_T;
- a and b semi-axes of the director ellipse, E, as well as the coordinates of its central point O;
- spatial coordinates of point V_C to determine the ellipsoid c semi-axis.

Points T_N, T_P, C_N, C_P, C_C and C_{N1} are placed on the Y_1-Y_2 plane (Figure A.3(a)), concordantly to the input parameters in Table A.1. Then, the straight

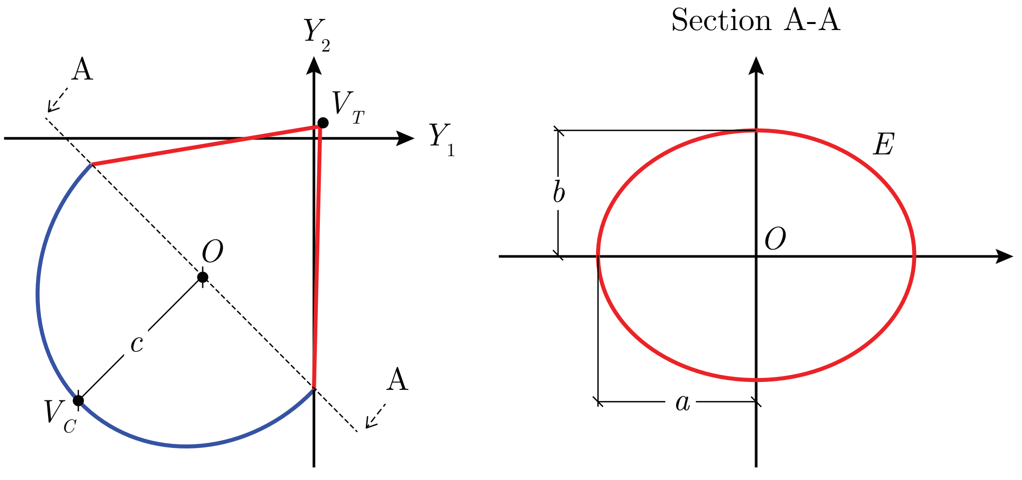

(a) (b)

Figure A.2: Damage limit surface: (a) projection on the Y_1-Y_2 plane and (b) director ellipse.

lines r and s are obtained by jointing T_N-C_P and T_P-C_N points, respectively. The intersection of r and s provides vertex V_T of the elliptic cone, as shown in Figure A.3(b). Semi-axis a of the director ellipse is determined as half distance between point C_N and D, with point D given by intersection of r with the line q joining points C_{N1} and C_N. Simple geometric construction allows also to determine location of the central point O of the ellipse (Figure A.3(b)). Regarding V_C point position, it results from intersection of the perpendicular line to q in O and the parallel line to Y_1-axis and passing for C_C. Furthermore, distance between V_C and O furnishes the c semi-axis of the ellipsoid (Figure A.3(c)). Finally, the b semi-axis of the director ellipse can be determined on the basis of the researched shear threshold Y_{s0}. This is done by considering point H in Figure A.3(d), which is defined by the intersection of q and t (this latter obtained by joining V_T with origin of the coordinate system) lines. Thus, with reference to the cross section B-B sketched in Figure A.3(e), the Y_3-coordinate (h) of the $\widetilde{H}$ point, belonging to the reached director ellipse E, is found by imposing the following relationship:

$$h : |HV_T| = Y_{s0} : d \, , \tag{A.7}$$

where d denotes distance between V_T and origin of the reference system. Once the h quantity is known, the b semi-axis can be determined by satisfying the belonging of $\widetilde{H}$ point to the ellipse E (see Figure A.3(f)).

A.2 Derivation of elliptic cone equation

In the following, the (Y_1, Y_2, Y_3) axes are denoted as (x, y, z) for sake of simplicity. The parametric equation of an ellipse $\widetilde{E}$ (see Figure A.4), lying on a plane parallel to the y-z plane, is written as:

$$\widetilde{E} = \begin{cases} x = x_0 \\ y(\theta) = y_0 + a\cos(\theta) \qquad \theta = [0, 2\pi] \ . \\ z(\theta) = z_0 + b\sin(\theta) \end{cases} \tag{A.8}$$

The center of the ellipse O (whose spatial coordinates are known as a consequence of the previous section):

$$O = (x_0, y_0, z_0) \tag{A.9}$$

and the generic point P:

$$P = (x, y(\theta), z(\theta)) \ , \tag{A.10}$$

identify the vector $\mathbf{e}$:

$$\mathbf{e}(\theta) = P - O = \begin{bmatrix} 0 \\ a\cos(\theta) \\ b\sin(\theta) \end{bmatrix} . \tag{A.11}$$

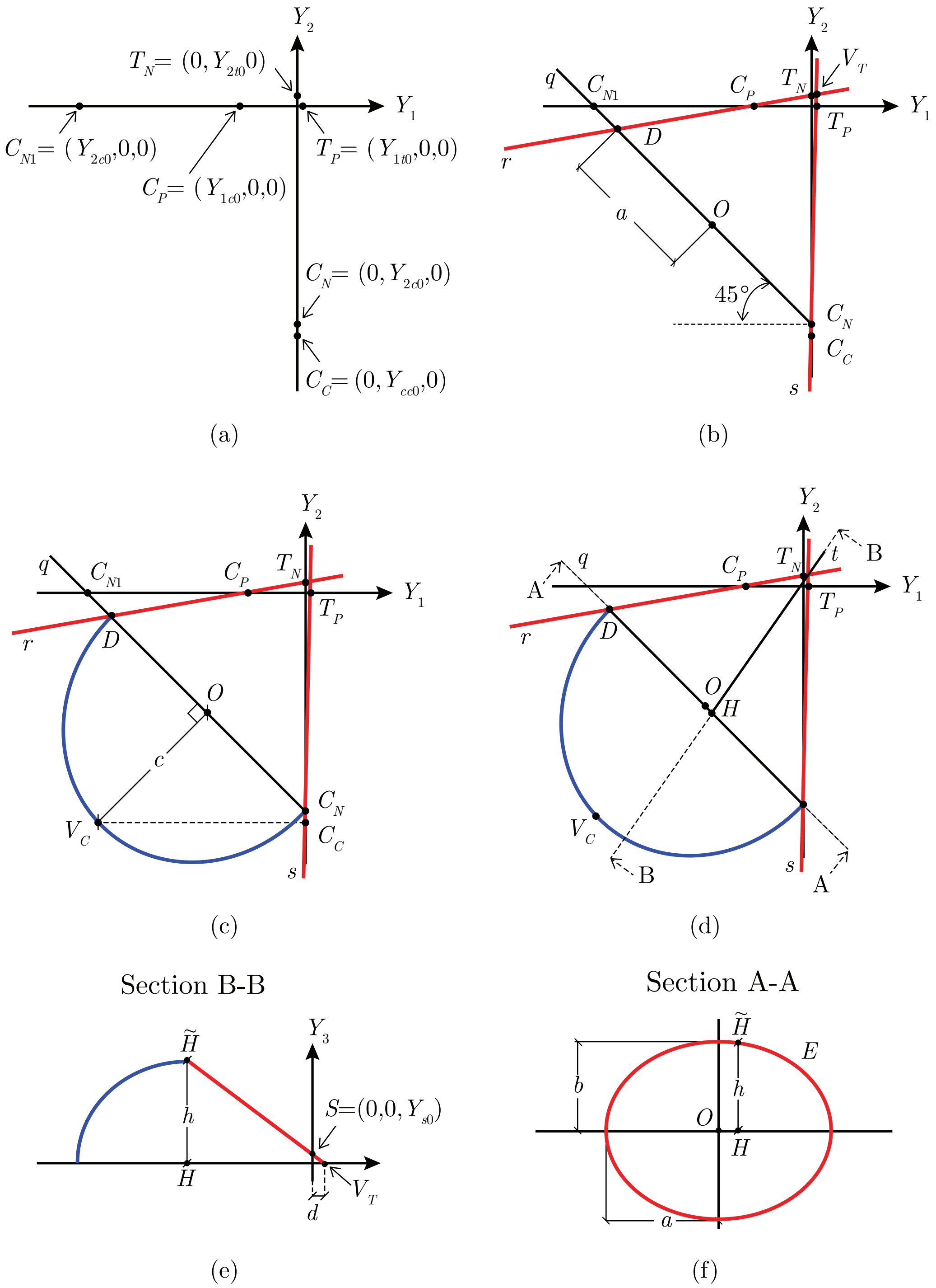

Figure A.3: Construction phases of the damage surface.

Furthemore, by defining the rotation matrix $\mathbf{Q}_z(\varphi)$ around the z axis:

$$\mathbf{Q}_z(\varphi) = \begin{bmatrix} \cos(\varphi) & -\sin(\varphi) & 0 \\ \sin(\varphi) & \cos(\varphi) & 0 \\ 0 & 0 & 1 \end{bmatrix}, \tag{A.12}$$

vector $\mathbf{r}$ can be obtained as:

$$\mathbf{r}(\varphi, \theta) = \mathbf{Q}_z(\varphi)\mathbf{e}(\theta) = \begin{bmatrix} -a\sin(\varphi)\cos(\theta) \\ a\cos(\varphi)\cos(\theta) \\ b\sin(\theta) \end{bmatrix}. \tag{A.13}$$

It should be noticed that the rotation angle φ is set equal to 45°, concordantly to the construction phase in Figure A.3(b). The generic point P, belonging to the rotated ellipse E of Figures A.2(b) and A.4, can be determined as:

$$P(\varphi, \theta) = O + \mathbf{r}(\varphi, \theta) = \begin{bmatrix} x_0 \\ y_0 \\ z_0 \end{bmatrix} + \begin{bmatrix} -a\sin(\varphi)\cos(\theta) \\ a\cos(\varphi)\cos(\theta) \\ b\sin(\theta) \end{bmatrix}. \tag{A.14}$$

On the basis of coordinates of the vertex V_T=(x_V, y_V, z_V), the vector $\mathbf{v}$ is obtained:

$$\mathbf{v}(\varphi, \theta) = P(\varphi, \theta) - V_T = \begin{bmatrix} x_0 \\ y_0 \\ z_0 \end{bmatrix} + \begin{bmatrix} -a\sin(\varphi)\cos(\theta) \\ a\cos(\varphi)\cos(\theta) \\ b\sin(\theta) \end{bmatrix} - \begin{bmatrix} x_V \\ y_V \\ z_V \end{bmatrix}. \tag{A.15}$$

Vector $\mathbf{v}$ can generate each point C of the elliptic cone, which satisfies the following relationship:

$$C(\kappa, \varphi, \theta) = V_T + \kappa\mathbf{v}(\varphi, \theta) \qquad \kappa \in \mathbb{R}^+ \tag{A.16}$$

Finally, the generic generatrix line g of the cone is described by the following vectorial equation:

$$g = \left\{P = V_T + \kappa\mathbf{v}, \kappa \in \mathbb{R}^+\right\}. \tag{A.17}$$

Therefore, a point $S = (x, y, z)$ belongs to the elliptic cone if:

$$S = C(\kappa, \varphi, \theta). \tag{A.18}$$

By explaining previous equations, the following equation system is obtained:

$$\begin{cases} x - x_V - \kappa(x_0 - a\cos\theta\sin\varphi - x_V) = 0 \\ y - y_V - \kappa(y_0 + a\cos\theta\cos\varphi - y_V) = 0 \\ z - z_V - \kappa(z_0 + b\sin\theta - z_V) = 0 \end{cases} \tag{A.19}$$

After some simple manipulations of Eqs. A.19, the cartesian form of the elliptic cone equation can be derived and used in the finite element code.

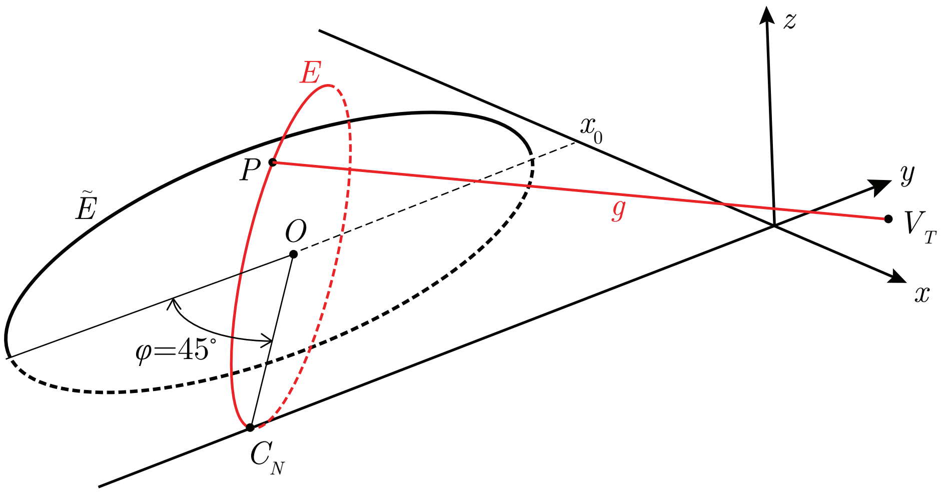

Figure A.4: Graphical representation of elliptic cone construction.

A.3 Derivation of ellipsoid equation

The cartesian equation of an ellipsoid centered in the cartesian coordinate system $oxyz$ is written as:

$$\frac{x^2}{a^2} + \frac{y^2}{c^2} + \frac{z^2}{b^2} = 1, \tag{A.20}$$

where a, b and c represent the ellipsoid semi-axes (see Figure A.5(a)). Translation and rotation of this surface allows to obtain equation of researched ellipsoid. The following transformation is introduced:

$$\begin{aligned} x &= \cos\varphi(X - x_0) - \sin\varphi(Y - y_0), \\ y &= \sin\varphi(X - x_0) + \cos\varphi(Y - y_0), \end{aligned} \tag{A.21}$$

where $(x_0,\ y_0,\ z_0)$ are the coordinates of central point O of the director ellipse E and φ is set equal to -45°, according to Figure A.3. By replacing Eqs. A.21 in Eq. A.20 and by considering a, b, c values determined in Section A.1, the researched ellipsoid equation is derived.

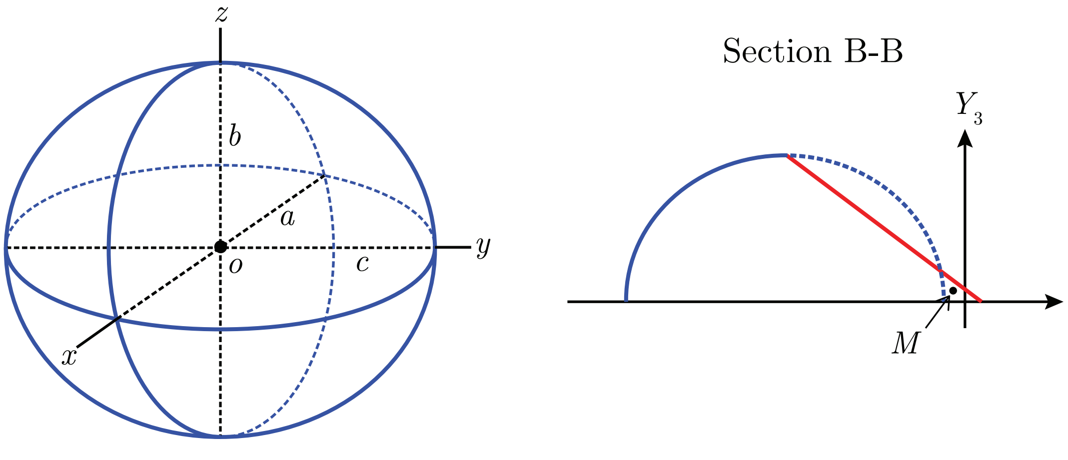

(a)

(b)

Figure A.5: (a) Ellipsoid centered in the cartesian axes system $oxyz$; (b) material point M inside the limit surface.

A.4 Conclusive remarks

This appendix showed that the damage surface definition is ruled by simple geometric construction phases, which involve control points with physical meaning. Indeed, only mechanical properties along masonry material axes are required to construct the surface. Cartesian equations of the elliptic cone and ellipsoid were also derived. On the basis of these equations, a MATLAB code (which is not shown here) was designed to automatically generate the surface equation when material parameters change is considered.

Finally, to underline a common drawback, an example case is sketched in Figure A.5(b). Here, material point M lies inside the surface, despite this is outside the ellipsoid. Consequently, this point represents a material state where no damage evolution occurs. Thus, attention should be paid in the finite element code implementation to establish if a material point lies inside the surface.

Bibliography

Abrams, D.P., AlShawa, O., Lourenço, P.B., Sorrentino, L., 2017. Out-of-plane seismic response of unreinforced masonry walls: conceptual discussion, research needs, and modeling issues. International Journal of Architectural Heritage 11, 22–30.

Acary, V., Jean, M., 1998. Numerical simulation of monuments by the contact dynamics method, in: Monument-98, Workshop on seismic perfomance of monuments. Lisbon, Portugal, pp. 69–78.

Addessi, D., 2014. A 2D Cosserat finite element based on a damage-plastic model for brittle materials. Computers and Structures 135, 20–31.

Addessi, D., Liberatore, D., Masiani, R., 2015. Force-based beam finite element (FE) for the pushover analysis of masonry buildings. International Journal of Architectural Heritage 9, 231–243.

Addessi, D., Marfia, S., Sacco, E., 2002. A plastic nonlocal damage model. Computer Methods in Applied Mechanics and Engineering 191, 1291–1310.

Addessi, D., Marfia, S., Sacco, E., Toti, J., 2014. Modeling approaches for masonry structures. The Open Civil Engineering Journal 8, 288–300.

Addessi, D., Sacco, E., 2012. A multi-scale enriched model for the analysis of masonry panels. International Journal of Solids and Structures 49, 865–880.

Addessi, D., Sacco, E., 2014. A kinematic enriched plane state formulation for the analysis of masonry panels. European Journal of Mechanics A/Solids 44, 188–200.

Alexandris, A., Protopapa, E., Psycharis, I., 2004. Collapse mechanisms of masonry buildings derived by the distinct element method, in: 13th World Conference on Earthquake Engineering. Vancouver, B.C., Canada.

AlShawa, O., de Felice, G., Mauro, A., Sorrentino, L., 2012. Out-of-plane seismic behaviour of rocking masonry walls. Earthquake Engineering and Structural Dynamics 41, 949–968.

Alshebani, M.M., Sinha, S.N., 2000. Stress-strain characteristics of brick masonry under cyclic biaxial compression. Journal of Structural Engineering 126, 1004–1007.

Anthoine, A., Magonette, G., Magenes, G., 1995. Shear-compression testing and analysis of brick masonry walls, in: Proceedings of the 10th European Conference on Earthquake Engineering, pp. 1657–1662.

Atkinson, R.H., Amadei, B.P., Saeb, S., Sture, S., 1989. Response of masonry bed joints in direct shear. Journal of Structural Engineering 115, 2276–2296.

Backes, H.P., 1985. On the behavior of masonry under tension in the direction of the bed joints. Aachen University of Technology. Ph.D. thesis.

Baggio, C., Trovalusci, P., 2000. Collapse behaviour of three-dimensional brick-block systems using non-linear programming. Structural Engineering and Mechanics 10, 181–195.

Benedetti, D., Carydis, P., Pezzoli, P., 1998. Shaking table tests on 24 simple masonry buildings. Earthquake Engineering and Structural Dynamics 27, 67–90.

Berto, L., Saetta, A., Scotta, R., Vitaliani, R., 2002. An orthotropic damage model for masonry structures. International Journal for Numerical Methods in Engineering 55, 127–157.

Betti, M., Vignoli, A., 2011. Numerical assessment of the static and seismic behaviour of the basilica of Santa Maria all'Impruneta (Italy). Construction and Building Materials 25, 4308–4324.

Binda, L., Mirabella Roberti, G., Tiraboschi, C., 1996. Problemi di misura dei parametri meccanici della muratura e dei suoi componenti, in: La meccanica della muratura tra teoria e progetto, Messina, pp. 45–54.

Braga, F., Liberatore, D., 1990. A finite element for the analysis of the response of masonry buildings under seismic actions, in: Proceedings of the 5th North American masonry conference. Urbana, IL: University of Illinois at Urbana-Champaign.

Brencich, A., Gambarotta, L., Lagomarsino, S., 1998. A macroelement approach to the three-dimensional seismic analysis of masonry buildings, in: 11th European Conference on Earthquake Engineering, Bisch, P., Labbè, P., Pecker, A. (eds). Balkema, Rotterdam.

Caliò, I., Marletta, M., Pantò, B., 2012. A new discrete element model for the evaluation of the seismic behaviour of unreinforced masonry buildings. Eng. Struct. 40, 327–338.

Candeias, P.X., Campos Costa, A., Mendes, N., Costa, A.A., Lourenço, P.B., 2017. Experimental assessment of the out-of-plane performance of masonry buildings through shaking table tests. International Journal of Architectural Heritage 11, 31–58.

Capecchi, D., Vestroni, F., 1985. Steady-state dynamic analysis of hysteretic systems. Journal of Engineering Mechanics 111, 1515–1531.

Capecchi, D., Vestroni, F., 1990. Periodic response of a class of hysteretic oscillators. International Journal of Non-Linear Mechanics 25, 309–317.

Cappelli, E., Di Egidio, A., Vestroni, F., 2018. Rocking of masonry wall: analysis and experiments, in: 16th European Conference on Earthquake Engineering.

Carocci, C.F., 2001. Guidelines for the safety and preservation of historical centres in seismic areas, in: Historical Constructions, Lourenço, P.B., Roca, P., (eds), pp. 145–165.

Casini, P., Vestroni, F., 2018. Nonlinear resonances of hysteretic oscillators. Acta Mechanica 229, 939–952.

Casolo, S., 2006. Macroscopic modelling of structured materials: relationship between orthotropic Cosserat continuum and rigid elements. International Journal of Solids and Structures 43, 475–496.

Cavaleri, L., Papia, M., Macaluso, G., Di Trapani, F., Colajanni, P., 2014. Definition of diagonal Poisson's ratio and elastic modulus for infill masonry walls. Materials and Structures 47, 239–262.

Chen, S.Y., Moon, F.L., Yi, T., 2008. A macroelement for the nonlinear analysis of in-plane unreinforced masonry piers. Engineering Structures 30, 2242–2252.

Chow, C.L., Wang, J., 1987. An anisotropic theory of elasticity for continuum damage mechanics. International Journal of Fracture 33, 3–16.

Chui, Y.H., Smith, I., 1990. Influence of rotatory inertia, shear deformation and support condition on natural frequencies of wooden beams. Wood Science and Technology 24, 233–245.

Comi, C., Perego, U., 2001. Fracture energy based bi-dissipative damage model for concrete. International Journal of Solids and Structures 38, 6427–6454.

Cordebois, J.P., Sidoroff, F., 1982. Endommagement anisotrope en élasticité et plasticité. Journal de Mécanique Théorique et Appliquée, Numéro spécial , 45–60.

Cundall, P.A., 1971. A computer model for simulating progressive, large-scale movement in blocky rock system, in: Proceedings of the Symposium of the International Society for Rock Mechanics, France, II-8.

De Bellis, M.L., 2009. A Cosserat based multi-scale technique for masonry structures. Sapienza University of Rome, Italy. Ph.D. thesis.

De Bellis, M.L., Addessi, D., 2011. A Cosserat based multi-scale model for masonry structures. International Journal for Multiscale Computational Engineering 9, 543–563.

Dhanasekar, M., Page, A.W., Kleeman, P.W., 1985. The failure of brick masonry under biaxial stresses. Proceedings of the Institution of Civil Engineers 79, 295–313.

Drucker, D., 1954. Coulomb friction, plasticity and plastic analysis of limit loads. Journal of Applied Mechanics 21, 71–74.

Drysdale, R.G., Hamid, A.A., 1982. Anisotropic tensile strength characteristics of brick masonry, in: 6th International Brick Masonry Conference, pp. 143–153.

Drysdale, R.G., Vanderkeyl, R., Hamid, A.A., 1979. Shear strength of brick masonry joints, in: 5th Internatinal Brick Masonry Conference, pp. 106–113.

Dvorak, G.J., 1992. Transformation field analysis of inelastic composite materials, in: Proceedings of the Royal Society of London. Series A, pp. 311–327.

Fichant, S., La Borderie, C., Pijaudier-Cabot, G., 1999. Isotropic and anisotropic descriptions of damage in concrete structures. Mechanics of Cohesive-frictional Materials 4, 339–359.

Frumento, S., Magenes, G., Morandi, P., Calvi, G.M., 2009. Interpretation of experimental shear tests on clay brick masonry walls and evaluation of q-factors for seismic design. Technical report, IUSS PRESS, Pavia, Italy.

Gambarotta, L., Lagomarsino, S., 1997. Damage models for the seismic response of brick masonry shear walls. Part I: the mortar joint model and its applications. Earthquake Engineering and Structural Dynamics 26, 423–439.

Ganz, H.R., Thürlimann, B., 1982. Tests on the biaxial strength of masonry. Rep. No. 7502-3, Institute of Structural Engineering, Zurich .

Gattulli, V., Antonacci, E., Vestroni, F., 2013. Field observations and failure analysis of the Basilica S. Maria di Collemaggio after the 2009 L'Aquila earthquake. Engineering Failure Analysis 34, 715–734.

Ghrib, F., Tinawi, R., 1995. Nonlinear behavior of concrete dams using damage mechanics. Journal of Engineering Mechanics 121, 513–527.

Gilbert, M., Casapulla, C., Ahmed, H.M., 2006. Limit analysis of masonry block structures with non-associative frictional joints using linear programming. Computers and Structures 84, 873–887.

Giuffrè, A., 1994. Seismic safety and strengthening of historical buildings and urban fabrics, in: Proceedings of the 10th World Conference on Earthquake Engineering, pp. 6583–6596.

Griffith, M.C., Lam, N.T.K., Wilson, J.L., Doherty, K., 2004. Experimental investigation of unreinforced brick masonry walls in flexure. Journal of Structural Engineering 130, 423–432.

Griffith, M.C., Vaculik, J., Lam, N.T.K., Wilson, J., Lumantarna, E., 2007. Cyclic testing of unreinforced masonry walls in two-way bending. Earthquake Engineering and Structural Dynamics 36, 801–821.

Heyman, J., 1982. The masonry arch.

Hilsdorf, H.K., 1969. Investigation into the failure mechanism of brick masonry loaded in axial compression. Designing engineering and constructing with masonry products , 34–41.

Hoffman, O., 1967. The brittle strength of orthotropic materials. Journal of Composite Materials 1, 200–206.

Hoffmann, G., Schubert, P., 1994. Compressive strength of masonry parallel to the bed joints, in: 10th International Brick and Block Masonry Conference, Shrive, N.G. and Huizer, A. (eds). University of Calgary, Canada, pp. 1453–1462.

Iwan, W.D., 1965. The steady-state response of the double bilinear hysteretic model. Journal of Applied Mechanics 32, 921–925.

Kachanov, L.M., 1958. Time of the rupture process under creep conditions, Izy. Akad. Nank. SSR,. Otd. Tech. Nauk. 8, 26–31.

Karapitta, L., Mouzakis, H., Carydis, P., 2011. Explicit finite-element analysis for the in-plane cyclic behavior of unreinforced masonry structures. Earthquake Engineering and Structural Dynamics 40, 175–193.

Kaushik, H.B., Rai, D.C., Jain, S.K., 2007. Stress-strain characteristics of clay brick masonry under uniaxial compression. Journal of Materials in Civil Engineering 19, 728–739.

Kouznetsova, V.G., 2002. Computational homogenization for the multi-scale analysis of multi-phase materials. Technische Universiteit Eindhoven. Ph.D. thesis.

Lacarbonara, W., 2013. Nonlinear structural mechanics: theory, dynamical phenomena and modeling. Springer, New York.

Lacarbonara, W., Vestroni, F., 2003. Nonclassical responses of oscillators with hysteresis. Nonlinear Dynamics 32, 235–258.

Lagomarsino, S., Penna, A., Galasco, A., Cattari, S., 2013. TREMURI program: an equivalent frame model for the nonlinear seismic analysis of masonry buildings. Engineering Structures 56, 1787–1799.

Lapczyk, I., Hurtado, J.A., 2007. Progressive damage modeling in fiber-reinforced materials. Composites: Part A 38, 2333–2341.

Lee, J., Fenves, G.L., 1998. Plastic-damage model for cyclic loading of concrete structures. Journal of Engineering Mechanics 124, 892–900.

Lemaitre, J., 1985. A continuous damage mechanics model for ductile fracture. Journal of Engineering Materials and Technology 107, 83–89.

Lemos, J.V., 2007. Discrete element modeling of masonry structures. International Journal of Architectural Heritage 1, 190–213.

Liberatore, D., Addessi, D., Sangirardi, M., 2017. A force-based macroelement for the nonlinear dynamic analysis of masonry buildings, in: 23rd Conference AIMETA, Ascione, L., Berardi, V., Feo, L., Fraternali, F., Tralli, A. M. (eds). Salerno, Italy, pp. 1368–1378.

Lishak, V.I., Yagust, V.I., Yankelevsky, D.Z., 2012. 2-D Orthotropic failure criteria for masonry. Engineering Structures 36, 360–371.

Lourenço, P.B., 1996. Computational strategies for masonry structures. Delft University of Technology. Ph.D. thesis.

Lourenço, P.B., De Borst, R., Rots, J.G., 1997. A plane stress softening plasticity model for orthotropic materials. International Journal for Numerical Methods in Engineering 40, 4033–4057.

Lourenço, P.B., Rots, J.G., 1997. Multisurface interface model for analysis of masonry structures. Journal of Engineering Mechanics 123, 660–668.

Lubliner, J., Oliver, J., Oller, S., Oñate, E., 1989. A plastic-damage model for concrete. International Journal of Solids and Structures 25, 299–326.

Magenes, G., Calvi, G.M., 1997. In-plane seismic response of brick masonry walls. Earthquake Engineering and Structural Dynamics 26, 1091–1112.

Magenes, G., Calvi, G.M., Kingsley, G.R., 1995. Seismic testing of a full-scale, two-story masonry building: test procedure and measured experimental response. Experimental and numerical investigation on a brick masonry building prototype–numerical prediction of the experiment, Rep. 3.0. University of Pavia, Italy .

Maimí, P., Camanho, P.P., Mayugo, J.A., Dávila, C.G., 2007. A continuum damage model for composite laminates: Part I–constitutive model. Mechanics of Materials 39, 897–908.

Marcari, G., Basili, M., Vestroni, F., 2017. Experimental investigation of tuff masonry panels reinforced with surface bonded basalt textile-reinforced mortar. Composites Part B: Engineering 108, 131–142.

Marfia, S., 2000. Modellazione del calcestruzzo fibrorinforzato. Università degli Studi di Roma Tor Vergata, Italy. Ph.D. thesis.

Massart, T.J., Peerlings, R.H.J., Geers, M.G.D., 2007. An enhanced multi-scale approach for masonry wall computations with localization of damage. International Journal for Numerical Methods in Engineering 69, 1022–1059.

Matzenmiller, A., Lubliner, J., Taylor, R.L., 1995. A constitutive model for anisotropic damage in fiber-composites. Mechanics of Materials 20, 125–152.

McNary, W.S., Abrams, D.P., 1985. Mechanics of masonry in compression. Journal of Structural Engineering 111, 857–870.

Mercatoris, B.C.N., Massart, T.J., 2011. A coupled two-scale computational scheme for the failure of periodic quasi-brittle thin planar shells and its application to masonry. International Journal for Numerical Methods in Engineering 85, 1177–1206.

Minga, E., Macorini, L., Izzuddin, B.A., 2018. A 3D mesoscale damage-plasticity approach for masonry structures under cyclic loading. Meccanica 53, 1591–1611.

Naraine, K., Sinha, S., 1991. Cyclic behavior of brick masonry under biaxial compression. Journal of Structural Engineering 117, 1336–1355.

Nayfeh, A.H., Mook, D.T., 2008. Nonlinear oscillations. John Wiley & Sons.

NTC, 2008. Ministero Infrastrutture e Trasporti (MIT). D.M. 14.01.2008. Norme Tecniche per le Costruzioni. Rome, Italy.

Oliveira, D.V., Lourenço, P.B., 2004. Implementation and validation of a constitutive model for the cyclic behaviour of interface elements. Computers and Structures 82, 1451–1461.

Page, A.W., 1981. The biaxial compressive strength of brick masonry. Proceedings of the Institution of Civil Engineers 71, 893–906.

Page, A.W., 1983. The strength of brick masonry under biaxial tension-compression. International Journal of Masonry Construction 3, 26–31.

Page, A.W., Kleeman, P.W., Dhanasekar, M., 1985. An in-plane finite element model for brick masonry, in: New Analysis Techniques for Structural Masonry, ASCE. pp. 1–18.

Pelà, L., Cervera, M., Roca, P., 2013. An orthotropic damage model for the analysis of masonry structures. Construction and Building Materials 41, 957–967.

Petracca, M., 2016. Computational multiscale analysis of masonry structures. Polytechnic University of Catalonia. Ph.D. thesis.

Pijaudier-Cabot, G., Bažant, Z.P., 1987. Nonlocal damage theory. Journal of Engineering Mechanics 113, 1512–1533.

Van der Pluijm, R., 1993. Shear behavior of bed joints, in: 6th North American Masonry Conference, pp. 125–136.

Van der Pluijm, R., 1997. Non-linear behaviour of masonry under tension. Heron 42, 25–54.

Van der Pluijm, R., Rutten, H., Ceelen, M., 2000. Shear behaviour of bed joints, in: 12th International Brick/Block Masonry Conference, pp. 1849–1862.

Raijmakers, T.M.J., Vermeltfoort, A.T., 1992. Deformation controlled tests in masonry shear walls. Report B-92-1156. TNO-Bouw, Delft, The Netherlands.

Roca, P., Cervera, M., Gariup, G., Pelà, L., 2010. Structural analysis of masonry historical constructions. Classical and advanced approaches. Archives of Computational Methods in Engineering 17, 299–325.

Sacco, E., 2009. A nonlinear homogenization procedure for periodic masonry. European Journal of Mechanics-A/Solids 28, 209–222.

Sacco, E., Toti, J., 2010. Interface elements for the analysis of masonry structures. International Journal for Computational Methods in Engineering Science and Mechanics 11, 354–373.

Saritas, A., Filippou, F.C., 2009. Numerical integration of a class of 3d plastic-damage concrete models and condensation of 3d stress–strain relations for use in beam finite elements. Engineering Structures 31, 2327–2336.

Simon, J.W., Höwer, D., Stier, B., Reese, S., Fish, J., 2017. A regularized orthotropic continuum damage model for layered composites: intralaminar damage progression and delamination. Computational Mechanics 60, 445–463.

Smoljanović, H., Živaljić, N., Nikolić, Ž., 2013. Overview of the methods for the modelling of historical masonry structures. Gradevinar 65, 607–618.

de Souza Neto, E.A., Peric, D., Owen, D.R.J., 2011. Computational methods for plasticity: theory and applications. John Wiley & Sons Ltd.

Taylor, R.L., 2017. FEAP-A finite element analysis program. Version 8.5. Department of Civil and Environmental Engineering, University of California at Berkeley, California.

Tesei, C., Ventura, G., 2016. A unilateral nonlocal tensile damage model for masonry structures. Procedia Structural Integrity 2, 2690–2697.

Toti, J., Gattulli, V., Sacco, E., 2015. Nonlocal damage propagation in the dynamics of masonry elements. Computers and Structures 152, 215–227.

Valente, M., Milani, G., 2016. Non-linear dynamic and static analyses on eight historical masonry towers in the North-East of Italy. Engineering Structures 114, 241–270.

Williams, K.V., Vaziri, R., Poursartip, A., 2003. A physically based continuum damage mechanics model for thin laminated composite structures. International Journal of Solids and Structures 40, 2267–2300.

Wong, C.W., Ni, Y.Q., Ko, J.M., 1994a. Steady-state oscillation of hysteretic differential model. II: Performance analysis. Journal of Engineering Mechanics 120, 2299–2325.

Wong, C.W., Ni, Y.Q., Lau, S.L., 1994b. Steady-state oscillation of hysteretic differential model. I: Response analysis. Journal of Engineering Mechanics 120, 2271–2298.

Zucchini, A., Lourenço, P.B., 2009. A micro-mechanical homogenisation model for masonry: application to shear walls. International Journal of Solids and Structures 46, 871–886.